https://doi.org/10.35662/unine-thesis-2992

University of Neuchâtel
Faculty of Science
Laboratory of Technologies for Heritage Materials

Analysis and assessment of degradation of polychrome metal artworks

Dissertation submitted to the University of Neuchâtel for the degree of *Doctor ès Sciences*

Presented by **Silvia Russo**

Main thesis supervisor:
Prof. Edith Joseph, University of Neuchâtel
Thesis co-supervisor:
Assoc. Prof. Laura Brambilla, Haute Ecole Arc Conservation Restauration, Switzerland

Jury members:
Prof. Edith Joseph, University of Neuchâtel, Switzerland
Assoc. Prof. Laura Brambilla, Haute Ecole Arc Conservation Restauration, Switzerland
Assoc. Prof. Jean Baptiste Thomas, Norwegian Institute of Science and Technology, Norway
Prof. Katrien Keune, University of Amsterdam, The Netherlands
Dr. MER Cécilia Griener Hurley, University of Neuchâtel, Switzerland

Private defence: 05 October 2022
Public defence: 25 November 2022

This page was intentionally left blank.

UNIVERSITÉ DE NEUCHÂTEL

Faculté des Sciences
Secrétariat-décanat de Faculté
Rue Emile-Argand 11
2000 Neuchâtel – Suisse
Tél : + 41 (0)32 718 21 00
E-mail : secretariat.sciences@unine.ch

IMPRIMATUR POUR THESE DE DOCTORAT

La Faculté des sciences de l'Université de Neuchâtel autorise l'impression de la présente thèse soutenue par

Madame Silvia RUSSO

Titre:

"Analysis and assessment of degradation of polychrome metal artworks"

sur le rapport des membres du jury composé comme suit:

- Prof. ass. Edith Joseph, directrice de thèse, Université de Neuchâtel,
- Prof. ass. Laura Brambilla, co-directrice de thèse, Haute Ecole Arc, Neuchâtel
- Prof. Katrien Keune, Universiteit van Amsterdam, NL
- Dr Cecilia Griener Hurley, Université de Neuchâtel,
- Prof. ass. Jean-Baptiste Thomas, Norwegian University of Science and Technology, Trondheim, Norvège

Neuchâtel, le 7 novembre 2022 Le Doyen, Prof. R. Bshary

This page was intentionally left blank.

To the immune system,
to the ones who gave me mine,
and to the ones who made it stronger.

This page was intentionally left blank.

Contents

List of Figures

List of Tables

As a general approach, and when not restricted by proprietary software or well-established conventions, figures, plots and graphs use colourblind-accessible palettes.

Cercare e saper riconoscere chi e cosa,
in mezzo all'inferno non è inferno, e
farlo durare, e dargli spazio.

Italo Calvino. Le città invisibili. 1972

La composition doit être vraie. Nous
devons décrire ce qui est, ce que nous
voyons, ce que nous entendons, ce que
nous faisons. (...) Le mots qui
définissent les sentiments sont très
vagues; il vaut mieux éviter leur
emploi et s'en tenir à la description
des objets, des êtres humains et de
soi-même, c'est-à-dire la description
fidèle des faits.

Agota Kristof. Trilogie des jumeaux.
1986-1991

This page was intentionally left blank.

A

Abstract

This work focuses on non-destructive imaging techniques to investigate degradation due to the formation of metal soaps, especially in the early stages of the reaction. Studying the initial stage of the degradation can help design preventive conservation strategies, for which the main variables involved in the process can be adjusted to slow the process down. Imaging techniques also allow for the monitoring of the process since they provide spatial information together with spectral data that can be used to locate the same area of interest repeatedly over time and, therefore, to monitor the evolution of the species investigated and follow the growth of the searched compounds on the same region of the artwork.

In particular, the analytical protocol established in this thesis was aimed at investigating a specific class of cultural heritage objects, i.e., painted metals. This category refers to artworks made of a metal support that was then painted by artists using a range of industrial and homemade formulations. Specifically, in this work, oil-based formulations were considered, either utilised solely as a coating or in a mixture with a pigment to create a paint. Objects made in this manner can be found in the 15th – 16th century (e.g., miniature portraits), 18th and 19th centuries (e.g., technical objects), and 20th centuries (e.g., sculptures and paintings on copper and aluminium).

The chosen approach for developing the analytical protocol relied on model samples, i.e., the simplest representation of a class of objects consisting of a metal coupon and an oil coating. Copper and zinc substrates were chosen based on their reactivity toward fatty acids. The model samples were designed following historical sources and scientific literature, and their surfaces were documented before and after coating application in terms of roughness, thickness and homogeneity of the coating. Roughness parameters and thickness of the coating were measured to highlight possible inhomogeneities and correlate them with differences in the behaviour of the two substrates. The coated samples were then artificially aged to induce the formation of metal soaps. The methodological aspects that defined the ageing parameters are presented, as well as the result of a multivariate approach based on design of experiment methods (DoE), i.e., full factorial design. All samples were monitored during artificial ageing and characterised using several non-destructive analytical techniques, such as μ-FTIR, OCT, LIBS, μ-Raman, XRD, HSI

and IR thermography. FTIR 2D chemical imaging allowed us to follow the evolution of the reaction at an early stage and to infer whether the detection of the species of interest was influenced by the morphological characteristics of the samples and by the thickness of the coating. Complementary Raman analyses helped identify the crystalline species forming. Moreover, to investigate the interface between the metal and the oil coating without sampling, OCT and LIBS were employed, which provided information on the stratigraphy of the object and allowed detecting metal-organic compounds forming in contact with the metal within the first few micrometres of the oil coating. The results obtained through preliminary tests using XRD, HSI and IR thermography did not allow the detection of metal soaps and would require further investigation and optimization of the analytical parameters. However, these techniques were able to analyse other system parameters.

This work showed that, granted an appropriate choice of the analytical parameters, a combination of non-invasive imaging techniques could help elucidate and monitor the evolution of the reaction of formation of metal soaps on coated and painted metals, allowing designing appropriate conservation measures to prevent future damage.

Keywords metal soaps, metal carboxylates, imaging, painted metals, metal conservation, metal artefacts, degradation.

Résumé Comprendre les mécanismes de formation des savons métalliques sur les objets du patrimoine culturel peints à l'huile et l'implication de la présence de ces composés dans la dégradation des œuvres d'art est fondamental pour élaborer des stratégies de préservation adéquates. Depuis qu'ils ont été observés pour la première fois dans "La Leçon d'anatomie du docteur Tulp" à la Mauritshuis (Pays-Bas) à la fin des années 90, les savons métalliques ont fait l'objet d'une grande attention de la part des chercheurs et chercheuses travaillant dans le domaine du patrimoine culturel ayant étudié les aspects du mécanisme et de la cinétique des réactions, la relation entre leur apparition et la teneur en eau ou en humidité, leur migration et leur cristallisation, ainsi que leur rôle dans le développement de protubérances sur la surface de peintures. Plusieurs techniques analytiques et outils informatiques sont disponibles pour aider à comprendre, simuler et modéliser les différents aspects de la réaction. Ce travail se concentre sur les techniques d'imagerie non destructives pour étudier les dégradations dues à la formation de savons métalliques, en particulier dans les premiers stades de la réaction. L'étude du stade initial de la dégradation peut aider à concevoir des stratégies de conservation préventive, pour lesquelles les principales variables impliquées dans le processus peuvent être ajustées afin de ralentir le processus. Les techniques d'imagerie permettent également de suivre le processus. Elles fournissent des informations spatiales, ainsi que des données spectrales qui peuvent être utilisées pour localiser la même zone d'intérêt de manière répétée dans le temps et par conséquent, pour surveiller l'évolution des espèces étudiées et suivre la croissance des composés recherchés sur la même zone de l'œuvre d'art. Le protocole analytique établi dans cette thèse vise à étudier en particulier une catégorie spécifique d'objets du patrimoine culturel, à savoir les métaux peints. Cette catégorie fait référence aux œuvres d'art faites d'un support métallique qui a ensuite été peint par des artistes utilisant une large gamme de formulations industrielles ou artisanales. Plus précisément, dans ce travail, les formulations à base d'huile ont été considérées, soit utilisées uniquement comme revêtement, soit mélangées à un pigment pour créer une peinture. On trouve

des objets fabriqués de cette manière aux 15e et 16e siècles (par exemple, des portraits miniatures), aux 18e et 19e siècles (par exemple, des objets techniques) et au 20e siècle (par exemple, des sculptures et des peintures sur cuivre et aluminium). L'approche choisie pour développer le protocole analytique s'est appuyée sur des échantillons modèles, c'est-à-dire la représentation la plus simple d'une classe d'objets constituée d'un coupon métallique et d'un revêtement d'huile. Les substrats de cuivre et de zinc ont été choisis en fonction de leur réactivité vis-à-vis des acides gras. Les échantillons modèles ont été conçus selon des sources historiques et la littérature scientifique. La rugosité, l'épaisseur et l'homogénéité du revêtement surfaces a été documentée avant et après l'application du revêtement. Les paramètres de rugosité et d'épaisseur du revêtement ont été mesurés afin de mettre en évidence d'éventuelles hétérogénéités et de les corréler avec les différences de comportement des deux substrats. Les échantillons revêtus ont ensuite été vieillis artificiellement pour induire la formation de savons métalliques. Les aspects méthodologiques qui ont défini les paramètres de vieillissement sont présentés, ainsi que le résultat d'une approche multivariée basée sur la méthode de plan d'expérience (Design of Experience - DoE), c'est-à-dire un plan factoriel complet. Tous les échantillons ont été suivis pendant le vieillissement artificiel et caractérisés à l'aide de plusieurs techniques analytiques non destructives, telles que la μ-FTIR, l'OCT, le LIBS, la μ-Raman, la XRD, l'HSI et la thermographie IR. L'imagerie chimique 2D par FTIR nous a permis de suivre l'évolution de la réaction à un stade précoce et de déduire si la détection des espèces d'intérêt a été influencée par les caractéristiques morphologiques des échantillons et par l'épaisseur du revêtement. Des analyses en spectroscopie Raman complémentaires ont permis d'identifier les espèces cristallines en formation. En outre, pour étudier l'interface entre le métal et le revêtement d'huile sans prise d'échantillon, l'OCT et la LIBS ont été utilisés. Ces méthodes d'analyse ont fourni des informations sur la stratigraphie de l'objet et ont permis de détecter les composés organométalliques se formant au contact du métal dans les premiers micromètres du revêtement d'huile. Les résultats obtenus lors des tests préliminaires utilisant la XRD, l'HSI et la thermographie IR n'ont pas permis de détecter les savons métalliques et nécessiteraient une étude plus approfondie et une optimisation des paramètres analytiques. Cependant, ces techniques ont permis d'analyser d'autres paramètres du système. Ce travail a montré que, moyennant un choix approprié des paramètres analytiques, une combinaison de techniques d'imagerie non invasives peut aider à détecter et surveiller l'évolution de la réaction de formation des savons métalliques sur les métaux revêtus et peints, permettant ainsi de concevoir des mesures de conservation appropriées pour prévenir les dommages futurs.

Mots clés: savons métalliques, carboxylates métalliques, imagerie, métaux peints, conservation des métaux, artefacts métalliques, dégradation.

This page was intentionally left blank.

I

Introduction

> Vedo me stesso essenzialmente come un lettore. Mi è accaduto di avventurarmi a scrivere, ma ritengo che quello che ho letto sia molto più importante di quello che ho scritto. Si legge quello che piace leggere, ma non si scrive quello che si vorrebbe scrivere, bensì quello che si è capaci di scrivere.
>
> Jorge Luis Borges. L'invenzione della poesia. 1968

The formation of metal soaps is a chemical phenomenon commonly associated with oil paintings that has interested heritage and conservation scholars for almost two decades. It results from the reaction between fatty acids, e.g., in the oil binder and metal ions that could come from different sources, typically mineral pigments. The occurrence of metal soaps has been evaluated to concern about 70% of the collected paintings on canvas (Casadio et al., 2019; Izzo et al., 2021); it has challenged conservators and conservation scientists who tried to understand its mechanism of formation and the consequences for the artworks.

Metal soaps are, in fact, found in the correspondence of protrusions and blisters that appear on the surface of the paintings, which could exert mechanical pressure on the paint layers and cause fractures, defects and delamination phenomena (Casadio et al., 2019). However, metal soaps are not only a degradation phenomenon, or "foes", to borrow a terminology used by M. Cotte and co-authors in 2016 (Cotte et al., 2017). They can, in fact, also have a positive influence on the painting since they accelerate the drying process and stabilise the pictorial film. For this reason, synthetic metal soaps are purposefully added to modern formulations as siccatives (Gorkum and Bouwman, 2005).

Aside from oil paintings, metal soaps can be found in objects of all sorts as long as a source of fatty acids interacts chemically with a source of metal ions. In leather and wood composite objects, where metal parts - in particular made of copper and copper-based alloys

- are present, conservator-restorers often identify metal soaps as greasy green efflorescence evolving from around the metal parts. This is a well-known degradation feature that is removed mechanically when necessary. However, the degradation process and effects on the preservation of the artwork are seldom investigated and clarified.

When the oil formulation is applied directly on a metal sheet as a coating or paint, metal soaps can form between the coating or paint layer and the support. Heritage scientists have so far understudied such a system, and it is not necessarily trivial to apply the knowledge acquired in understanding the formation of metal soaps within the paint layers of paintings on canvas to this peculiar class of artworks. For this reason, an investigation of the peculiarities of the interfacial process that brings to the formation of metal soaps, both at an early stage and later stages of degradation, is needed and represents the focus of this work. The aim is to start the conversation on this class of composite artworks with the hope that the results presented herein may interest the reader and be useful to some.

Objectives and research questions The work presented here focused on the study of the formation of metal carboxylates (soaps) on painted metals. The aim of the research was to understand the mechanism of degradation of paintings on metal due to metal soaps formation and to develop a methodology based on multi-modal analyses for the assessment of the different factors related to the degradation processes of coated and polychrome metallic artworks. Complementary state-of-the-art spectroscopic and imaging techniques were deployed to study this degradation phenomenon.

A set of research questions were defined in order to achieve the main goal:

- Do metal soaps form on coated/painted metals?
- Do metal soaps form at the interface between the metal and the oil paint or coating? In other words, is the presence of the pigment competing with the metal substrate in providing metal ions for the reaction? And can migration of species be observed, that could result in detection of metal soaps outside of the interfacial area between the metal and the paint/coating layer?
- What are the characteristics of the chemical process involved, and what is its relationship with the metal constituting the support?
- What are the main compounds formed, and how are they spatially distributed?
- How to optimise the analytical protocol to allow the proper identification of metal soaps' early formation on the painted metal objects?
- How to monitor the changes due to the ongoing degradation process over a certain period of time?

Answers to these questions are distributed throughout the manuscript, with the ultimate scope to contribute to the preservation of such fascinating and complex composite artworks.

Structure of the manuscript This manuscript is divided into four chapters, designed to be independent yet linked by a narrative.

In the first chapter, an introduction to the physico-chemical characteristics of metal soaps and the chemistry of their formation is provided. An overview of the presence and use of metal soaps in different industrial applications is presented. In addition, a section

dedicated to their occurrence in the cultural heritage context is given. This compendium is corroborated by analyses conducted on museum objects thanks to collaborations with the conservator-restorers members of the research team at the Haute Ecole Arc Conservation Restauration (HE-Arc) in Neuchâtel, namely Elodie Granget, Julie Schröter and Naïma Gutknecht, the Bachelor and Master students of the HE-Arc (Léa Girardin, Alessandra Lefebvre, Florentine Le Vaillant), Markus Küffner (Hochschule der Künste Bern (HKB)), and Jacek Martusewicz (Academy of Fine Arts, Krakow).

The second chapter provides information and results of the methodological choices made in the design of model samples that would be representative of copper and zinc coated and painted metal objects. In detail, this discusses the choice of substrate and surface finishing and the consequences of the final characteristics on the quality of the applied oil coating. Proofs of their effectiveness and solutions to encountered problems are provided. Additionally, the accelerated ageing methodology is discussed through the results of a study based on a multivariate approach using full factorial design of experiment.

The third chapter concerns aspects of the detectability of metal soaps. Here, non-destructive analytical techniques were deployed on copper and zinc model samples. In particular, the results, limits and potentialities of mid-infrared and Raman microspectroscopies, visible-near infrared and short-wave infrared hyperspectral imaging, X-ray diffraction and infrared thermography are presented.

Using the information given by infrared spectroscopic data in Chapter 3, **the fourth chapter** builds up on the use of 2D chemical imaging to investigate aspects of the mechanism of formation of metal soaps. The results of the chemical mapping are integrated with Spectral Domain - Optical Computed Tomography (SD-OCT) and Laser-Induced Breakdown Spectroscopy (LIBS) analyses to infer the interface characteristics of the reaction. OCT and LIBS analysis were performed at ITN-CHANGE partner institution Centre de recherche et de restauration des musées de France (C2RMF), under the supervision of Dr. Xueshi Bai.

General conclusions of the study and future perspectives are commented in **Chapter five**.

General context of the project: the MSCA ITN-CHANGE Programme This three years-long project, which started in September 2019, was conducted in the framework of the Innovative Training Network Marie Sklodowska Curie Action - Cultural Heritage Analysis for New GEnerations (MSCA ITN-CHANGE, grant agreement No. 813789, `(https://change-itn.eu/)`.

The ITN-CHANGE project aimed at forming fifteen young professionals (Early Stage Researchers, ESRs) in the field of imaging and conservation science by offering a collaborative and interdisciplinary environment. Multi-modal imaging techniques could be accessed in association with more traditional and state-of-the-art analytical methods to assess and monitor changes occurring on cultural heritage artefacts over time. In particular, the candidate worked on the above-mentioned objectives as ESR11.

The University of Applied Sciences and Arts Western Switzerland (HES-SO) represented by the Conservation Research Unit at Haute Ecole Arc (UR-Arc CR), located in Neuchâtel, Switzerland was one of the nine beneficiaries of the project. Within this framework, collaborations with partner Institutions were established. In particular, the secondments at the Rijksmuseum and the Centre de recherche et de restauration des musées de France (C2RMF) greatly contributed to the development of this research project.

Bibliography

Casadio, F., Keune, K., Noble, P., Van Loon, A., Hendriks, E., Centeno, S. A., and Osmond, G., eds. (2019). *Metal Soaps in Art: Conservation and Research*. Cultural Heritage Science. Cham: Springer International Publishing. ISBN: 978-3-319-90617-1.

Cotte, M., Checroun, E., De Nolf, W., Taniguchi, Y., De Viguerie, L., Burghammer, M., Walter, P., et al. (Jan. 2, 2017). Lead soaps in paintings: Friends or foes? *Studies in Conservation* **62**(1): 2–23. DOI: 10.1080/00393630.2016.1232529.

Gorkum, R. van and Bouwman, E. (2005). The oxidative drying of alkyd paint catalysed by metal complexes. *Coordination Chemistry Reviews* **249**(17): 1709–1728. DOI: 10.1016/j.ccr.2005.02.002.

Izzo, F. C., Kratter, M., Nevin, A., and Zendri, E. (2021). A Critical Review on the Analysis of Metal Soaps in Oil Paintings. *ChemistryOpen* **10**(9): 904–921. DOI: 10.1002/open.202100166.

CHAPTER 1

But aren't all soaps metal soaps?

A review of physico-chemical properties of metal soaps, applications, and their occurrence in cultural heritage studies

Adapted from Russo S., Brambilla L., Thomas J.B., and Joseph E. 2022. But aren't all soaps metal soaps? A review of applications, physico-chemical properties of metal soaps and their occurrence in cultural heritage studies, [in preparation]

Metal soaps, i.e., the organic salts resulting from the interaction of fatty acids and metal cations, arouse interest in the scientific field because of their versatility in a great range of chemical applications. This chapter presents a review of the synthetic pathways used to produce metal soaps, their relevant physico-chemical properties, and how these reflect in their applications. Common industrial uses of metal soaps are reported, with particular focus on those that have an impact on the cultural heritage field (ancient cosmetics, paints, and coatings production). In addition, the occurrence of metal soaps in cultural heritage studies is presented, ranging from archaeological and ethnographic artefacts to fine arts objects, and discussed per class of materials. An overview of the presence or absence of metal soaps on a series of historical artefacts analysed during this doctoral work is given herein. This showed a variety of situations in which metal soaps – particularly copper soaps – can form on stored and displayed composite objects made of wood, leather, metal or metal alloys in the presence of fatty-acid-containing materials.

1.1 Introduction

From a purely chemical perspective, soaps consist of a metal cation and a carboxylate anion. However, in the common acceptance of the term, only the alkaline salts – those of soda and potash – and the ones of ammonia are regarded as soaps (Whitmore and Lauro, 1930). Even so, many soaps are made from other metals, typically heavy-metal

cations, and they differ from alkaline soaps because of their water insolubility and increased solubility in non-polar solvents (Bossert, 1950). They are referred to as metal soaps to distinguish them from ordinary alkaline-metal soaps, and they have been employed in various applications based on their chemical properties. Twenty-seven metals, including Al, Ca, Zn, Mg, Pb, Mn, Cu, and Co, in combination with common fatty acids such as stearic, palmitic, oleic, linoleic, and less mentioned ones such as naphthenic, tall-oil and rosin acids have been reported to form metal soaps (Bossert, 1950).

Production of soaps and metal soaps Saponification is the alkaline hydrolysis of fatty acid esters that results in the formation of the metal salt of a fatty acid. The general reaction mechanism, which is catalysed by a strong acid or base, consists of three main steps (alkaline-catalysed hydrolysis is shown here) (Smith and March, 2020):

a) Nucleophilic attack on the carbonyl group of the ester by the hydroxide anion, with the production of the orthoester **(1)**;

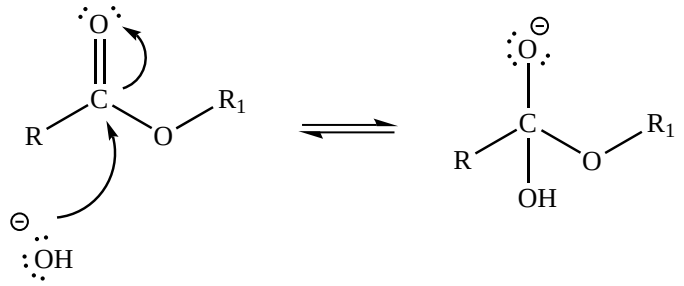

(1)

b) Leaving group removal, and generation of the carboxylic acid and the alkoxide **(2)**;

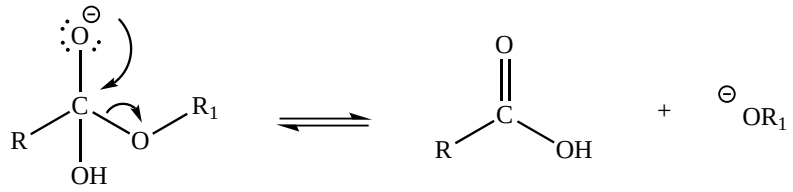

(2)

c) Deprotonation of the carboxylic acid by the alkoxide ion (strong base) and production of the carboxylate ion and the alcohol **(3)**.

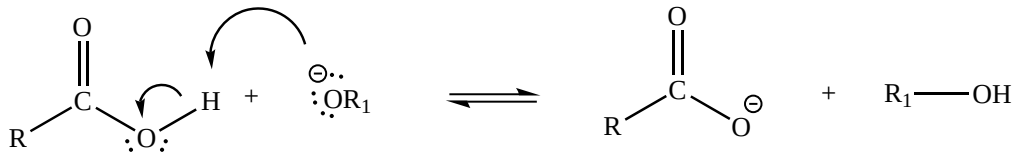

(3)

Alternatively, the soap industry also utilises the neutralisation method, i.e., a reaction where the carboxylic acid is neutralised in the presence of a base to synthesise metal soaps derived from magnesium, transition metals, and aluminium. This method is ideal for the selective production of single fatty acids soaps. Moreover, this is a required synthetic step in producing soaps with controlled physico-chemical characteristics (Bossert, 1950; Pearl, 2016).

Soaps of heavy metals are prepared through two main chemical mechanisms of synthesis, i.e., precipitation and fusion (Bossert, 1950; Pearl, 2016). The first method is a double

decomposition reaction (metathesis), where an aqueous-alcoholic solution of a soluble salt (typically sulphates, nitrates, or chlorides of a metal (M)) is made to react with a soluble alkali salt of the fatty acid **(4)** (Whitmore and Lauro, 1930; Bossert, 1950; Essien et al., 2012). This reaction which transforms a soap into another soap is also called "trans-saponification" as an adaptation of the "trans-esterification" mechanism (Sutrisno et al., 2021). The metal soaps made following this process appear as a highly hydrated precipitate at the bottom of the solution.

$$MSO_4 + 2\,RCOONa \longrightarrow (RCOO)_2M + Na_2SO_4 \quad \textbf{(4)}$$

In a work by Corbeil and Robinet, this two-step precipitation method was used to synthesise soaps of zinc, lead, and copper cations (Corbeil and Robinet, 2002). However, only the oleate of zinc, lead and copper ions, and zinc linoleate were obtained as solid crystalline salts; the other combinations of oleic and linoleic salts with Zn, Pb, and Cu cations resulted in amorphous agglomerates. Other studies have reported poor crystallinity of synthetic metal soaps depending on the solvent in which the reaction occurs (Bossert, 1950).

In the *fusion method*, the carboxylic acid and the oxides, hydroxides (Yu et al., 2004) and salts of the desired metal, e.g., carbonates (Bossert, 1950), nitrates (Whitmore and Lauro, 1930; Lin and Kim, 2012), and acetates (Hermans et al., 2014) are made to react directly at an elevated temperature ($180 - 300$ °C) (Bossert, 1950). By using this method, Yu et al. produced iron (III) oleate as precursors of iron oxide nanoparticles (Yu et al., 2004). A description of the general reaction is provided below, using oxides, hydroxides, and carbonates as reagents (**(5)** – **(7)**).

Since the 1950s, several patents were granted that describe the synthetic pathways for the manufacture of metal soaps (e.g., U.S. Pat. No. 2,650,932 (Kebrich and Pitrot, 1953), U.S. Pat. No. 2,890,232 (H Rogers and R Blew, 1959), U.S. Pat. No. 2,945,051 (Davis, 1960), U.S. Pat. No. 3,803,188 (Scott et al., 1974), and U.S. Pat. No. 4,316,852 (Blachford, 1982)).

$$2\,RCOOH + MO \longrightarrow (RCOO)_2M + H_2O \quad \textbf{(5)}$$

$$2\,RCOOH + M(OH)_2 \longrightarrow (RCOO)_2M + 2\,H_2O \quad \textbf{(6)}$$

$$2\,RCOOH + M(CO)_3 \longrightarrow (RCOO)_2M + H_2O + CO_2 \quad \textbf{(7)}$$

Other synthesis methods include electrochemical methods. Scientific literature primarily refers to the synthesis of copper carboxylates through electrochemical methods (Nordin et al., 2015; Carvalho, 2022). These methods are employed because they present several advantages concerning reaction selectivity, rate control and the possibility of having a "reagent-free" reaction (Nordin et al., 2015). The reaction occurs in the organic phase between carboxylic acids and Cu(II) ions generated in the aqueous phase solution from the corroded anode (in presence of chlorides) (**(8)** – **(11)**).

Anode $\mathrm{Cu^0 \longrightarrow Cu^{2+} + 2\,e^-}$ **(8)**

Catode $\mathrm{2\,e^- + 2\,H_2O \longrightarrow H_2 + 2\,OH^-}$ **(9)**

$\mathrm{2\,OH^- + 2\,CH_3(CH_2)_7CH{=}CH(CH_2)_7COOH \longrightarrow 2\,H_2O + 2\,CH_3(CH_2)_7CH{=}CH(CH_2)_7COO^-}$ **(10)**

Overall reaction $\mathrm{Cu^0 + {}_2CH_3(CH_2)_7CH{=}CH(CH_2)_7COOH \longrightarrow Cu[CH_3(CH_2)_{16}COO]_2 + H_2}$ **(11)**

Similarly to the traditional chemical methods, electrochemical reactions can also be multi-step, where an alkaline metal soap is first produced and then made to react with the copper corrosion products formed locally at the anode (Carvalho, 2022). According to Carvalho (2022), by using this method from palmitates as precursors, a pure compound could not be obtained, but rather a mixture of copper palmitate ($\mathrm{C_{64}H_{128}Cu_2O_8}$), cuprite ($\mathrm{Cu_2O}$) and atacamite ($\mathrm{Cu_2Cl(OH)_3}$), due to the presence of chlorides in the electrolytic cell to increase the conductivity of the electrolyte. The proposed anodic (**(12)** – **(17)**) and cathodic (**(18)** – **(20)**) reactions for this process, which is inspired by the production of verdigris pigment, are:

Anode $\mathrm{2\,Cu + H_2O \rightleftharpoons Cu_2O + 2\,H^+ + 2\,e^-}$ **(12)**

$\mathrm{2\,Cu + 3\,H_2O + Cl^- \rightleftharpoons Cu_2(OH)_3Cl + 3\,H^+ + 2\,e^-}$ **(13)**

$\mathrm{Cu^{n+} + nRCOONa \rightleftharpoons (RCOO)_nCu + nNa^+}$ **(14)**

$\mathrm{Cu^{n+} + nRCOO^- \rightleftharpoons (RCOO)_nCu}$ **(15)**

$\mathrm{Cu \rightleftharpoons Cu_2^+ + e^-}$ **(16)**

$\mathrm{Cu \rightleftharpoons Cu^+ + e^-}$ **(17)**

Catode $\mathrm{2\,e^- + 2\,H_2O \longrightarrow H_2 + 2\,OH^-}$ **(18)**

$\mathrm{e^- + Na^+ \longrightarrow Na}$ **(19)**

$\mathrm{Cu^{2+} + 2\,e^- \longrightarrow Cu^0}$ **(20)**

Properties of metal soaps Physico-chemical properties of metal soaps are strongly related to their structure and the nature of the metal. Colour is dictated by the electronic configuration of the cation, resulting in a similar colouration to the one of their most common salts. Nickel and copper soaps will therefore be expected to assume green colouration; saponification of lead, zinc, aluminium and alkaline metals will result in white soaps, manganese soaps will be lavender in colour, and iron soaps show red-to-brown hues (Whitmore and Lauro, 1930; Bossert, 1950; Sutrisno et al., 2021).

Due to the difficulties in obtaining such compounds in the purest form, melting points are not uniquely defined, and a range of temperatures is instead provided (Bossert, 1950). Nevertheless, the melting point of different metal soaps showed trends that can be related to the characteristics of the cations and can provide interesting information about their expected spectral behaviour (Sutrisno et al., 2021). In a dedicated study, Sutrisno and co-workers demonstrated that the synthesis and characterisation of Zn, Al, and Mg soaps from

sunflower oil showed inverse proportionality between melting points and ionic character, or, in other words, a positive correlation between the metal soaps melting point values and the covalent character of the corresponding cation-anion bond (Sutrisno et al., 2021). The ionic character of a bond is determined by the polarisation of the ions, which is a combination of the ionic radius and the effective nuclear charge. In practical terms, ions having a smaller ionic radius and a higher charge will be more prone to polarise the bond strongly. The result of this is that Zn^{2+} ions that have a greater nuclear charge than K^{+}, Mg^{2+} and Al^{3+}, even though they have a larger ionic radius, will be more capable of polarising carboxylate anions than other cations (Sutrisno et al., 2021).

Along with the decrease and increase in melting point, other properties of the carboxylate compounds are affected by the presence or absence of polarisation. For instance, when the covalent character of the bond increases, the solubility of the soap in polar solvents will also reduce, and the corresponding IR spectra will show a shift in the carboxylate stretching vibrations (νCOO^{-}) (Sutrisno et al., 2021). A shift towards higher frequency will be noticed for the COO^{-} asymmetrical stretching band, whilst the symmetrical band will be found at a lower frequency.

Metal soaps are highly hygroscopic. They are poorly soluble in water but solubilise easily in organic solvents such as benzene or fatty oils. Additionally, heavy-metal carboxylates possess a combination of polar and non-polar functions within the same molecule (Bossert, 1950), see Figure 1.1). This property, which can be quantified by hydrophilic-lipophilic balance (HLB) values in the range 13-16 (Griffin, 1949; Gadhave, 2014), determines most of their applications that exploit the alkyl chain's hydrophobicity and the metal cation's catalytic action. Table 1.1 provides a summary of the properties of different soaps.

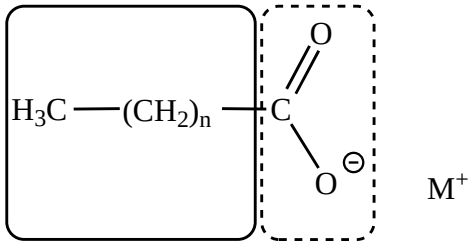

Figure 1.1: The hydrophobic – hydrophilic double nature of metal carboxylates. The full and dotted lines highlight the hydrophobic alkyl radical and the carboxylate group, respectively.

Table 1.1: Table of properties of a selection of metal soaps. The table is compiled from Bossert, 1950; Whitmore and Lauro, 1930; Dalen and Mamza, 2010; Shekhter et al., 1975; PubChem, 2022; ChemSrc, 2022; ChemicalBook, 2022; American Elements, 2022.

Group	IA	IIA	
Metal	Na	K	Mg
Phase	Solid Liquid (myristate)	Solid and liquid (myristate liquid only)	Solid
Microscopic structure	White crystals or yellow amorphous granules	Crystalline and amourphous (oleate)	Crystalline and amorphous (oleate)
Color	White to yellow	White to yellow-brown	White
Melting point	44 (laurate) - 290 °C (palmitate)	44 (laurate) - 240 °C (oleate)	44 (laurate) - 200 °C (stearate)
Solubility (room temperature)	Soluble in water (oleate)	Soluble in water, alcohol and ether (oleate)	Soluble in linseed oil (oleate) Insoluble in water
Common soaps	Oleate Stearate Palmitate Laurate Myristate Erucate	Oleate Stearate Palmitate Laurate Myristate Erucate	Oleate Stearate Palmitate Laurate Myristate
Uses	Rubber latex paints and inks, emulsifier of pigments in paints, thickening agents for inks and gels, lubricant, creams, lotions, food packaging	Emulsifier, lubricant, thickener	Lubricant and release agent, extrusion and molding of ABS and SAN polymers, anti-tacking agent in uncured rubber stock applications

Table 1.1: Table of properties of a selection of metal soaps (continued).

Group	IIA		VIIB
Metal	Ca	Ba	Co
Phase	Solid (stearate, laurate) Liquid (oleate, palmitate, myristate)	Solid (stearate, laurate) Liquid (oleate)	Solid (stearate)
Microscopic structure	Mustly crystalline	Mostly crystalline	Crystalline or amorphous
Color	White	White	Lavander (crystalline), brown (amorphous)
Melting point	44 (laurate) - 179 °C (stearate)	225 °C (stearate)	110 (stearate) - 235 °C (oleate)
Solubility (room temperature)	Slightly soluble in water (stearate) Insoluble in alcohol and ether (stearate)	Slightly soluble in water (stearate)	Insoluble in water (oleate, stearate) Soluble in alcohol, ether (oleate)
Common soaps	Oleate Stearate Palmitate Laurate Myristate	Oleate Stearate Palmitate Laurate Myristate	Oleate Stearate Palmitate Laurate Myristate
Uses	Acid scavenging agent, lubricant, mold release agent, polyolefin polymerization to consume residual catalyst	Co-stabiliser for PVC, coloring and glossing agent, lubricant, optical coating	Driers for paints and varnishes [CB]

Table 1.1: Table of properties of a selection of metal soaps (continued).

Group	VIIIB	IB	
Metal	Ni	Cu	Ag
Phase	Solid Liquid (oleate)	Crayon-like mass (oleate) to powder	Solid
Microscopic structure	Mostly crystalline	Mostly amorphous	Amorphous (water solution) Can be prepared crystalline (alcohol solution) Except for oleate
Color	Bluish-green to green	Blue to light blue	Gray-white to yellowish
Melting point	18 (oleate) - 100 °C (stearate)	100 (oleate) - 135 °C (stearate)	200 °C
Solubility (room temperature)	Soluble in water (oleate) [whitmore 1930] Insolube in water (stearate)	Quite soluble in water (palmitate) [1930, whitmore] Slightly soluble in water (laurate, erucate) Soluble in ether (oleate)	Soluble in water Soluble in alcohol
Common soaps	Oleate Stearate Palmitate Laurate Myristate Erucate	Oleate Stearate Palmitate Laurate Myristate Erucate	Oleate Stearate Palmitate Laurate Myristate Erucate
Uses	They are widely used as lubricants, slipping agents, heat-stabilizers, mold releasing agents, and accelerants in plastic, machinery engineering, rubber, paints, and inks industry.	Used in anti-fouling paints, textile and wood preservatives, and as a catalyst.	Comprehensive information not readily available.

Table 1.1: Table of properties of a selection of metal soaps (continued).

Group	IIB		
Metal	Zn	Cd	Hg
Phase	Waxy powder (oleate, erucate) Light, fluffy powder (stearate, palmitate, laurate)	Solid powder (stearate)	Semi-liquid (oleate) Fine powder (starate, palmitate, laurate) Parafifin-like solid (erucate)
Microscopic structure	Amorphous to crystalline	Crystalline	Amorphous to crystalline
Color	Cream-coloured (oleate) to white	White	White
Melting point	70 (oleate) - 130 °C (stearate, palmitate)	110 °C (stearate)	(-39 (oleate) - 112 °C (stearate)
Solubility (room temperature)	Insoluble in polar solvents Soluble in aromatic hydrocarbons when heated	Slightly soluble to insoluble in water	Insoluble in water Slightly soluble alcohol, ether Very soluble in fixed oils
Common soaps	Oleate Stearate Palmitate Laurate Myristate Erucate	Oleate Stearate Palmitate Laurate Myristate	Oleate Stearate Palmitate Laurate Erucate
Uses	Provides hydrophobic effect Thickening and dispersing agent Activator in rubber sulphur vicanization Stabiliser for PVC Acid scavenger in polyethylene polyurethanes, and polystyrene processing Sanding agent in wood varnishes, lubricant	Heat and light stabiliser for PVC Restricts UV degradation and yellowing of plastic Lubricant and stabilizer for polyvinyl chloride	Used in medicine, antiseptic and antifouling paint.

Table 1.1: Table of properties of a selection of metal soaps (continued).

Group	IIIA	IVA
Metal	Al	Pb
Phase	Solid powder (stearate)	Wax-like solid (oleate) Solid (stearate)
Microscopic structure	Mostly crystalline	Crystalline
Color	White (oleate) to yellow (palmitate)	White to yellow (oleate; when melted)
Melting point	63 (palmitate) - 118 °C (stearate)	50 °C (oleate) - 113 °C (palmitate)
Solubility (room temperature)	Insoluble in water (stearate, palmitate) Soluble in mineral oils (oleate) Soluble in oil turpentine (palmitate)	Insoluble in water (stearate) Soluble in hot alcohol (stearate)
Common soaps	Oleate Stearate Palmitate Laurate Myristate	Oleate Stearate Palmitate Laurate Erucate
Uses	Lubricants Gelling plasticisers Coating formulations Ink manufacturing Metal processing Grease manufacturing	External lubricant for PVC and heat stabiliser Varnishes and extreme pressure lubricants

Uses of metal soaps As previously mentioned, the hydrophobic-hydrophilic nature of the two extremities of the metal carboxylate molecules allows for a wide range of applications. They can be utilised as emulsifiers for water-in-oil (W/O) emulsions. For this reason, they are often found in cosmetics and lubricants as additives.

Besides their colloidal and surface-active properties, they are also used in cosmetic and pharmaceutical applications for their antibacterial properties (copper soaps) or excipients. Cosmetic and pharmaceutical properties of lead oleate have been known since antiquity, as reported by the Greek physician, pharmacologist, and botanist Dioscorides in De materia medica (1st century AD) (Whitmore and Lauro, 1930). Evidence of the presence of lead palmitate in cosmetic products was also found in Ancient Egyptian (18^{th} dynasty) containers preserved at the Louvre Museum, possibly being a degradation product from lead-based compounds added to the ancient formulation (Cotte et al., 2005). In contemporary times, some countries have authorised sodium stearates in creams, lotions, animal food, and packaging[1,2,3]. In cosmetics, sodium and zinc stearates are added as a lubricant and thickening agent to improve texture; aluminium, magnesium, calcium and zinc stearate are used as pharmaceutical excipients in the manufacture of ointments, powders, and tablets[4].

In the plastics industry, metal soaps are widely used in the manufacture of PVC products and during the processing of numerous plastics, including polyamide, polyethene, polypropylene, acrylonitrile butadiene styrene (ABS), and fibre-reinforced plastics (sheet moulding compound, SMC, and bulk moulding compound BMC). In addition, calcium stearate, barium stearate, and their laurates, used as internal lubricants in PVC formulations, also act as co-stabilisers that increase the heat stability of plastics. Other examples include mixed calcium/zinc soaps, which are used as a heat stabiliser for polyvinyl chloride (Putrawan et al., 2022). Among zinc soaps that are used as external lubricants in PVC formulations, zinc stearate and zinc laurate also have a reducing effect on the initial colouring (Ye et al., 2019). Some metallic soaps have catalytic properties and are used as colour binders or activators in rubber vulcanisation.

The hydrophobicity of metal soaps is exploited in the building industry, where they are added as water-resistant agents. Additionally, they are used as surcharge and lubricating agents in a variety of applications in the pencil, grease, metal, and paper industries. In the latter, metal soaps also serve as chelating agents for pigments.

A relevant field of application is that of the paint industry, where metal soaps are added to the paint to obtain matte and abrasive coatings and to accelerate the drying process of the industrial formulations. An overview of industrial uses of metal soaps can be found in Bossert, 1950.

---

[1] *Food Additives Permitted for Direct Addition to Food for Human Consumption - Gums, Chewing Gum Bases and Related Substances* (Mar. 29, 2022). 21CFR172.615.

[2] *Food Additives Permitted for Direct Addition to Food for Human Consumption - Multipurpose Additives* (Mar. 29, 2022). 21CFR172.863.

[3] *Food Additives Permitted in Feed and Drinking Water of Animals - Food Additive Listing* (Mar. 29, 2022). 21CFR573.280.

[4] Final Report of the Safety Assessment of Lithium Stearate, Aluminum Distearate, Aluminum Stearate, Aluminum Tristearate, Ammonium Stearate, Calcium Stearate, Magnesium Stearate, Potassium Stearate, Sodium Stearate, and Zinc Stearate (1990). *Journal of the American College of Toxicology*, **1**(2): 143–177. Doi: 10.3109/10915818209013152.

Metal soaps as oil paint siccative The use of metal soaps as siccatives (drying agents or driers) that act as catalysers in the polymerisation reaction of oil paints is particularly relevant for art conservation.

Driers can be grouped into three categories:

- primary driers (also called active or oxidation driers),
- secondary driers (also called through-driers),
- auxiliary driers.

Primary driers are autoxidation catalysts that act when the surface dioxygen concentration is the highest. Autoxidation catalysis depends on the two accessible valence states of the metal drier to perform hydroperoxide decomposition. Cobalt is the most widely used metal in primary driers. Its advantages reside in effectiveness at room temperature and compatibility with a broad range of coatings and varnishes. However, cobalt soaps have been reported to incur deactivation problems, or the so-called "loss of dry", through the formation of insoluble cobalt(III) hydroxides (Boer et al., 2013). Loss of drying occurs in pigment-containing paints upon ageing, where the drying times stretch and become ineffective after a particular storage time. The reason for this phenomenon can be identified in the failure of the drier's action due to surface adsorption, hydrolysis (especially for waterborne paints), and, like in the case of cobalt driers, the formation of insoluble compounds of the drier metal (Boer et al., 2013). For this reason, most researchers are investigating the possibility of replacing cobalt in the design of new driers. In several studies, manganese was examined as a substitute for cobalt (Bouwman and Gorkum, 2007, Gezici-Koç et al., 2016).

Manganese soaps were already used as primary driers, often in combination with cobalt soaps. The addition of amine ligands was found to significantly enhance the autoxidation activity of manganese soaps. However, a disadvantage of using manganese is the brown colour of its compounds in trivalent state, which makes them not compatible for applications to light coloured or white paints (Bouwman and Gorkum, 2007, Gezici-Koç et al., 2016).

Iron complexes are known for their redox catalytic properties in aqueous solutions. However, in apolar solvents and at room temperature, they are not good dryer catalysts since Fe(III) ions are not easily reduced (Gorkum and Bouwman, 2005). This behaviour impedes the redox cycle necessary for catalytic hydroperoxide decomposition. Moreover, like manganese soaps, iron complexes are intensely coloured, narrowing their application possibilities (Gorkum and Bouwman, 2005).

As a general practice, primary driers are used only in co-presence with a secondary or auxiliary drier (Gorkum and Bouwman, 2005).

Secondary driers are responsible for cross-linking of the paint layer. Lead has traditionally been used as a secondary drier. After its ban worldwide, zirconium has been widely accepted as its replacement. Alkyd paints have been reported to dry quicker with a combination of bismuth soaps and cobalt driers. Barium, strontium, and aluminium are other known alternatives to lead-based driers. However, the latter can cause embrittlement of the paint layers (Gorkum and Bouwman, 2005).

As their name suggests, *auxiliary driers* are used in combination with other driers, i.e., primary driers, to enhance their activity. Their molecular mechanism of action is not

known – some of them are only known for retarding the action of the primary drier – but they have visible positive effects on the overall quality of the paint film. Calcium is one of the most used auxiliary driers. It improves the hardness and gloss of the paint films, also under harsh environmental conditions (Gorkum and Bouwman, 2005). Zinc, lithium, and potassium driers are used in combination with cobalt driers in paint films, where they help regulate the overall drying rate, hence inhibiting the wrinkling of the paint film (Gorkum and Bouwman, 2005). Driers are often used in combination to increase viscosity rate change in the paint film. Frequently used drier combinations are, for example, Co/Zr/Ca, Co/Pb/Ca, or Mn/Zr/Ca (Gorkum and Bouwman, 2005).

Cobalt, manganese, iron, and lead soaps are ubiquitously added to modern paint formulations to promote the oxidation and cross-linking of unsaturated oils. In the 90s, when metal soap investigation developed in the cultural heritage field (Noble, 2019), some studies focused on the history of siccative compounds for oil formulations.

According to a comprehensive work by Leslie Carlyle on driers in 19th century Britain, during this period, the oxidative mechanisms through uptake of oxygen from the oil medium were understood, and driers were defined as agents that would catalyse the process of curing of the oil (Carlyle, 1999). Until the 1860s, these were mainly metal compounds and their pigments, often based on lead, zinc, and occasionally, copper in the form of verdigris. However, after this period, and especially after the 1890s, British oil painting manuals started mentioning the use of manganese-based compounds as driers. Historical sources hint that cobalt driers were also known, but they do not appear in catalogues or handbooks of the time (Carlyle, 1999).

Litharge, white lead, and red lead were the lead-based driers used in the preparation of drying oil during the 19th century. However, until the 1890s, lead acetate was the only lead drier available in 19th-century artists' colourmen's catalogues. Scott Taylor reported in 1890 that lead pigments and compounds, especially those containing at least 30% lead hydroxide, would be chemically active, which would be detrimental to the oil and other pigmented oil formulations. The role of lead soaps as driers was only mentioned in the early 1970s of the 20th century.

Zinc-based compounds were deployed as drier *de facto* throughout the 19th century; manganese was introduced later as a replacement for lead (Carlyle, 1999).

In the early 1920s, metal naphthenates became the first modern driers to be developed for the purpose (Gorkum and Bouwman, 2005). The most recent siccatives are based on synthetic acids, such as 2-ethyl hexanoic acid and versatic acid. Due to their branched structure, these have the advantage of being highly soluble in apolar mediums like the oil-binder system (Gorkum and Bouwman, 2005).

1.2 Metal soaps studies in Cultural Heritage

Besides their intentional presence as dryers in modern formulations, metal soaps also form naturally as the result of a saponification reaction that occurs in fatty-acids-rich materials when the organic component is in intimate contact with a source of metal ions. Numerous composite objects exist where metal ions are provided by a metal substrate or by a core element of mineral pigments. In the same way, the reactive fatty acids can be present in many organic elements of the object, such as wood, fabric, and leather, or as breakdown products of lipid-containing organic remains in archaeological findings

(Filopoulou et al., 2021). In traditional paintings, the metal ions are only provided by the mineral pigments, whereas the fatty acids are contained in the binder both in its original composition and as the result of its degradation. As the name suggests, oil paintings rely on the use of oils, particularly drying oils such as linseed, poppyseed, and walnut oil, as a medium in which the pigment is dispersed. From a chemical point of view, drying oils are triglycerides of unsaturated and polyunsaturated fatty acids, containing carbon-carbon double bonds in the aliphatic chains. Linseed oil, in particular, is a mixture of mono- and polyunsaturated triacylglycerides (TAGs), oleic acid (C18:1), linoleic acid (C18:2) and linolenic acid (C18:3). Known for solidifying at room temperature, this class of oils dry – or cure – to a tough, solid film after exposure to air at room temperature. The hardening mechanism has been widely investigated in the past decades (Wexler, 1964; Mallégol et al., 1999; Tumosa and Mecklenburg, 2013; Viguerie et al., 2016). It is a multi-step process involving metal-catalysed radical autoxidation, i.e., the reaction between atmospheric oxygen and unsaturated C-C double bonds (Nardelli et al., 2021), followed by polymerisation and cross-linking to a molecular network (Figure 1.2). This way, high molecular weight polymers suitable for film formation are produced from low molecular weight unsaturated triglycerides.

Already during the curing of the oil, several degradation reactions take place. Radical reactions occur due to the presence of peroxide species, which give rise to secondary and tertiary products, i.e., epoxy, hydroxyl, oxo and carbonyl moieties (Baij et al., 2019; Izzo et al., 2021; Nardelli et al., 2021; Pizzimenti et al., 2021). In linseed oil-based binders, the autoxidation process, which implies autoxidation of allylic moieties of the fatty acids' side chains, allows the formation of a crossed-linked structure – the polymer network – through ether and peroxy-bonds (Baij et al., 2019). Higher oxidation products also form over time, resulting in aldehydes and carboxylic groups. Spontaneous hydrolysis of the ester bonds also occurs with the production of additional free saturated fatty acids. The COOH groups are therefore formed following two different paths – oxidation and hydrolysis – and can later react with metal ions, resulting in metal soap formation.

Structure of the ligands In the formation of metal soaps, there are four main chemical structures carboxylates can assume, characterised by different levels of symmetry: (i) ionic or uncoordinated form, (ii) unidentate coordination, (iii) bidentate chelating coordination and (iv) bridging bidentate coordination (Palacios et al., 2004; Filopoulou et al., 2021). These are illustrated in Figure 1.3.

Structures (i) and (iii) are characterised by higher symmetry, which gives them characteristic spectral features, that will be discussed in detail in Chapter 3 (Filopoulou et al., 2021). These structures and their spectral features are highly influenced by the characteristics of the metal cation (e.g., effective charge, electronegativity), but they are generally insensitive to alkyl chain length. Regarding ions that form metal soaps, some relevant studies showed how zinc, lead, and copper ions are more likely to form metal soaps naturally in the paint film compared to other cations. In 2008, Mazzeo and co-workers showed the pigment-binder interaction between a series of cations and fatty acids within different binders (Mazzeo et al., 2008). This work demonstrated that, in accordance with what is known about the reactivity of specific ions towards fatty acids, lead soaps were formed for all lead-based pigments considered – i.e., red lead, litharge, lead white, Naples yellow and lead-tin yellow. Zinc, manganese, and copper soap formed in both oil and egg tempera paints. Iron soaps were only identified in co-presence with manganese in burnt and raw sienna and burnt

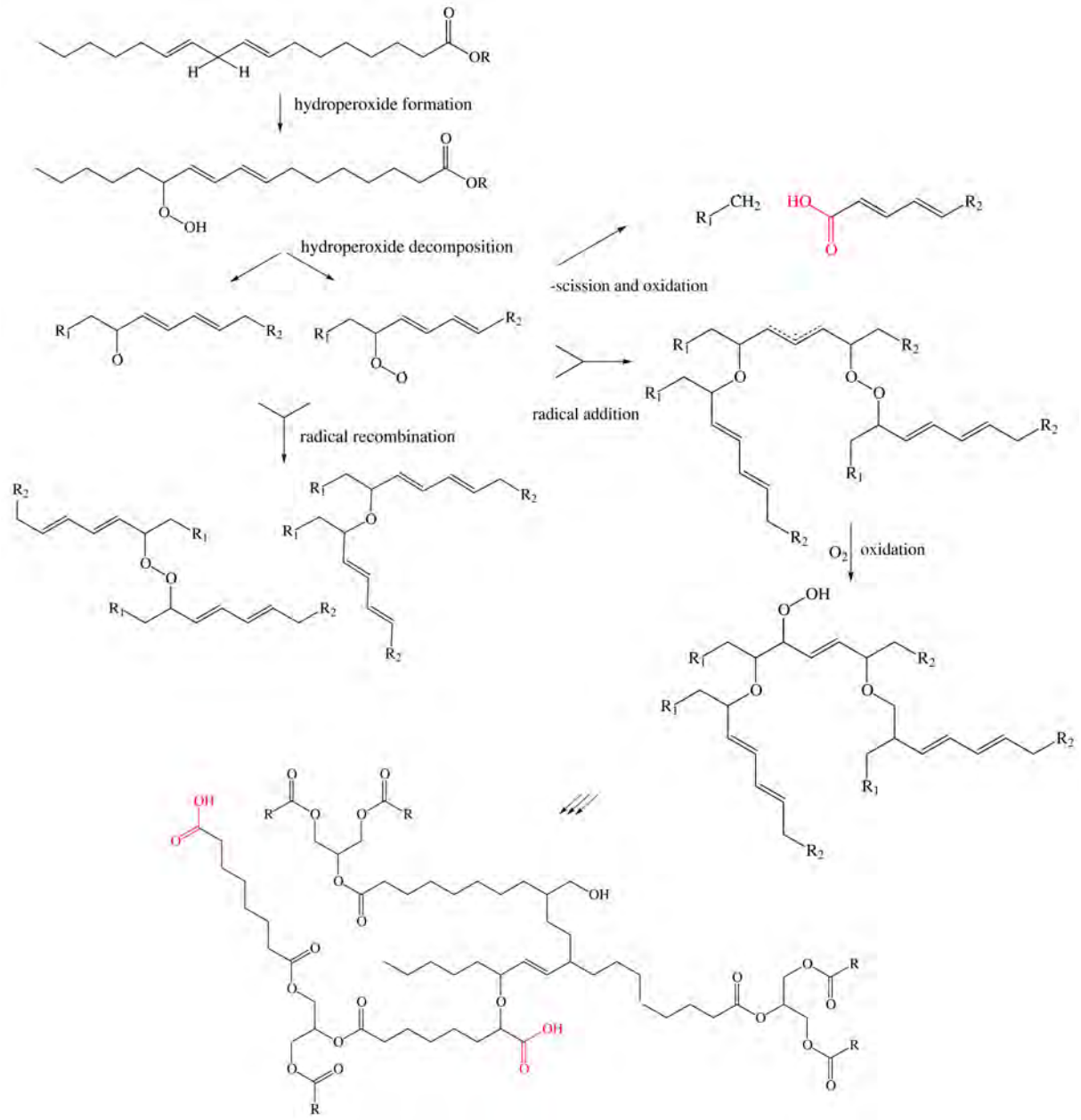

Figure 1.2: Mechanisms of the chemical reactions involved in the curing of linseed oil (adapted from Hermans, 2017).

and raw umber paint reconstructions (Mazzeo et al., 2008).

Hereafter, a timely report of current knowledge on the structure of metal soaps formed with ions of interest for this work is provided. This information is also expected to guide the reader in understanding the following chapters.

Zinc

Together with lead soaps, zinc soaps are the most synthesised, utilised and found metal carboxylates on oil-painted surfaces. In particular, zinc oxide, the main component of zinc white pigments, is a good adsorption substrate for carboxylic acid functionalities. Several studies have been carried out on the different configurations of zinc carboxylate

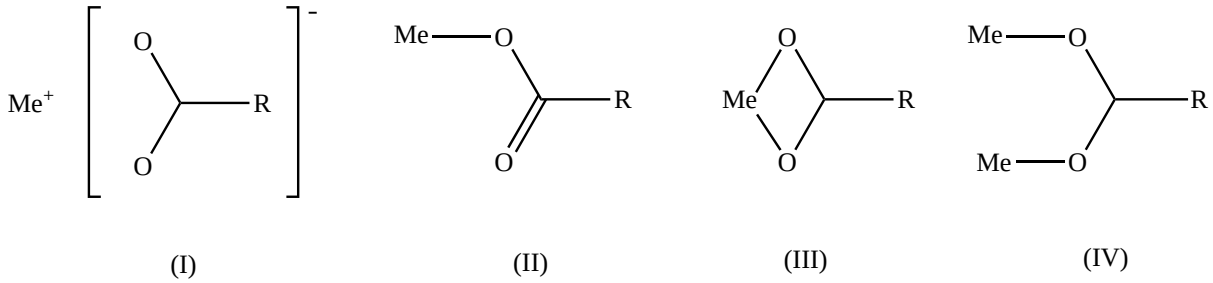

Figure 1.3: Chemical structures of metal carboxylates (adapted from Palacios et al., 2004; Filopoulou et al., 2021).

coordination structures. Four different coordination geometries were identified by Hermans and co-workers (Hermans et al., 2019; Hermans et al., 2021). In oil paintings, the bonding of zinc oxide to carboxyl groups occurs through dissociative bridging adsorption (Figure 1.3-IV and Figure 1.4), where carboxyl groups attach to two Zn atoms and the dissociated hydrogen bonds to another Zn atom (Artesani, 2020). The energy of adsorption of carboxyl groups to Zn atoms is a function of increasing fatty acid chain length. It decreases with additional forces acting in the lateral chain-chain interactions, hence with increasing length of the chain (Artesani, 2020).

In oil paints, once the oil polymeric network is formed and metal-carboxylic group interactions are created, metal cations can migrate and be exchanged between carboxylate groups, forming the so-called ionomer network. This is a cross-linked structure, where ionic groups and metal cations exist and neutralise each other (Hermans, 2017; Izzo et al., 2021). Zinc soaps, particularly palmitate, are also found to crystallise at about 121 – 124 °C, in a multi-step process that involves nucleation, growth and diffusion of metal ions and fatty acids towards metal soaps nuclei. This implies that zinc palmitate is often trapped in an amorphous form within the polymerised linseed oil network (Hermans, 2017).

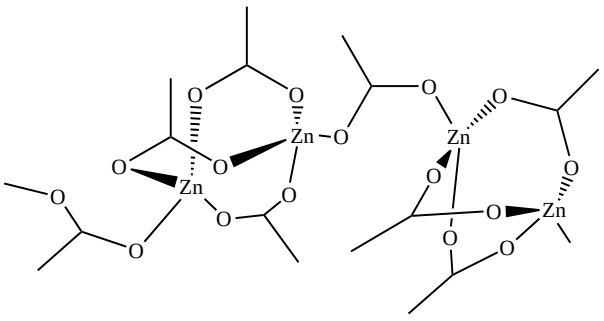

Figure 1.4: Zinc oxide – fatty acids polymeric network, showing bridging bidentate coordination (adapted from Artesani, 2020).

Copper

Copper has been used by humans since the Neolithic, and, through the centuries, copper and bronze metalwork masterpieces were produced for artistic purposes that we can still admire today (Scott, 2002). Besides its use in sculpture, copper-based compounds (e.g., malachite or azurite) have been extracted from natural ores to produce green and

blue pigments that artists have used for the production of their paintings for centuries (Scott, 2002).

As previously mentioned, due to their interaction with fatty acids, copper ions can form carboxylates as secondary products. Since copper(II) acetate hydrate was reported by van Niekerk and Schoening in 1953 as the first copper(II) carboxylate dimer, a series of studies on the different structures of copper carboxylates have taken place (Nordin et al., 2015). Copper(II) can, in fact, coordinate four carboxylate groups from the fatty acids ligands, giving rise to a square pyramidal structure with D_4h symmetry. Whether the oxygen of the carboxylate group utilises one or two lone electron pairs to bond to Cu(II) ions, single complexes (paddle-wheel dimers) or polymeric structures can be formed, respectively. In the latter, the carboxylic oxygen is bonded to a copper(II) ion from a second paddle-wheel dimer (Figure 1.5) (Nordin et al., 2015).

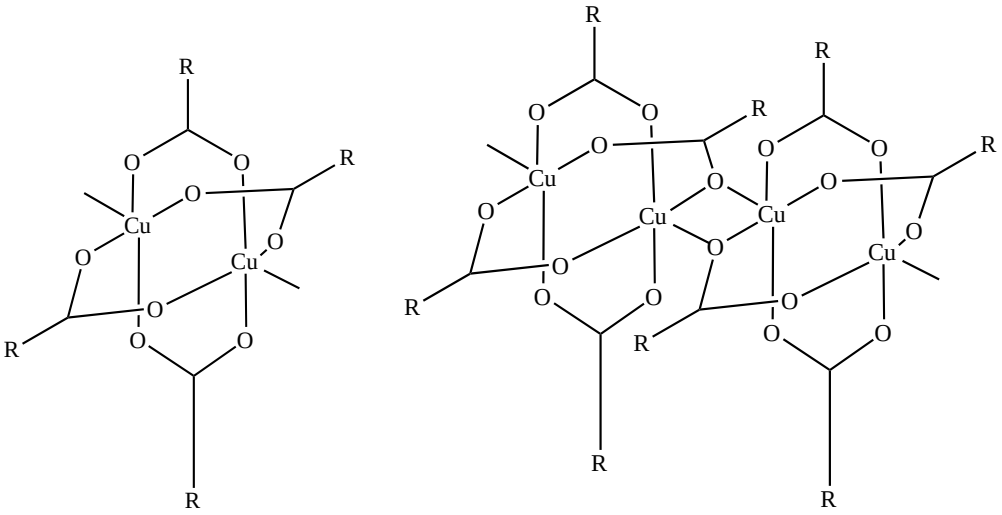

Figure 1.5: Structure of paddle-wheel dimer and polymeric network of Cu(II) carboxylates (adapted from Nordin et al., 2015).

Aluminium

Aluminium is one of the most abundant metallic elements on Earth's crust and it is found in natural minerals, like micas, zeolites, or feldspars (Loiseau et al., 2015). Aluminium(III) ions, predominant in aqueous solution, are normally complexed by anionic species in different coordination geometries depending on the pH values. At low pH values, Al(III) complexes assume octahedral geometry (exa-coordinated); at high pH, tetrahedral coordination is prevalent (tetra-coordinated). In rare cases, trigonal bipyramid (penta-coordinated) coordination geometry is allowed (Loiseau et al., 2015). In octahedral and tetrahedral coordination, the small ionic radius of aluminium ions (0.53 Armstrong for tetrahedral and 0.675 for octahedral) make them strong Lewis acids, hence prone to react with OH^-, F^-, PO_4^{3-}, SO_4^{2-}, but also with organic N- or O-donor ligands (RNH_2, RO^-, $RCOO^-$). Aluminium mononuclear and polynuclear carboxylates are typically found in octahedral geometry (Loiseau et al., 2015). In the medical field, they are widely studied to understand the interaction of Al with small organic models and their role in the development of neurodegenerative diseases (Loiseau et al., 2015). Aluminium soaps are also used in the paint industry as dryers (Section 1.1 – Metal soaps as oil paint siccative).

Mono- and poly-nuclear motifs are available, where different configurations are obtained,

involving sharing edges and corners of Al octa- and tetrahedra (Loiseau et al., 2015). In the 1950s, A.E. Alexander and V.R. Gray concluded that di-soaps were mainly formed from the reaction of alkoxide/fatty acids reaction, as well as from processes in the presence of water (Alexander and Gray, 1950; Figure 1.6).

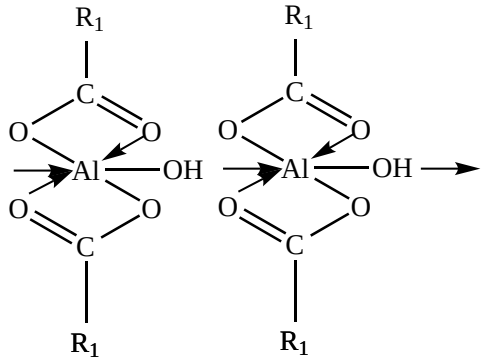

Figure 1.6: Structure of aluminium di-soaps (adapted from Alexander and Gray, 1950).

Iron

Archaeological evidence shows that iron-based pigmented substances have been in use for several purposes for over 300 000 years of human history (Mastrotheodoros and Beltsios, 2022). Both +2 and +3 iron oxidation states can result in iron carboxylates. Four possible coordination structures are proposed for iron(III) carboxylates and described in Figure 1.7: ionic, unidentate, bidentate and bridging (Lin and Kim, 2012).

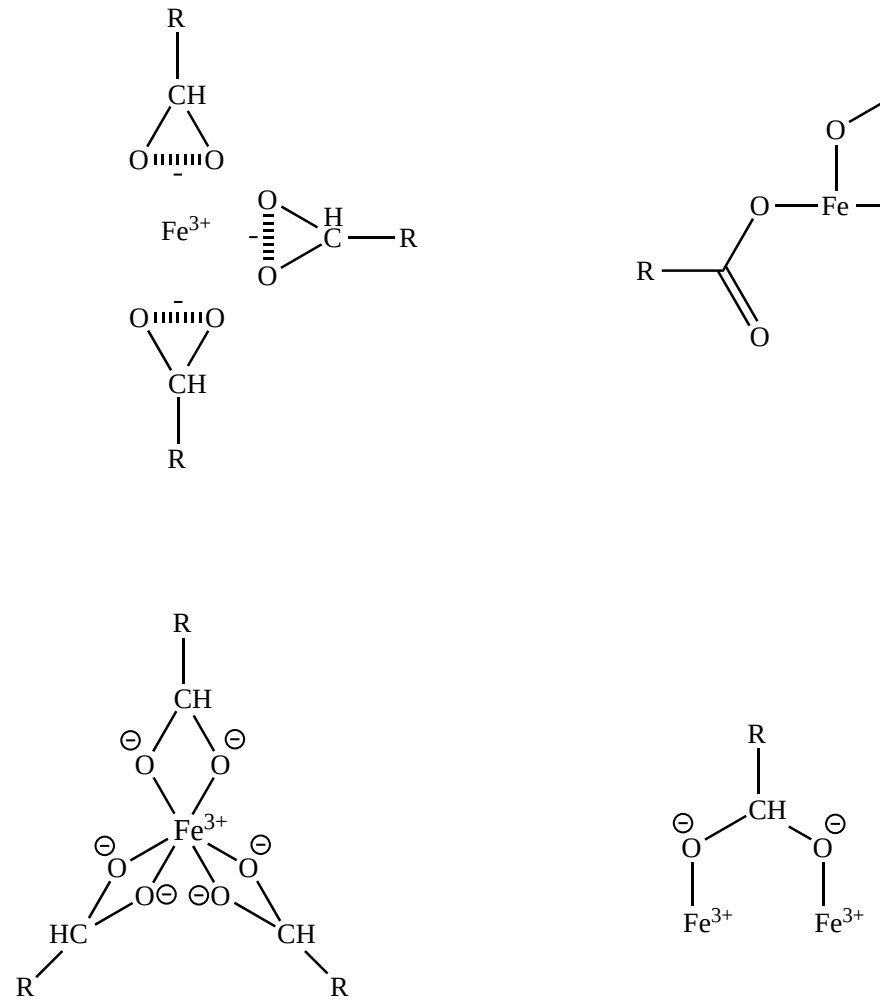

Figure 1.7: Coordination structures of iron carboxylates: (from left to right) ionic, unidentate, bidentate and bridging (adapted from Lin and Kim, 2012).

1.2.1 Metal soaps occurrence in cultural heritage objects

Scientific literature is rich in studies investigating the formation of metal soaps on different materials, ranging from archaeological objects and decorative art to modern and contemporary artworks. Since the first report of metal soaps in the early 90s (Noble, 2019), many studies have investigated the saponification reaction between free fatty acids in oil binders and the metal ions from mineral pigments. These studies have targeted pigment-binder interactions (Mazzeo et al., 2008), crystallisation, and migration (Rimer et al., 1999; Mecklenburg et al., 2013; Hermans and Helwig, 2020; Švarcová et al., 2020; Hermans et al., 2021), and more recently, early-stage formation (Garrappa et al., 2020).

Hereafter, an overview of the main classes of cultural heritage objects where metal soaps could be detected is collected and presented to show their ubiquitous nature. Two main categories are identified here:

- archaeological and ethnographic objects, where the metal soaps are formed between a metal and fatty acids-rich components of the functional and utilitarian objects,
- fine arts objects, where oil paint is applied on different supports (e.g., panel, stone, and metal) from different historical contexts and periods.

Archaeological and ethnographic objects Since the development of a protocol for extracting archaeological organic residues from ceramics between the 80s and the 90s, several studies have been carried out aiming to understand dietary habits, agricultural, and ritual practices of past civilisations (Evershed, 2008). In 2022, a work was published which investigated organic residues from copper-based containers of archaeological interest (Carvalho, 2022). A multi-analytical approach was proposed to fully characterise copper–organic complexes and organic residues trapped in archaeological copper corrosion (Carvalho, 2022). Data from Fourier Transform Infrared Spectroscopy (FTIR), Raman Spectroscopy, X-ray Photoelectron Spectroscopy (XPS), X-ray Diffraction (XRD), and Mass Spectrometry were presented and discussed, providing a comprehensive analytical characterisation of copper-organic complexes for cultural heritage applications (Carvalho, 2022).

Ethnographic organic-inorganic composite objects also present degradation phenomena associated with the presence of fatty acids. This can occur due to the interaction between metal parts and organic components, like leather or wood parts (Raphael, 1993; Werner et al., 2012; Jefcoat Burton, 2020), or organic coatings or protective treatments (Moffett, 1996). Leather conservation-restoration protocols, for instance, entail the use of so-called dressings, which consist of oils, fats, waxes, or oil emulsions. Waxy components of most commercial stearic acid-based lubrication or softening products formulated with 50% stearic acid, 45% palmitic acid, and 5% oleic acid tend to migrate through the pores of leather grain and exudate on the surface as bloom (Jefcoat Burton, 2020).

Protective wax coatings were and still are sometimes used in conservation-restoration treatments of metal objects. These protectives can be purchased as commercial formulations or prepared in conservation laboratories and are used as a barrier against moisture and oxygen, contamination due to handling, and as a protective layer (Plenderleith and Werner, 1971; Moffett, 1996). Both the natural colour of the wax and the colouration given through the addition of pigments are exploited in protective waxes to ensure desired aesthetical properties of the object (Moffett, 1996). Pigmented wax-resin infills for paint

loss reintegration are still exploited for copper-based artefacts (Vega, 2016).

Copper formate was found on a Benin statue from the National Museum of African Art in correspondence with wax conservation treatments (Moffett, 1996; Scott, 2002). Pigmented beeswax was also identified in Egyptian antiquities, and copper acetate was associated with its presence (Daniels, 2007). Another example of wax-metal interaction is that of wax statutes having a metal – copper – core. A study from 2015 showed that the interaction between the two is likely to induce the formation of metal soaps (Gramtorp et al., 2015).

Fine arts

a) Canvas

Metal soaps were first associated with oil painting degradation and pigment-binder interaction in the 90s, when crater-like protrusions, later attributed to the presence of crystalline lead soaps, were identified on the surface of the oil painting on canvas *The Anatomy Lesson of Dr. Nicolaes Tulp* (1632) by Rembrandt, preserved at the Mauritshuis museum (The Hague, The Netherlands) (Noble, 2019). Since then, much work has been done towards understanding their mechanism of formation within paint layers. Such studies mostly related to the formation of lead and zinc soaps, since these have been reported as the most frequent soaps forming in oil painting (Keune, 2005; Keune and Boon, 2007; Hermans et al., 2014 Hermans et al., 2015; Hermans et al., 2016; Baij et al., 2018; Baij et al., 2019; Casadio et al., 2019; Hermans et al., 2019; Hermans and Helwig, 2020; Hermans et al., 2021). A relevant evolution of those studies was the observation that metal soaps form very early in the life of the oil paint, even when they were not initially present as driers, like in the case of modern formulations. For similar reasons, metal soaps are commonly found in modern and contemporary artwork all around the globe. Significant improvements in the non-invasive investigation of metal soaps on contemporary oil paintings were given by a project started at the Georgia O'Keefe museum in Santa Fez (USA) in 2007 when during a routine condition survey, micro-protrusions were identified on the surface of the paintings (Ortiz Miranda et al., 2020). In a recent work, the presence of these protrusions on a selection of paintings realised between the years 1924 and 1950 was related to the type of preparation of the canvas and their ground layers (pre-primed vs prepared by the artist), the pre-primed canvases causing increased vulnerability to the painted surfaces due to formation of lead soaps protrusions (Ortiz Miranda et al., 2020).

Renowned contemporary art masterpieces have been found to be rich in lead and zinc soaps. Of these, we report a list of the most recent and relevant scientific works for the detection and understanding of their distribution: The Menaced Assassin (1927) by René Magritte from the collection of the Museum of Modern Art (MoMA) (Duffy et al., 2014), Alkemy (1947) by Jackson Pollock (Gabrieli et al., 2017), Chemistry (1914-16) by Edward Munch at the Munch Aula in Oslo (Porsmo Stoveland et al., 2021), as well as other paintings by Edvard Munch, František Kupka (Košařová et al., 2016), Salustiano Asenso Arozarena, Salvador Abril I Blasco, Enrique Navas Escuriet and José Bellver Delmás (1871-1943) (Caravá et al., 2020), Karel Appel and Asger Jorn (1946–1971), and Argentine concrete art paintings (1940–1960) (Castellá et al., 2020). Other authors have instead based their work on the chemical origins of such reactions, focusing on the water sensitivity of modern oil paintings. It was found that low cross-linking and saponification degree, i.e., the nature of the ionomeric

and polymeric network, and high amounts of dicarboxylic acids are responsible for water sensitivity of the 20th century oil paints (Banti et al., 2018; Lee et al., 2018; Bonaduce et al., 2019; La Nasa et al., 2019; Ma et al., 2022).

b) Wall paintings

Identifying organic materials in wall paintings is often challenging for conservation scientists since these are typically added in smaller quantities with respect to the inorganic component (pigments and mortar) and tend to degrade faster than the inorganic materials with which they coexist in the complex wall painting stratigraphy. For this reason, advanced methods of investigation that rely on optimal spatial and spectral resolution, such as those using synchrotron radiation, have been deployed in several studies (Sotiropoulou et al., 2016). It was demonstrated that organic materials were used in wall paintings far more frequently than was previously thought (Nevin et al., 2008; Gelzo et al., 2014; Linn et al., 2018; Aceto, 2021; Casoli, 2021). These are primarily polysaccharidic or proteinaceous materials – i.e., vegetable gum exudates, honey, egg, animal glue, milk, and casein - used to confer protection, adhesion, and consolidation to the wall painting. However, oil binders can also be encountered (Casadio et al., 2004; Gelzo et al., 2014; Sotiropoulou et al., 2016; Aceto, 2021). Due to their consolidating capability, egg-based fixatives or synthetic resins were also used in conservation interventions, somehow contaminating the original composition and making identifying the original organic components more difficult (Casoli, 2021).

When outdoors, wall paintings are exposed to harsh environmental conditions that may affect their preservation. According to the model for organic binders' degradation, the formation of metal carboxylates occurs because of the adjacent presence of mobile free fatty acids and reactive metals from the pigments or ground layers, such as lead, calcium, manganese, copper and zinc, leading to the formation of metal carboxylates. In addition, metal oxalate salts formation is often promoted by metal – oxalic acid interaction and usually occurs at the surface of the mural painting as a thin coloured patina depending on the metal ion (e.g., green for copper) (Nevin et al., 2008; Sotiropoulou et al., 2016). In previous studies, the presence of oxalic acid has been attributed to the microbiological activity or photo-oxidation of proteinaceous materials, catalysed by Fe(III)-based pigments (Sotiropoulou et al., 2016). Metal carboxylates and oxalates have been identified in several Roman (Gelzo et al., 2014), Greek (Linn et al., 2018), Cypriot (Nevin et al., 2008), and Byzantine (Sotiropoulou et al., 2016) wall paintings.

c) Panel

Oil paintings on panel were very common in easel painting practices, especially before canvas came into general use at the end of the 16th century (Pantoja de la Cruz, 2010; Wadum, 1998). Metal soaps can be commonly detected on oil paintings on panel in correspondence to zinc and lead pigments (Platania et al., 2020; Romano et al., 2020). Secondary products from the mineralisation of lead soaps in oil paints, associated with lead red and lead-tin yellow type I in paint cross-sections, have been identified from a Late-Medieval painted wing in the Museum of Cultural History at the University of Oslo (Platania et al., 2020). Wood supports are not reported

to have a chemical influence on the formation of metal soaps. However, the wood grains' morphology can contribute to generating nucleation centres and preferential directions of formation (Campos et al., 2016).

d) Stone

During the 15th century, Italian artist Sebastiano del Piombo (1485-1547) pioneered the creation of paintings on marble, alabaster, lapis lazuli, and amethyst (Mann, 2020). Such experimentation continued within Europe into the early 18th century. Painting practices on stone are recently gaining popularity, as confirmed by dedicated exhibitions organised in the past few years by Brimo Di Castro Kugel (Manhattan, USA, 2017), the Museo Nacional del Prado (Madrid, Spain, 2018), and the Saint Louis Art Museum (St. Louis, USA, 2022). As oil paintings, these artefacts are also not immune to degradation due to metal soap formation. There is no evidence that support plays a role in the degradation mechanism. However, metal soaps can be found in the pictorial layers. In a work by Vichi and co-workers, lead soaps, investigated through optical coherence tomography (OCT), were identified on a polychrome carbonate sculpture dated around the 15th - 16th century (Vichi et al., 2019).

e) Metal

Simultaneously with the development of painting practices on stone, the art of painting on metal also saw its highest expression. This was due to the increasing interest in experimenting with new supports to obtain new virtuous visual effects and challenging the artist's skills and dexterity (Terenzi et al., 2006). Painted metals being the focus of this research, a more detailed report of such practices and their implications for preserving painted metal objects is provided in the following chapters. However, despite being a neglected field of study, it is worth mentioning the occurrence of metal soaps on some selected exemplars of fine painting on metal or in association with oil-coatings on metal technical and industrial objects.

A first example is a 17th-century miniature portrait of Italian school, painted on a copper substrate (Albini et al., 2020). Here, copper soaps were identified within some green corrosion products that made their way through the paint layer to the surface of the painting (Albini et al., 2020). In a second example, two aluminium-based works by Frank Stella, namely *Gobba, zoppa e collotorto (1985)* and *Cricche, crocche e manico d'uncino* (1986), were analysed following the observation of crystalline growths in correspondence with dark red and blue paints (Rimer et al., 1999). These features were associated with the presence of alizarine crimson oil paint, but not further characterised (Rimer et al., 1999). Lead soaps were identified in the paint layers of some iron objects belonging to the Conservatoire National des Arts et Métiers (CNAM) collection in Paris in a recent work by Gordon and co-workers (Gordon et al., 2019).

Technical objects and industrial heritage often consist of copper or iron-based alloys where oil is applied for corrosion inhibition or as a lubricant to ensure movement of the mechanical parts. When a pigment is added to the coating, metal soaps are often found within the paint layers. However, it is not always possible to identify metal soaps between the metal and the protective layer. The case of iron soaps

is particularly interesting, especially since, in the cultural heritage field, there is no mention of the presence of iron carboxylates, except in a few wax statues by Gustave Moreau pigmented with iron oxides[1]. Nevertheless, from a chemical point of view, iron carboxylates exist as stable organometallic complexes that are synthesised for metal-organic frameworks (MOFs) drug delivery systems, water desalinisation membranes, or as prodegradants to enhance the photodegradability of polypropylene (PP) (Rajakumar et al., 2010; Devi et al., 2020). Additionally, they are encountered on moving components in industrial machinery (Gellman and Spencer, 2002). For this reason, their formation is widely studied in the framework of tribological studies, which have shown that iron carboxylates can form within layers of lubricants when these are in intimate contact with a metal surface in motion (Bahari, 2017; Grebe and Ruland, 2022). This is a well-established issue in the tribology field since the formation of crystalline species is responsible for stiffness and malfunctioning of the mechanism. Iron soaps are believed to form since fatty acids are typically added to lubricants to improve their anti-friction capabilities. However, an excess of such species can induce a reaction with the metal substrate. While in industrial applications lubricants and corroded parts can be replaced and this might not be perceived as a sensible issue, in industrial heritage studies, where parts often cannot be replaced to maintain the originality and history of the object, this can determine poor preservation of the artwork. Additionally, in some cases (e.g., kinetic art objects), the mechanisms and functionality of the artwork must be preserved as part of their artistic life and performance. This adds a layer of complexity to the selection of the correct preservation strategies for the objects in the presence of organic salts (Lauridsen et al., 2014).

1.2.2 Direct analyses on museum objects

Collaborations with conservator-restorers from the Haute Ecole Arc Conservation Restauration (HE-Arc CR), Hochschule der Künste Bern (HKB) and Swiss museum institutions lead to the investigation of the presence of metal soaps on different objects. In particular, different samples were analysed for the presence of metal soaps, coming from:

- Ethnographic Museum at the University of Zurich (Völkerkundemuseum, VMZ),
- Musée Jurassiens d'Art et d'Histoire, Delémont,
- Historical Army Museum (HAM) in Thun,
- Musée Condé, Chantilly[2],
- Musée du Léman (Nyon),
- Academy of Fine Arts in Cracow,
- Hochschule der Künste Bern (HKB),
- Musée d'Art et d'Histoire de Neuchâtel,

[1] Borel, T., Le Hô, A.-S., Langlois, J., and Vandenberghe, Y. (2010) Examen et analyse scientifiques des cires de Gustave Moreau. À la recherche d'une chronologie par les examens de laboratoire. From an exhibition catalogue dedicated to Gustave Moreau.

[2] Investigation performed in the framework of preliminary studies in conservation carried out by the *Centre de Recherche et de Restauration des Musées de France* (C2RMF).

- private collectors,
- local flea markets.

Specifically, the 28 objects ranged from a small collection of late 19th - early 20th century toy and house objects to composite three-dimensional ethnographic and archaeological objects, paintings on copper and zinc support, shop signs and gramophones (Table 1.2).

The products sampled from the objects had various appearances: the conservator-restorers reported the presence of both intensely green greasy compounds (e.g., sword with fur scabbard, Ethiopia), as well as powdery greenish products (e.g., saber with leather scabbard, Algeria, Sahara, and sword with leather scabbard, D. R. Congo). Hereafter, the results of the Attenuated Total Reflectance (ATR) FTIR analyses are presented (Table 1.2).

Of the 28 objects analysed, 23 were found to contain metal soaps, whereas five –i.e., the toy cars and soldiers collection – did not. Only in 19 of the 23 objects were metal soaps formed directly between the metal and the source of fatty acid and not in paint layers. In particular, copper-based objects, making the majority of the objects analysed, were more susceptible to metal soap formation, with a prevalence of copper palmitate and oleate alone and in combination. Interestingly, zinc soaps were also found in association with copper ones on brass objects.

Painted zinc objects (i.e., shop sign Lido 1830 and St.Therese d'Avila, oil on zinc) could not easily be associated with zinc soaps. For the painting representing St.Therese d'Avila, some minor features related to the presence of zinc soaps could be identified within a noisy signal from the substrate accessible through paint lacunas. However, for the shop sign Lido 1830, no evidence of zinc soaps coming from the support could be found. One reason for their absence could be associated with the fact that the support is made of galvanised iron. Although one could expect the zinc coating to be reactive towards fatty acids, as reported earlier, iron is not found to produce metal soaps in common pH, temperature, and humidity conditions. Zinc soaps were detected within the zinc-based paint layers of the grammophone from the Musée d'Art et d'Histoire de Neuchâtel.

Lead soaps could not be detected on the toys with the current setup. However, lead soaps were found within the paint layers of the shop sign Lido 1830 (Musée du Léman (Nyon), in correspondence with lead-rich pigments.

ATR-FTIR relevant spectra for the relevant 19 objects are provided in the supplementary materials (Section S.1).

Table 1.2: Table of objects analysed through FTIR micro-spectroscopy. PubChem, 2022

Object description	Inventory number	Provenance	Metal soaps found	Relevant images
Horn handle with decorative wire art, Sahara Tamanrasset, Algeria. Wooden scabbard covered with red leather, secured with Cu-based wire.	11127b	VMZ, Zurich	Copper palmitate	
Wood handle with decorative wire art, Sahara Tamanrasset, Algeria. Wooden scabbard covered with red leather. Cu-based buckle and leather loop.	11127c	VMZ, Zurich	Copper palmitate and zinc stearate	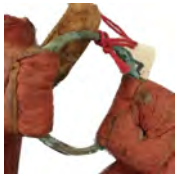
Wood handle with decorative wire art, Sahara Tamanrasset, Algeria. Wooden scabbard covered with red leather. Cu-based buckle and leather loop.	11127d	VMZ, Zurich	Copper palmitate and copper oleate	
Sword in a leather scabbard, D. R. Congo. Decorated with 2 different Cu-based thick wires. The surface of the scabbard appeared very dry with localised white powdery deposits.	09733b	VMZ, Zurich	Copper palmitate and zinc stearate	
Sword and scabbard, Ethiopia. Sword in a thick leather scabbard with a leather belt and Cu-based buckle	12137c	VMZ, Zurich	Copper palmitate	
Wooden statue with decorative Cu-based elements, D. R. Congo. Looking at the aspect of the wook, it was probably waxed or oiled.	11228b	VMZ, Zurich	Copper palmitate and zinc stearate	

Object description	Inventory number	Provenance	Metal soaps found	Relevant images
Wooden statue with decorative Cu-based elements, D. R. Congo. Looking at the aspect of the wook, it was probably waxed or oiled. The face seems like it was darkened with tar or other black waxy material.	10315	VMZ, Zurich	Copper palmitate	
Scabbard of a sword, possibly of Mongolian origin. Dyed leather work assembled with thin copper threads.	oNr. 0563	VMZ, Zurich	Copper palmitate and zinc stearate	
Unknown object, possibly of Mongolian origin. Dyed leather work assembled with thin copper threads.	oNr. 0564	VMZ, Zurich	Copper palmitate and copper oleate	
Dagger with leather scabbard and belt, Ethiopia. Sample taken from the copper thread used to attach the leather on the scabbard.	oNr. 4096	VMZ, Zurich	Copper palmitate and copper oleate	
Sword with fur scabbard, Ethiopia. Metal decors on the scabbard, blue-green greasy corrosion on the skin and metal. Same on the wooden handle, decorated with Cu-pins.	12205e	VMZ, Zurich	Copper palmitate and zinc soaps	
Dagger and scabbard, Ethiopia.	17982	VMZ, Zurich	Copper palmitate and zinc stearate	

Object description	Inventory number	Provenance	Metal soaps found	Relevant images
Fetish figure "Domo" from the village of Mancantau. She is said to belong to a man's secret boy and kept hidden. Priests smeared the figure with blood of sacrificial animals.	12687	VMZ, Zurich	Copper oleate and copper palmitate	
Stoup	MJ.1989.61	Musée Jurassiens d'art et d'histoire, Delémont	Copper oleate and copper palmitate	
Pochette	N/A	HAM, historical army museum, Thun	Copper oleate	
Cartonnier de Lalive de July (1757)	N/A	Musée Condé, Chantilly	Copper palmitate and copper oleate	
Possibly St. Joseph - Paint on copper	D.131	HKB	Copper palmitate	
Possibly St. Catherine - Paint on copper	D. 130	HKB	Copper palmitate and copper oleate	

Object description	Inventory number	Provenance	Metal soaps found	Relevant images
St. Therese of Avila. Oil on zinc. Spanish school, early 18th century, unknown artist	N/A	Private	Possibly zinc and copper soaps	
Madonna with the green cushion, after Andrea Solari, unknown artist. Probably zinc support.	N/A	Academy of Fine Arts, Cracow	Attribution nontrivial	
Zinc-based Prussian blue toy car – early 1900s	N/A	Flee market	Slight presence of zinc soaps	
Iron-based zinc and possibly titanium white toy car – early 1900s	N/A	Flee market	None detected	
Lead-based toy soldier	N/A	Flee market	None detected	
Lead-based toy soldier	N/A	Flee market	None detected	

Object description	Inventory number	Provenance	Metal soaps found	Relevant images
Iron-based painted metal tray, Napoleon III	N/A	Flee market	None detected	
Painted metal box, early 1900s	N/A	Flee market	None detected	
Shop sign "Lido 1870", galvanised iron	ML/2019/0830	Musée du Léman (Nyon)	Lead soaps detected within the paint layer	
Pathé Salon n°5 gramophone, 1910 ca.	N/A	Musée d'Art et d'Histoire de Neuchâtel	Zinc soaps detected within the paint layer	

Bibliography

Aceto, M. (2021). Pigments — the palette of organic colourants in wall paintings. *Archaeological and Anthropological Sciences* **13**(10): 159. DOI: 10.1007/s12520-021-01392-3.

Albini, M., Ridolfi, S., Giuliani, C., Pascucci, M., Staccioli, M. P., and Riccucci, C. (2020). Multi-Spectroscopic Approach for the Non-invasive Characterization of Paintings on Metal Surfaces. *Frontiers in Chemistry* **8**: 289. DOI: 10.3389/fchem.2020.00289.

Alexander, A. E. and Gray, V. R. (1950). Aluminium soap, their nature and gelling properties. *Proceedings of the Royal Society of London. Series A. Mathematical and Physical Sciences* **200**(1061): 162–168. DOI: 10.1098/rspa.1950.0005.

Artesani, A. (2020). Zinc oxide instability in drying oil paint. *Materials Chemistry and Physics* **255**: 123640. DOI: 10.1016/j.matchemphys.2020.123640.

Bahari, A. (2017). *Investigation into Tribological Performance of Vegetable Oils as Biolubricants at Severe Contact Conditions*. PhD thesis. University of Sheffield.

Baij, L., Chassouant, L., Hermans, J. J., Keune, K., and Iedema, P. D. (2019). The concentration and origins of carboxylic acid groups in oil paint. *RSC Advances* **9**(61): 35559–35564. DOI: 10.1039/C9RA06776K.

Baij, L., Hermans, J. J., Keune, K., and Iedema, P. (2018). Time-Dependent ATR-FTIR Spectroscopic Studies on Fatty Acid Diffusion and the Formation of Metal Soaps in Oil Paint Model Systems. *Angewandte Chemie International Edition* **57**(25): 7351–7354. DOI: 10.1002/anie.201712751.

Banti, D., La Nasa, J., Tenorio, A. L., Modugno, F., Jan van den Berg, K., Lee, J., Ormsby, B., et al. (2018). A molecular study of modern oil paintings: investigating the role of dicarboxylic acids in the water sensitivity of modern oil paints. *RSC Advances* **8**(11): 6001–6012. DOI: 10.1039/C7RA13364B.

Blachford, J. (1982). Manufacture of metallic soaps. U.S. pat. 4316852A. Blachford H L Ltd.

Boer, J. W. de, Wesenhagen, P. V., Wenker, E. C. M., Maaijen, K., Gol, F., Gibbs, H., and Hage, R. (2013). The Quest for Cobalt-Free Alkyd Paint Driers. *European Journal of Inorganic Chemistry* **2013**(21): 3581–3591. DOI: 10.1002/ejic.201300205.

Bonaduce, I., Duce, C., Lluveras-Tenorio, A., Lee, J., Ormsby, B., Burnstock, A., and Berg, K. J. van den (2019). Conservation Issues of Modern Oil Paintings: A Molecular Model on Paint Curing. *Accounts of Chemical Research* **52**(12): 3397–3406. DOI: 10.1021/acs.accounts.9b00296.

Bossert, R. G. (1950). The metallic soaps. *Journal of Chemical Education* **27**(1): 10. DOI: 10.1021/ed027p10.

Bouwman, E. and Gorkum, R. van (2007). A study of new manganese complexes as potential driers for alkyd paints. *Journal of Coatings Technology and Research* **4**(4): 491–503. DOI: 10.1007/s11998-007-9041-0.

Campos, M. F., Carlyle, L., and Melo, M. J. (2016). Beneath the surface: paint losses due to zinc soap formation within ground layers from a late 19th century oil painting. In: *Metal Soaps in Art symposium*. (poster presentation). Amsterdam, 14-15 March 2016.

Caravá, S., Roldán García, C., Vázquez de Agredos-Pascual, M. L., Murcia Mascarós, S., and Izzo, F. C. (2020). Investigation of modern oil paints through a physico-chemical integrated approach. Emblematic cases from Valencia, Spain. *Spectrochimica Acta Part A: Molecular and Biomolecular Spectroscopy* **240**: 118633. DOI: 10.1016/j.saa.2020.118633.

Carlyle, L. (1999). Paint Driers Discussed in 19th-Century British Oil Painting Manuals. *Journal of the American Institute for Conservation* **38**(1): 69–82. DOI: 10.1179/019713699806113538.

Carvalho, L. d. C. (2022). *Beyond Copper Soaps: Characterization of Copper Corrosion Containing Organics*. SpringerBriefs in Applied Sciences and Technology. Cham: Springer International Publishing. DOI: 10.1007/978-3-030-97892-1.

Casadio, F., Giangualano, I., and Piqué, F. (2004). Organic materials in wall paintings: the historical and analytical literature. *Studies in Conservation* **49** (sup1): 63–80. DOI: 10.1179/sic.2004.49.Supplement-1.63.

Casadio, F., Keune, K., Noble, P., Van Loon, A., Hendriks, E., Centeno, S. A., and Osmond, G., eds. (2019). *Metal Soaps in Art: Conservation and Research*. Cultural Heritage Science. Cham: Springer International Publishing. ISBN: 978-3-319-90617-1.

Casoli, A. (2021). Research on the Organic Binders in Archaeological Wall Paintings. *Applied Sciences* **11**(19): 9179. DOI: 10.3390/app11199179.

Castellá, F., Pérez-Estebanez, M., Mazurek, J., Monkes, P., Learner, T., Niello, J. F., Tascon, M., et al. (2020). A multi-analytical approach for the characterization of modern white paints used for Argentine concrete art paintings during 1940–1960. *Talanta* **208**: 120472. DOI: 10.1016/j.talanta.2019.120472.

Corbeil, M.-C. and Robinet, L. (2002). X-ray powder diffraction data for selected metal soaps. *Powder Diffraction* **17**(1): 52–60. DOI: 10.1154/1.1431950.

Cotte, M., Dumas, P., Richard, G., Breniaux, R., and Walter, P. (2005). New insight on ancient cosmetic preparation by synchrotron-based infrared microscopy. *Analytica Chimica Acta* **553**(1): 105–110. DOI: 10.1016/j.aca.2005.07.067.

Dalen, M. B. and Mamza, P. (2010). Some physico-chemical properties of prepared metallic soap-driers of aluminium, copper and zinc. *Science World Journal* **4**: 7–9.

Daniels, V. (2007). Analyses of Copper- and Beeswax-Containing Green Paint on Egyptian Antiquities. *Studies in Conservation* **52**(1): 13–18. DOI: 10.1179/sic.2007.52.1.13.

Davis, G. M. (1960). Metallic salts of commercial stearic acid. U.S. pat. 2945051A. Wyeth Holdings LLC.

Devi, Y., Ang, I., Soetaredjo, F. E., Santoso, S. P., Irawaty, W., Yuliana, M., Angkawijaya, A. E., et al. (2020). An iron–carboxylate-based metal–organic framework for Furosemide loading and release. *Journal of Materials Science* **55**(28): 13785–13798. DOI: 10.1007/s10853-020-05009-3.

Duffy, M., Martins, A., and Boon, J. J. (2014). Metal Soaps and Visual Changes in a Painting by René Magritte – The Menaced Assassin, 1927. In: *Issues in Contemporary Oil Paint*. Ed. by K. J. van den Berg, A. Burnstock, M. de Keijzer, J. Krueger, T. Learner, A. Tagle de, and G. Heydenreich. Cham: Springer International Publishing: 197–203. DOI: 10.1007/978-3-319-10100-2_13.

Essien, E. A., Umoren, S. A., Essien, E. E., and Udoh, A. P. (2012). Preparation and Evaluation of Cucumeropsis mannii Naud. Seed Oil Metallic Soaps as Driers in Gloss Paint. *Journal of Materials and Environmental Science* **3**(3): 477–484.

Evershed, R. P. (2008). Organic Residue Analysis in Archaeology: The Archaeological Biomarker Revolution. *Archaeometry* **50**(6): 895–924. DOI: 10.1111/j.1475-4754.2008.00446.x.

Filopoulou, A., Vlachou, S., and Boyatzis, S. C. (2021). Fatty Acids and Their Metal Salts: A Review of Their Infrared Spectra in Light of Their Presence in Cultural Heritage. *Molecules* **26**(19): 6005. DOI: 10.3390/molecules26196005.

Gabrieli, F., Rosi, F., Vichi, A., Cartechini, L., Pensabene Buemi, L., Kazarian, S. G., and Miliani, C. (2017). Revealing the Nature and Distribution of Metal Carboxylates in Jackson Pollock's *Alchemy* (1947) by Micro-Attenuated Total Reflection FT-IR Spectroscopic Imaging. *Analytical Chemistry* **89**(2): 1283–1289. DOI: 10.1021/acs.analchem.6b04065.

Gadhave, A. (2014). Determination of Hydrophilic-Lipophilic Balance Value. *International Journal of Science and Research (IJSR)* **3**(4): 373–375.

Garrappa, S., Kočí, E., Švarcová, S., Bezdička, P., and Hradil, D. (2020). Initial stages of metal soaps‘ formation in model paints: The role of humidity. *Microchemical Journal* **156**: 104842. DOI: 10.1016/j.microc.2020.104842.

Gellman, A. J. and Spencer, N. D. (2002). Surface chemistry in tribology. *Proceedings of the Institution of Mechanical Engineers, Part J: Journal of Engineering Tribology* **216**(6): 443–461. DOI: 10.1243/135065002762355352.

Gelzo, M., Grimaldi, M., Vergara, A., Severino, V., Chambery, A., Dello Russo, A., Piccioli, C., et al. (2014). Comparison of binder compositions in Pompeian wall painting styles from Insula Occidentalis. *Chemistry Central Journal* **8**(1): 65. DOI: 10.1186/s13065-014-0065-0.

Gezici-Koç, Ö., Thomas, C. A., Michel, M.-E. B., Erich, S. J., Huinink, H. P., Flapper, J., Duivenvoorde, F. L., et al. (2016). In-depth study of drying solvent-borne alkyd coatings in presence of Mn- and Fe- based catalysts as cobalt alternatives. *Materials Today Communications* **7**: 22–31. DOI: 10.1016/j.mtcomm.2016.03.001.

Gordon, J., Normand, L., Genachte-Le Bail, A., Mirabaud, S., Loeper-Attia, M.-A., Catillon, R., Carré, A.-L., et al. (2019). New strategies for the conservation of paintings on metal. In: *Metal 2019 proceedings of the Interim Meeting of the ICOM-CC Metals Working Group, September 2-6, 2019, Neuchâtel, Switzerland*. Ed. by C. Chemello, L. Brambilla, and E. Joseph. Neuchatel: International Council of Museums - Committee for Conservation (ICOM-CC). ISBN: 978-92-9012-458-0.

Gorkum, R. van and Bouwman, E. (2005). The oxidative drying of alkyd paint catalysed by metal complexes. *Coordination Chemistry Reviews* **249**(17): 1709–1728. DOI: 10.1016/j.ccr.2005.02.002.

Gramtorp, D., Botfeldt, K., Glastrup, J., and Simonsen, K. P. (2015). Investigation and conservation of Anne Marie Carl-Nielsen's wax models. *Studies in Conservation* **60**(2): 97–106. DOI: 10.1179/2047058413Y.0000000111.

Grebe, M. and Ruland, M. (2022). Influence of Mechanical, Thermal, Oxidative and Catalytic Processes on Thickener Structure and Thus on the Service Life of Rolling Bearings. *Lubricants* **10**(5): 77. DOI: 10.3390/lubricants10050077.

Griffin, W. C. (1949). Classification of surface-active agents by "HLB". *Journal of the Society of Cosmetic Chemists*: 311–326.

H Rogers, J. R. and R Blew, J. W. (1959). Manufacture of metal soaps. U.S. pat. 2890232A. JBS USA LLC.

Hermans, J. (2017). *Metal soaps in oil paint: structure, mechanisms and dynamics*. PhD thesis. Vianen ut: Proefschriftmaken.

Hermans, J., Keune, K., Loon, A. van, Stols-Witlox, M., Corkery, R., and Iedema, P. (2014). The synthesis of new types of lead and zinc soaps: a source of information for the study of oil paint degradation. In: *Building strong culture through conservation: preprints ICOM-CC 17th Triennial Conference*. Melbourne, 17-19 September 2014. Ed. by J. Bridgland. ISBN: 978-92-9012-410-8.

Hermans, J. and Helwig, K. (2020). The Identification of Multiple Crystalline Zinc Soap Structures Using Infrared Spectroscopy. *Applied Spectroscopy* **74**(12): 1505–1514. DOI: 10.1177/0003702820935183.

Hermans, J., Zuidgeest, L., Iedema, P., Woutersen, S., and Keune, K. (2021). The kinetics of metal soap crystallization in oil polymers. *Physical Chemistry Chemical Physics* **23**(39): 22589–22600. DOI: 10.1039/D1CP03479K.

Hermans, J. J., Keune, K., Loon, A. van, Corkery, R. W., and Iedema, P. D. (2016). Ionomer-like structure in mature oil paint binding media. *RSC Advances* **6**(96): 93363–93369. DOI: 10.1039/C6RA18267D.

Hermans, J. J., Keune, K., Loon, A. van, and Iedema, P. D. (2015). An infrared spectroscopic study of the nature of zinc carboxylates in oil paintings. *Journal of Analytical Atomic Spectrometry* **30**(7): 1600–1608. DOI: 10.1039/C5JA00120J.

Hermans, J. J., Baij, L., Koenis, M., Keune, K., Iedema, P. D., and Woutersen, S. (2019). 2D-IR spectroscopy for oil paint conservation: Elucidating the water-sensitive structure of zinc carboxylate clusters in ionomers. *Science Advances* **5**(6): DOI: 10.1126/sciadv.aaw3592.

Izzo, F. C., Kratter, M., Nevin, A., and Zendri, E. (2021). A Critical Review on the Analysis of Metal Soaps in Oil Paintings. *ChemistryOpen* **10**(9): 904–921. DOI: 10.1002/open.202100166.

Kebrich, L. M. and Pitrot, A. R. (1953). Method of preparing metallic soaps of fatty acids. U.S. pat. 2650932A. NL Industries Inc.

Keune, K. (2005). *Binding medium, pigments and metal soaps characterised and localised in paint cross-sections*. MolArt 11. Amsterdam: FOM Institute for Atomic and Molecular Physics. ISBN: 978-90-77209-10-3.

Keune, K. and Boon, J. J. (2007). Analytical Imaging Studies of Cross-Sections of Paintings Affected by Lead Soap Aggregate Formation. *Studies in Conservation* **52**(3): 161–176. DOI: 10.1179/sic.2007.52.3.161.

Košařová, V., Hradil, D., Hradilová, J., Čermáková, Z., Němec, I., and Schreiner, M. (2016). The efficiency of micro-Raman spectroscopy in the analysis of complicated mixtures in modern paints: Munch's and Kupka's paintings under study. *Spectrochimica Acta Part A: Molecular and Biomolecular Spectroscopy* **156**: 36–46. DOI: 10.1016/j.saa.2015.11.027.

La Nasa, J., Lee, J., Degano, I., Burnstock, A., Berg, K. J. van den, Ormsby, B., and Bonaduce, I. (2019). The role of the polymeric network in the water sensitivity of modern oil paints. *Scientific Reports* **9**(1): 3467. DOI: 10.1038/s41598-019-39963-z.

Lauridsen, C. B., Sanyova, J., and Simonsen, K. P. (2014). Analytical study of modern paint layers on metal knight shields: The use and effect of Titanium white. *Spectrochimica Acta Part A: Molecular and Biomolecular Spectroscopy* **124**: 638–645. DOI: 10.1016/j.saa.2014.01.077.

Lee, J., Bonaduce, I., Modugno, F., La Nasa, J., Ormsby, B., and Berg, K. J. van den (2018). Scientific investigation into the water sensitivity of twentieth century oil paints. *Microchemical Journal* **138**: 282–295. DOI: 10.1016/j.microc.2018.01.017.

Lin, M. M. and Kim, D. K. (2012). In situ thermolysis of magnetic nanoparticles using non-hydrated iron oleate complex. *Journal of Nanoparticle Research* **14**(2): 688. DOI: 10.1007/s11051-011-0688-1.

Linn, R., Bonaduce, I., Ntasi, G., Birolo, L., Yasur-Landau, A., Cline, E. H., Nevin, A., et al. (2018). Evolved Gas Analysis-Mass Spectrometry to Identify the Earliest Organic Binder in Aegean Style Wall Paintings. *Angewandte Chemie International Edition* **57**(40): 13257–13260. DOI: 10.1002/anie.201806520.

Loiseau, T., Volkringer, C., Haouas, M., Taulelle, F., and Férey, G. (2015). Crystal chemistry of aluminium carboxylates: From molecular species towards porous infinite three-dimensional networks. *Comptes Rendus Chimie* **18**(12): 1350–1369. DOI: 10.1016/j.crci.2015.08.006.

Ma, X., Pavlidis, G., Dillon, E., Beltran, V., Schwartz, J. J., Thoury, M., Borondics, F., et al. (2022). Micro to Nano: Multiscale IR Analyses Reveal Zinc Soap Heterogeneity in a 19th-Century Painting by Corot. *Analytical Chemistry* **94**(7): 3103–3110. DOI: 10.1021/acs.analchem.1c04182.

Mallégol, J., Gardette, J.-L., and Lemaire, J. (1999). Long-term behavior of oil-based varnishes and paints I. Spectroscopic analysis of curing drying oils. *Journal of the American Oil Chemists' Society* **76**(8): 967–976. DOI: 10.1007/s11746-999-0114-3.

Mann, J. W., ed. (2020). *Paintings on stone: science and the sacred, 1530-1800*. St. Louis : Munich: Saint Louis Art Museum ; Hirmer. ISBN: 978-0-89178-006-9.

Mastrotheodoros, G. P. and Beltsios, K. G. (2022). Pigments—Iron-based red, yellow, and brown ochres. *Archaeological and Anthropological Sciences* **14**(2): 35. DOI: 10.1007/s12520-021-01482-2.

Mazzeo, R., Prati, S., Quaranta, M., Joseph, E., Kendix, E., and Galeotti, M. (2008). Attenuated total reflection micro FTIR characterisation of pigment–binder interaction in reconstructed paint films. *Analytical and Bioanalytical Chemistry* **392**(1): 65–76. DOI: 10.1007/s00216-008-2126-5.

Mecklenburg, M. F., Tumosa, C. S., and Vicenzi, E. P. (2013). The Influence of Pigments and Ion Migration on the Durability of Drying Oil and Alkyd Paints. In: *New Insights into the Cleaning of Paintings: Proceedings from the Cleaning 2010 International Conference, Universidad Politecnica de Valencia and Museum Conservation Institute*. Ed. by M. F. Mecklenburg, A. E. Charola, and R. J. Koestler. Washington, DC: Smithsonian Institution: Smithsonian Contributions to Museum Conservation: 59–67.

Moffett, D. L. (1996). Wax Coatings on Ethnographic Metal Objects: Justifications for Allowing a Tradition to Wane. *Journal of the American Institute for Conservation* **35**(1): 1–7. DOI: 10.1179/019713696806124557.

Nardelli, F., Martini, F., Lee, J., Lluvears-Tenorio, A., La Nasa, J., Duce, C., Ormsby, B., et al. (2021). The stability of paintings and the molecular structure of the oil paint polymeric network. *Scientific Reports* **11**: 14202. DOI: 10.1038/s41598-021-93268-8.

Nevin, A., Melia, J. L., Osticioli, I., Gautier, G., and Colombini, M. P. (2008). The identification of copper oxalates in a 16th century Cypriot exterior wall painting using micro FTIR, micro Raman spectroscopy and Gas Chromatography-Mass Spectrometry. *Journal of Cultural Heritage* **9**(2): 154–161. DOI: 10.1016/j.culher.2007.10.002.

Noble, P. (2019). A Brief History of Metal Soaps in Paintings from a Conservation Perspective. In: *Metal Soaps in Art: Conservation and Research*. Ed. by F. Casadio, K.

Keune, P. Noble, A. Van Loon, E. Hendriks, S. A. Centeno, and G. Osmond. Cultural Heritage Science. Cham: Springer International Publishing. DOI: 10.1007/978-3-319-90617-1.

Nordin, N., Samad, W. Z., Yusop, R. M., and Othman, M. R. (2015). Synthesis And Characterization of Copper(II) Carboxylate with Palm-Based Oleic Acid by Electrochemical Technique. *Malaysian Journal of Analytical Sciences* **19**(1): 236–243.

Ortiz Miranda, A. S., Kronkright, D., and Walton, M. (2020). The influence of commercial primed canvases in the manifestation of metal soaps protrusions in Georgia O'Keeffe's oil paintings. *Heritage Science* **8**(1): 107. DOI: 10.1186/s40494-020-00451-7.

Palacios, E., Juárez-López, G., and Monhemius, A. (2004). Infrared spectroscopy of metal carboxylates. *Hydrometallurgy* **72**: 139–148. DOI: 10.1016/S0304-386X(03)00137-3.

Pantoja de la Cruz, J. (2010). The evolution of preparations for painting on canvas in sixteenth century Spain. *Boletín del Museo del Prado* **XXVIII**(46): 39–59.

Pearl, E. N. (2016). Synthesis, Characterization and Permofarmance Activity of Metal Soap of Calcium, Cobalt, Iron and Copper from Palm Kernel Oil as a Drier in Paint. *Advances in Bioscience and Bioengineering* **4**(6): 85–90. DOI: 10.11648/j.abb.20160406.14.

Pizzimenti, S., Bernazzani, L., Tinè, M. R., Treil, V., Duce, C., and Bonaduce, I. (2021). Oxidation and Cross-Linking in the Curing of Air-Drying Artists' Oil Paints. *ACS Applied Polymer Materials* **3**(4): 1912–1922. DOI: 10.1021/acsapm.0c01441.

Platania, E., Streeton, N. L., Vila, A., Buti, D., Caruso, F., and Uggerud, E. (2020). Investigation of mineralization products of lead soaps in a late medieval panel painting. *Spectrochimica Acta Part A: Molecular and Biomolecular Spectroscopy* **228**: 117844. DOI: 10.1016/j.saa.2019.117844.

Plenderleith, H. J. and Werner, A. E. A. (1971). *The conservation of antiquities and works of art: treatment, repair and restoration.* 2d ed. London, New York: Oxford University Press. ISBN: 978-0-19-212960-4.

Porsmo Stoveland, L., Frøysaker, T., Stols-Witlox, M., Grøntoft, T., Steindal, C. C., Madden, O., and Ormsby, B. (2021). Evaluation of novel cleaning systems on mock-ups of unvarnished oil paint and chalk-glue ground within the Munch Aula Paintings Project. *Heritage Science* **9**(1): 144. DOI: 10.1186/s40494-021-00599-w.

Putrawan, I. D. G. A., Indarto, A., and Octavia, Y. (2022). Thermal stabilization of polyvinyl chloride by calcium and zinc carboxylates derived from byproduct of palm oil refining. *Heliyon* **8**(8): e10079. DOI: 10.1016/j.heliyon.2022.e10079.

Rajakumar, K., Sarasvathy, V., Thamaraichelvan, A., Chitra, R., and Vijayakumar, C. T. (2010). Effect of iron carboxylates on the photodegradability of polypropylene. I. Natural weathering studies. *Journal of Applied Polymer Science* **118**(5): 2601–2612. DOI: 10.1002/app.32582.

Raphael, T. (1993). Leather Dressing: To Dress Or Not To Dress. *Conserve O Gram* **9**(1): ed. by E. McCrady.

Rimer, B. W., Fiedler, I., Miller, M., Cunningham, M., and Jorrit D. J., v. d. B. (1999). Investigation of fatty acid migration in alizarin crimson oil paint in two works by Frank Stella. In: *Postprints (American Institute for Conservation of Historic and Artistic Works. Paintings Specialty Group).*

Romano, C., Lam, T., Newsome, G. A., Taillon, J. A., Little, N., and Tsang, J.-s. (2020). Characterization of Zinc Carboxylates in an Oil Paint Test Panel. *Studies in Conservation* **65**(1): 14–27. DOI: 10.1080/00393630.2019.1666467.

Scott, D. A. (2002). *Copper and bronze in art: corrosion, colorants, conservation*. In collab. with G. C. Institute. Los Angeles: Getty Conservation Institute. ISBN: 978-0-89236-638-5.

Scott, L., Strachan, H., and Closkey, C. M. (1974). Manufacture of metallic soaps. U.S. pat. 3803188A. Norac Co.

Shekhter, Y. N., Bogdanova, T. I., Teterina, L. N., Fuks, I. G., and Zaslavskaya, I. R. (Sept. 1975). Polarity and functional properties of soaps of stearic acid. *Chemistry and Technology of Fuels and Oils* **11**(9): 734–737. DOI: 10.1007/bf00730325.

Smith, M. and March, J. (2020). *March's advanced organic chemistry: reactions, mechanisms, and structure*. 8th ed. Hoboken, NJ: John Wiley. ISBN: 978-1-119-37179-3.

Sotiropoulou, S., Papliaka, Z. E., and Vaccari, L. (2016). Micro FTIR imaging for the investigation of deteriorated organic binders in wall painting stratigraphies of different techniques and periods. *Microchemical Journal* **124**: 559–567. DOI: 10.1016/j.microc.2015.10.002.

Sutrisno, S., Wijaya, H. W., Sukarianingsih, D., and Santiaji, M. N. D. (2021). Synthesis and characterization of metal soap (Zn-, Al-, and Mg-soap) from sunflower oil and its potential as sunscreen. In: *AIP Conference Proceedings*. Surabaya, 14-15 July 2020: 020042. DOI: 10.1063/5.0051616.

Švarcová, S., Kočí, E., Bezdička, P., Garrappa, S., Kobera, L., Plocek, J., Brus, J., et al. (2020). Uncovering lead formate crystallization in oil-based paintings. *Dalton Transactions* **49**(16): 5044–5054. DOI: 10.1039/D0DT00327A.

Terenzi, M. G., Ferrucci, F., and Amadori, M. L. (2006). *Dipinti su rame: storia, tecnica, fenomeni di degrado, diagnostica, indicazioni per la conservazione e il restauro*. I talenti 19. Padova: Il prato. ISBN: 978-88-89566-36-7.

Tumosa, C. S. and Mecklenburg, M. F. (2013). Oil Paints: The Chemistry of Drying Oils and the Potential for Solvent Disruption. In: *New Insights into the Cleaning of Paintings: Proceedings from the Cleaning 2010 International Conference, Universidad Politecnica de Valencia and Museum Conservation Institute*. Ed. by M. F. Mecklenburg, A. E. Charola, and R. J. Koestler. Washington, DC: Smithsonian Institution: Smithsonian Contributions to Museum Conservation: 51–58.

Vega, D. E. (2016). *Oil painting on copper: characterization of the copper support and the feasibility of using pigmented wax-resin infills for paint loss reintegration*. Master's Thesis. NOVA University Lisbon.

Vichi, A., Artesani, A., Cheung, C. S., Piccirillo, A., Comelli, D., Valentini, G., Poli, T., et al. (2019). An exploratory study for the noninvasive detection of metal soaps in paintings through optical coherence tomography. In: *Proceedings Volume 11058, Optics for Arts, Architecture, and Archaeology VII*. Münich 24-27 June 2019. Ed. by P. Targowski, R. Groves, and H. Liang: 4. DOI: 10.1117/12.2527569.

Viguerie, L. de, Payard, P., Portero, E., Walter, P., and Cotte, M. (2016). The drying of linseed oil investigated by Fourier transform infrared spectroscopy: Historical recipes and influence of lead compounds. *Progress in Organic Coatings* **93**: 46–60. DOI: 10.1016/j.porgcoat.2015.12.010.

Wadum, J. (1998). The Study of Painting Techniques and Materials in Support of Art Historical Research. In: *Looking Through Paintings: The Study of Painting Techniques and Materials in Support of Art Historical Research*. Ed. by E. Hermens. Vol. 11: 179–198. ISBN: 978-1873132565.

Werner, U., Selwyn, L. S., Stone, T., McKinnon, W. R., MacKay, A., and Grant, T. (2012). The removal of metal soaps from brass beads on a leather belt. *Studies in Conservation* **57**(1): 20–3. DOI: 10.1179/2047058411Y.0000000004.

Wexler, H. (1964). Polymerization of Drying Oils. *Chemical Reviews* **64**(6): 591–611. DOI: 10.1021/cr60232a001.

Whitmore, W. F. and Lauro, M. (1930). Metallic Soaps—Their Uses, Preparation, and Properties. *Industrial & Engineering Chemistry* **22**(6): 646–649. DOI: 10.1021/ie50246a026.

Ye, F., Ye, Q., Zhan, H., Ge, Y., Ma, X., and Wang, X. (2019). Synthesis and Study of Zinc Orotate and its Synergistic Effect with Commercial Stabilizers for Stabilizing Poly(Vinyl Chloride). *Polymers* **11**(2): 194. DOI: 10.3390/polym11020194.

Yu, W. W., Falkner, J. C., Yavuz, C. T., and Colvin, V. L. (2004). Synthesis of monodisperse iron oxide nanocrystals by thermal decomposition of iron carboxylate salts. *Chemical Communications* 20): 2306. DOI: 10.1039/b409601k.

Sitography

American Elements (July 12, 2022). *American Elements - The Advanced Materials Manufacturer*. URL: https://www.americanelements.com/.

ChemicalBook (July 12, 2022). *ChemicalBook - Chemical Search Engine*. URL: https://www.chemicalbook.com/.

ChemSrc (July 11, 2022). *ChemSrc - CAS Number Search*. URL: https://www.chemsrc.com/en/.

Jefcoat Burton, M. (Dec. 22, 2020). *All Dressed Up: A Study of Stearate Growth Occurring on Anne Morrow Lindbergh's Leather Flight Helmet*. URL: https://airandspace.si.edu/stories/editorial/study-stearate-growth-anne-morrow-lindbergh.

PubChem (July 11, 2022). *PubChem - open chemistry database at the National Institutes of Health (NIH)*. URL: https://pubchem.ncbi.nlm.nih.gov/.

Chapter 2

Painted metal model samples

methodological aspects

Adapted from Russo S., Farinini, E., Leardi, R., Brambilla L., Thomas J.B., and Joseph E. 2022. Artificial ageing optimisation for metal soaps formation on painted metal model samples: A multivariate approach using full-factorial design, [in preparation]

In conservation science, most approaches exploit model samples designed to represent a specific artefact or a general class of heritage objects. These substitutes can assume different names and meanings (e.g., replicates, model samples, mock-ups) depending on their scope, design, or application, but they all help understand the physico-chemical behaviour of the material under chosen conditions. Many aspects contribute to the creation of model samples that enable insights into the mechanisms investigated while being representative of the system to which they refer. On the other hand, a wrong selection of characteristics could result in poorly informative or misguiding model samples. For this reason, efforts have been devoted to searching the single methodological aspects that could affect the accuracy of the analyses performed or that might undermine the understanding of the phenomenon under study. In particular, the formation of metal soaps on painted metal objects, a process that occurs between metal ions and fatty acids, is the focus of this research. The rationale behind the choices made in preparing model samples for the study of metal soap formation on painted metals is described here.

Several parameters must be considered to represent this complex class of composite materials made of metal support and oil paint. The criteria for the choice of appropriate metal substrates – i.e., the ones that would react with the free fatty acids in the oil binder to give metal soaps – and their surface finishing are discussed herein. Surface finishing was chosen according to historical sources as well as surface properties. These aspects are then put in relation to the properties of the oil coating, and solutions are proposed to the problem of the inhomogeneity of the oil film. Considerations on the preparation of cross-sections of the model samples for stratigraphy studies are presented.

Such cross-sections would allow us to access the interface directly and validate the hypothesis and results obtained using the non-invasive approach. In the last section, an ageing protocol aimed to exert the formation of the species of interest is commented through the discussion of the results of a design of experiment performed with the aim to optimise the ageing process. A collection of the different attempts needed to find the right combination of parameters that would produce the desired result and allow monitoring of the model samples is presented. Selected uni- and multivariate perspectives are taken into consideration.

2.1 Introduction

Mock-ups, replicates, and model samples are substitutes for cultural heritage objects that are widely used in conservation science since they allow for studies under controlled parameters facilitating documentation, comparison, sampling, analysis, statistics and molecular modelling (Porsmo Stoveland et al., 2021). They constitute simplified representations of the systems under study, which grant understanding of their properties while ensuring the preservation of the significance and integrity of the objects according to current ethical guidelines and regulations (Appelbaum, 2010). As such, they play a central role in scientific experiments (Burnstock et al., 2014). Model samples have also been proven able to stimulate serendipitous discoveries concerning the systems investigated, paving the way for intuitions, discoveries and new experimental ideas (Porsmo Stoveland et al., 2021). In the conservation science jargon, model samples differ from mock-ups in that they do not emulate specific objects or case studies, but they aim to represent a class of materials or artefacts, of which they make the simplified reproduction (Porsmo Stoveland et al., 2021).

In the study of metal soaps, model samples represent a valuable resource that has been employed for the understanding of their mechanisms of formation and consequences for the artworks. An advantage of the use of model samples is that they can serve as ”sacrificial” objects, hence they can, for instance, be cut and prepared as cross-sections for a deeper study of their stratigraphy and interfaces (e.g., by means of scanning electron microscopy-energy dispersive X-ray spectrometry, SEM-EDS). SEM techniques have enabled visualisation of the morphology of genuine and reconstructed zinc white (ZnO) oil paint samples and early-stages of crystalline soap growth (Kaszowska et al., 2013; Hermans et al., 2018) and clarification of the main aspects of the formation of lead soap aggregates in paintings (Keune and Boon, 2007; Casadio et al., 2019). Improvements in the detection and discrimination of backscattered electrons allowed identification of local precipitation processes with small atomic number contrast (Hermans et al., 2018).

In this study, model samples were crucial for understanding the mechanisms of the formation of metal soaps on painted metal objects. In this perspective, the system investigated was conceived as made of two single components in interaction: the linseed oil coating or paint and the metal support.

2.1.1 Model samples' preparation

For the preparation of well-founded painted metal model samples, several aspects needed to be taken into consideration:

a) available literature (i.e., historical recipes and scientific sources), to drive the decision about the substrate's selection and elucidate any particular practices to follow in the preparation of the surface or in the act of painting it with oil formulations,
b) the surface finishing, which characteristics should be chosen not to create impediments in the analytical response that would be detrimental to the correct interpretation of the results;
c) the coating thickness, that not only needed to be limited to represent that observed on painted metal artworks from museum collections (Terenzi et al., 2006) but also needed not exceed the limits of penetration and detectability given by the chosen analytical techniques.

Upon literature review, four substrates were identified, all of them commonly utilised by European and American artists during the 17^{th} – 18^{th} centuries and then later during the 20^{th} century: copper, zinc, iron and aluminium. In particular, copper was extensively extracted from the mineral ore in the 17^{th} – 18^{th} century and prepared as support for miniature portraits and bigger-size paintings (Terenzi et al., 2006). In contrast, in the 20^{th} century, metal supports of different kinds were taken from the production offcuts of the secondary sector to create several masterpieces. Other than copper, these mostly consisted of iron and iron-based alloys, aluminium, and zinc (Sasse, 2005).

Surface finishing was an essential variable in the design of model samples for this study, since different surface finishes provide different physico-chemical properties, both in terms of adhesion of the coating as well as reflection properties that can result in distortions in collected analytical signals. Several finishing alternatives were tested, which results will be discussed in Section 2.3.2. The consultation of historical sources for painted metals hinted toward the need to roughen the surface of the metal to improve the adhesion of the paint onto the support, which was achieved using different methods (Watin, 1773; De Piles and Jombert, 1766). Some Old Masters' sources, for instance, recommended using abrasive materials (e.g., pumice stone) to polish the surface before applying single or multiple layers of oil as a primer. These sources also suggested to proceed creating a rippled surface by repeatedly pressing on the oil with the fingers or the hand (Watin, 1773; De Piles and Jombert, 1766; Vega et al., 2018).

In attempting scientific reproducibility of the model samples for this study, industrial methods were considered, as they would allow consistent surface finishing due to increased precision given by the machine-based process. In particular, for the roughened surface, an industrial process called *hair-brushing* was utilised, which exploits the action of abrasive filamentary materials (brushes) to create unidirectional lines giving a satin finish (Rapid Direct, 2021). Several types of brushes are used to achieve a brushed metal finish, which are utilised for different surface effects. Steel brushes are primarily employed as they are non-loading materials, meaning they do not accumulate debris and particles when used on painted surfaces or other similar coatings (Krüss Scientific, 2022). The type of metal and its surface finishing also influence the homogeneity of the oil film applied. The balance between the intermolecular reaction of a liquid film with a solid surface and cohesive forces existing within the liquid film determines its ability to maintain contact with a solid phase. This property is addressed to with the term "wettability" (Israelachvili, 2011). In the

drying of an oil coating, in fact, two interfaces must be considered: one, where the oil is in contact with the air, which allows polymerisation and curing of the oil film through air-oil interface autoxidative processes (Orlova et al., 2021); the other, where the metal is in contact with the oil, and that depends on the physico-chemical affinity of one for the other. Incrementing the wettability of the surface of the metal by micro-oxidation can help improve the surface properties (Belkind and Gershman, 2008).

Plasma treatment is an industrial technique implemented in several applications in semiconductor processing and microchip fabrication, metallurgy, optics, dentistry, medical technologies and food packaging. It has been extensively studied in corrosion science, where obtaining firmly adherent and durable interfaces to prevent attack from corrosive species such as oxygen, ions, acids, bases, and water is a fundamental necessity (Belkind and Gershman, 2008; Török et al., 2015; Tiňo et al., 2019). Plasma treatment approaches, which can be seen as a tool for interface design and engineering, consist of the removal of contaminants using a plasma source and micro-oxidation – functionalisation – of the surface to improve the affinity for a coating (Lin et al., 1997). Plasma functionalisation of surfaces can be performed using air, hydrogen, nitrogen or oxygen at atmospheric pressure (Lin et al., 1997).

With the increased wettability, the surface is ready to receive a coating. Two major standard industrial procedures allow us to obtain homogeneous coatings with controlled thickness: *dip and spin coating* (Scriven, 1988). These two technologies are widely used in the electronics and optics fields to improve the performance of materials having different geometries (e.g., plates, fibres, tubes) when different fluids are applied as coating agents (Gans et al., 2019; Rehg and Higgins, 1992).

Dip coating entails deposition of a liquid film on a surface after immersion and withdrawal from a liquid bath (Scriven, 1988). It is the oldest commercially available coating process – it was patented by Jenaer Glaswerk Schott & Gen. in 1939 for sol-gel derived silica films – and it is still widely used for a manifold range of applications, including chemical solution deposition (CSD)-derived coatings, inorganic and hybrid coating materials (Brinker, 2013). The process consists of three main stages (Figure 2.1a):

a) immersion and dwell time, where the substrate is dipped in the liquid phase at a constant speed and kept in immersion for a certain period of time to allow interaction between the substrate and the coating solution;
b) deposition and drainage, during which the substrate is withdrawn from the liquid phase and a thin layer is entrained; the excess is let to drain from the surface;
c) traditionally, evaporation of the solvent from the fluid and drying of the thin film, promoted by heating, when necessary. Heating can also be adopted as a subsequent treatment to eliminate residual organics or induce crystallisation of the functional oxides (Brinker, 2013).

Spin coating was developed explicitly for paint and pitch coatings. It is a "transient process of flow and mass transfer" (Bornside et al., 1989), where the coating thickness and uniformity depend on the competition between centrifugal forces – that drive the liquid flow outwards – and the forces determining the evaporation of solvents with consequent retainment of the thin residual film (viscous forces and surface tension). Falling diffusivity, rising viscosity, and changing rheology as solvents evaporate from the remaining film complicate the process. Such a process allows for controlled coating thickness ranging

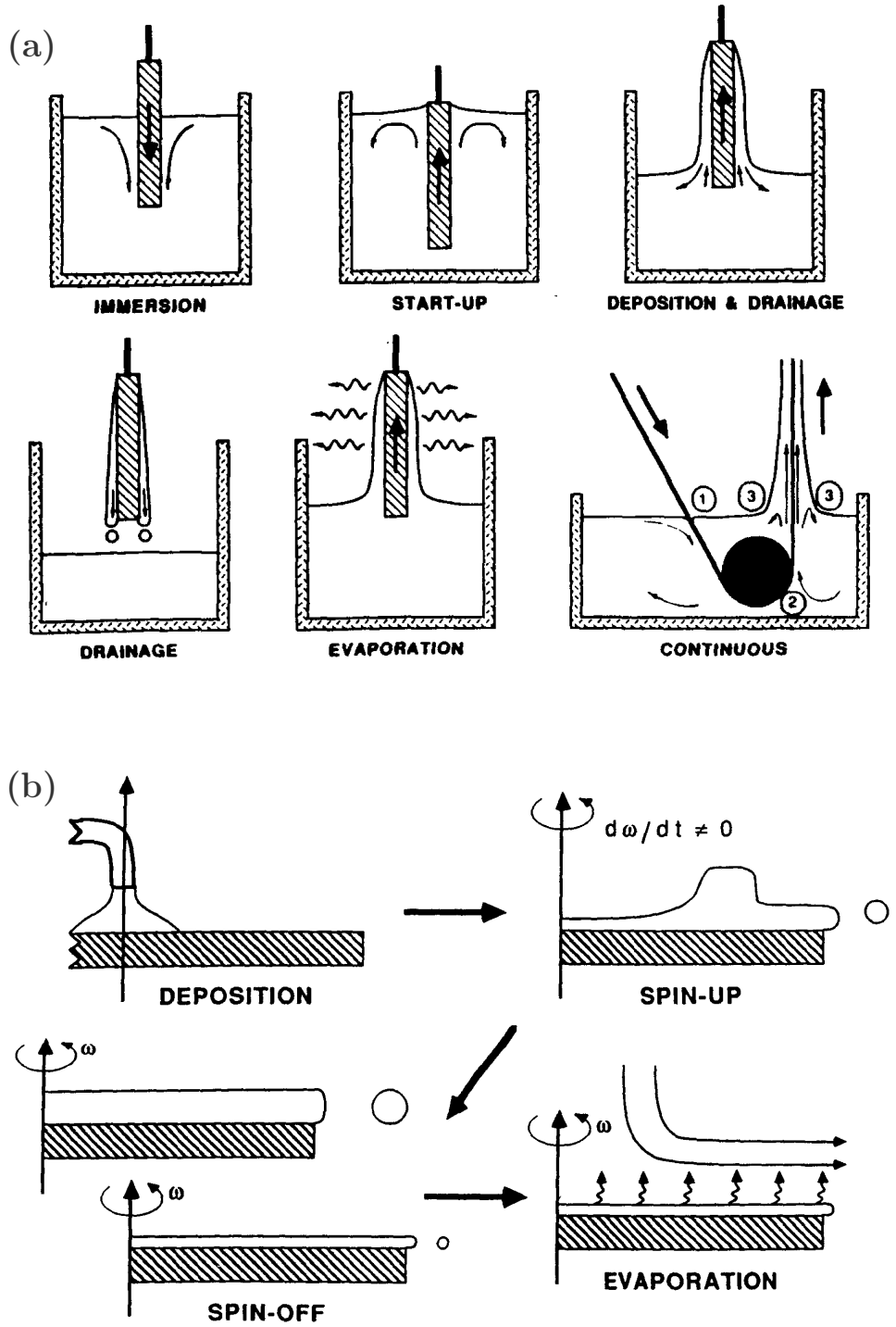

Figure 2.1: Main steps of the dip coating (a) and the spin coating (b) processes (from Scriven, 1988).

from 1 to 200 μm (Bornside et al., 1989; Tyona, 2013). Several stages can be identified in the spin-coating process (Figure 2.1b):

a) fluid apportion;
b) spin-up;
c) spin-off or outflow;

d) drying of the coating through evaporation.

By examining stages a) and b), the importance of the spin speed parameter can be inferred. Together with the viscosity of the coating material, this parameter represents the most critical variable in the spin-coating process. Although overlapping mechanisms, stages c) and d), controlled by flow and evaporation, respectively, can have subsequent dominating times on the process and be engineered separately.

2.1.2 Ageing protocol and definition of its parameters through design of experiment (DoE)

Artificial ageing is a common practice in conservation science, as it allows us to infer the behaviour of model samples or mock-ups when exposed to particular conditions. In practice, harsh conditions of relative humidity, temperature, and, in some cases, UV irradiation or pollutants are commonly chosen to exert relevant changes on the samples and understand mechanisms of degradation or resistance of the material to physical or chemical deterioration. Many parameters are associated with ageing and deterioration processes, which relate to the chemical and physical changes of the material (Smidt et al., 2013). The study of metal soaps also exploits ageing protocols in order to understand and induce their formation. Such protocols involve chemical and physical degradation due to moisture and water content (Garrappa et al., 2020), temperature (Hermans et al., 2016), and presence of reactive chemical species (Baij et al., 2018), amongst others. The changes occurring in the system can then be evaluated or monitored using a range of analytical methods that allow the characterisation of the different materials and phases of degradation.

Multivariate approach Depending on the question to be answered, a large number of multivariate methods are available that can help plan the experiments most conveniently and effectively or visualising and interpreting the results obtained (so-called pattern recognition methods, of which exploratory analysis such as principal components analysis – PCA – is part) (Brereton, 2018). Design of experiment (DoE) applies statistical methods to plan, conduct, analyse, and interpret controlled tests. It entails the systematic evaluation of factors that control the weight of a parameter or group of parameters on the process investigated. Differently from the univariate approach, this set of multivariate statistical applications provides information on the relationship between multiple input variables – i.e., factors – and their responses (Anderson and McLean, 1974).

In a design of experiment, the factors are not changed one at a time (one-factor-at-a-time – OFAT – experiments), but they are rather considered as a system composed of individual contributions, as well as their interactions (Czitrom, 1999).

This characteristic makes it an essential tool for the effective optimisation of chemical processes, both for industrial applications and for fundamental research studies. In the full factorial design experiment, two levels are established for each factor, and a model is created that is composed of linear, quadratic and interaction terms (cross-terms) (Cheng, 2019). One advantage of factorial designs is that they bring to conclusions that have validity in a range of experimental conditions because they put in relation the effects of a factor with several levels of other ones (Cheng, 2019).

2.2 Materials and methods

2.2.1 Choice of metal substrates

To appraise the ability of different metal supports to produce metal soaps, copper and zinc samples were purchased as $60 \times 60 \times 1$ mm^3 sheets from Tartaix, France, whereas aluminium and iron samples were obtained from Distrelec, Switzerland. The choice of the sample size was made to permit characterisation by employing most analytical techniques – i.e., so that the samples would fit instruments that require limited dimensions of the object – while allowing to identify several areas of interest to be analysed to ensure representativity. After rinsing the samples with absolute ethanol (VWR Chemicals) to remove eventual dust and deposits, the formation of metal soaps was induced by adding 1 µL drop of palmitic acid (PA, $\geq$ 98%, Sigma Aldrich) in ethanol solution (7.8×10^{-2} M) on the surface of the coupons. Palmitic acid is one of the reactive components of oil formulations towards metal ions, and it represents the 6% of the fatty acid composition of liseed oil (Bayrak et al., 2010). The samples were left to react overnight at room temperature, then analysed through Fourier transform infrared spectroscopy using a Thermo Scientific™ Nicolet™ iN10 MX infrared microscope. The spectra were collected in reflectance mode with a spectral resolution of 4 cm^{-1}, 16 accumulations per spectrum, and with an aperture of 150×150 µm^2.

2.2.2 Choice of surface finishing

To investigate the properties given by different surface finishing to the oil coating, the $60 \times 60 \times 1$ mm^3 copper and zinc sheets were selected and underwent hair-brushed and mirror polishing finish. The hair-brushed surface finishing was commissioned to a specialist at Gravadhoc Hoffmann, Neuchatel. Mirror polishing was performed using a Bergeon 6880 polisher. The procedure utilised to polish the sample consisted of four steps (supplies purchased at artsupport.ch):

a) brushing with a Wood Hub Wheel Brush, black, 5-rows, inner diameter 40 mm and outer diameter 80 mm, with polishing paste Tripel;
b) polishing with a fine yellow cotton buff, diameter 150 mm, width 15 mm, with a combination of Dialux Super finishing composition blue and white, for all metals;
c) using a miniature brush, cotton x-full, mounted, diameter 22 mm, for refinement;
d) rinsing with ethanol in an ultrasonic bath.

Before applying the oil coating, all surfaces were documented in a photographic tent equipped with LED strip lights positioned at the sides of the base (Amazon, generic brand) using a Canon EOS600D camera. Surface roughness measurements were achieved at the Institute of Materials – Tribology and Interfacial Chemistry Group (TIC) of the Ecole Polytechnique Fédérale de Lausanne (EPFL) using a Keyence VK – X260 3D laser scanning microscope (20x objective). Three areas were measured per sample, and the results were compared to estimate the variability per substrate (Figure 2.2).

Surface roughness was described by its relevant parameters, i.e., *Ra* and *Rz* for line roughness (Figure 2.3) and *Sa*, *Sz* and *Str* for area roughness, where (Brown, 2017)

- Ra is the arithmetic mean deviation value. It is one of the most widely used parameters for the stability of the results it provides. In particular, it describes

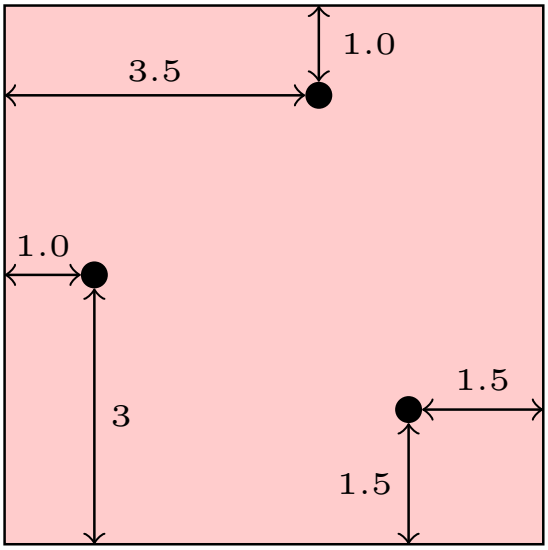

Figure 2.2: The location of the three areas documented using 3D laser scanning microscopy on each sample; all values in cm.

the mean of the sum of the height differences (in absolute value) from the average surface along the considered line, and it is not significantly influenced by surface defects or measurement noise (Figure 2.3a).

- Rz is the maximum height, i.e., the sum of the maximum peak amplitude (Rp) and the maximum trough amplitude (Rv, in absolute value) from the average surface (Figure 2.3b). Not being a statistical quantity, as opposed to Ra, the maximum height Rz is highly affected by single outliers. This characteristic makes it a highly sensitive parameter for roughness measurements.
- Sa and Sz are the two-dimensional equivalents of Ra and Rz, respectively, i.e., the arithmetic mean deviation value and the maximum height value of the considered area.
- Str, i.e., the texture aspect ratio, is a measure of the spatial anisotropy of the surface. It takes values between 0 and 1, where 1 corresponds to a perfectly isotropic surface and values approaching 0 signify strongly anisotropic surfaces.

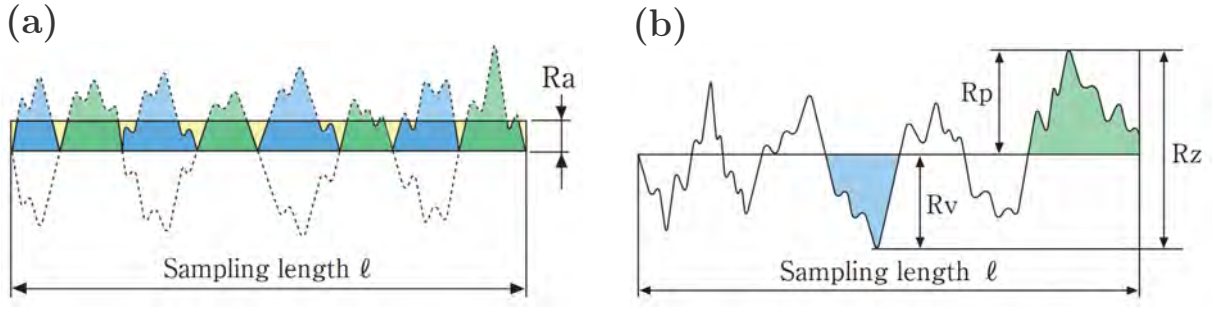

Figure 2.3: Graphical representation of the line roughness parameters Ra (a), and Rz (b) (from Brown, 2017).

2.2.3 Coating application and homogeneity

After the surface finishing treatment (Section 2.2.2), some tests were performed using simple to more sophisticated methodologies to deposit a homogeneous layer of linseed oil on the copper and zinc samples:

a) A first attempt was performed by depositing ~ 80 µL of cold-pressed linseed oil (Kremer Pigmente) on the surface of the metal and spread using a 6 cm painter's spatula. The coating thickness was maintained as homogeneous as possible by framing and securing the samples using commercial cellulose acetate office tape (3M Company, 0.56 mm thickness) (Figure 2.4).

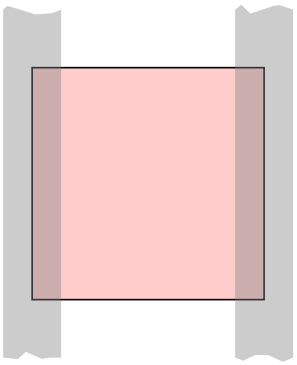

Figure 2.4: Framing of the sample with commercial tape to facilitate coating using a painter's spatula.

b) A second attempt involved plasma treatment followed by dip or spin coating, performed at the department of Engineering of the Haute Ecole Arc, Micro and Nanosystems group by Laure Jeandupeaux. Radiofrequency (RF) plasma was used with 2×10^{-2} mbar O_2 partial pressure to achieve 3.6×10^{-2} mbar pressure during the treatment. The samples were deposited on microscope slides at the bottom electrode of the machine. The treatment lasted 2 min with a plasma power of 80 W. The coating was performed during the following 5 min.

For the coating process, several combinations of parameters were tested so to find satisfying coating specifications for zinc and copper coupons, such as type of finishing (polished or brushed), type of coating method used (dip or spin coating), speed, and heating conditions during the curing of the oil (Table 2.1).

The thickness of the coating was evaluated by averaging nine measurements per sample (3×3 points on a grid), using the coating thickness gauge Surfix® by Phynix. Calibration was performed on a bare metal sheet having the same topography as the samples and on a standard 8 ± 0.5 µm hard-plastic films placed on the bare metal sample to account for the physical characteristics of the metal surface. Homogeneity of the coating was investigated on a selection of samples (Table 2.2) using a Keyence VK – X260 3D laser scanning microscope at the Institute of Materials – Tribology and Interfacial Chemistry Group (TIC) of the Ecole Polytechnique Fédérale de Lausanne (EPFL). The images presented were all acquired using a 20x objective.

Table 2.1: Tested parameters for coating the copper and zinc samples with linseed oil. Heating was achieved using a laboratory oven (SalvisLab Vacucenter).

Sample	Surface	Method	Speed	Curing temperature
Cu03	Polished	Dip-coating	100 mm/min	Room temperature
Cu04	Polished	Dip-coating	100 mm/min	Room temperature
Cu45	Brushed	Dip-coating	100 mm/min	80 °C oven
Cu46	Brushed	Dip-coating	100 mm/min	80 °C oven
Zn03	Polished	Dip-coating	20 mm/min	Room temperature overnight, then 80 °C oven
Zn04	Polished	Dip-coating	100 mm/min	Room temperature
Zn48	Brushed	Dip-coating	100 mm/min	Room temperature
Zn49	Brushed	Dip-coating	100 mm/min	Room temperature
Cu01	Polished	Spin-coating	1000 rpm	Room temperature
Cu02	Polished	Spin-coating	1000 rpm	Room temperature overnight, then 80 °C oven
Cu43	Brushed	Spin-coating	500 rpm	80 °C oven
Cu44	Brushed	Spin-coating	500 rpm	80 °C oven
Cu40	Brushed	Spin-coating	500 rpm	Ramp 20 to 80 °C overnight
Cu41	Brushed	Spin-coating	500 rpm	Ramp 20 to 80 °C overnight
Zn01	Polished	Spin-coating	1000 rpm	Room temperature
Zn02	Polished	Spin-coating	1000 rpm	Room temperature overnight, then 80 °C oven
Zn45	Brushed	Spin-coating	1000 rpm	80 °C oven
Zn46	Brushed	Spin-coating	1000 rpm	80 °C oven
Zn36	Brushed	Spin-coating	500 rpm	Ramp 20 to 80 °C overnight
Zn37	Brushed	Spin-coating	500 rpm	Ramp 20 to 80 °C overnight

Table 2.2: Final parameters for coating the copper and zinc samples with linseed oil.

Sample	Surface	Method	Speed	Curing temperature
Cu35	Brushed	Spin-coating	500 rpm	Ramp 20 to 80 °C overnight
Cu36	Brushed	Spin-coating	500 rpm	Ramp 20 to 80 °C overnight
Cu37	Brushed	Spin-coating	500 rpm	Ramp 20 to 80 °C overnight
Cu38	Brushed	Spin-coating	500 rpm	Ramp 20 to 80 °C overnight
Cu39	Brushed	Spin-coating	500 rpm	Ramp 20 to 80 °C overnight
Cu47	Brushed	Spin-coating	500 rpm	Ramp 20 to 80 °C overnight
Zn31	Brushed	Spin-coating	500 rpm	Ramp 20 to 80 °C overnight
Zn32	Brushed	Spin-coating	500 rpm	Ramp 20 to 80 °C overnight
Zn33	Brushed	Spin-coating	500 rpm	Ramp 20 to 80 °C overnight
Zn34	Brushed	Spin-coating	500 rpm	Ramp 20 to 80 °C overnight
Zn35	Brushed	Spin-coating	500 rpm	Ramp 20 to 80 °C overnight
Zn38	Brushed	Spin-coating	500 rpm	Ramp 20 to 80 °C overnight

2.2.4 Preparation of cross-sections for stratigraphy studies

Cross-sections of aged samples (12 months, Cu08; 10 months, Zn10) were obtained using a benchtop "guillotine" metal cutter. Similarly to a paper cutter, this works by placing the sample on the base and bringing a blade down until the sample is cut as desired. Two sets of samples were prepared:

- one, where cured oil-coated samples were cut and then mounted directly on slotted screw vise stubs (TedPella Inc), without the need to embed them in resin;
- in a second set, the metal was first embedded in epoxy resin (EpoFix Kit by Stuers) and then polished with successively finer grades of micromesh abrasive cloths (600, 800, 1200 and 4000 mesh) to a smooth flat surface. A 1 mm-width guide was drilled in the resin with a microdrill to expose a few mm of the embedded metal. Cold-pressed linseed oil (Kremer Pigmente) was poured with the help of a Pasteur pipette until this space was filled (Figure 2.5).

The scanning electron microscopy (SEM) analyses were performed at the *centre Suisse d'électronique et de microtechnique (CSEM)* using a Thermo Fisher Scientific FIB (focused ion beam) Scios 2 DualBeam scanning electron microscope (Thermo Fisher Scientific, Waltham, MA, USA) coupled with an energy-dispersive X-ray analyser (EDX). The samples were observed using an Everhart–Thornley detector (EDT) for secondary electrons, an acceleration potential of $15 - 20$ kV, and a $7 - 8$ mm working distance.

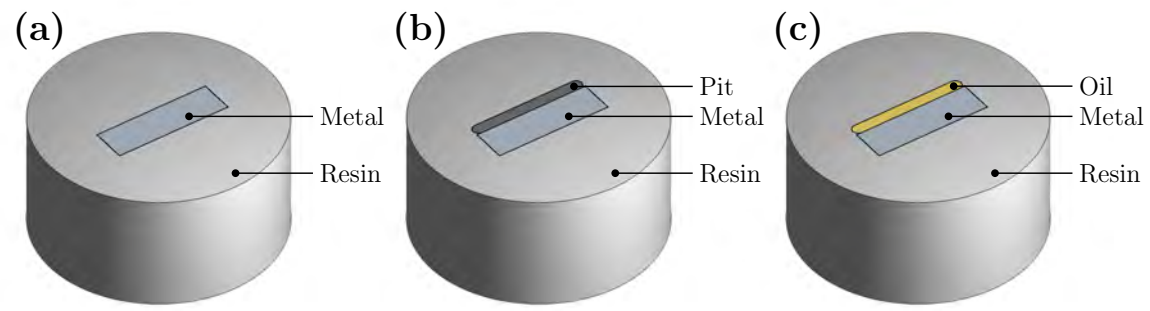

Figure 2.5: Schematic showing the preparation of cross-sections for stratigraphy studies; (a) metal embedded in resin, (b) pit drilled in the embedding resin and in contact with the embedded metal, (c) oil deposited in the pit and let cure.

2.2.5 Establishment of the ageing protocol

In order to establish the most effective artificial ageing protocol to promote the formation of metal soaps on the metal samples in the absence of a climatic chamber, three distinct methods were used, for which both linseed oil (LO) alone (hereafter referred to as 'coating' and linseed oil-zinc oxide (LoZnO) formulations (hereafter defined as 'paint') were prepared and applied on $60 \times 60 \times 1$ mm^3 zinc and copper substrates (Tartaix). LOZnO samples were prepared to add a level of complexity to the system and evaluate the possibility of using this protocol in future experiments involving the presence of pigments. For the painted samples, a zinc oxide-based oil formulation was made following historical practices, where zinc white (ZnO) and cold-pressed LO purchased from Kremer Pigmente were intimately ground in a ceramic mortar ($20 - 25\%$ LO in ZnO w/w) (Feller et al., 1986). LO-coated samples were prepared using a painter's spatula in the same fashion described in Section 2.2.3, method a). Metal soaps formation due to artificial ageing was investigated using a Thermo Scientific^{TM} Nicolet^{TM} iN10 MX infrared microscope (μ-FTIR) by collecting single-scan spectra in reflectance mode (4 cm^{-1} resolution, aperture 150×150 μm^2) on an area of 1500×10500 μm^2.

The three protocols are described hereafter and shown schematically in Figure 2.6:

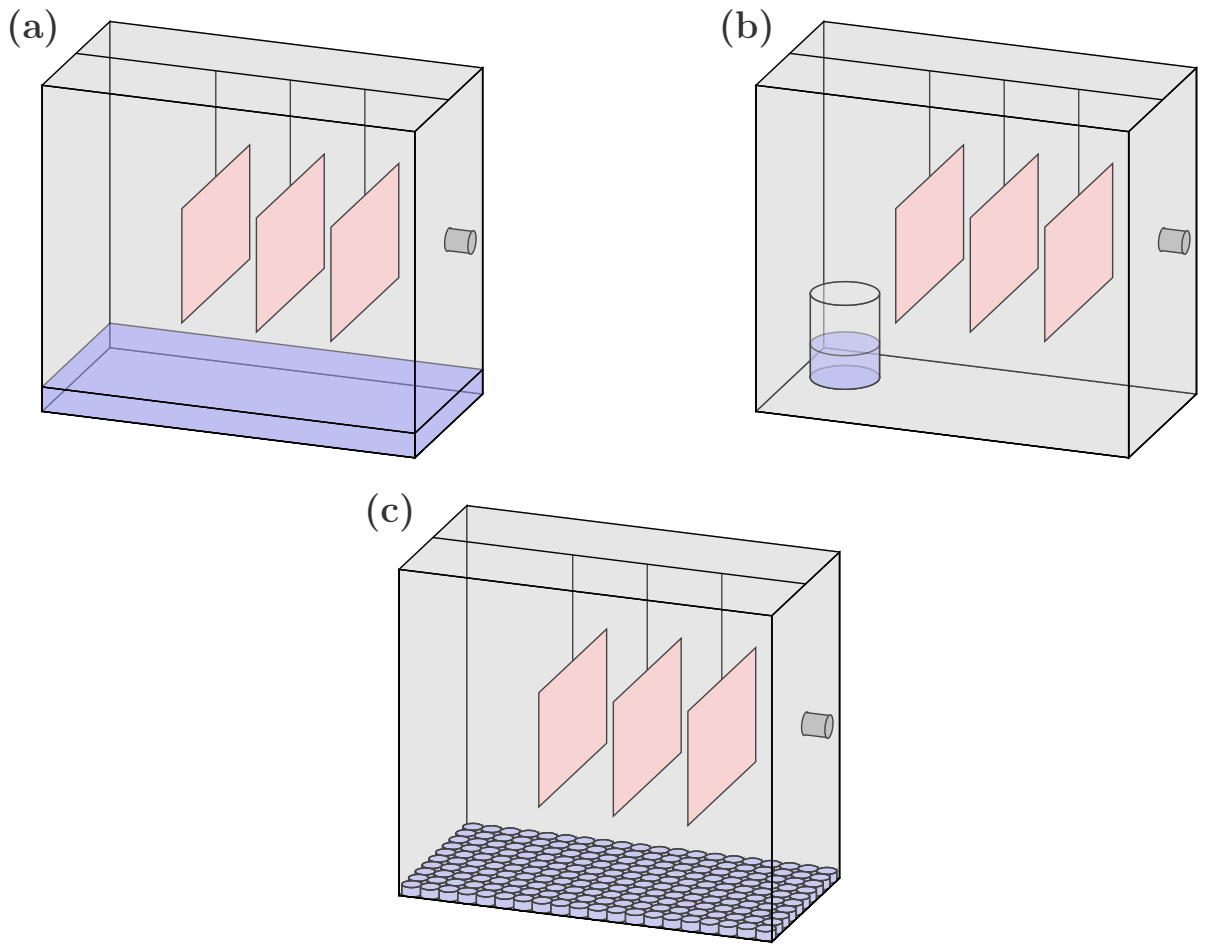

Figure 2.6: Schematic overview of the three setups utilised to age the copper and zinc samples artificially. The immersion probe of the datalogger is shown schematically as the small grey cylinder on the side of the box.

a) The first attempt was made using commonly available materials purchased at Praxis City Eindhoven[1]. The coated copper and zinc samples were cured in a kitchen oven (Severin TO 2058) at 80 °C as indicated by an electronic cooking thermometer ('Fantast' by IKEA). A drop of a concentrated solution of palmitic acid in ethanol was deposited on a selected area of the coupons using a Pasteur pipette (Figure 2.7) to evaluate the differences in ageing rates when the concentration of reagents was increased. The samples were then divided into rubber-sealed food-compatible plastic boxes, each containing three samples that were kept hanging in the box chamber through a nylon wire secured to the sides of the box (Figure 2.6a). A sodium chloride saturated water solution was added in the box, granting $\sim 80\%$ relative humidity (RH) values at room temperature for a month (O'Brien, 1948; Greenspan, 1977). Temperature and relative humidity levels were recorded using a datalogger (PeakTech 5185) equipped with an immersion probe that could be inserted through a hole in the side of the box and then sealed with commercial silicone glue. This indicated 70–80% RH for temperatures oscillating between 20 and 30 °C for the duration of the month-long experiment. The samples were photographed using a Nikon D5600 camera at spaced time intervals in standardised conditions in a commercially available portable photographic tent with integrated LEDs (Amazon, generic brand). A colour test chart (X-Rite ColorChecker®) was kept in the frame to allow white balance for consistent white points representation across multiple images.

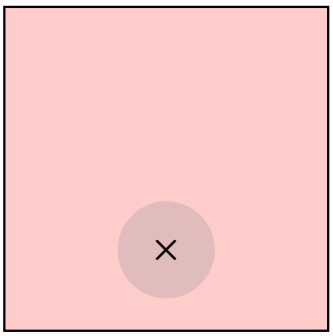

Figure 2.7: Location of the 1 µL palmitic acid drop deposited on samples prepared using ageing protocol a).

b) The second protocol made use of a laboratory oven (SalvisLab Vacucenter) and temperature-resistant polypropylene boxes by Buchsteiner GmbH & Co. A similar system to the one mentioned above was used to array the samples in the boxes for homogeneous exposure to the environmental conditions. The relative humidity value ($\sim 70 - 80\%$) was ensured at 80 °C using a 1:1 glycerol:water solution (Forney and Brandl, 1992) kept in a beaker inside of the box for a month (Figure 2.6b).

c) A third attempt was made utilising the same boxes and laboratory oven system as above (protocol b), but employing pre-conditioned silica gel beads ($\sim 2 - 5$ mm) at 60 °C for a month (Figure 2.6c). The pre-conditioning process consisted of positioning the silica gel beads in an inert tray that would ensure a large surface area and exposing them to the desired 80% RH level in a climatic chamber at 60 °C temperature for 24 hours.

[1] This protocol was designed to be conducted outside of the laboratory environment. It was necessitated by the inaccessibility of equipped laboratories during the lock-down enforced to mitigate the spread of COVID-19 in March 2020.

Design of experiment Full factorial design was chosen as experimental design method to optimise the ageing parameters. Five variables were identified (Table 2.3), that correspond to

- environmental conditions: indoor uncontrolled conditions (NC) as implicit level, and two levels characterised by high humidity and room temperature (**A**, rt.hi/ro.hi) or harsh conditions of temperature and relative humidity (**B**, 80 °C/80%);
- absence (level −1) or presence (+1) of zinc oxide in the paint formulation (System);
- copper (level −1) or zinc (level +1) support (Substrate);
- thickness of the coating (thin, −1, and thick, +1),
- monitoring time every week from 0 hours (−1) to 28 days (+1).

Table 2.3: Variables considered in structuring the DoE.

		Levels		
Var. ID	**Variable**	**Implicit level**	**A**	**B**
X1	Environmental conditions (°C/%RH)	Natural conditions (NC)	Room temperature/80% (rt.hi)	80 °C/80% (hi.hi)
			-1	**+1**
X2	System		LO	LOZnO
X3	Substrate		Cu	Zn
X4	Thickness		Thin	Thick
X5	Time (5 levels)		0	28

The experimental matrix showing the 27 experiments (24 different experiments and three replicates) is given in Table 2.4. The three replicates, indicated by the decimal experiment number (i.e., 5.2, 11.2, 24.2), were chosen randomly from each of the three environmental conditions (room conditions (NC), room temperature and high humidity (rt.hi/ro.hi), and high temperature and high humidity (hi.hi)) to evaluate the experimental variability, following the logic of the fractional factorial $2^{(3-1)}$, for which replication is one fundamental condition (Montgomery, 2019). Experimental matrices and design models were computed by the CAT (Chemometric Agile Tool) software, an open-source software based on the R platform (The R Foundation for Statistical Computing, Vienna, Austria).

Every DoE experiment was monitored at five different times within 28 days by means of Fourier transform infrared spectroscopy. Spectra were collected on all samples in reflectance mode using a Thermo Scientific^{TM} Nicolet^{TM} iN10 MX infrared microscope with a spectral resolution of 4 cm^{-1}, 16 accumulations per spectrum, and with an aperture of 150×150 μm^2, for a total of 135 spectra collected. The order of the analyses was randomised at each time point to account for experimental errors. The spectra were cropped to the relevant wavenumbers for this study, i.e., from $1495 - 1660$ cm^{-1}, to include characteristic absorption due to asymmetric vibration of the carboxyl group ($\nu_a COO^-$).

From a preliminary analysis of the 135 (27 experiments × 5 time points) spectra acquired, 18 showed anomalous features (outliers) and were therefore not considered in the subsequent data processing. Standard normal variates (SNV) transformation was applied to the data

Table 2.4: Experimental matrix showing the 27 experiments performed following the full factorial design approach.

Exp.	X1	X2	X3	X4
1	NC	LO	Cu	Thin
2	NC	LOZnO	Cu	Thin
3	NC	LO	Zn	Thin
4	NC	LOZnO	Zn	Thin
5.1	NC	LO	Cu	Thick
6	NC	LOZnO	Cu	Thick
7	NC	LO	Zn	Thick
8	NC	LOZnO	Zn	Thick
9	hi.hi	LO	Cu	Thin
10	hi.hi	LOZnO	Cu	Thin
11.1	hi.hi	LO	Zn	Thin
12	hi.hi	LOZnO	Zn	Thin
13	hi.hi	LO	Cu	Thick
14	hi.hi	LOZnO	Cu	Thick
15	hi.hi	LO	Zn	Thick
16	hi.hi	LOZnO	Zn	Thick
17	rt.hi	LO	Cu	Thin
18	rt.hi	LOZnO	Cu	Thin
19	rt.hi	LO	Zn	Thin
20	rt.hi	LOZnO	Zn	Thin
21	rt.hi	LO	Cu	Thick
22	rt.hi	LOZnO	Cu	Thick
23	rt.hi	LO	Zn	Thick
24.1	rt.hi	LOZnO	Zn	Thick
5.2	NC	LO	Cu	Thick
11.2	hi.hi	LO	Zn	Thin
24.2	rt.hi	LOZnO	Zn	Thick

to eliminate the effect of the baseline. In this way, it was possible to highlight differences in the shape of the spectra.

Principal component analysis (PCA) was then performed, allowing individuation of four significant components that explain the 51.7%, 20.1%, 13.4% and 11.4% of the variance, respectively (96.6% total explained variance, Figure 2.8).

The interpretability of the four significant components was improved by the application of a Varimax rotation, a statistical operation that maximises the intelligibility of the results by performing an orthogonal rotation of the factors axis towards the direction of maximum variance of the squared loadings (Kaiser, 1958). The factors obtained allowed us to explain 46.3%, 18.36%, 16.4% and 15.5% of the total variance, respectively.

Before proceeding with the computation of the model, the dispersion of the replicates in the score plot was evaluated, so to verify that the experimental variability was acceptable

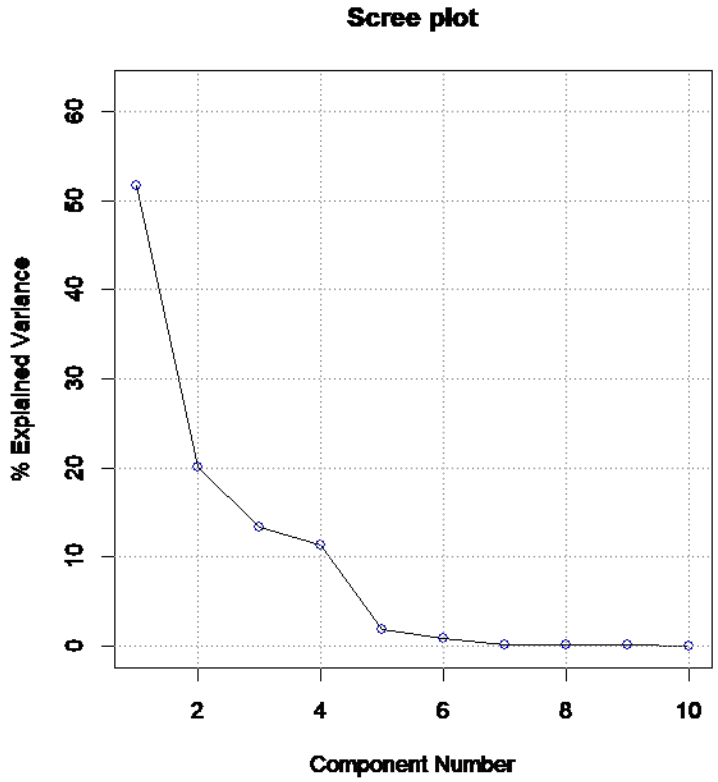

Figure 2.8: Scree plot showing the main principal components; the first four explain 96.6% of the total variance.

and not higher than the induced variability. In the following plots (Figure 2.9), points corresponding to the same time point of the two experimental replicates were connected by a segment (0 = 0 days, 1 = 7 days, 2 = 15 days, 3 = 21 days, 4 = 28 days). At each time point, the replicates were relatively close, indicating that the experimental variability was acceptable.

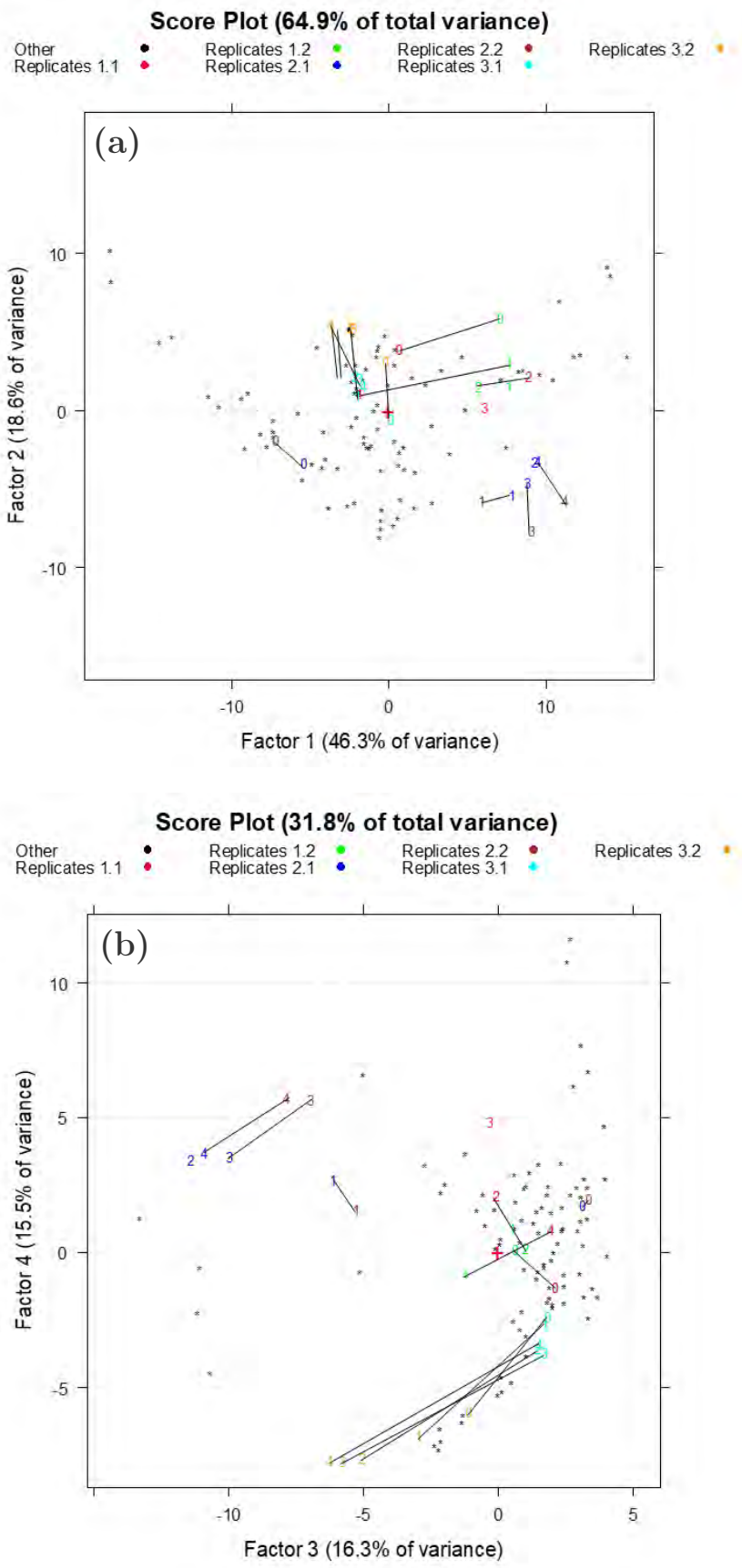

Figure 2.9: Evaluation of the experimental variability from the dispersion of the replicates for each time-point (decimal experiment numbers) in the score plot (0 = 0 days, 1 = 7 days, 2 = 15 days, 3 = 21 days, 4 = 28 days).

2.3 Results and discussion

2.3.1 Choice of metal substrates

As stated in Chapter 1, copper, zinc, aluminium and iron, all produce stable metal-organic salts of synthesis; hence they technically classified to be considered in this study. By depositing 1 μL of a concentrated solution of palmitic acid (7.8×10^{-2} M) on the surface of each four different metal substrates, and collecting FTIR spectra to reveal the presence of metal soaps formed, differences were highlighted: for copper and zinc (Figure 2.10), metal palmitates could be identified (1587 and 1541 cm^{-1}, respectively) (Otero et al., 2014; Izzo et al., 2021), whereas for iron and aluminium (Figure S - 20) such formation of metal-organic compounds was not observed at the expected wavenumbers (1575 and 1561 cm^{-1}, respectively) (Palacios et al., 2004; Xu et al., 2019). For this reason, the choice of the substrate for further experiments fell on the metals belonging to groups 11 and 12 of the periodic table of the elements (i.e., copper and zinc). These are characterised by having the same oxidation number of the metal cation (II) and similar crystal and effective ionic radius r_{ion} for the ion in oxidation state 2+ (87/73 pm and 88/74 pm for copper and zinc, respectively) (Shannon, 1976).

Aluminium and iron-based sheets were not further considered given the test results, confirmed by literature documentation, where there is no reported occurrence of iron metal soaps in paintings. However, iron soaps can be synthesised as stable compounds, and it is not excluded that iron-based pigments and supports might give metal soaps in certain conditions (e.g., in industrial machines, when lubricated parts are in relative motion, composite objects, as reported in Chapter 1, p. 23).

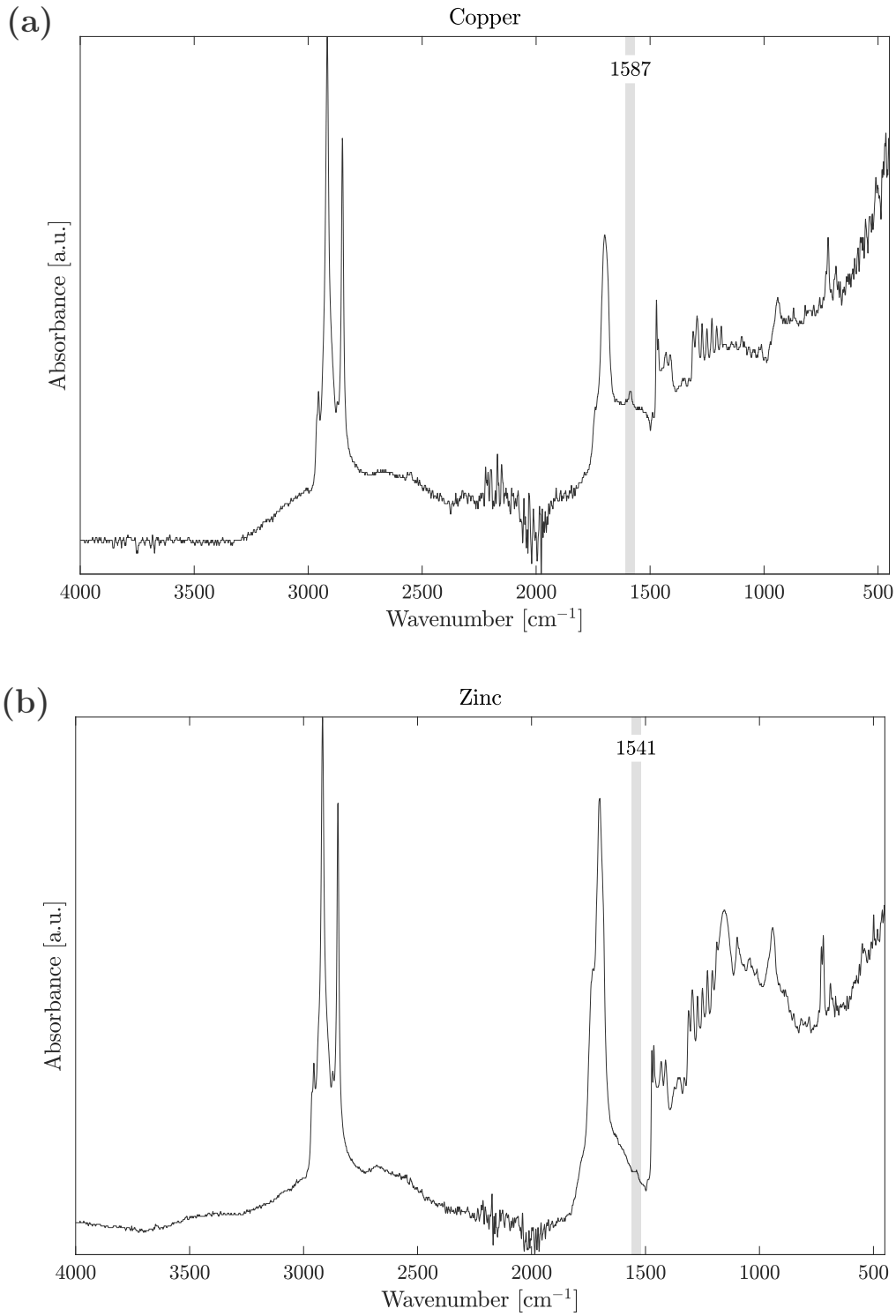

Figure 2.10: FTIR spectra of (a) copper (Cu01) (b) zinc (Zn01) coupons after reaction overnight with palmitic acid. The shaded area highlights the characteristic peak for the carboxylate group vibrational mode $\nu_a COO^-$.

2.3.2 Choice of surface finishing

Surface roughness was documented using 3D laser scanning microscopy. This was a preliminary step aimed at documenting surface roughness before investigating the implications of the chosen finishing in terms of homogeneity of the coating (Section 2.3.3) and spectroscopic properties (Chapter 3). Figure 2.11 shows the results of the measurements on a selected area of the copper and zinc polished and brushed coupons (Figure 2.11A-B-C). In Figure 2.11A, referring to the polished surface, expected marks from the polishing process were observed. By comparing the arithmetic mean deviation values Ra for the line roughness of polished and brushed samples, it can be noticed how Ra for the polished copper sample (Ra = 0.263 μm) showed significantly lower values than for the brushed one (Ra = 1.521 μm). This was expected since Ra is, by definition, higher when more variability is present in the sample. In this case, the variability was introduced by the presence of the vertical lines due to the brushed finishing.

The Rz value for the copper polished sample (Rz = 2.229 μm) indicated a non-perfectly polished surface, which would otherwise give values closer to 0 μm. The irregularities and scratches visible on the sample's surface are responsible for this behaviour. As previously mentioned, in fact, Rz is highly affected by the presence of outliers.

For copper and zinc brushed samples, Rz values were notably higher than the ones of the polished surface, indicating that the brushed lines were not all equally deep. This behaviour could be confirmed by visual inspection of the profile plots of the two samples. By comparing copper and zinc samples, it can be noticed that both line roughness quantities Ra and Rz were comparable between the two substrates, with zinc samples having slightly higher values. The same similarities could be seen when comparing area roughness values. This is an indication that the hair-brushing industrial process was consistent, and the main peak-trough differences repeat similarly over the chosen area. As expected, strong anisotropy could be observed for both substrates, as indicated by the texture aspect ratio (Str) values lower than 0.3 μm (Str $<$ 0.3 μm) (Brown, 2017).

(A)

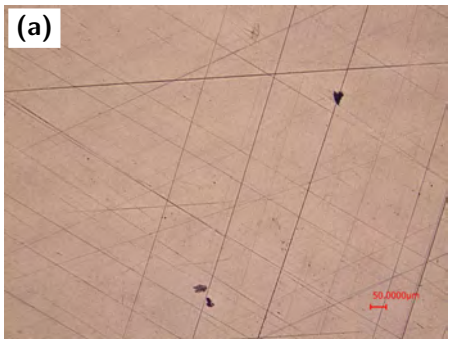

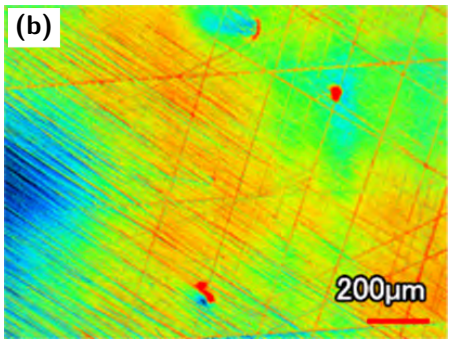

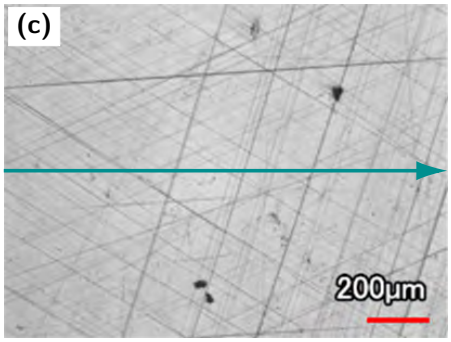

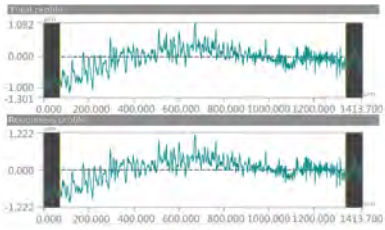

Line		Area		
Ra*	Rz*	Sa*	Sz*	Str
0.263	2.229	0.294	5.256	0.575

* Sa, Sz, Ra, Rz expressed in µm.

(B)

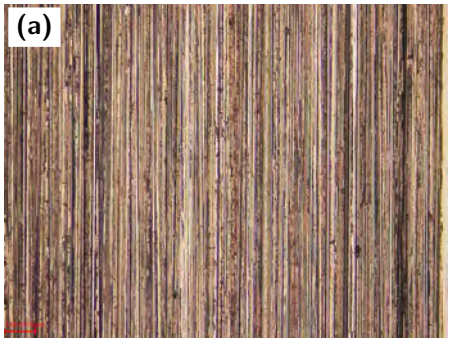

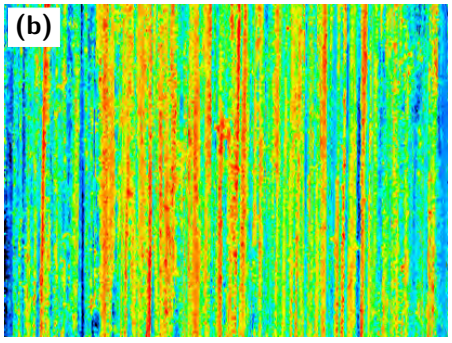

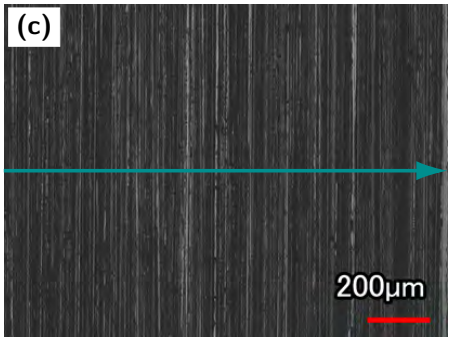

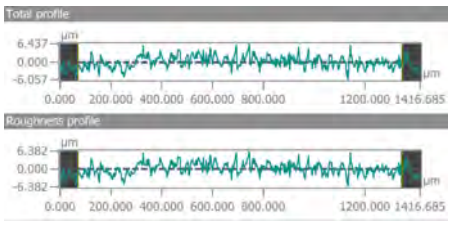

Line		Area		
Ra*	Rz*	Sa*	Sz*	Str
1.521	12.494	1.618	18.974	0.022

* Sa, Sz, Ra, Rz expressed in µm.

Figure 2.11: 3D laser scanning microscopy measurements on a selected area of (A) polished copper (Cu00_polished), (B) brushed copper (Cu35) and (C) brushed zinc (Zn31) coupons. (a), (b) and (c) correspond to optical image, surface roughness heatmap (red signifies elevated topography), and laser image with indication of line profile location (arrow), respectively. Line and area roughness parameters are shown in the table.

(C)

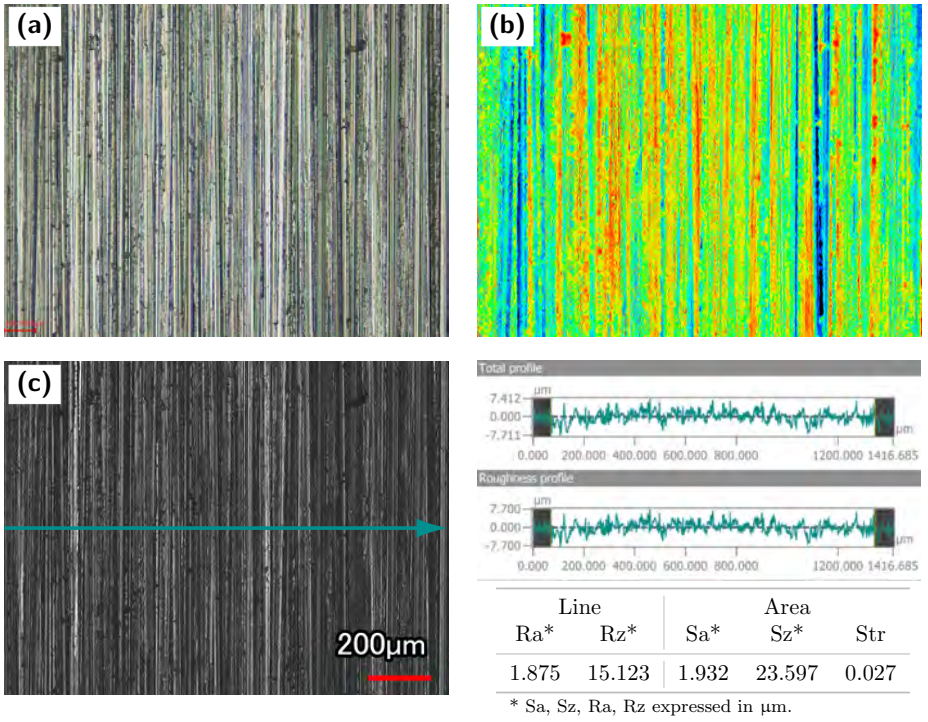

Line		Area		
Ra*	Rz*	Sa*	Sz*	Str
1.875	15.123	1.932	23.597	0.027

* Sa, Sz, Ra, Rz expressed in µm.

Figure 2.11: 3D laser scanning microscopy measurements on a selected area of (A) polished copper (Cu00_polished), (B) brushed copper (Cu35) and (C) brushed zinc (Zn31) coupons. (a), (b) and (c) correspond to optical image, surface roughness heatmap (red signifies elevated topography), and laser image with the indication of line profile location (arrow), respectively. Line and area roughness parameters are shown in the table (continued).

2.3.3 Coating application and homogeneity

The samples were coated merely with linseed oil to understand the reactivity and dynamic of the reaction in the absence of competing sources of metal ions (e.g., the mineral pigments). For the coating procedure utilising a painter's spatula, full control over the homogeneity of the coating or its thickness could not be guaranteed. In fact, linseed oil would shrink upon curing and create isolated areas with higher thickness (Figure 2.12).

Three areas of local homogeneity were visually defined on the samples, characterised by qualitatively lower, medium and higher thicknesses. It could be observed that the average values for brushed oil-coated zinc samples were generally higher than for copper ones (Table 2.5). The overall average thickness resulted in 6 μm for the copper samples and 11 μm for the zinc ones.

The variability of the collected data, represented by the standard deviation and reflecting the coating inhomogeneity, was generally lower in the case of brushed copper samples, showing that a smaller variation in the coating thickness and significant local and general homogeneity was characteristic for this metal substrate.

When the same measurements were performed on the polished copper samples, the average value and standard deviation were significantly higher (3 to 10 times). In Figure 2.13, it can be noticed how this is confirmed by a very uneven coating reaching elevated thickness values (darker areas).

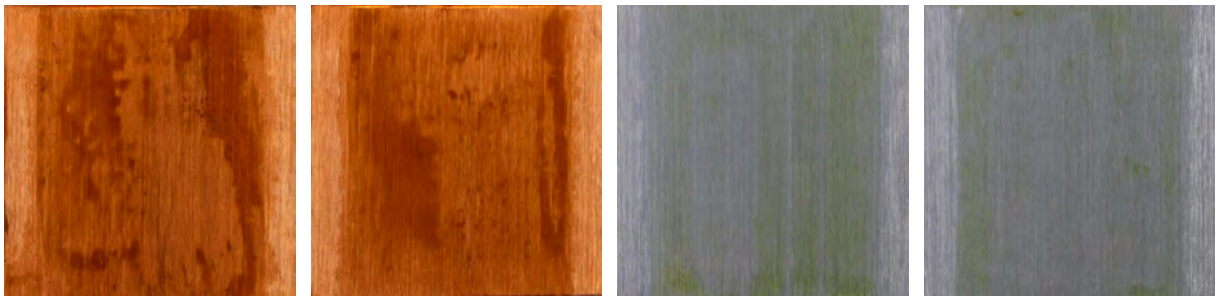

Figure 2.12: Copper (Cu07, Cu08) and zinc (Zn08, Zn09) coupons coated with linseed oil using a painter's spatula, showing areas with different coating thicknesses (darker areas correspond to thicker coatings).

Figure 2.13: mirror-polished copper coupon (Cu00_polished) coated with linseed oil.

Table 2.5: Average values and standard deviation of the oil coating thickness in thinner, medium and thicker areas on copper and zinc samples. Each value is the average over nine points within an area of homogeneous thickness.

	Thin area	Medium area	Thick area
Copper (polished)	4.0 ± 2.7 µm	32.1 ± 13.9 µm	75.8 ± 3.0 µm
Copper (brushed)	1.5 ± 0.6 µm	3.4 ± 1.1 µm	13.7 ± 2.5 µm
Zinc (brushed)	3.3 ± 1.0 µm	6.7 ± 1.3 µm	21.9 ± 8.8 µm

Brushed samples were therefore preferred in further experiments. However, because of the inhomogeneities observed, new sets of oil-coated brushed samples were prepared by pre-treating the surface using plasma to improve wettability; this procedure was then followed by industrial coating techniques such as spin and dip coating to ensure thickness control. The parameters used are listed in Table 2.1. The plasma treatment generally improved the coating homogeneity, with spin coating giving better results, especially when a gradual increase of curing temperature was used to avoid dewetting phenomena (Figure 2.14). In all attempts, the results were generally more satisfactory for copper than for zinc substrates. For both substrates, coating thickness after plasma treatment was generally higher than the one of untreated samples (average thickness was assessed to be around 15 µm, Table 2.6).

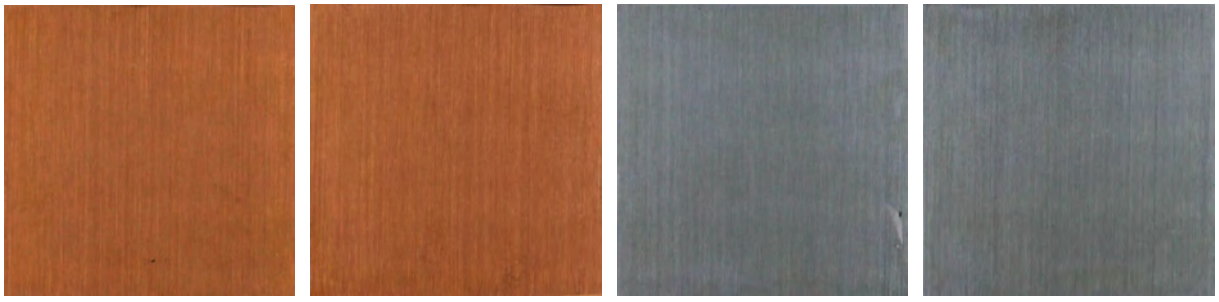

Figure 2.14: Linseed oil spin coated copper (Cu36, Cu38) and zinc (Zn32, Zn33) coupons after radiofrequency plasma pre-treatment (3.6×10^{-2} mbar during treatment).

Table 2.6: Average values and standard deviation of the oil coating thickness in thinner, medium and thicker areas on copper and zinc samples. Each value is the average over ten points within an homogeneous area of similar thickness.

	Thin area	Medium area	Thick area
Copper (brushed, plasma + spin)	5.1 ± 1.0 µm	12.3 ± 1.2 µm	26.0 ± 9.2 µm
Zinc (brushed, plasma + spin)	5.4 ± 1.2 µm	12.9 ± 2.2 µm	28.7 ± 3.3 µm

3D laser scanning microscope measurements were performed after curing of the oil coating overnight in accordance with Table 2.2 (Figure 2.15). The results highlighted differences between the two oil-coated metal substrates. In particular, the line profile indicated that the oil coating appeared more homogeneous for copper than for zinc samples (lower Ra and Rz values — see also Table 2.7 for an overview of all the samples). Additionally, for copper samples, values were comparable with the ones observed in the absence of the coating

($Ra = 1.521$ µm, Rz = 12.494 µm), suggesting that the coating followed the pattern left by the brushed finishing somehow regularly. For the zinc samples, line roughness parameter Ra was a bit more than double the value of the ones in absence of coating (Ra = 1.875 µm), indicating significantly more inhomogeneous average surface. Similarly to the uncoated samples (Figure 2.11), the area roughness values were comparable to the line profile data for mean deviations (Sa and Ra, respectively). However, they differed significantly between copper and zinc samples, indicating a higher variability in the coating for the zinc than for copper samples. That is, as observed through the comparison between thickness values (Table 2.6), zinc oil coatings were generally less homogeneous than copper ones. This is to be attributed to the higher oleophobicity of zinc substrates compared to copper ones (higher contact angle) (Barthwal and Lim, 2015; Khedir, 2016). These observations were consistent between different areas of the samples considered. Stronger anisotropicity could also be observed on coated zinc samples compared to the respective uncoated samples and to copper ones (smaller Str value), probably indicating a preferred shrinking direction of the oil upon curing, which followed the brushed vertical lines pattern (Figure 2.15B(b)).

Table 2.7: Roughness parameters for hair-brushed and mirror-polished copper and zinc samples.

		Ra*	**Rz***	**Sa***	**Sz***	**Str**
Polished	before coating	0.263	2.229	0.294	5.256	0.575
Brushed Cu	before coating	1.521	12.494	1.618	18.974	0.022
	after coating	1.756	16.052	1.710	21.575	0.033
Brushed Zn	before coating	1.875	15.123	1.932	23.597	0.027
	after coating	4.074	21.755	4.077	29.535	0.019

*Ra, Rz, Sa, Sz expressed in µm.

(A)

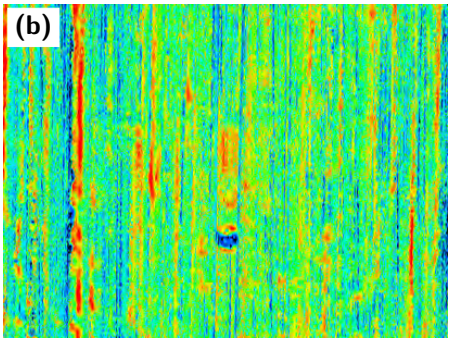

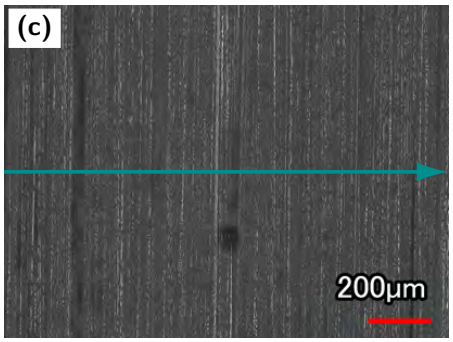

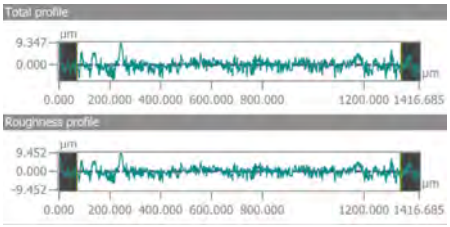

Line		Area		
Ra*	Rz*	Sa*	Sz*	Str
1.756	16.052	1.710	21.575	0.033

* Sa, Sz, Ra, Rz expressed in µm.

(B)

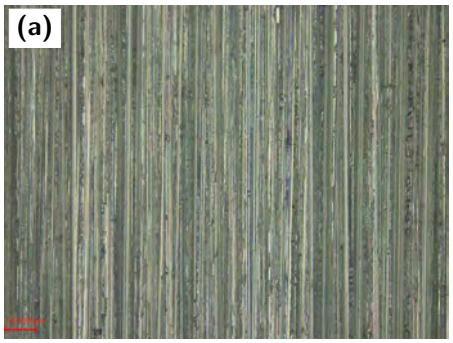

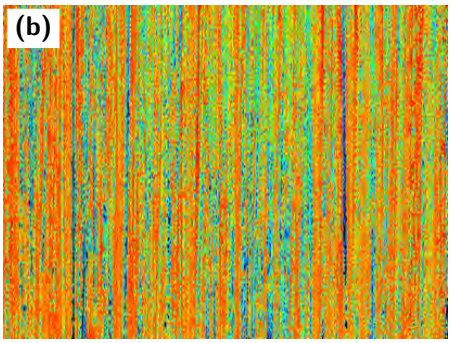

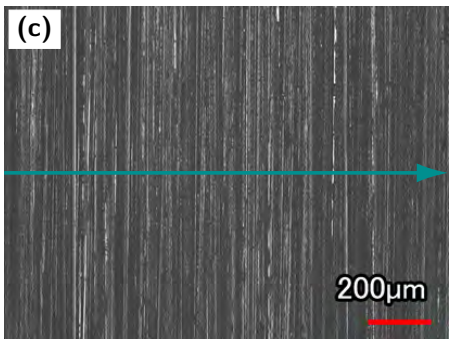

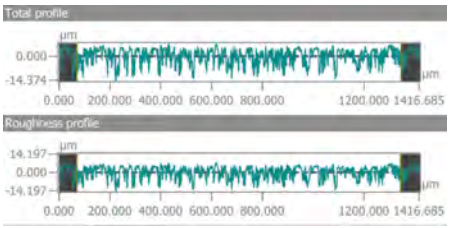

Line		Area		
Ra*	Rz*	Sa*	Sz*	Str
4.074	21.755	4.077	29.535	0.019

* Sa, Sz, Ra, Rz expressed in µm.

Figure 2.15: 3D laser scanning microscopy measurements on a selected area of (A) brushed copper (Cu35) and (B) brushed zinc (Zn31) coupons after plasma treatment and spin coating. (a), (b) and (c) correspond to optical image, surface roughness heatmap (red signifies elevated topography), and laser image with the indication of line profile location (arrow), respectively. Line and area roughness parameters are shown in the table.

2.3.4 Preparation of cross-sections for stratigraphy studies

The two protocols tested (i.e., the one where the metal samples were first coated, cured and then cut and embedded in resin, and the one where the oil was added to the metal already embedded) showed several limitations. In particular, the samples cut using the metal cutter were characterised by wavy surfaces due to the movement of the blade along the section of the sample.

After embedding in epoxy resin, polishing of these samples was not possible due to the residual softness and stickiness of the oil coating, that would cause contamination of the sample with particulate from the abrasive material. When no polishing was performed, the surface of the samples would result in an irregular surface, unsuitable for precise analyses of the metal-oil interface (Figure 2.16).

SEM analyses were affected by the differences in electron conductivity of the two components: the metal, a good electron conductor, and the oil, an insulator and heat dissipation agent (Rouabeh et al., 2019). For this reason, the oil coating would charge upon irradiation with X-rays and heat to a viscous material (Figure 2.16).

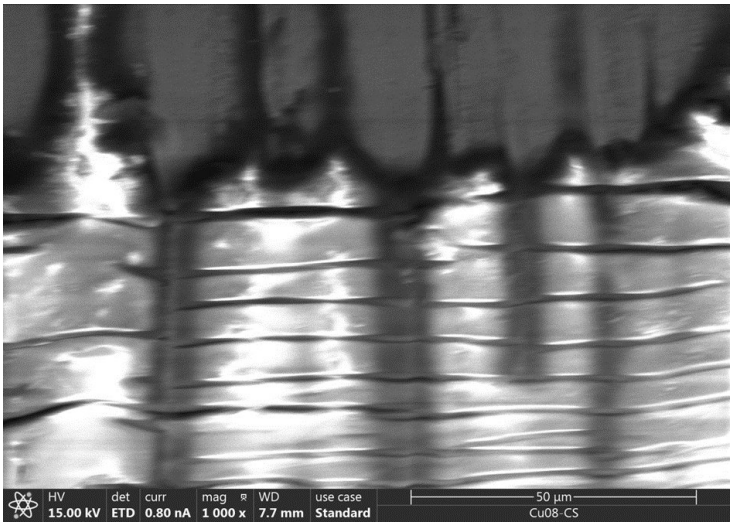

Figure 2.16: SEM image of the interface between linseed oil (brighter) and copper substrate (darker) (Cu08).

The preparation of the samples using the second methodology never reached optimisation; therefore, SEM analyses were not performed on them. In particular, although this sample preparation methodology would allow direct monitoring of the metal-oil interface from the curing of the oil until the consequent formation of metal soaps, the oil would tend to shrink upon drying, leaving voids in the dedicated pit. At this stage, it was therefore not possible to obtain a dry smooth section to be observed and analysed through SEM. One option could be to use an iterative approach, where the linseed oil is added and let dry (hence shrink) in cycles until it reaches the surface. Further tests are necessary to develop a proper methodology.

2.3.5 Establishment of the ageing protocol

The three ageing protocols a), b), c) presented in Section 2.2.5, differed primarily in that they employed different methods for producing and maintaining constant and elevated relative humidity values (80%). The observations made during the three experiments (a, b, c) are discussed below:

a) By visual inspection, it was observed that the samples were ageing over the time considered (20 days, Figure 2.17a–f). Already after the first day of ageing (Figure 2.17d), the copper samples were showing signs of green corrosion, probably due to the presence of chloride ions from the NaCl water solution. At the beginning of the ageing time, this was mostly localised at the uncoated edges of the coupon. In the location where the drop of palmitic acid solution was deposited (Figure 2.17d, region A), a smaller light feature appeared after two days which edges progressively darkened to brown (Figure 2.17e, region B). Both degradation of the metal due to the presence of chlorides, and the one exerted by addition of palmitic acid, increased during the ageing time (Figure 2.17).

For the zinc samples, dark corrosion features localised at the raw edges of the metal coupon were observed later than copper (day six), and they progressively darkened (Figure 2.18e-f). In the coated area of the coupon, no evidence of chemical changes could be visually assessed.

FTIR maps were collected at the end of the ageing period, confirming the presence of metal soaps on the samples for both substrates (Figures 2.19, 2.20). In particular, it can be noticed that copper palmitate (1587 cm^{-1}) was mostly concentrated in corrosion feature B.

b) As expected, in the absence of chloride ions in the system, the samples did not show the same corrosion features as the previous ones and could be monitored regularly using μ-FTIR spectroscopy. The formation of metal soaps was observed at different rates for copper and zinc. The results of such monitoring are described in depth in Chapter 4. A problem encountered when utilising this procedure was given by the inability of the boxes to contain water vapour. For this reason, water drops were often found on the oven door, and several outliers were observed in the temperature and relative humidity values that needed to be monitored closely and restored often by adding the missing component to the solution for the duration of the experiment.

c) This proved to be the most effective method in terms of avoiding contamination of the samples while accelerating the reaction that forms metal soaps, but it was the least stable protocol in terms of relative humidity fluctuations. Additionally, the pre-conditioned silica gel was not granting consistent relative humidity values for temperatures above 50 °C, which were decaying rapidly within a week. Silica beads needed to be replaced during the experiment to maintain stable 80% relative humidity values. Nevertheless, it was deemed to be a useful protocol for further experiments.

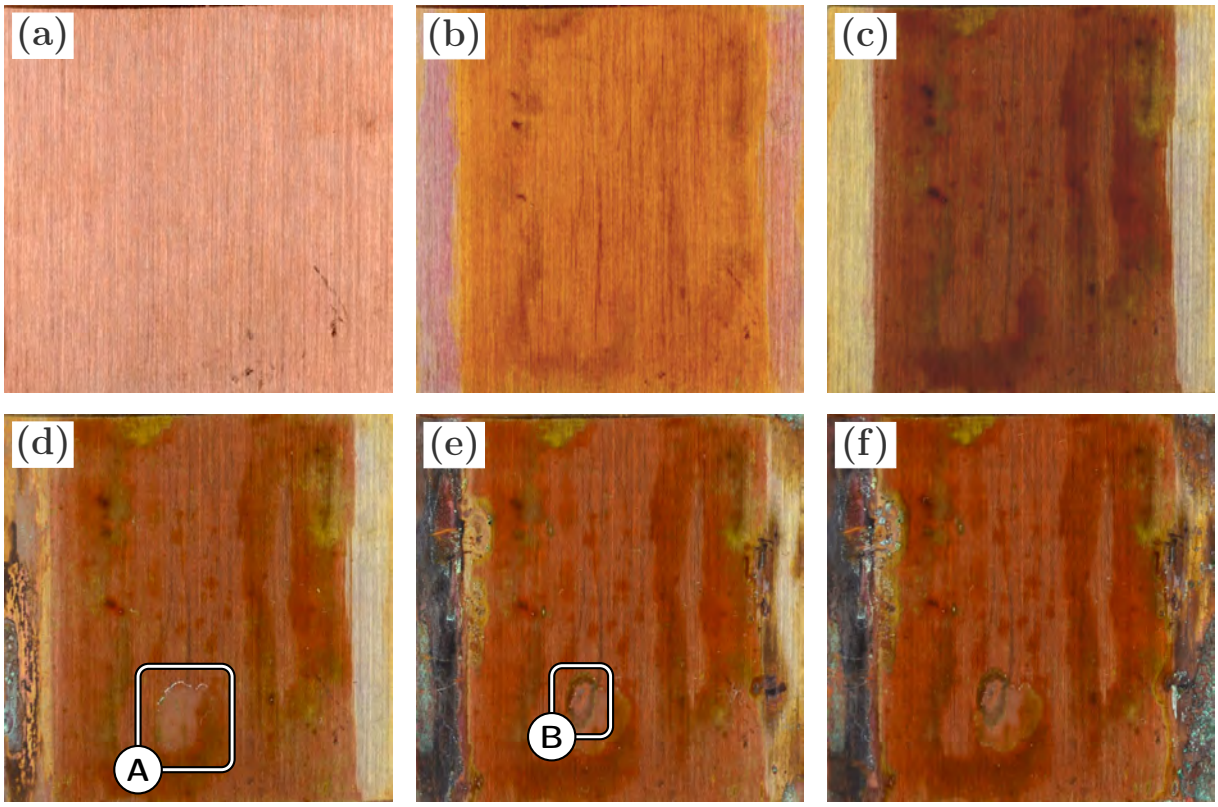

Figure 2.17: Evolution of a copper coupon (Cu03) exposed to 80% RH at room temperature (sodium chloride saturated water solution), from (a) bare metal, to (b) linseed oil coated sample, (c) cured coating (80 °C overnight), (d, e, f) 1, 10, 20 days of artificial ageing. Region A identifies the area where a concentrated solution of palmitic acid (7.8×10^{-2} M) was added to exert the formation of metal soaps, and region B highlights visible corrosion features.

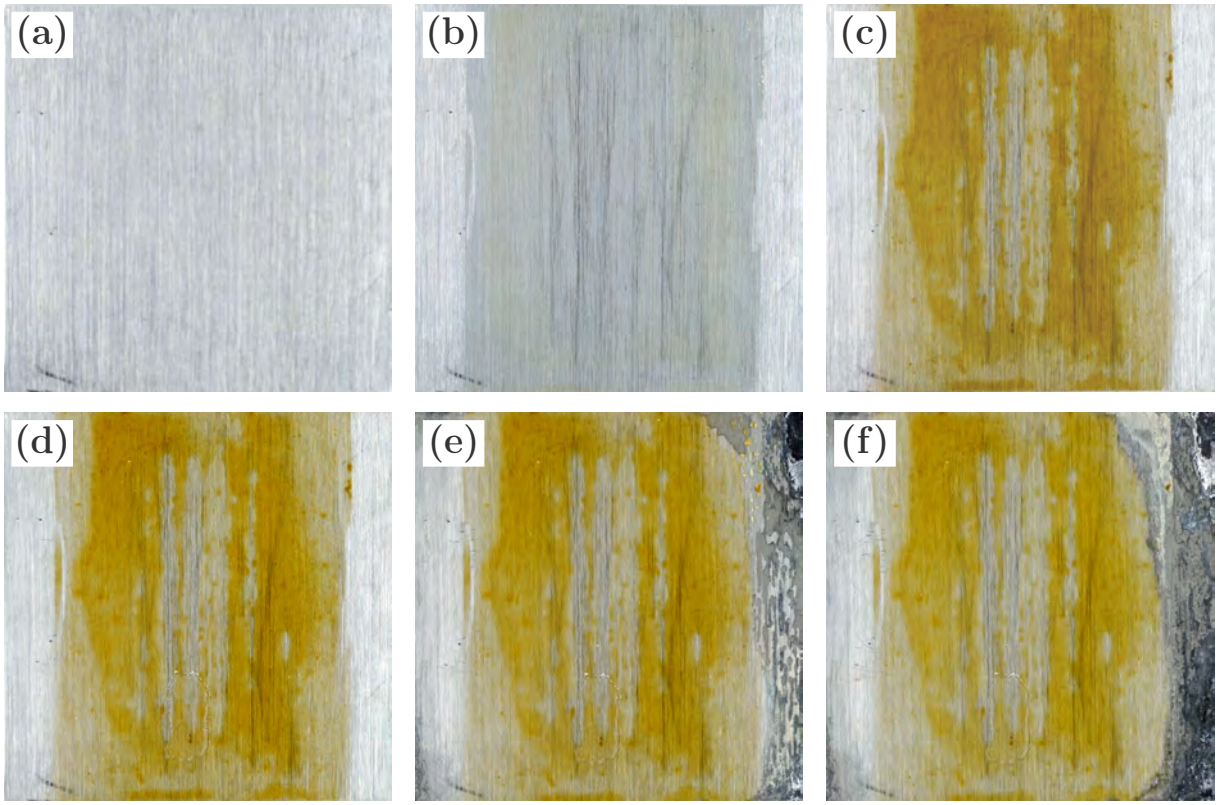

Figure 2.18: Evolution of a zinc coupon (Zn03) exposed to 80% RH at room temperature (sodium chloride saturated water solution), from (a) bare metal, to (b) linseed oil coated sample, (c) cured sample (80 °C overnight), (d, e, f) 1, 10, 20 days of artificial ageing. Dark corrosion features are visible at the edges in Figures (e) and (f).

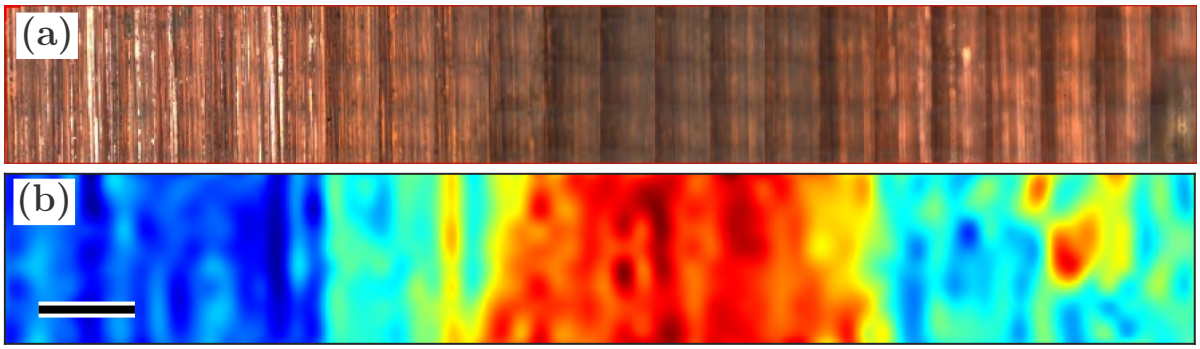

Figure 2.19: 2D μ-FTIR chemical image ($\nu_a COO^-$ at 1589 cm^{-1}) of the area around the corrosion feature of the copper sample (Cu03) after the ageing period of one month. Red pixels correspond to a higher signal for copper palmitate. The scale bar indicates 1000 μm.

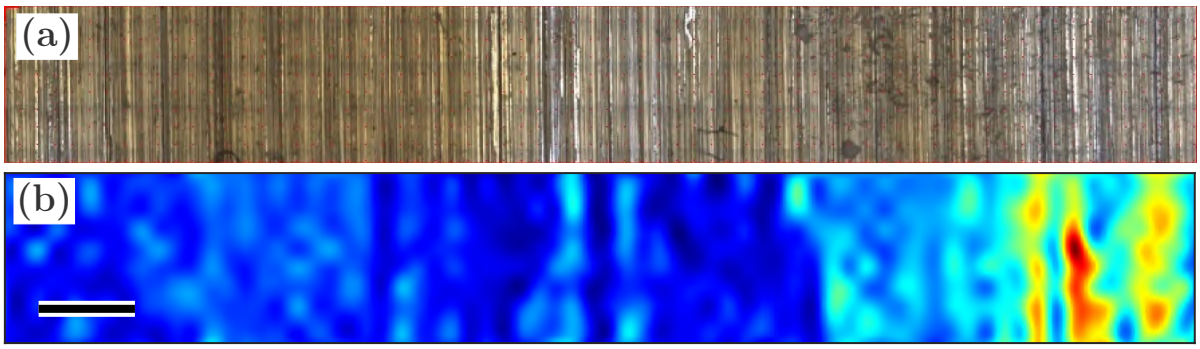

Figure 2.20: 2D μ-FTIR chemical image ($\nu_a COO^-$ at 1540 cm^{-1}) of the area where palmitic acid was added on the zinc sample (Zn03). The map was acquired after the ageing period of one month. Red pixels correspond to a higher signal for zinc palmitate. The scale bar indicates 1000 μm.

Design of experiment In the absence of a climatic chamber and in order to find the best compromise between laboratory possibilities and effective ageing of the samples, a full factorial design of experiment (DoE) was performed. By observing the original FTIR spectra using a simple colour classification based on the different systems (LO in black and LOZnO in red, Figure 2.21), one can notice how the painted samples – in which the pigment ZnO is present – are characterised by having a higher signal intensity than the ones coated with linseed oil alone. This is probably due to the fact that, for these samples, it was more difficult to obtain thin paint layers, hence their FTIR signal tended to saturate.

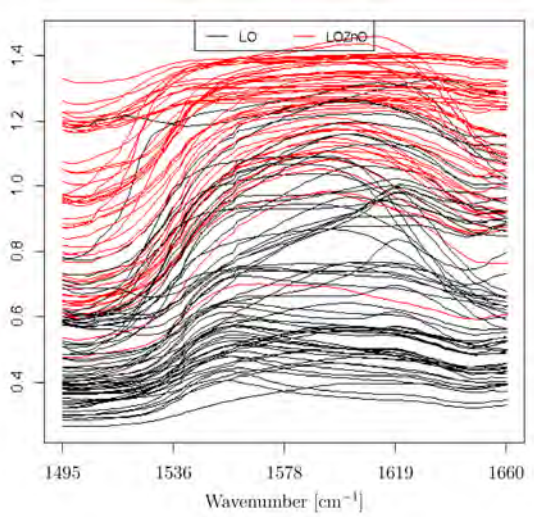

Figure 2.21: Original FTIR spectra before SNV transformation. Red lines correspond to LOZnO, whereas black lines to LO.

After SNV transformation, It was possible to identify six different regions for the linseed oil samples (Figure 2.22a):

a) a flat area ($1495 - 1522$ cm^{-1})
b) a slope towards the first peak ($1524 - 1537$ cm^{-1})
c) the first peak area ($1539 - 1578$ cm^{-1})
d) the area between two peaks ($1579 - 1612$ cm^{-1})
e) the second peak ($1614 - 1647$ cm^{-1})
f) non-structured signal ($1649 - 1660$ cm^{-1})

Areas c), d) and e) were particularly interesting for this study, since those ranges include values referring to the $\nu_a COO^-$ asymmetric copper and zinc carboxylate vibration (1587 and 1540 cm^{-1}, respectively), and more amorphous geometries ($1544 - 1630$ cm^{-1}) (Hermans et al., 2021). Differences according to the thickness of the coating or of the paint are highlighted in Figure 2.22b (thick coatings in black and thin ones in red). Two opposite trends were observed for the LO samples and the LOZnO samples, where LO samples tended to fall under the classification "thin", whereas LOZnO samples were generally thicker ("thick") in nature. For LOZnO painted samples, this seemed to confirm the hypothesis for which sample thickness would be one of the reasons for the high reflectance values encountered. A peculiar feature of the LO spectra was the prevalence of the first peak (centred at about 1560 cm^{-1}) in thinner samples, whereas the second peak (centred at

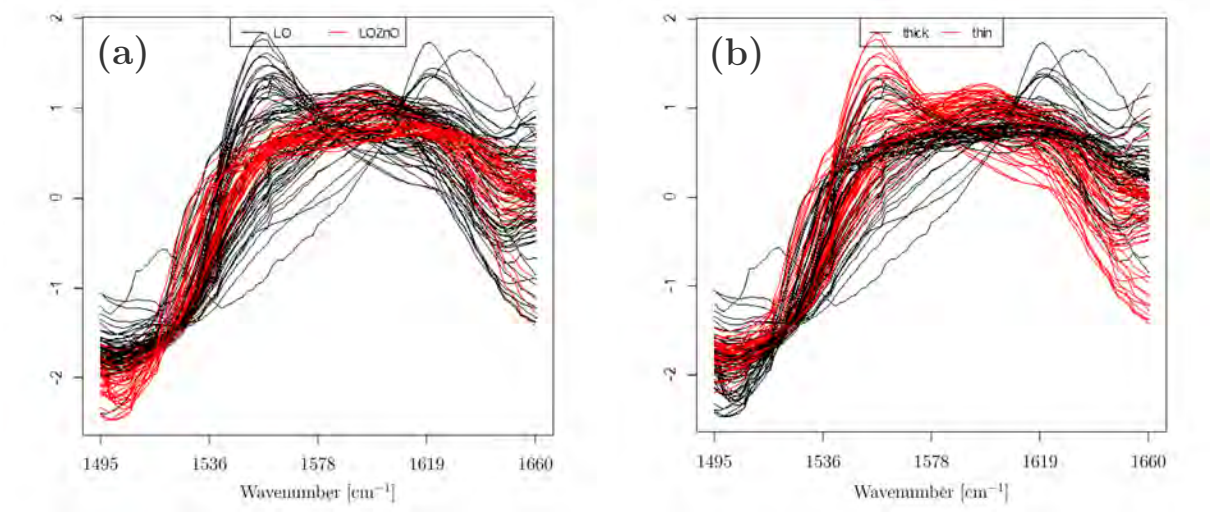

Figure 2.22: FTIR spectra in the region of interest ($1495 - 1660$ cm^{-1}), where red and black lines represent (a) linseed oil (LO) and linseed oil + zinc oxide (LOZnO) formulations, and (b) samples coated and painted using different thickness. Here, the black line signifies thick coatings, whereas the red line represents thinner oil coating applied.

about 1624 cm^{-1}) was primarily present in thicker ones.

After identification of the four significant principal components (Figure 2.8), explaining 96.6% of the total variance, the loadings line plots helped understand and interpret the system under study. By overlapping the previously identified significant regions on this new graph (colour-coded shaded areas, Figure 2.23), it was possible to notice how each factor provided information on one or more particular regions:

a) Factor 1 (black) explained regions C and E, i.e., the contrast between the first and the second peak. Hence, a sample with positive scores would be characterised by a more prevalent first peak over the second one;
b) Factor 2 (red) explained region D, i.e., the area between the two peaks, hence a sample with positive scores would be characterised by a lower signal in that area;
c) Factor 3 (green) explained principally region B, i.e., the area characterised by increasing signal (slope), hence a sample with positive scores would be characterised by a lower signal intensity in this region;
d) Factor 4 (blue) explained region A, meaning that a sample with positive scores would be characterised by higher values in this region.

It is worth remembering at this point that areas C, D and E were those of interest for this study since they overlap with the peaks in the range $1539 - 1578$ cm^{-1}, $1579 - 1612$ cm^{-1} and the ones at $1614 - 1647$ cm^{-1}, respectively, that are indicative of the presence of different geometries of copper and zinc metal soaps (Hermans et al., 2019; Hermans et al., 2021). For this reason, the discussion will focus on Factors 1 and 2.

Let us first examine Factor 1 (regions C and E) and calculate the model (equation (1)) to comprehend the effect of the variables alone and in combination (standard deviation of

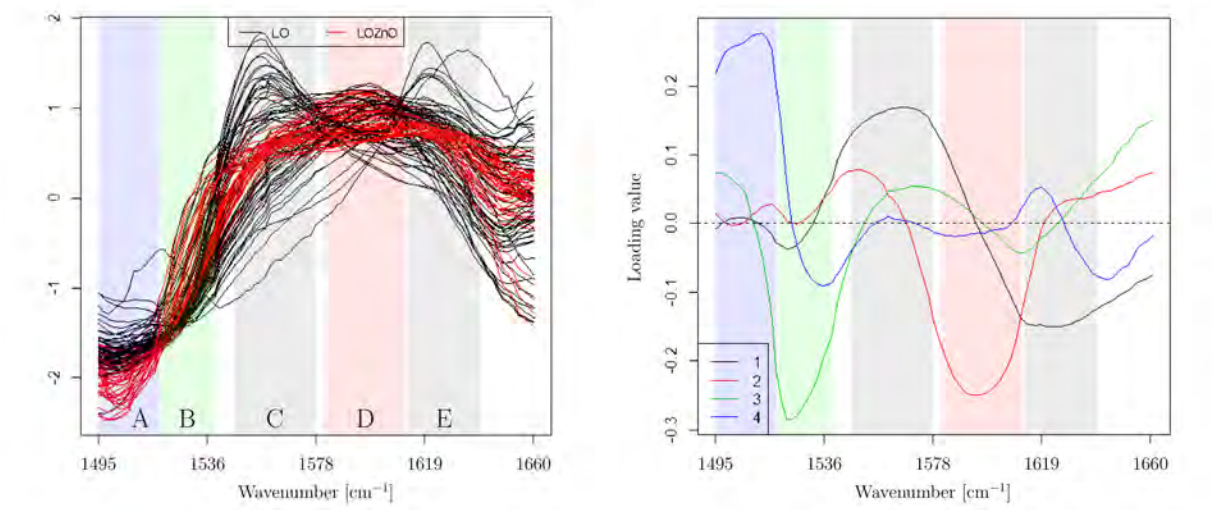

Figure 2.23: Comparison between FTIR spectra after SNV transformation and loadings plots according to the five regions identified (shaded areas, A–E). The colour code represents the factors that explain the signal in a specific area.

the residuals 4.6, explained variance 46.3%):

$$\begin{aligned} Y = {} & 0.8 + 0.2X_{1A} - 3.8X_{1B}(***) - 0.6X_2 - 0.9X_3 - 2.7X_4(***) - 0.2X_5 \\ & + 2.2X_2X_3(***) + 1.7X_2X_4(***) - 1.2X_2X_5(*) + 0.9X_3X_4(*) \\ & + 1.7X_3X_5(**) - 0.2X_4X_5 + 0.1X_5^2. \end{aligned} \tag{1}$$

All variables had an effect on Factor 1 (Figure 2.24). The variables *environmental conditions* and *thickness* had a highly significant linear term, whereas the variables *system*, *substrate* and *time* were involved in relevant interactions (cross-terms).

For what concerns the *environmental conditions* (hi.hi or ro.it), it could be concluded that at room temperature and 80% relative humidity (ro.hi), there was an intensity increase of the second peak ($1614 - 1647$ cm^{-1}) at the expense of the first peak ($1539 - 1578$ cm^{-1}). From a chemical point of view, this can be explained by the effect of relative humidity on the system. Recent studies have already shown the dependence of the formation of amorphous zinc soaps on the relative humidity levels and water content (Hermans et al., 2019), whereas the temperature seems more related to their crystallisation (Hermans et al., 2021). Being able to balance these two parameters (RH and temperature), therefore, becomes of paramount importance. By observing these results, we could see how a combination of high temperature and relative humidity (hi.hi) was inconclusive for the question of the optimisation of the ageing protocol towards the formation of metal soaps (low significance and low positive coefficient). The model also showed that increasing the relative humidity alone had the highest impact, but fewer crystalline species that could, in some cases, be precursors of the species of interest would be produced. This might imply that either cycles of high and low relative humidity and temperature values should be utilised, or compromise values should be identified with the aid of new experimental designs in a new sub-range, reflecting different levels within the experimental design.

As for the other highly significant linear term, i.e., the *thickness* (Thick) of the coating or of the paint, the results showed that thicker layers were associated with a decreased signal

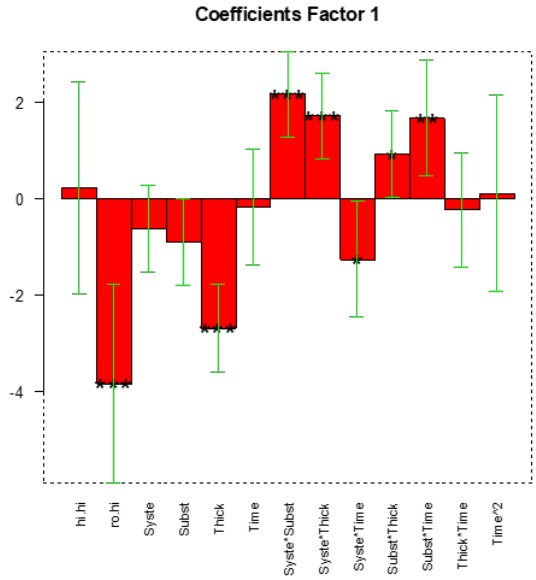

Figure 2.24: Histogram representing the weight of each variable considered alone or in combination (cross-terms) according to the mathematical model presented in Equation **(1)**.

of the metal soaps (negative influence of the variable on PC1 signifies an increase of the second peak ((1614 − 1647 cm^{-1}), region D) at the expense of the first one ((1539 − 1578 cm^{-1}), region C)). This could be due to the lack of such species in thicker coatings or, more probably, to the inability of the analytical technique to detect species located above the limit of penetration of the source radiation (here, the infrared beam)[1]. The implications of this observation will be discussed in detail in Chapter 4. *Thickness* was also involved in relevant cross-terms (e.g., *system-thickness*). This interaction showed that the linseed oil positively impacted the signal of zinc soaps for thin coatings. Once again, this could be a problem of detectability of the species of interest. For this reason, new design of experiments are advised that consider the effect of the variable for each system separately.

Other relevant interactions were *system-substrate* and *substrate-time*. These interactions were more concerned with the reactivity of the substrate rather than the ageing protocol; hence they will not be discussed here. The cross-terms representing the *system-time* and the *substrate-thickness* interactions were at the limit of statistical significance and characterised by a low coefficient (−1.2 and 0.9, respectively), hence less relevant for Factor 1. The only non-significant interaction was *thickness-time*, which is only logical considering that thickness was a fixed parameter of the samples, that was not modified over time during the experiment.

Similar considerations could be drawn about Factor 2, which explained the signal between the two peaks (region D), i.e., the region between 1579 and 1612 cm^{-1}, where copper soaps can be found ($\nu_a COO^-$=1587 cm^{-1}). The computed model indicated the weight of the different variables and their interaction (standard deviation of the residuals 4.6, explained

[1] For the infrared beam, the limit of penetration depends strongly on the refractive index of the material; for oil paintings, this was experimentally estimated to be about 15µ)

variance 46.3%), as represented in Figure 2.25:

$$\begin{aligned} Y = &-1.1 + 0.8X_{1A} - 2.0X_{1B}(***) + 0.0X_2 - 2.0X_3(***) - 2.0X_4(***) - 0.3X_5 \\ &+ 1.2X_2X_3(***) + 1.3X_2X_4(***) + 1.3X_2X_5(***) + 0.4X_3X_4(*) \\ &+ 0.1X_3X_5 + 0.2X_4X_5 + 0.7X_5^2. \end{aligned} \quad \textbf{(2)}$$

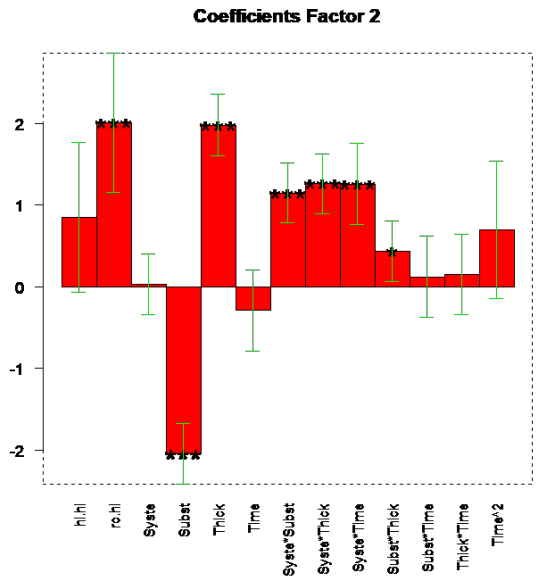

Figure 2.25: Histogram representing the weight of each variable considered alone or in combination (cross-terms) according to the mathematical model presented in Equation **(2)**.

Similarly to Factor 1, the *environmental conditions*, with room temperature and 80% relative humidity (ro.hi) being more relevant, had a positive effect on this factor, hence a negative effect on the intensity of the peak in area D. This means that these conditions were again unsuitable for producing metal soaps. *Thickness* was another important variable to consider in the designing of the model samples to be artificially aged for the study of metal soaps formation since the FTIR signal of metal soaps showed a dependency on it: the highest the thickness, the least the possibility to observe metal (copper) soaps in the samples analysed. According to Factor 2, the *substrate* had a high impact on the formation of metal soaps. In this case, this confirmed that this area of the signal was specific for the identification of copper soaps. The variable *system* did not have a significant linear term, but it was involved in relevant interactions: *system-substrate*, *system-thickness* and *system-time*. For this last interaction, the contour plot helped us understand the effect of these interactions on the formation of copper soaps with time (Figure 2.26).

This in fact showed how with thin layers of coating or ZnO-based paint, the variable *time* had an effect only for the linseed oil (LO) system – reduced answer, hence augmented signal in area D –, whereas for LOZnO no difference could be noticed. This indicated that copper soap formation was higher with time in the absence of zinc-based pigments. This could be due to the fact that paint layers affect the detectability of the copper carboxylates, but it could also hint toward the possibility of competition between substrate and pigment in reacting with the fatty acids from the oil binder. More targeted experiments are necessary

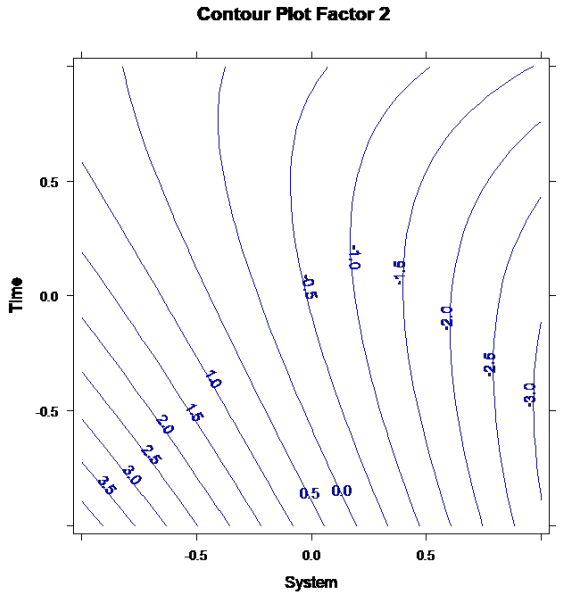

Figure 2.26: Contour plot showing the entity of the system-time interaction for copper (level −1), thin layers applied (level −1) and indoors natural environmental conditions (NC).

to clarify this behaviour, where the two substrates should be made react in the presence and absence of zinc and copper pigments within the oil formulation.

2.4 Conclusions

The rationale behind the methodological approach chosen for the preparation of representative and reproducible model samples for the study of the formation of metal soaps on painted metal supports was presented in this chapter. The aspects concerning the choice of the metal substrate, surface finishing and pre-treatment, coating homogeneity and thickness, and ageing protocols were discussed.

After a selection based on historical sources, the choice of the metal supports was made considering their ability to produce metal soaps when in contact with a concentrated ethanol solution of palmitic acid, one of the reactive components in oil formulations for the formation of metal soaps. By doing so, copper and zinc samples were selected for further studies since iron and aluminium samples did not produce metal soaps even after exposure overnight to the palmitic acid solution.

For the surface finishing, an evaluation between mirror-polished and brushed surfaces was made considering surface properties. Roughened surface confirmed the ability to grip the paint better, as indicated by historical sources, and to provide thinner oil coatings even when using a painter's spatula for the linseed oil application. However, when using the spatula, the homogeneity of the coating was insufficient for the desired monitoring applications using analytical techniques such as FTIR – also considering the limit of penetration of infrared radiation in a semi-transparent sample. For this reason, plasma treatment was attempted, followed by dip and spin coating methods. The spin coating method showed more coherent results, with the average thickness being around 15 µm. The wettability of zinc samples was such that they presented generally thicker coatings characterised by inhomogeneities when compared to the copper samples. This was shown by average values of thickness gauge measurements and confirmed by 3D laser scanning microscopy observations.

Preparation of the samples as cross-sections to study the interface metal-oil proved non-trivial. Cutting the sample together with the cured oil coating brought to uneven surfaces that were not easy to investigate via SEM. Additionally, the differences in electric conductivity of the two materials made it such that the interface was not easily accessible for investigation.

A multivariate approach based on a full factorial design of experiment was utilised to optimise the artificial ageing parameters for producing metal soaps on the model samples. The observation of the FTIR collected spectra, together with the analysis of the mathematical model and the impact of each variable alone and in combination, suggested that neither high levels of temperature and humidity (80°C and 80% RH) nor a combination of room temperature and high relative humidity would be sufficient to give crystalline copper and zinc metal soaps in the time-frame considered (28 days). A solution could be to utilise ageing cycles where temperature and humidity are varied drastically between extreme low and high values for a certain period of time, or to find compromise values of temperature and relative humidity. For the study of the formation of metal soaps on coated model samples using different analytical techniques (Chapter 3 and 4), the series produced using the different preparation and ageing methods described and discussed here were used, keeping into consideration their final characteristics (e.g., homogeneity and thickness of the coating).

Bibliography

Anderson, V. L. and McLean, R. A. (1974). *Design of Experiments: A Realistic Approach*. 1st ed. CRC Press. DOI: 10.1201/9781315141039.

Appelbaum, B. (2010). Conservation treatment methodology. *Journal of the American Institute for Conservation* **49**(1): 53–55. DOI: 10.2307/41320433.

Baij, L., Hermans, J. J., Keune, K., and Iedema, P. (2018). Time-Dependent ATR-FTIR Spectroscopic Studies on Fatty Acid Diffusion and the Formation of Metal Soaps in Oil Paint Model Systems. *Angewandte Chemie International Edition* **57**(25): 7351–7354. DOI: 10.1002/anie.201712751.

Barthwal, S. and Lim, S.-H. (2015). Fabrication of long-term stable superoleophobic surface based on copper oxide/cobalt oxide with micro-nanoscale hierarchical roughness. *Applied Surface Science* **328**: 296–305. DOI: 10.1016/j.apsusc.2014.11.182.

Bayrak, A., Kiralan, M., Ipek, A., Arslan, N., Cosge, B., and Khawar, K. (2010). Fatty Acid Compositions of Linseed (*Linum Usitatissimum* L.) Genotypes of Different Origin Cultivated in Turkey. *Biotechnology & Biotechnological Equipment* **24**(2): 1836–1842. DOI: 10.2478/V10133-010-0034-2.

Belkind, A. and Gershman, S. (2008). Plasma cleaning of surfaces. *Vacuum Technology and Coating*.

Bornside, D. E., Macosko, C. W., and Scriven, L. E. (1989). Spin coating: One-dimensional model. *Journal of Applied Physics* **66**(11): 5185–5193. DOI: 10.1063/1.343754.

Brereton, R. G. (2018). Principal Component Analysis and Unsupervised Pattern Recognition. In: *Chemometrics*. Chichester, UK: John Wiley & Sons Ltd: 163–214. DOI: 10.1002/9781118904695.ch4.

Brinker, C. J. (2013). Dip Coating. In: *Chemical Solution Deposition of Functional Oxide Thin Films*. Ed. by T. Schneller, R. Waser, M. Kosec, and D. Payne. Vienna: Springer Vienna: 233–261. DOI: 10.1007/978-3-211-99311-8_10.

Brown, A. (2017). *Introduction to Surface Roughness Measurement*. Olympus.

Burnstock, A., Keijzer, M. de, Tagle, A. de, Heydenreich, G., Krueger, J., Learner, T., and Berg, K. J. van den, eds. (2014). *Issues in Contemporary Oil Paint*. 1st ed. Cham: Springer International Publishing : Imprint: Springer. ISBN: 978-3-319-10100-2.

Casadio, F., Keune, K., Noble, P., Van Loon, A., Hendriks, E., Centeno, S. A., and Osmond, G., eds. (2019). *Metal Soaps in Art: Conservation and Research*. Cultural Heritage Science. Cham: Springer International Publishing. ISBN: 978-3-319-90617-1.

Cheng, C.-s. (2019). *Theory of factorial design: single- and multi-stratum experiments*. ISBN: 978-0-367-37898-1.

Czitrom, V. (1999). One-Factor-at-a-Time versus Designed Experiments. *The American Statistician* **53**(2): 126. DOI: 10.2307/2685731.

De Piles, R. and Jombert, C. (1766). *Les Premiers Eléments de la Peinture Pratique*. Amsterdam.

Feller, R. L., Roy, A., FitzHugh, E. W., and Berrie, B. H., eds. (1986). *Artists' pigments: a handbook of their history and characteristics*. Vol. 1. 3 vols. Washington: National Gallery of Art. ISBN: 978-0-89468-086-1.

Forney, C. F. and Brandl, D. G. (1992). Control of Humidity in Small Controlled-environment Chambers using Glycerol-Water Solutions. *HortTechnology* **2**(1): 52–54. DOI: 10.21273/HORTTECH.2.1.52.

Gans, A., Dressaire, E., Colnet, B., Saingier, G., Bazant, M. Z., and Sauret, A. (2019). Dip-coating of suspensions. *Soft Matter* **15**(2): 252–261. DOI: 10.1039/C8SM01785A.

Garrappa, S., Kočí, E., Švarcová, S., Bezdička, P., and Hradil, D. (2020). Initial stages of metal soaps‘ formation in model paints: The role of humidity. *Microchemical Journal* **156**: 104842. DOI: 10.1016/j.microc.2020.104842.

Greenspan, L. (1977). Humidity fixed points of binary saturated aqueous solutions. *Journal of Research of the National Bureau of Standards Section A: Physics and Chemistry* **81A**(1): 89. DOI: 10.6028/jres.081A.011.

Hermans, J., Osmond, G., Loon, A. van, Iedema, P., Chapman, R., Drennan, J., Jack, K., et al. (2018). Electron Microscopy Imaging of Zinc Soaps Nucleation in Oil Paint. *Microscopy and Microanalysis* **24**(3): 318–322. DOI: 10.1017/S1431927618000387.

Hermans, J., Zuidgeest, L., Iedema, P., Woutersen, S., and Keune, K. (2021). The kinetics of metal soap crystallization in oil polymers. *Physical Chemistry Chemical Physics* **23**(39): 22589–22600. DOI: 10.1039/D1CP03479K.

Hermans, J. J., Keune, K., Loon, A. v., and Iedema, P. D. (2016). The crystallization of metal soaps and fatty acids in oil paint model systems. *Physical Chemistry Chemical Physics* **18**(16): 10896–10905. DOI: 10.1039/C6CP00487C.

Hermans, J. J., Baij, L., Koenis, M., Keune, K., Iedema, P. D., and Woutersen, S. (2019). 2D-IR spectroscopy for oil paint conservation: Elucidating the water-sensitive structure of zinc carboxylate clusters in ionomers. *Science Advances* **5**(6): DOI: 10.1126/sciadv.aaw3592.

Israelachvili, J. N. (2011). *Intermolecular and Surface Forces: Revised Third Edition.* Burlington: Elsevier Science. ISBN: 978-0-12-391933-5.

Izzo, F. C., Kratter, M., Nevin, A., and Zendri, E. (2021). A Critical Review on the Analysis of Metal Soaps in Oil Paintings. *ChemistryOpen* **10**(9): 904–921. DOI: 10.1002/open.202100166.

Kaiser, H. F. (1958). The varimax criterion for analytic rotation in factor analysis. *Psychometrika* **23**(3): 187–200. DOI: 10.1007/BF02289233.

Kaszowska, Z., Malek, K., Pańczyk, M., and Mikołajska, A. (2013). A joint application of ATR-FTIR and SEM imaging with high spatial resolution: Identification and distribution of painting materials and their degradation products in paint cross sections. *Vibrational Spectroscopy* **65**: 1–11. DOI: 10.1016/j.vibspec.2012.11.018.

Keune, K. and Boon, J. J. (2007). Analytical Imaging Studies of Cross-Sections of Paintings Affected by Lead Soap Aggregate Formation. *Studies in Conservation* **52**(3): 161–176. DOI: 10.1179/sic.2007.52.3.161.

Khedir, K. R. (2016). Superhydrophobic and Highly Oleophobic Zinc Sheet Surfaces Developed by a Simple Technique. *Journal of Materials Science and Engineering B* **6**(4): DOI: 10.17265/2161-6221/2016.7-8.003.

Lin, T., Antonelli, J., Yang, D., Yasuda, H., and Wang, F. (1997). Plasma treatment of automotive steel for corrosion protection – a dry energetic process for coatings. *Progress in Organic Coatings* **31**(4): 351–361. DOI: 10.1016/S0300-9440(97)00094-5.

Montgomery, D. C. (2019). *Design and analysis of experiments*. 10th ed. Hoboken, NJ: Wiley. ISBN: 978-1-119-49247-4.

O'Brien, F. E. M. (1948). The Control of Humidity by Saturated Salt Solutions. *Journal of Scientific Instruments* **25**(3): 73–76. DOI: 10.1088/0950-7671/25/3/305.

Orlova, Y., Harmon, R. E., Broadbelt, L. J., and Iedema, P. D. (2021). Review of the kinetics and simulations of linseed oil autoxidation. *Progress in Organic Coatings* **151**: 106041. DOI: 10.1016/j.porgcoat.2020.106041.

Otero, V., Sanches, D., Montagner, C., Vilarigues, M., Carlyle, L., Lopes, J. A., and Melo, M. J. (2014). Characterisation of metal carboxylates by Raman and infrared spectroscopy in works of art: Characterisation of metal carboxylates by Raman and infrared spectroscopy in works of art. *Journal of Raman Spectroscopy* **45**(11): 1197–1206. DOI: 10.1002/jrs.4520.

Palacios, E., Juárez-López, G., and Monhemius, A. (2004). Infrared spectroscopy of metal carboxylates. *Hydrometallurgy* **72**: 139–148. DOI: 10.1016/S0304-386X(03)00137-3.

Porsmo Stoveland, L., Frøysaker, T., Stols-Witlox, M., Grøntoft, T., Steindal, C. C., Madden, O., and Ormsby, B. (2021). Evaluation of novel cleaning systems on mock-ups of unvarnished oil paint and chalk-glue ground within the Munch Aula Paintings Project. *Heritage Science* **9**(1): 144. DOI: 10.1186/s40494-021-00599-w.

Rehg, T. J. and Higgins, G. (1992). Spin coating of colloidal suspensions. *AIChE Journal* **38**(4): 489–501. DOI: 10.1002/aic.690380403.

Rouabeh, J., M'barki, L., Hammami, A., Jallouli, I., and Driss, A. (2019). Studies of different types of insulating oils and their mixtures as an alternative to mineral oil for cooling power transformers. *Heliyon* **5**(3): e01159. DOI: 10.1016/j.heliyon.2019.e01159.

Sasse, J. (2005). *Paint on metal: modern and contemporary explorations and discoveries, January 29 - May 1, 2005*. Arizona: Tucson Museum of Art. ISBN: 978-0-911611-30-4.

Scriven, L. E. (1988). Physics and Applications of DIP Coating and Spin Coating. *MRS Proceedings* **121**: 717. DOI: 10.1557/PROC-121-717.

Shannon, R. D. (1976). Revised effective ionic radii and systematic studies of interatomic distances in halides and chalcogenides. *Acta Crystallographica Section A* **32**(5): 751–767. DOI: 10.1107/S0567739476001551.

Smidt, E., Schwanninger, M., Tintner, J., and Bohm, K. (2013). Ageing and Deterioration of Materials in the Environment – Application of Multivariate Data Analysis. In: *Multivariate Analysis in Management, Engineering and the Sciences*. Ed. by L. Freitas. InTech. DOI: 10.5772/53984.

Terenzi, M. G., Ferrucci, F., and Amadori, M. L. (2006). *Dipinti su rame: storia, tecnica, fenomeni di degrado, diagnostica, indicazioni per la conservazione e il restauro*. I talenti 19. Padova: Il prato. ISBN: 978-88-89566-36-7.

Tiňo, R., Vizárová, K., and Krčma, F. (2019). Plasma Surface Cleaning of Cultural Heritage Objects. In: *Nanotechnologies and Nanomaterials for Diagnostic, Conservation and Restoration of Cultural Heritage*. Elsevier: 239–275. DOI: 10.1016/B978-0-12-813910-3.00011-2.

Török, T., Urbán, P., and Lassú, G. (2015). Surface cleaning and corrosion protection using plasma technology. *International Journal of Corrosion and Scale Inhibition* **4**(2): 116–124. DOI: 10.17675/2305-6894-2015-4-2-116-124.

Tyona, M. (2013). A theoritical study on spin coating technique. *Advances in materials Research* **2**(4): 195–208. DOI: 10.12989/AMR.2013.2.4.195.

Vega, D., Cardoso, I. P., and Carlyle, L. (2018). Painting on copper: research on the materials and techniques used on ground layer according to historical treatises and

analytical study of two paintings attributed to the Portuguese and Flemish schools. *Conservar Património* **27**: 23–35. DOI: 10.14568/cp2016040.

Watin, J.-F. (1773). *L'art du peintre, doreur, vernisseur*. 2nd ed. sold by Grangé, Durand and the author.

Xu, W., Rajan, K., Chen, X. G., and Sarkar, D. (2019). Facile electrodeposition of superhydrophobic aluminum stearate thin films on copper substrates for active corrosion protection. *Surface and Coatings Technology* **364**: 406–415. DOI: 10.1016/j.surfcoat.2019.02.070.

Sitography

Krüss Scientific (2022). *Roughness (surface roughness)*. URL: https://www.kruss-scientific.com/en/know-how/glossary/surface-roughness (visited on 09/01/2022).

Rapid Direct (Nov. 11, 2021). *Brushing Finish Guide: Principle, Applications, and Must-Know Facts*. URL: https://www.rapiddirect.com/blog/brushing-finish-guide/#:~:text=Brushing%20surface%20finish%20involves%20using,They%20are%20filamentary%20in%20nature..

CHAPTER 3

Detection of metal soaps

on copper and zinc model samples using imaging techniques

Adapted from Russo S., Brambilla L., Thomas J.B., and Joseph E. 2022. Revealing degradation patterns: imaging techniques for the study of metal soap formation on painted metal objects. In: *Proceedings of the interim meeting of the ICOM-CC Metal Working Group*, Helsinki 5 – 9 September 2022.

The detection of metal soaps on painted metal artworks using non-invasive, non-destructive techniques (NDTs) was one primary goal of this research. For this reason, Fourier transform infrared (FTIR) spectroscopy, one of the most employed diagnostic analytical techniques for metal soap detection, was utilised on metal model samples to assess the presence of metal soaps and investigate the FTIR signal collected. In particular, a discussion on the effect of the substrate and its surface characteristics on the FTIR response is proposed. Mirror-polished and hair-brushed copper and zinc coupons were compared in terms of reactivity towards fatty acids and possible deformation of the FTIR signal using a chemometric approach based on principal components analysis (PCA). FTIR analyses showed formation of metal soaps on both copper and zinc substrates. Characteristic vibrational bands were identified and commented on in terms of their position and shape as an indication of soap type, crystallinity, and purity.

Complementary Raman and X-ray diffraction (XRD) studies were attempted to gain insights into the geometry and crystallinity of the formed metal soaps. These preliminary endeavours showed technical challenges and raised issues that are briefly discussed herein. Additionally, in order to prospect the use of less exploited techniques for the detection of metal soaps, the samples were analysed using two hyperspectral cameras, operating in the visible-near infrared (VNIR) and short-wave infrared (SWIR) spectral ranges. The appropriateness of the two cameras in the investigation of metal soaps and the effect of the thickness of the coating on the data obtained is discussed here. Colorimetric data were used to support the results observed in terms of the dependency of

the signal on the thickness of the oil coating. Active IR thermography was also performed to assess the possibility of this technique to provide indicators of the formation of metal soaps.

3.1 Introduction

A fundamental preliminary step in studying any chemical reaction is assessing the possibility of chosen analytical techniques to provide chemical information about the species under investigation. This chapter focuses on selected non-invasive analyses and their ability to provide information on the presence of metal soaps on painted metals. The appropriateness of Fourier transform infrared and Raman micro-spectroscopies (μ-FTIR, μ-Raman), X-ray diffraction (XRD), hyperspectral imaging (HSI), and IR thermography for the detection of metal soaps was evaluated on copper and zinc model samples.

3.1.1 FTIR spectroscopy for metal soap detection and properties of the signal

The potential of μ-FTIR spectroscopy for detecting metal soaps, i.e., a vibrational molecular spectroscopy method based on the interaction of an infrared source with diverse materials, is well demonstrated by the scientific literature of the last couple of decades (Hermans, 2017; Casadio et al., 2019; Garrappa et al., 2020; Hermans et al., 2021). In a recent article, Filoupoulou and co-authors reviewed the spectroscopic behaviour of fatty acids and their calcium, sodium and zinc soaps in the mid-infrared range (Filopoulou et al., 2021). According to this work, several diagnostic features can be observed that indicate the type of soaps and their coordination geometry. These aspects affect the band maxima and the shape of the curve in the range $1600 - 1400$ cm^{-1}, where the symmetric and asymmetric carboxylate vibrations have their characteristic spectral features (e.g., for zinc soaps, $\nu_a COO^-$ at $1575 - 1530$ cm^{-1} and $\nu_s COO^-$ at $1460 - 1400$ cm^{-1}). Furthermore, the $\Delta\nu$ value, defined as the difference in wavenumbers between the asymmetric and symmetric signals, is determined by the coordination geometry, where structures having lower symmetry result in higher $\Delta\nu$ values. Specifically, unidentate complexes (Chapter 1, Figure 1.3), which have lower symmetry, will have maximum values for the asymmetric vibration closer to the ones of the corresponding carboxylic acids (Filopoulou et al., 2021).

The length of the fatty acid chains can, in some cases, such as for zinc soaps, cause splitting of the carboxylate (COO^-) band: for shorter chains (i.e., caprylic and decanoic acids), paired signals at 1550 and 1410 cm^{-1} ($\Delta\nu$ = 139 cm^{-1}), and 1532 and 1399 cm^{-1} ($\Delta\nu$ = 133 cm^{-1}) appear for the asymmetric and the symmetric stretching of $C8_2Zn$ and $C10_2Zn$, respectively, showing a shift of several tens of cm^{-1} with respect to longer chains. The C−H stretching vibration, which falls at higher wavenumbers ($2960 - 2850$ cm^{-1}), does not vary much if not in the presence of organic additives, inorganic materials, solvents, or degradation products trapped in the crystal structure (Filopoulou et al., 2021). For copper palmitate (C16:0), stearate (C18:0), and oleate (C18:1), the COO^- asymmetric and symmetric stretching vibrations fall in a narrow range of wavelengths between $1588 - 1583$ cm^{-1} and $1426 - 1414$ cm^{-1}, respectively (Izzo et al., 2021; Carvalho, 2022). The corresponding C−H stretching vibrations are

characterised within the wavelength range $2914 - 2846$ cm^{-1}. Copper linoleate (C18:2) shows higher frequency, with COO^- asymmetric stretching at 1601 cm^{-1} and higher $\Delta\nu$ values (188 cm^{-1}) (Carvalho, 2022).

Multivariate approaches to spectroscopic data When a large number of spectroscopic data needs to be examined at once, multivariate chemometric approaches can prove helpful in data exploration and identification of patterns and outliers. Wold and Kowalski introduced the term *chemometrics* in the early 1970s as a set of statistical methods that were originally developed for organic chemistry applications (Héberger, 2008; Santos et al., 2013). More recently, chemometrics has been widely applied in pharmaceutics (El-Gindy and Hadad, 2012), food research (Marini, 2013) and cultural heritage. In the past decades, several chemometrics approaches, as well as quantitative methods (e.g., partial least square approach, PLS), have been reliably used in the cultural heritage field for data exploration, clustering and classification (e.g., principal components analysis, PCA). Their applications extend to many heritage materials such as pigments (Duchene et al., 2010), colorants (Manfredi et al., 2017), paper (Trafela et al., 2007; Lichtblau et al., 2008) or metals (Visco et al., 2015), where data collected using a range of analytical techniques can be used (e.g., chromatography, Raman (Peris-Díaz et al., 2018) and FTIR spectroscopies (Capobianco et al., 2017; Luna and Gois, 2018)), as well as more complex imaging datasets (Geladi et al., 1994; Sciutto et al., 2012; Cutajar et al., 2022).

PCA is one of the most utilised exploratory statistical approaches. Early versions of the method were already mentioned in the 1800s, although its recognised first appearance in scientific literature goes back to the year 1901 (Brereton, 2018). PCA allows summarising the main characteristics of multi-dimensional data in a visual form, giving insights into the data structure (Marini, 2013). To do so, PCA helps identify a set of orthogonal coordinates – a low-dimensional subspace – that maximises the variance (i.e., the distance of each sample in the dataset from the mean value, or, in other words, the dispersion of data around the sample's mean), and on which the coordinates of the samples can be projected (Figure 3.1) (Rao, 1964).

PCA has been widely used in association with FTIR data since it allows visualisation of relationships that cannot be easily detected by observing the single spectra (Wertz et al., 2022). Practically, a matrix containing samples (rows) and wavenumbers (columns) is generated. Eigenvalues and eigenvectors are calculated for the linear transformation identified by Equation **(1)**

$$\underset{r\times\nu}{\mathbf{X}}\ \underset{\nu\times F}{\mathbf{P}} = \underset{r\times F}{\mathbf{T}} \tag{1}$$

where $\mathbf{X}$ is the original matrix, $\mathbf{P}$ is the matrix of the coefficients of the transformation (eigenvalues, or loadings), and $\mathbf{T}$ is the matrix containing the coordinates of the samples in the new set of orthogonal directions (scores). The eigenvectors are referred to as principal components (Marini, 2013; Wertz et al., 2022). This method permits discrimination of smaller contributions to the FTIR spectrum and allows identification of differences between samples with similar FTIR spectra (Jolliffe and Cadima, 2016).

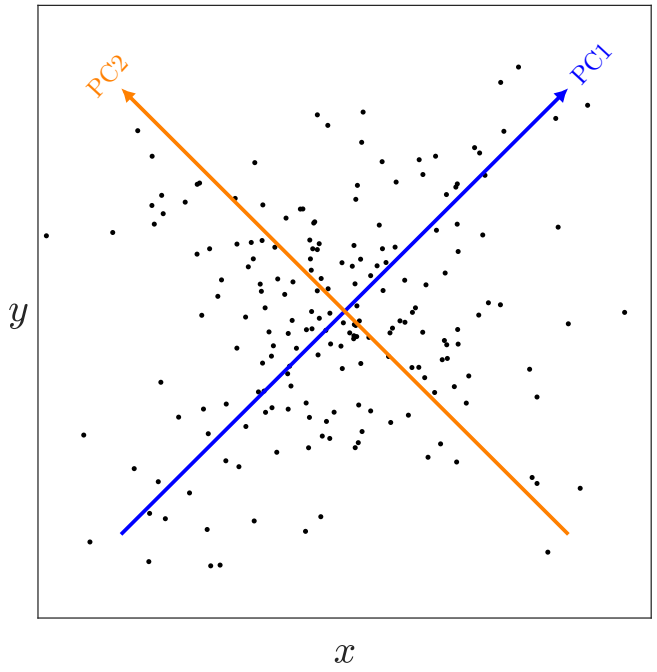

Figure 3.1: The identified principal components on an example dataset representing the directions of the samples' maximum variance.

3.1.2 Raman spectroscopy for metal soap detection

Raman spectroscopy is a vibrational spectroscopic technique that relies on measuring the intensity distribution of inelastically scattered photons from a sample (Raman effect) after its interaction with a monochromatic light source as a function of wavelength (Vandenabeele, 2013). It is often used to complement information obtained through FTIR spectroscopy. Several studies have deployed Raman spectroscopy to investigate the chemical characteristics of fatty acids and their metal soaps. A selection of saturated and unsaturated fatty acids was investigated by Otero and co-authors (Otero et al., 2014), who, confirming the work previously carried out by Robinet and Corbeil (Robinet and Corbeil, 2003), reported how Raman spectra of saturated acids resemble the respective FTIR spectra in the $1180 - 1320$ cm^{-1} spectral range (CH_2 wagging, ω). C−C stretching vibrational bands appear with low intensity in the Raman spectra between 1050 and 1150 cm^{-1} (i.e., at 1098 and 1104 cm^{-1} for palmitic and stearic acid, respectively). Raman shifts of unsaturated fatty acids differ from the FTIR signals, with C=C stretching vibration found between 1675 and 1640 cm^{-1} (Otero et al., 2014).

Otero et al. observed that spectra of metal carboxylates do not differ significantly from the ones of their respective fatty acids for Raman shifts higher than 1000 cm^{-1} (Otero et al., 2014). Specifically, the spectral range above 1700 cm^{-1} is considered to be non-diagnostic for discrimination between different fatty acids and metal soaps (Robinet and Corbeil, 2003). Raman characteristic spectral features of metal carboxylates can be found in the region between 900 and 1000 cm^{-1}, where CH_2 rocking (ρ) and OH out-of-plane deformations can be identified. In the study of metal soaps using Raman spectroscopy, it was shown that differentiation between carbon chain lengths and different metal cations is not straightforward and might necessitate the use of chemometric

approaches (Otero et al., 2014).

Therefore, four main regions of the Raman spectra of fatty acids and their relative metal soaps can be identified (Otero et al., 2014; Izzo et al., 2021):

- The CH_2 rocking vibration region ($900 - 950$ cm^{-1}, ρ), where differences in metal soaps from diverse metal cations or the presence of di-acids can be identified;
- The C−C stretching vibration region ($1050 - 1150$ cm^{-1}, ν), where different carbon chain lengths can be discriminated;
- CH_2 wagging modes ($1180 - 1380$ cm^{-1}, ω), that can, in some cases, indicate the chain length (e.g., for lead palmitates and stearates);
- The C=C stretching vibration ($1640 - 1675$ cm^{-1}, ν), where unsaturated carbon chains can be identified.

The characteristic bands for copper and zinc soaps in the spectral range 950-1130 cm^{-1} are listed in Table 3.1.

Table 3.1: Characteristic Raman signals for copper and zinc soaps (Otero et al., 2014; Izzo et al., 2021).

	Palmitate	**Stearate**	**Oleate**	**Azelate**	**Assignment**
Copper	1128–1130 m	1128–1130 s–m	1120 w	1095 s	νC−C
	1098 w	1103–1104 w	1085–1092 m	1091–1095 s	
	1062 m	1062 m–s	1064 m–s	1061–1062 w	
	931–946 w	937–947 w	946–959 w	947–959 s–m	ρCH_2
Zinc	1130–1131 m	1129–1131 s	1122 w		νC−C+δC−C−C
	1101–1107 w	1104–1110 w	1097 m	1103 s	
	1061–1063 m	1061–1063 s	1065 m	1064 m	
	950–952 w	948–952 w	952 w	950 m	ρCH_2

s = strong, m = medium, w = weak signal. All values are expressed in cm^{-1}.

One of the potentials of Raman spectroscopy is given by the possibility of coupling the equipment with a microscope to obtain simultaneous spectral and spatial information about specific compounds under study. This allows for the mapping of an area of interest, as well as the collection of data from different layers of the sample along the z-axis. Several methods are available to investigate deeper layers of a target sample that allow overcoming the surface nature of the analysis when the sample is not transparent to the chosen laser wavelength (Vandenabeele et al., 2017).

Depth profiling is a spatially resolved method suitable for those samples that can be considered transparent to specific laser wavelengths. It allows for the collection of characteristic Raman signals from spots or regions located at different depths of multi-layered targets by focusing the excitation laser beam at different positions along the z-axis (Casadio et al., 2016).

Offsets Raman spectroscopy (SORS) serves a similar purpose to the depth profiling method, but it is suitable for diffused scattering from turbid or opaque samples (Bersani et al., 2016). There are two main micro-SORS modalities: defocusing and full micro-SORS. The defocusing method can be performed on conventional Raman micro-spectrometers, hence

it is preferred for its versatility (Bersani et al., 2016; Casadio et al., 2016). In a SORS experiment, at least two single-point analyses are performed, one where the laser is focused at the surface of the object like in a conventional acquisition, and one, where the distance between the sample and the microscope objective is increased, hence at a position where the excitation laser beam is out of focus. This allows to collect a signal from a bigger area (i.e., from inner layers), which dimension is directly proportional to the defocusing distance Δz (Bersani et al., 2016; Rousaki et al., 2017; Vandenabeele et al., 2017).

3.1.3 X-ray diffraction

Literature evidence of systematic investigation of metal soaps and their recrystallisation due to temperature increases by X-ray diffraction (XRD) can be found as early as the 1940s (Vold and Hattiangdi, 1949). The aim of these studies was mainly to allow differentiation of metal soaps according to the different metal cations or to the type and length of the aliphatic chain and to identify various phases present in the solid samples and their degree of crystallinity (Vold and Hattiangdi, 1949; Ogino and Saito, 1977; Robinet and Corbeil, 2003). The patterns of different zinc and copper soaps were found to resemble each other below 20°, 2θ, sharing the five most intense peaks at similar d-spacings around 4.2, 2.1, 1.4, 1.1, and 0.9 nm (Corbeil and Robinet, 2002). The distinction between zinc and copper soaps having different chain lengths and saturation is possible considering the lower intensity peaks in the region $20 - 30°$, 2θ. The region $12 - 18°$, 2θ, present additional low intensity peaks characteristic of copper palmitate, that allow its identification (Corbeil and Robinet, 2002).

More recently, high resolution for metal soap detection in paint layers was obtained by analysing thin-sections in transmission mode using synchrotron light sources (Salvadó et al., 2019). Chemical imaging techniques, like synchrotron radiation 2D-XRD (2D-SR-XRD), allow for the investigation of the spatial distribution of the soaps together with their chemical composition (Salvadó et al., 2019; Gonzalez et al., 2020).

3.1.4 Hyperspectral imaging

Hyperspectral imaging (HSI) techniques are a set of non-invasive, non-destructive techniques based on the acquisition of separate images at narrow intervals of wavelengths (< 10 nm), called bands, that can then be analysed as a function of the chemical composition of an object (Amigo, 2019). Although HSI systems are not always readily available, they have proven to be successful in the field of cultural heritage (Grillini et al., 2021; Cutajar et al., 2022). Depending on the resolution of the camera, they can, in fact, be used on relatively small and large objects to identify pigments or binders or to monitor conservation treatments. In cultural heritage applications, hyperspectral cameras mainly operate in reflectance mode, and cover the visible (Vis), near-infrared (NIR) or short-wave infrared (SWIR) regions of the electromagnetic spectrum. Specifically, pigments have a strong characteristic signal in the visible and near-infrared range (VNIR, $400 - 1050$ nm), whereas binders typically have a strong spectral signature in the short-wave infrared spectral range (SWIR, $1050 - 2500$ nm) that makes their identification possible (Cucci et al., 2019; Amato et al., 2020). Although it is not common to approach the study of metal soaps in spectral ranges different than the mid-wave-infrared (MWIR, $4000 - 400$ cm^{-1}), in the pharmaceutical field, common soaps used as lubricants in the manufacturing of tablets are sometimes characterised in the SWIR range of wavelengths (Kauffman et al., 2008). How-

ever, the distinction between metal soaps and oils in the SWIR is not trivial since the two share a significant number of signature features (Dooley et al., 2017; Amato et al., 2020; Zuena et al., 2020).

There are few commercial and prototyped cameras available, which cutting-edge technology differs in sensors (hence the range of wavelength covered), camera models, and methods used to collect the datacube (Picollo et al., 2020). The major acquisition methods as single detector readout are (Fischer and Kakoulli, 2006; Li et al., 2013; Picollo et al., 2020):

a) *whisk-broom* or *point-scanning* imaging mode, where reflected light is collected through rotating mirrors that direct the radiation to the detector. Either the sample or the detector is moved in the collection phase, and the images are acquired one point at a time;
b) *push-broom* or *line-scanning* approach, where the information is collected on a slid, hence by scanning through the spatial dimension, where each spatial point corresponds to a spectrum;
c) *stating* or *band sequential* method, where the image is acquired one spectral band at a time (hence scanning through the spectral dimension), with a total number of bands acquired depending on the user's decision;
d) *snapshot* imaging spectrometers, also called *single-shot*, that, as the name suggests, acquire both spatial and spectral information with one exposure, hence without the need to scan in the spatial or the spectral dimensions.

Recent applications of hyperspectral imaging techniques in colour vision research have explored the possibility of rendering the hyperspectral data as colorimetric representations (Foster and Amano, 2019). Hyperspectral radiance images can, in fact, be mapped onto appropriate colour spaces under specific compensation for different illuminations (Foster and Amano, 2019; Raza et al., 2022). Several ASTM (American Society for Testing and Materials) standards are available that can be applied to hyperspectral imaging for the colour evaluation of objects (e.g., E 1164-94, E 308-95 (Kleiman, 2003)). However, different factors need to be considered that may affect the accuracy of the transformation from radiance – or reflectance, depending on the application – to colorimetric data. These factors include the effect of the chosen illuminant and the uniformity of the colour space (Foster and Amano, 2019). Additionally, although hyperspectral devices were often found to have acceptable radiometric and photometric accuracy for chromatic content, light sources and colour patches were found to affect the colorimetric accuracy (Raza et al., 2022). Therefore, an alternative approach is to complement hyperspectral imaging data with colorimetric measurements using a spectrocolorimeter (George et al., 2018).

3.1.5 Infrared Thermography

Thermography is a thermal, non-contact, non-destructive imaging method that has been used since the 1960s for many implementations in military applications, medicine, engineering, maintenance of buildings (Grinzato, 2012) and, more recently, fluid-dynamics studies (Korukçu and Kilic, 2009), and airport monitoring of swine flu and COVID-19 cases (Khaksari et al., 2021; Perpetuini et al., 2021). It involves the detection of IR electromagnetic radiation emitted by the object under study (Balaras and Argiriou, 2002). Its potential lies in the fact that it allows examination of large and small surfaces to investigate defects, voids, inclusions, delamination, and accumulation of water and moisture

(Tomita and Chew, 2022). The principle is based on different thermal conductivity and thermophysical properties of the materials.

In particular, IR thermograms are influenced by several factors, such as (a) temperature of the environment in which the object is placed, which directly affects the camera lens and its performance, (b) ambient relative humidity, which can attenuate infrared radiation and scatter the radiation of the object when high values are registered, (c) wavelength emitted from the body under investigation, and, most importantly, (d) emissivity ε of the object (Korukçu and Kilic, 2009). Emissivity can assume values ranging from 0 to 1, where 0 corresponds to a mirror and 1 to an ideal black body (Table 3.2[1]). This quantity, which is material specific, determines the response of the object when infrared thermography is performed (Korukçu and Kilic, 2009).

There are two main methodologies used in thermography-based studies: passive and active thermography. Passive thermography uses natural heat sources to investigate the target surface through steady images (like in the case of airport monitoring practices). In active thermography, the surface is excited by heating it using lamps or air guns. The thermal input, which can consist of continuous or intermittent heating, is recorded using a thermal camera to monitor the heating and the cooling phases (Tomita and Chew, 2022).

Table 3.2: Emissivity values for different materials. Values of interest for this work are highlighted in bold. Other values are provided for comparison.

Material	Emissivity
Aluminium (polished)	0.10–0.05
Aluminium (oxidised)	0.10–0.40
Brass (polished)	0.05
Brass (oxidised)	0.50–0.60
Brass (burnished)	0.30
Copper (polished)	**0.10**
Copper (oxidised)	**0.20–0.80**
Iron (oxidised)	0.50–0.95
Iron (rusted)	0.50–0.70
Iron (wrought, dull)	0.90
Iron oxide	0.85
Oil (animal/vegetable)	0.95–1.00
Oil (mineral)	0.90–1.00
Oil (0.001" thick)	0.25
Oil (0.002" thick)	0.46
Oil (0.005" thick)	0.70
Paint (bronze paint)	**0.80**
Paint (on metal)	**0.60–0.90**
Zinc (polished)	**0.05**
Zinc (oxidised)	**0.10**
Zinc (galvanised)	**0.20–0.30**

[1] Based on `https://www.optotherm.com/emissivity` and `https://www.instrumart.com/pages/209/metals-emissivity-table`

3.2 Materials and methods

3.2.1 Samples preparation

Fourier transform infrared (FTIR) signal evaluation Model samples were prepared as $60 \times 60 \times 1$ mm^3 hair-brushed (Gravadhoc Hoffmann, Neuchatel) and mirror-polished (Bergeon 6880 polisher) copper sheets. The hair-brushed finishing – an industrial process which consists in utilising an abrasive material to create unidirectional lines giving a satin finish – was chosen to mimic the artists' common practice of scratching the surface of the metal prior to painting in order to increase the grip of the paint on the metallic support (see Chapter 2). After the removal of contaminants using absolute ethanol (VWR Chemicals), the samples were divided into three parts, as shown in Figure 3.2:

- one, that was left uncoated (Raw);
- a second one coated with ~ 80 µL of cold-pressed linseed oil using a rectangular painter's spatula (LO, Kremer Pigmente);
- and a third one, that was painted with a zinc oxide-based oil formulation using a rectangular painter's spatula ($20-25\%$ LO in $80-75\%$ ZnO w/w) (LOZnO). Zinc oxide and cold-pressed linseed oil were provided by Kremer Pigmente.

The samples were then cured overnight at 80 °C. On all three parts, 1 µL drop of five different solutions of palmitic acid in ethanol, having increasing concentration 7.8×10^{-5} M, 7.8×10^{-4} M, 7.8×10^{-3} M, 3.9×10^{-2} M and 7.8×10^{-2} M were added to the surface of the sample (Figure 3.2a). The inhomogeneities of the oil coating and paint were measured using the coating thickness gauge Surfix by Phynix, resulting in average ranges of thickness (over 10 points) from 4 to 30 µm for LO-coated copper and zinc samples, respectively, and from 44 to 49 µm for LOZnO.

Detection of metal soaps For the detection of metal soaps, two sets of copper and zinc samples were considered, following protocols b) and c) in Chapter 2, Figure 2.6. Hair-brushed copper and zinc samples were coated merely with linseed oil (~ 80 µL) using a painter's spatula. The coated samples were cured overnight at 80 °C, and artificially aged at 80 °C and 80% relative humidity in a laboratory oven for 30 days, then left in uncontrolled conditions (room temperature and relative humidity) for additional 11 months. The triplets were kept in a sealed box at constant relative humidity using glycerol–water solution (50% w/w) (Forney and Brandl, 1992). The samples were then left at room temperature and relative humidity for an additional 11 months. The relative humidity and temperature levels were monitored using a PeakTech 5185 datalogger equipped with an immersion probe.

3.2.2 Fourier transform infrared spectroscopy

FTIR spectra were collected using a Thermo Scientific^{TM} Nicolet^{TM} iN10 MX infrared microscope, with 4 cm^{-1} spectral resolution and 16 scans. In particular, for the signal evaluation, spectra were collected

- every 45 min for 6 hours starting from 30 minutes, then at 24 and 48 hours, for brushed copper samples (135 spectra in total, per replicate),

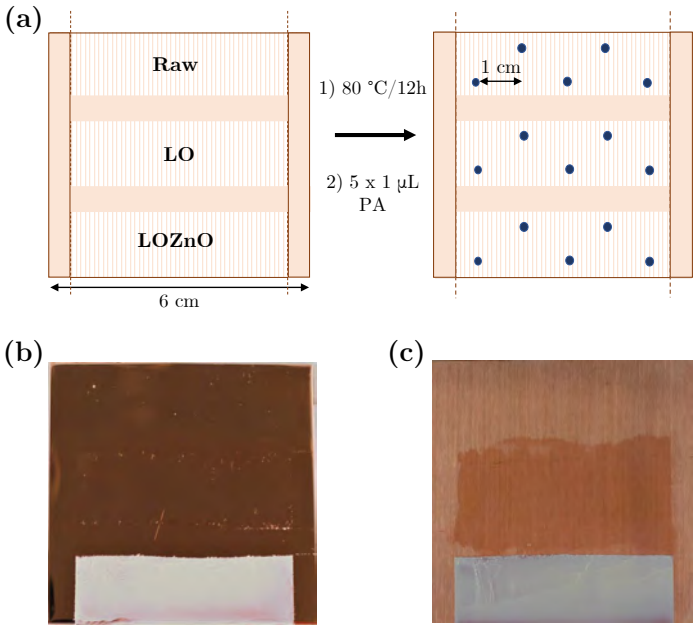

Figure 3.2: (a) The samples prepared for the experiment and divided in three parts (Raw, LO, LOZnO), on which palmitic acid was added as a drop (blue dots); (b) the final result on a mirror-polished (Cu01_polished_drop) and (c) hair-brushed sample (Cu25).

- every 60 min for 6 hours starting from 30 minutes, then at 24 and 48 hours, for polished copper samples (120 spectra),
- every 60 min for 4 hours and 15 minutes starting from 15 minutes, for brushed zinc samples (75 spectra),
- every 60 min for 4 hours and 15 minutes starting from 15 minutes, for polished zinc samples (75 spectra),

For the detection of metal soaps, spectra of the copper and zinc samples after the curing of the oil and after 70 days are provided.

Principal component analysis (PCA) was performed to explore the FTIR data. A script was generated using the `ChemoSpec` package for chemometric analysis of spectra (Hanson, 2022) in the R Project for Statistical Computing – a free software environment for statistical analysis and graphics (R Core Team, 2022). Visualization of the results was performed using the `ggplot2` package (Wickham, 2016). Data pre-processing consisted of baseline correction (six- degrees modified polynomial fitting), normalisation (probabilistic quotient normalisation, PQN), and atmospheric corrections to remove residual signatures of atmospheric CO_2 and water in the spectra. The modified polynomial fitting method, which uses a least-squares-based polynomial curve-fitting function, is an iterative process where the curve is fitted by minimising the variance of the unbiased estimators of the coefficients, under the assumptions that Gauss–Markov theorem is valid and subsequentially reassigning the peaks to their original intensity (Lieber and Mahadevan-Jansen, 2003). The final corrected spectra were reached after 100 iterations (0.001 tolerance).

The probabilistic quotient normalisation (PQN) method was employed for comparative purposes. This method identifies a normalisation factor, which assigns a weight to the different peaks/bands of a spectrum when compared to a reference spectrum. The reference spectrum can be a database-quality signal, as well as, like in the case of this study, the mean or median of all the spectra collected in the dataset (Dieterle et al., 2006). All the collected spectra were considered in building the corresponding PCA models, i.e., 135, 120, and 75 for brushed copper, polished copper, and brushed and polished zinc, respectively. The classic approach was employed, where the samples are all considered with their own weight to explain the maximum variability of the dataset. Four principal components were considered after examination of the scree plots of the copper samples (S - 21 and S - 22). Only the results of the first two principal components are presented, which together explained 62% and 69% of the total variance for the hair-brushed (Cu25) and mirror-polished (Cu01_polished_drop) samples, respectively. Given the substantial number of spectra ($n > 30$), normal sample distribution was assumed per the central limit theorem (CLT). Nevertheless, the Shapiro-Wilks test was performed to confirm normal distribution of the samples for each wavelength. The data was mean-centred and autoscaled. PCA analyses are presented as 2D score plots, where the ellipses express 95% confidence level. The spectra were cropped to the relevant wavenumbers ($1850 - 950$ cm^{-1}) to remove the influence of non-diagnostic peaks for metal soaps.

3.2.3 Raman spectroscopy

A Virsa^{TM} fibre-optic-coupled Raman micro-spectrometer was employed for the analysis of the samples. The system is equipped with an *xyz*-motorised stand, 785 nm and 532 nm laser probes in stacked configuration, and uses a video-unit with integrated software-controlled LEDs illumination and coloured video-camera for image acquisition. A microscope nosepiece equipped with 5x, 20x, 50x, 50x-LWD, 100x and a 100x-LWD objectives complete the setup. The Wire 5 software for system control and spectral elaboration was employed. The spectra are given as raw, and no correction other than removal of cosmic rays, when necessary, was performed. Three different analyses were performed, with a laser emitting at 532 nm in the static range $180 - 1650$ cm^{-1}, a 2400 lines/mm grating, and with varying parameters as summarised in Table 3.3:

- *Single point analyses*, to assess the presence of metal soaps and to identify them;
- *Depth profiling*, to obtain information on the depth distribution of the soaps within the samples, using a long working-distance objective (50x-LWD). 10 spectra were consecutively collected at 2 μm incremental steps on the samples prepared for metal soap detection to investigate the interface between the metal and the oil coating, in accordance with the measured values of oil coating thickness (i.e., total average thickness ~ 15 μm).
- *Spatially offset Raman spectroscopy (SORS)*, to acquire a bigger area of the sample including deeper layers. 10 spectra consecutively shifted by 2 μm were acquired per each analysis.

Raman spectra were collected on 10 and 26-month-old copper samples and 10 and 21-month-old zinc oil-coated coupons. Depth profiling and SORS Raman spectra were acquired after curing overnight in an oven at 80 °C and after 70 and 120 days of ageing, respectively.

Table 3.3: Parameters chosen for the Raman experiments aimed to identify metal soaps on copper and zinc LO-coated coupons.

	Objective	Power (mW)	Accumulations	Exposure time (s)
Point analysis	100x	15	20	20
Depth profiling	50x-LWD	5	5	5
SORS	50x-LWD	5	5	5

3.2.4 X-ray diffractometry

Preliminary analyses were performed on uncoated brushed copper and zinc sheets and linseed oil-coated samples (naturally aged for 7 to 9 months) of the same metals, where a drop of a concentrated palmitic acid solution (3.9×10^{-2} M) was added. Copper and zinc coupons were cut to 3×3 cm^2 pieces to fit the instrument restrictions for the sample size of the zero-background sample holder; one square piece for each sample was analysed. Analyses were performed using a Malvern Panalytical X'Pert Pro MPD multi-purpose powder diffractometer equipped with the Cu K anode (= 1.5405 Å) and Goebel mirror in the primary optics. Due to the strong diffraction pattern given by the bulk metals, grazing incidence XRD experiments were chosen for the uncoated copper and zinc sheets and the respective LO-coated samples. This method, which is used in the analysis of thin films, consists of utilising small incident angles ($< 5°$) between the beam and the surface of the sample, to minimise the penetration into the bulk material and enhance the intensity of the signal due to the interaction with other components of the sample (Sakata and Nakamura, 2013). The diffractograms were collected under reflection mode in the range $1 - 100°$ in 2θ with a time per step of 75 s, and step size of 0.026°. Three repetitions were performed per each diffractogram, giving a total acquisition time of 1h.

Additionally, a monitoring protocol was put in place, where one uncoated sample per each metal substrate was prepared and monitored after the addition of ten drops of a 3.9×10^{-2} M solution of palmitic acid in ethanol. The drops were added so that they would cover a sufficient area of the sample without overlapping (following a flower shape) and therefore allow detection within the area of analysis of 4 mm. Consecutive diffractograms were collected at 2-hours intervals, and 71 cycles were performed on each sample for a total monitoring time of 3 days. The diffractograms presented herein were cut at 5° to eliminate the signal of the X-ray source.

3.2.5 Hyperspectral imaging

A 14 and a 9-month-aged copper and zinc samples (ageing protocol b)), respectively, were analysed using push-broom HySpex VNIR-1800 and SWIR-384 hyperspectral cameras by Norsk Elektro Optikk. The acquisition geometry was standard at 45°/0°, and the focus was set at 30 cm, with a field of view of 16°, yielding a pixel size of approximately 50 μm. The model samples and the 99% white diffuse reflectance standard (Spectralon) were placed in-plane on a flat translational stage with mounted broadband spectral coverage tungsten–halogen lamps at 45° and the camera at 90°. Acquisitions were performed in the dark, with the white standard playing the role of a wide spectral range Lambertian reflector with uniform response, to correct for the reflectance of the light source. The bundled OEM software was used to implement dark current correction and calibrate the sensor in the pre-processing stage of the dataset. The HyspexRadV2.0 software was used to convert the

raw data into radiance pixel values. The processing of the data to obtain interpretable and comparable relative reflectance spectra was carried out using the Fiji open-source software (Schindelin et al., 2012). After re-slicing of the datacube at the top without interpolation, the data acquired both in the VNIR and SWIR ranges were corrected for illuminance, i.e., the dataset was divided by the radiance values of the Spectralon white diffuse reflectance standard, after re-slicing and adjusting its size to that of the samples (Babini et al., 2021). For the extraction of the spectra, an area of analysis of 1000×1000 μm^2 (20×20 px^2) was chosen as a good compromise between signal quality (S/N ratio) and occurrence of representative regions of interest of comparable size within the sample. Data from three areas selected on each different thickness region of the oil coating were extracted from each sample and averaged.

3.2.6 Colorimetry

An XRite® Ci62x spectrocolorimeter was deployed to collect colorimetric data, which provides reflectance spectra as well as measured parameters in the L*a*b* CIELAB colour space. The CIELAB colour space expresses colour as 3 values: L* represents the lightness scale ranging from 0 (black) to 100 (white); a* the green-red value from $-x$ (green) to $+x$ (red); b* the blue-yellow value from $-y$ (blue) to $+y$ (yellow). For this protocol, illuminant D65 (standard daylight) was used with d/8° geometry, 10° observer, and measurement area diameter of 4 mm. Since the scope of these measurements was to compare reflectance spectra with those obtained using hyperspectral imaging methods, ΔE* values that give an indication of perceived colour variation were not calculated for this study. Data visualisation was achieved using Matlab2020b. Two measures are given from two of the three samples within the triplicate. Per each samples, three different areas were analysed, characterised by varying thickness (thin, ~ 4 μm; medium, $\sim 12 - 15$ μm; thick, > 20 μm).

3.2.7 Infrared thermography

The system available at the Laboratoire de Recherche des Monuments Historiques (LRMH) was utilised, which consists of a FLIR SC655 micro-bolometer camera, equipped with a macro-lens and positioned at about 5 cm from the sample for optimal focus and so to improve readability and accuracy of the results. The area measured covered 100×75 mm^2.

Active thermography was performed by placing two 500 W halogen light sources at both sides of the sample with 45° angle with respect to its normal to homogenise the heating flux. The samples were excited by continuous exposure to heat for 1 min. Areas were selected so that they could contain simultaneous information about thick and thin parts of the samples. Five samples were considered: the one used for FTIR signal evaluation (1 μL of a 3.9×10^{-2} M palmitic acid solution in ethanol), and one per each of the two ageing protocols and substrates already characterised by the previously mentioned techniques (21 and 5-month-aged copper and 16 and 5-month-aged zinc samples). In the rendered infrared thermograms, warmer colours (red − orange − yellow) correspond to a higher temperature, whereas colder colours (purple and blue) indicate colder areas of the sample.

3.3 Results and discussion

3.3.1 FTIR signal evaluation using multivariate analysis

Considerations on the effects of surface finishing and coating inhomogeneities on the FTIR signal are presented through the observation of patterns between the spectra collected on two copper samples (Cu25 and Cu01_polished_drop). These are presented in Figure 3.3a,b, where three different groups of spectra can be identified based on their spectral features in the region $1850 - 950$ cm^{-1}: i) the set of spectra representing the bare metal substrates (Raw, blue), ii) the spectra of the linseed oil-coated area (LO, purple) and iii) the spectra related to the area painted with a zinc-oxide-based oil formulation (LOZnO, orange).

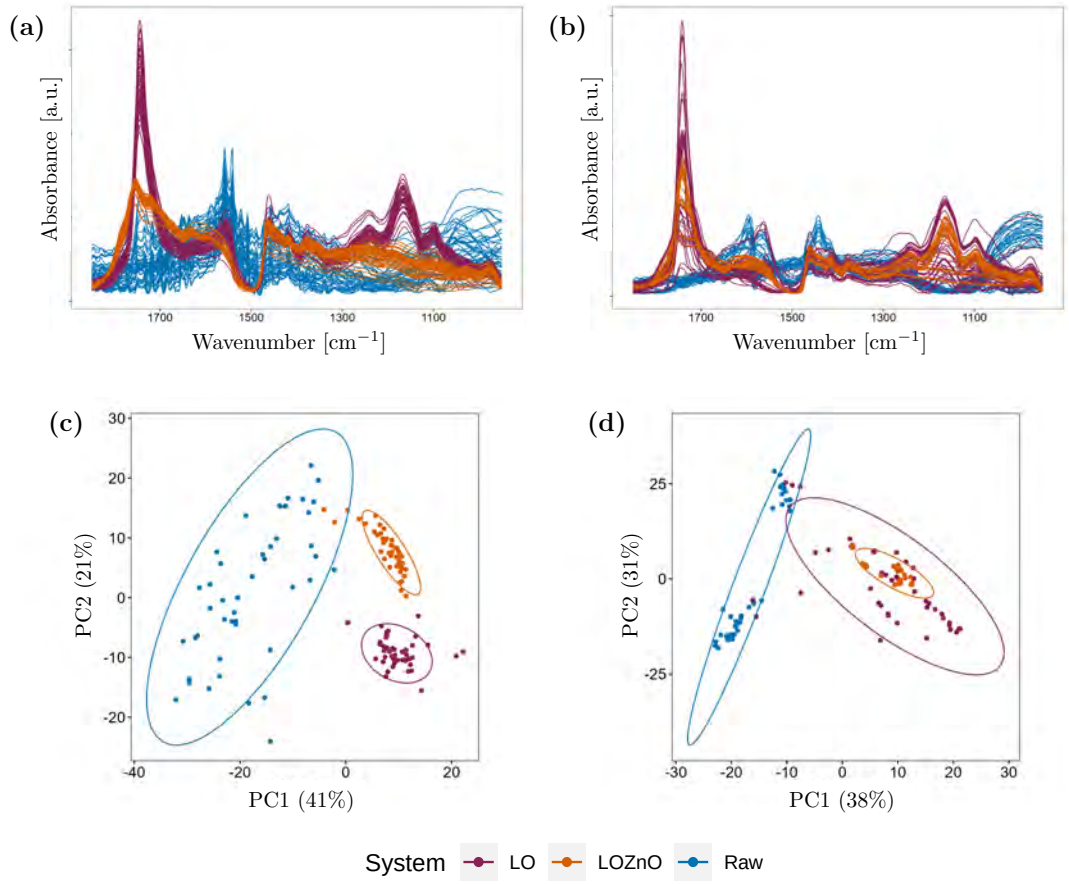

Figure 3.3: Results of the PCA analysis on the copper hair-brushed (Cu25, left) and mirror-polished (Cu01_polished_drop, right) samples. (a) and (b) show the FTIR spectra acquired and cropped to highlight the region of interest ($1850 - 950$ cm^{-1}); (c) and (d) show the score plots for hair-brushed and mirror-polished samples, respectively.

By observing the score plot for the brushed sample (Cu25; Figure 3.3c), three corresponding clusters could be observed:

- The blue cluster, which was characterised by significantly scattered data for the uncoated surface (Raw). The dispersed nature of the cluster suggested that the uncoated surface (Raw) was unsuitable for acquiring reproducible spectra of the metal

alone. This was probably due to the roughness of the surface, exerting non-specular reflection (Babu and Baldev, 2003; Silvennoinen et al., 2008).

- The purple cluster, smaller, containing data referring to the oil-coated surface (LO) and found at more positive values along the PC1 axis, showed less variability. Some samples were found outside of the 95% confidence ellipse.
- The orange cluster, which encapsulates data from the zinc-oxide-based painted area (LOZnO), grouped closer to the linseed oil-coated samples, indicating that these two formulations shared most of the characteristic signals that allow separation along the PC1 axis. However, this set was found at higher values along the PC2 axis.

By considering the loadings plot (Figure 3.4), which describes the effect of the variables (i.e., the different wavelengths) on the position of the clusters along the PC axes, it could be noticed how separation along PC1 was given by the set of wavelengths between 1650 and 1490 cm^{-1}, which negatively affected the loadings. In other words, more negative PC1 values in the score plot were correlated with an increased signal between 1650 and 1490 cm^{-1}. This spectral range was of interest for this study since it contains the diagnostic peak for the asymmetric stretching vibration of the carboxylate group $\nu_a COO^-$ that allows identification of metal soaps (Izzo et al., 2021). The score plot (Figure 3.3c) thus indicated that the raw surface (Raw, blue cluster) showed more signals related to the presence of metal soaps than the other systems (LO and LOZnO). This could be due to the fact that the direct reaction between the metal and the palmitic acid was more efficient than for the other systems.

The PC2 axis, meanwhile, showed a negative contribution between $1780 - 1710$ cm^{-1} (Figure 3.4), i.e., more negative PC2 values in the score plot were correlated with an increased signal between 1780 and 1710 cm^{-1}. This interval contains the diagnostic peak centred around 1745 cm^{-1}, attributable to the νC=O vibration indicative of drying oils (Viguerie et al., 2016). Thus, the separation observed between the LO (purple) and LOZnO (orange) clusters in the score plot (Figure 3.3c) might be partially explained by the relative abundance of linseed oil in the former system.

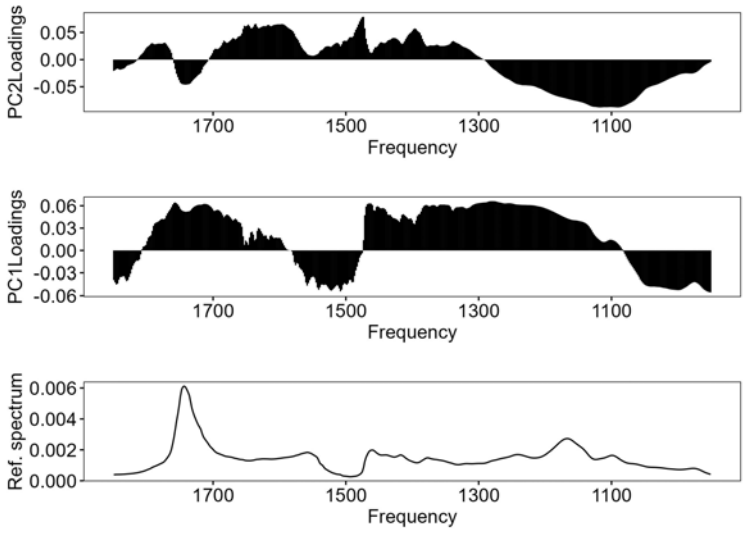

Figure 3.4: PCA loadings associated with the hair-brushed copper sample (Cu25).

Similarly to the brushed surface, three clusters could be identified for the mirror-polished sample (Cu01_polished_drop) (Figure 3.3b,d), that correspond to the uncoated (Raw, blue), the oil coated (LO, purple) and the painted (LOZnO, orange) regions of the coupon.

The linseed oil (LO, purple) and zinc-oxide-based oil (LOZnO, orange) clusters for this substrate exhibited a different behaviour than for the hair-brushed sample. Expressly, the LOZnO cluster was completely contained within the LO one. The higher variability of the LO data may be related to the relative inhomogeneity of the film thickness, which affected the acquisition of the FTIR spectra (e.g., the limit of penetration of the infrared beam in the oil with a refractive index of ~ 1.5), and indicated that the mirror surface was less suitable for obtaining reproducible FTIR analyses of oil-coated metal samples.

Turning to the loadings (Figure 3.5) it was shown how PC1 allowed separation based on the wavenumbers in the region $1850 - 1650$ cm^{-1}: spectra having more intense spectral features in this range result in more positive scores along PC1. As a validation, Raw samples, that do not contain linseed oil, hence should not show signals typical of the νC=O vibrational band of the esters, were found at more negative scores than the LO and LOZnO data-points.

The data referring to the Raw system, appeared to contain two sub-clusters, separated both along the PC1 and PC2 axes. In particular, the wavenumbers in the range $1680 - 1535$ cm^{-1}, where copper palmitate can be found, explained the separation along PC2, with positive scores having more intense signal in this spectral region. Returning to the spectra in Figure 3.3b, it can be seen that there were, in fact, two types of blue spectra — those with significant peaks in the indicated regions and those which remained comparatively flat. The different spectral behaviour explained the separation within the cluster along PC2, and might indicate that metal soap formation was not consistent on the "raw" mirror-polished samples.

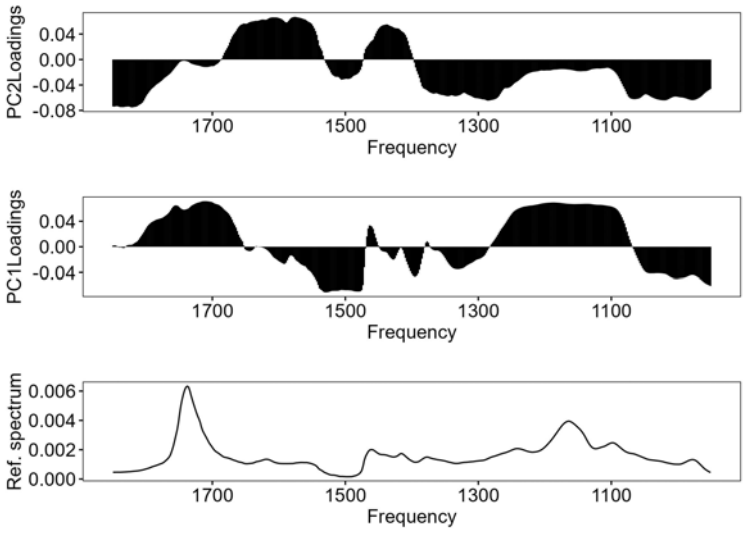

Figure 3.5: PCA loadings associated with the polished copper sample (Cu01_polished_drop).

The scree plots for the PCA analysis presented herein are available in the supplementary materials section (Section S.3), together with the PCA results for two analogous zinc samples.

In the zinc brushed sample dataset (Figure S - 23), the data for the Raw metal followed the trend of higher variability compared to LO and LOZnO already observed for copper samples. Here, most wavenumbers contributed to the separation along both PC1 and PC2, hence making it difficult to interpret the influence of a specific spectral feature on the clustering. However, it could be seen that, in the ranges of interest (centred at 1750 and 1540 cm^{-1}, for the presence of linseed oil and zinc palmitate, respectively), two relevant contributions were present (Figure S - 24). One range, containing the νC=O at 1750 cm^{-1}, had a positive effect on the separation, whereas the other one, containing the $\nu_a COO^-$ for zinc palmitate at 1540 cm^{-1}, had a negative effect. This might mean that samples with more positive scores (LO for PC1 and LOZnO for PC2) were characterized by having a more intense peak for the carbonyl stretching of the linseed oil (νC=O), whereas the ones in the third quadrant (bottom-left, Raw) were characterized by the presence of zinc soaps, as previously seen (Figure S - 23c). By observing the spectra (Figure S - 23a), it can, in fact, be seen that zinc soaps ($\nu_a COO^-$ at 1540 cm^{-1}) were heavily formed on the Raw system, similarly to what observed for the copper ones.

3.3.2 Metal soap detection by means of FTIR spectroscopy

Zinc and copper samples were investigated for the presence of metal soaps formed between the oil-coating and the metal support. The FTIR spectra of the linseed oil-coated zinc and copper substrates are presented in Figure 3.6.

The two spectra presented refer to two different monitoring time-points, particularly after curing the coupons in a laboratory oven overnight and after 70 days of artificial ageing (protocol c), Chapter 2) and additional 40 days of ageing in uncontrolled indoor conditions. Seven major spectral regions were identified on the spectra (Figure 3.6):

- The area between $3600 - 3300$ cm^{-1}, where the broad band characteristic of the acidic OH hydrogen bonding is located (blue);
- The area defined by the two sharp peaks at $2940 - 2930$ and 2857 cm^{-1}, typical of methylene-group ($-CH_2$) asymmetric and symmetric stretching vibrations (orange);
- The carbonyl stretching vibration ($1760 - 1700$ cm^{-1}), which maximum is shifted towards lower or higher frequency depending on the acidic nature of the bond – lower frequency for more acidic bonds. Both the peaks of the ester ($1754 - 1751$ cm^{-1}) and the carboxylic acid ($1723 - 1719$ cm^{-1}) are present here. Since the peak of the carboxylic acid was not present after the curing of the oil (blue line), but only at a later stage, it could be hypothesised that this was the result of the degradation processes occurring within the oil medium (yellow);
- The carboxylate group asymmetric vibration ($1600 - 1500$ cm^{-1}), with its characteristic shift depending on the metal ion involved in the bond and the crystallinity and geometry of the molecule (green);
- The carboxylate group symmetric vibration ($1440 - 1400$ cm^{-1}), overlapping part of the CH_2 scissoring region ($1475 - 1400$ cm^{-1}) (grey);
- The CH_2 wagging and twisting region ($1350 - 1045$ cm^{-1}, ω) (purple);
- The two bands indicating the presence of dimers ($2750 - 2500$ and $943 - 935$ cm^{-1}), (dashed lines).

By observing the diagnostic spectral region for metal soaps ($1600 - 1400$ cm^{-1}), the presence of a set of convolved signals could be observed, giving a larger band. These enlarged bands have previously been associated with lack of crystallinity of the species present - hence to more amorphous geometries - as opposed to sharper peaks, indicating crystalline phases (Hermans et al., 2021).

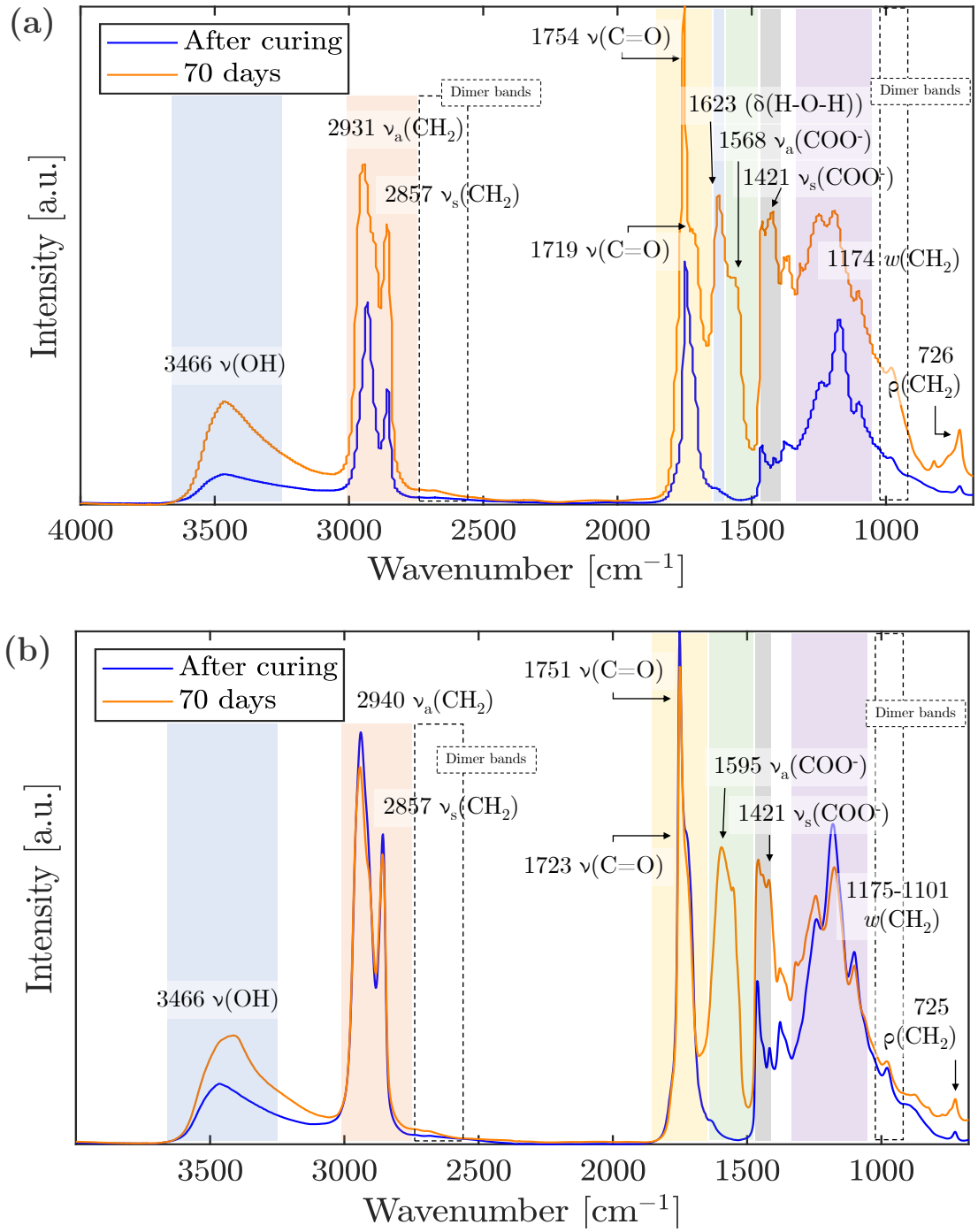

Figure 3.6: The different vibrational bands identified on the FTIR spectra of (a) copper (Cu37) and (b) zinc (Zn33) oil-coated samples after curing (blue line) and after 70 days ageing (orange line).

3.3.3 Raman spectroscopy

In the 10-month-aged copper sample (Figure 3.7, blue line), a broad band at 1087 cm^{-1} could be observed, followed by a peak at 1104 cm^{-1}, both ascribable to C−C stretching vibrations (νC−C) due to the possible co-presence of copper oleate and stearate. The presence of copper oleate could be corroborated by the observed peaks at 1439 and 1464 cm^{-1} (Robinet and Corbeil, 2003; Otero et al., 2014). Given the presence of a band at 1302, the peak at 1439 cm^{-1} could also be assigned to drying oils according to scientific publications (Schönemann and Edwards, 2011). The large band of convolved signals centred at 1576 cm^{-1} could generically be attributed to carbon materials not completely identified at the current state of the research (Coccato et al., 2015).

Raman spectra acquired from the 26-month-aged linseed-oil-coated copper sample (Figure 3.7, orange line) showed the presence of low intensity signals at 960 (ρCH_2), 1092 (νC−C), 1439 (δCH_2) and 1464 (δCH_2) cm^{-1}, suggesting the presence of copper oleate according to scientific literature (Robinet and Corbeil, 2003; Otero et al., 2014; Izzo et al., 2021).

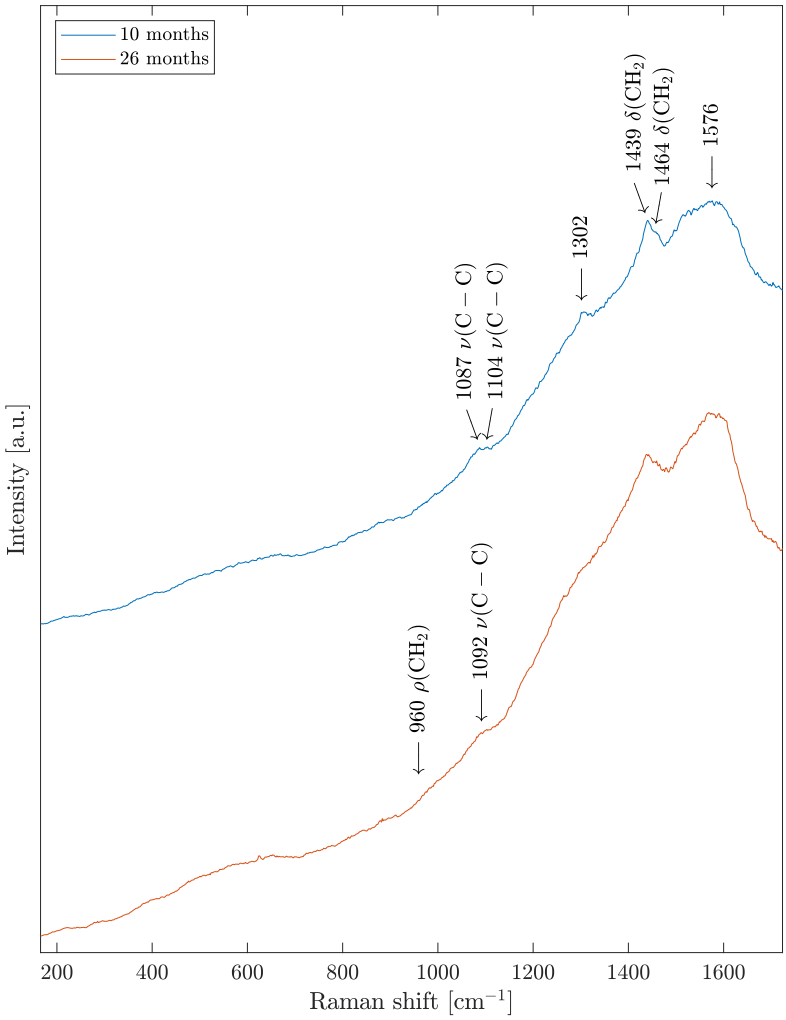

Figure 3.7: Raman spectra of 10- and 26-month-aged linseed oil-coated copper samples (blue (Cu35) and orange (Cu07) line, respectively). Relevant vibrational modes for copper soaps are indicated.

In the 10-month-aged zinc sample (Figure 3.8, blue line), with the exception of the peak at 1090 cm^{-1}, the bands presented themselves as broad and poorly resolved signals, centred at 1353, 1446, and 1590 cm^{-1}, respectively. The 1090 cm^{-1} peak, together with the two large signals at 1353 and 1446 cm^{-1} hinted towards the presence of zinc soaps that could not be better identified at this stage. The position of the peaks, that does not correspond to the common species characterised by Robinet and Corbeil, 2003, Otero et al., 2014, and Izzo et al., 2021, could be due to lack of crystallinity of the carboxylates formed.

The 21-month-aged zinc sample (Figure 3.8, orange line) showed instead more defined characteristic Raman signals. The peaks detected at 950, 1063, 1101, 1131, 1295, 1398, 1439, 1458 and 1463 cm^{-1} implied the presence of zinc stearate and palmitate, where they are normally found as the result of methylene groups rocking vibration (ρCH_2), C−C stretching vibrations (νC−C), and methylene groups scissoring vibration (δCH_2) (Robinet and Corbeil, 2003).

Raman depth profiling of copper and zinc samples after curing of the oil at 80 °C overnight showed peaks typical of drying oils at 1085, 1303, and 1449 cm^{-1} (Schönemann and Edwards, 2011). Such spectral features were more prominent at the surface of the oil coating than for inner layers, where the signal became more intense and less resolved (Figures 3.9 and 3.10). However, after 60 days of ageing of the samples, the distinction between layers ceased to be clear (Figures S - 28 and S - 29), and fluorescence phenomena were more common, with loss of definition of the characteristic bands of linseed oil. High fluorescence is often observed in combination with the presence of aged organic materials (Casadio et al., 2016), which may hinder the identification of features of interest. Moreover, the added turbidity given by the darkening of the oil upon ageing might constitute an obstacle for depth-profiling approaches that require transparent samples (Bersani et al., 2016).

Therefore, the SORS approach was tested because it is reportedly suitable for more turbid materials, and since fluorescence of the top layer can be suppressed or significantly reduced by using this technique, it allows improved characterisation of inner layers (Casadio et al., 2016). The preliminary analyses performed (Figures S - 30 and S - 31), however, did not provide results that would allow for the monitoring of the evolution of the forming metal soaps along the vertical section of the samples. In particular, similarly to the depth profiling of aged samples, only low-intensity and poorly resolved peaks attributed to the presence of a drying oil could be observed. Therefore, more attempts would be needed to optimise the protocol, exploiting different combinations of parameters and the added flexibility of this method, also given by the possibility to use different objectives (hence working at different magnifications and different distances from the object).

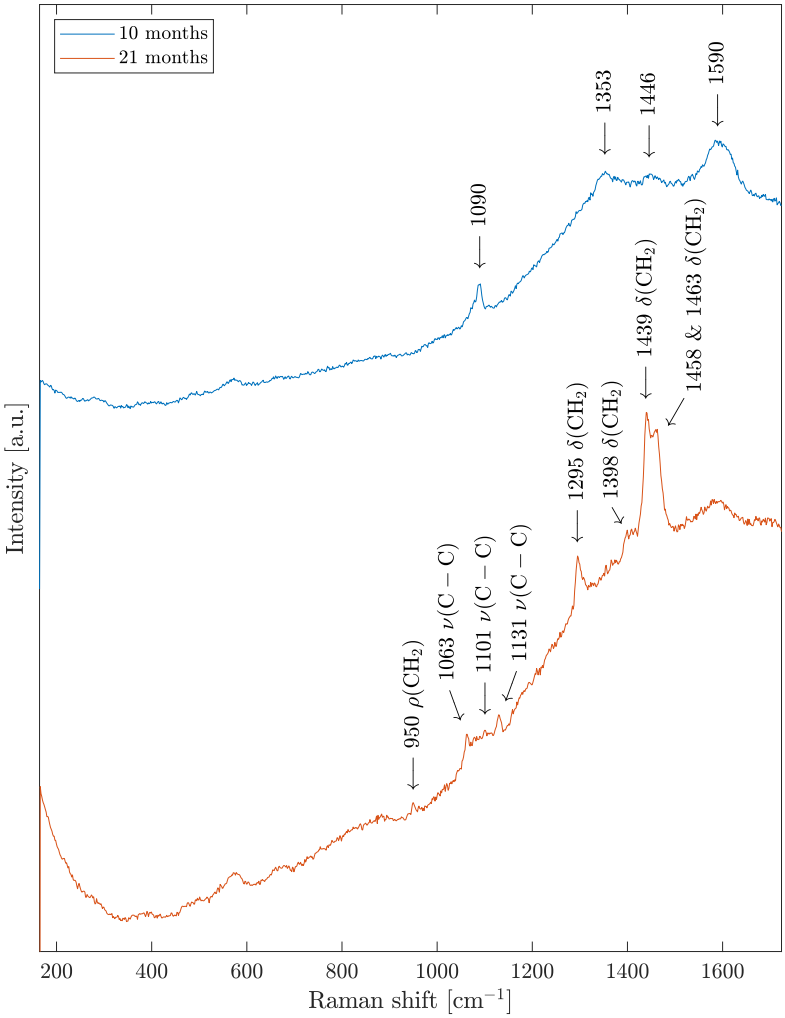

Figure 3.8: Raman spectra of 10- and 21-month-aged linseed oil-coated zinc samples (blue (Zn31) and orange (Zn08) line, respectively). Relevant vibrational modes for zinc soaps are indicated.

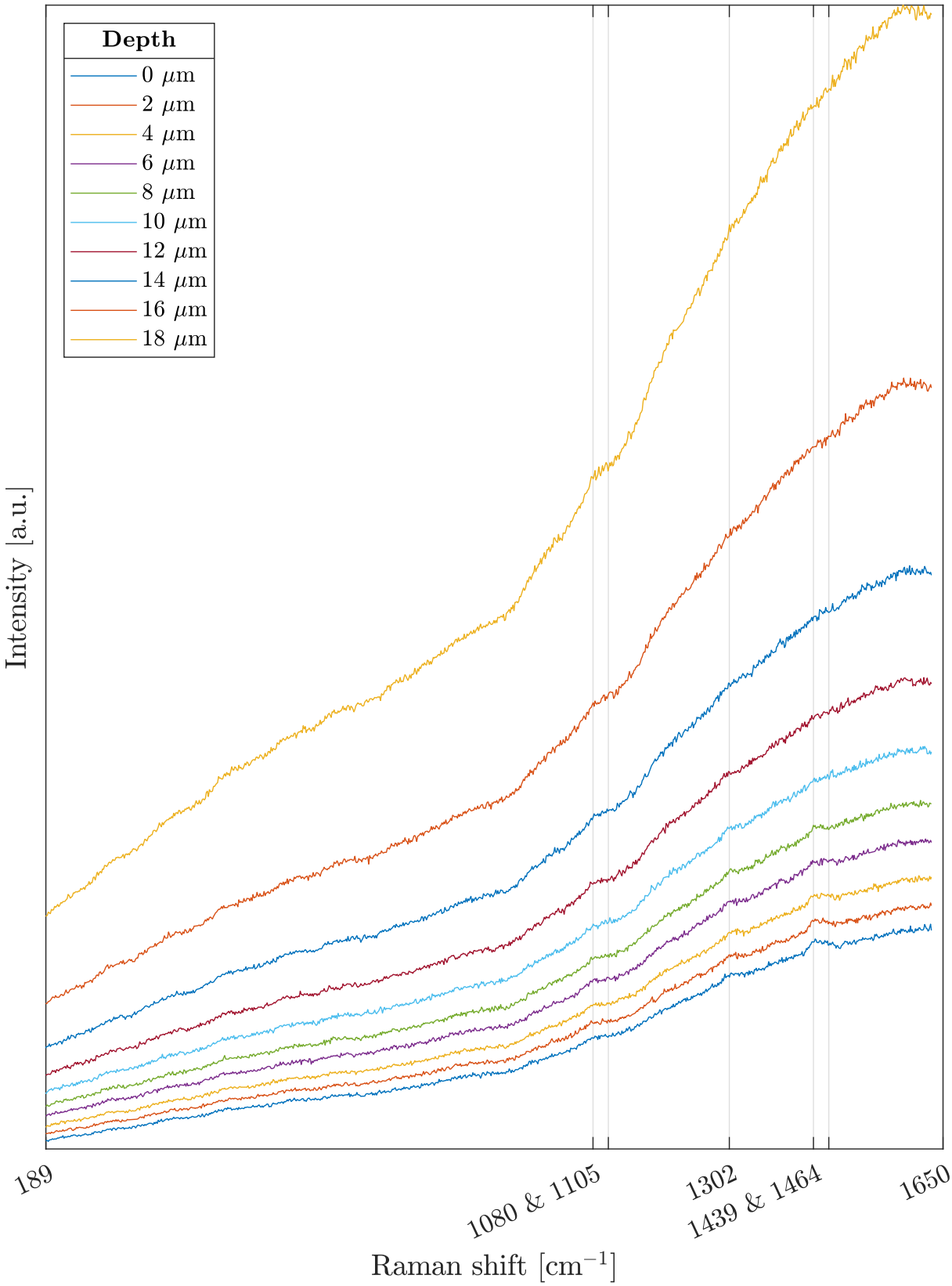

Figure 3.9: Raman depth profiling spectra of a linseed oil-coated copper sample (Cu35) after curing overnight in an oven at 80 °C. The depth goes from 0 µm to 18 µm with respect to the surface of the oil, as indicated in the figure legend.

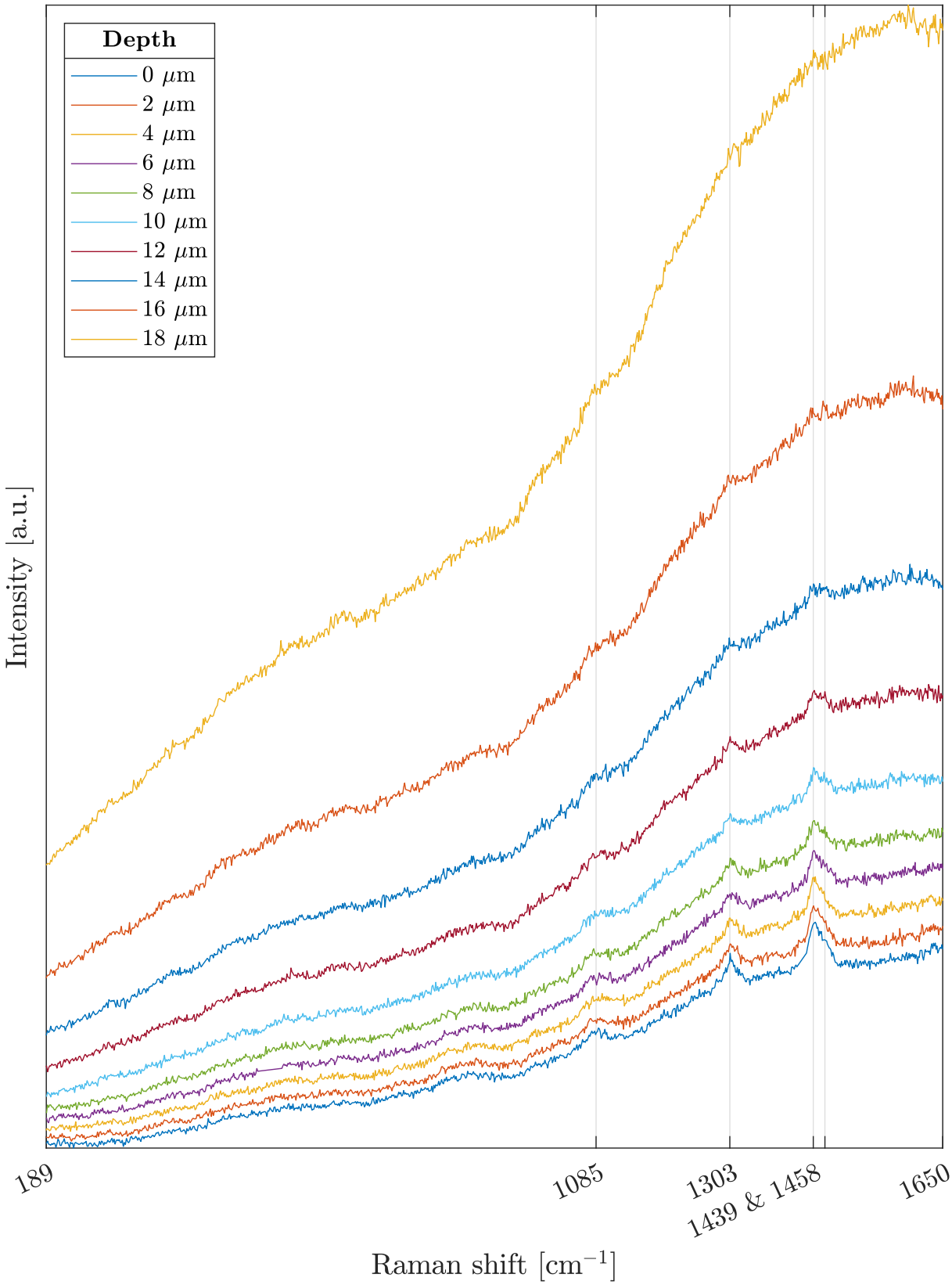

Figure 3.10: Raman depth profiling spectra of a linseed oil-coated zinc sample (Zn32) after curing overnight in an oven at 80 °C. The depth goes from 0 µm to 18 µm with respect to the surface of the oil, as indicated in the figure legend.

3.3.4 X-ray diffractometry

The X-ray diffractograms collected on the uncoated copper and zinc showed the characteristic XRD patterns of the two metals. For the copper sample, these corresponded to a sequence of sharp diffraction peaks at 43.5°, 50.6°, 74.3°, 90.0° and 95.0°, characteristic of the face centred cubic (FCC) copper lattice with Miller indices (111), (200), (220), (311) and (222), respectively (Figure 3.11a) (Maeda et al., 2017). This bulk XRD pattern was dominant in all samples. A band, which broad shape centred at 20° indicated an amorphous compound, suggested the presence of organic material. This was attributed to linseed oil, given its prominent presence for higher coating thicknesses (Figure 3.11a, orange line). By clamping the range of diffraction angles to enhance this region, i.e., $5-30°$ (Figure 3.11b), it was possible to observe the increasing signal intensities at around 7° and 20° as the thickness of the oil coating increased (yellow and orange lines). A peak at 5.9° appeared for the thicker coating, which could not be interpreted at this stage.

For the zinc samples (Figure 3.11c), characteristic signals of the zinc substrates could be identified at 36.5°, 39.2°, 43.5°, 54.6°, 70.3°, 77.4°, 82.2°, 86.7°, 90.1°, and 95.0°, indexed as (002), (100), (101), (102), (103), (004), (112), (201), (104) and (202), respectively (Vourlias, 2020). The overall lower intensity bands corresponding to the oil coating (Figure 3.11d) – compared to the copper samples – is due to the fact that the analysis was performed on overall thinner coating layers. For the thin coating, diffraction peaks at 18.4° and 27.2° were visible. Zinc soaps, and especially zinc palmitate, are reported to have low intensity XRD peaks at compatible angles (Corbeil and Robinet, 2002; Robinet and Corbeil, 2003). However, the relative intensity of the characteristic signals reported in literature does not fully support this conclusion.

The limitations imposed by the equipment utilised could have played a role in the difficulties encountered in the detection and identification of metal soaps. Specifically, the setup only allowed to repeat analyses on the same spot at the centre of the sample, hence the spatial aspects of the distribution of the species could not be investigated. This implies that the probability of finding metal soaps at that specific sample location strongly impacted the results obtained.

For both copper and zinc samples, the monitoring experiment resulted in signal features of the two metals that would stay unchanged for the entire duration of the experiment, i.e., 72 hours (Figure S - 32). Overall, the experiment did not allow us to gain further insights into the presence and nature of metal soaps formed on the samples under study.

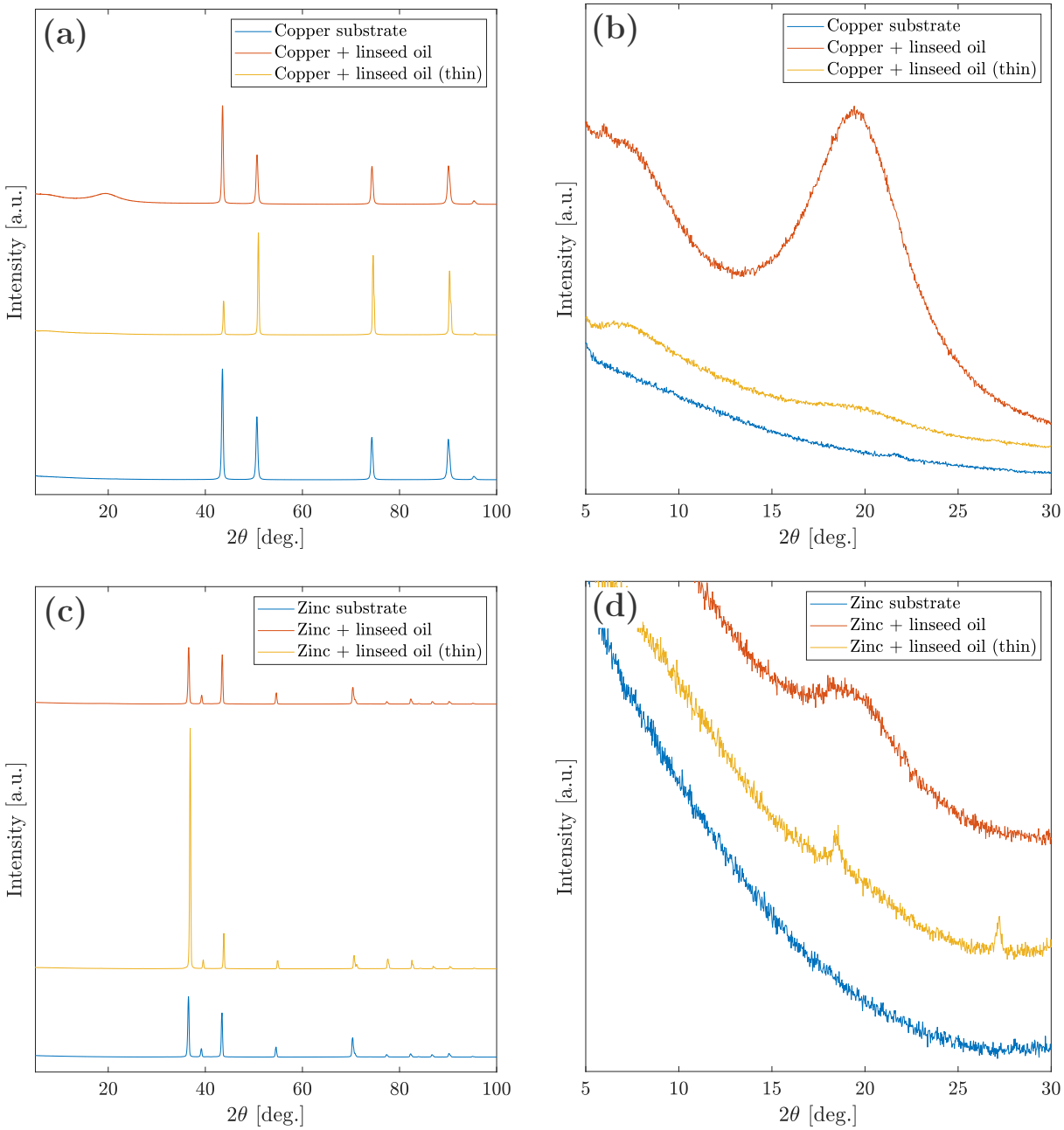

Figure 3.11: X-ray diffractograms for the copper (a, b; Cu31, Cu45, DoE_drop_5) and zinc (c, d; Zn26, Zn46, DoE_drop_6) samples, in their full range of diffraction angles scanned (a, c) and an enlarged region between 5° and 30° (b, d).

3.3.5 Hyperspectral imaging

From the analysis of the spectra, some observations could be made, highlighting differences in the substrate and coating responses in the two ranges of wavelengths considered. In particular, in the visible-near infrared (VNIR) spectral range, it was possible to identify the characteristic reflectance spectra of the copper and zinc bare metals (Shanks et al., 2016; Chebwogen et al., 2020). In the case of copper, this took the shape of an initial slope until 550 nm, followed by a band centred around 600 nm (orange hue of copper), and a second increasing slope that terminates in a plateau after 1000 nm, i.e., outside of the range of wavelengths considered here ($400 - 1000$ nm). For zinc, which colour is silvery-grey, the reflectance curve featured an initial slope until 470 nm, and a slowly decaying trend for higher wavelengths.

It could be observed that, as the thickness of the coating increased ($1 - 25$ μm; blue, orange and purple lines), the relative reflectance values, shape and position of the peaks of the metal support changed. For the copper substrate, the presence of the coating influenced the shape of the signal and its intensity, but it affected its position only marginally (Figure 3.12). In particular, the intensity of the main band at about 600 nm followed an inversely proportional trend with the thickness of the coating, with a simultaneous minor shift towards higher wavelengths (bathochromic (red) shift).

For the zinc, where the colour of the metal was significantly different from that of the coating, a shift in the main band was visible, corresponding to the variation in colour of the coating from yellowish to orange-brownish (bathochromic shift) as the thickness increases (Figure 3.13).

The results obtained suggest that VNIR hyperspectral imaging could be used to indirectly determine the thickness of the oil coating, either from the changes in relative reflectance (copper) or from the shifts in wavelengths observed (zinc).

In the short-wave infrared (SWIR) range, where the oil binder has strong signature spectral features, the characteristic spectrum of a drying oil was observed on the copper sample (Amato et al., 2020), with relative reflectance values increasing with the thickness of the oil coating between $1250 - 2250$ nm (Figure 3.14). Therefore, the SWIR camera could potentially be a complementary tool to the VNIR camera to be employed for direct estimation of the thickness of the oil.

However, from the analysis of the dataset, it was not possible to identify spectral features for the presence of metal soaps in the VNIR and SWIR spectral ranges. In the case of the VNIR camera, this is probably due to the lack of characteristic signals in this range of wavelengths, whereas for the SWIR camera, a reason could also lie in the significant overlap of metal soaps and drying oil signals (Kauffman et al., 2008; Amato et al., 2020; Zuena et al., 2020).

HSI analyses in the middle-wave infrared range of wavelengths would be necessary to shed some clarity on the presence or absence of metal soaps on such samples.

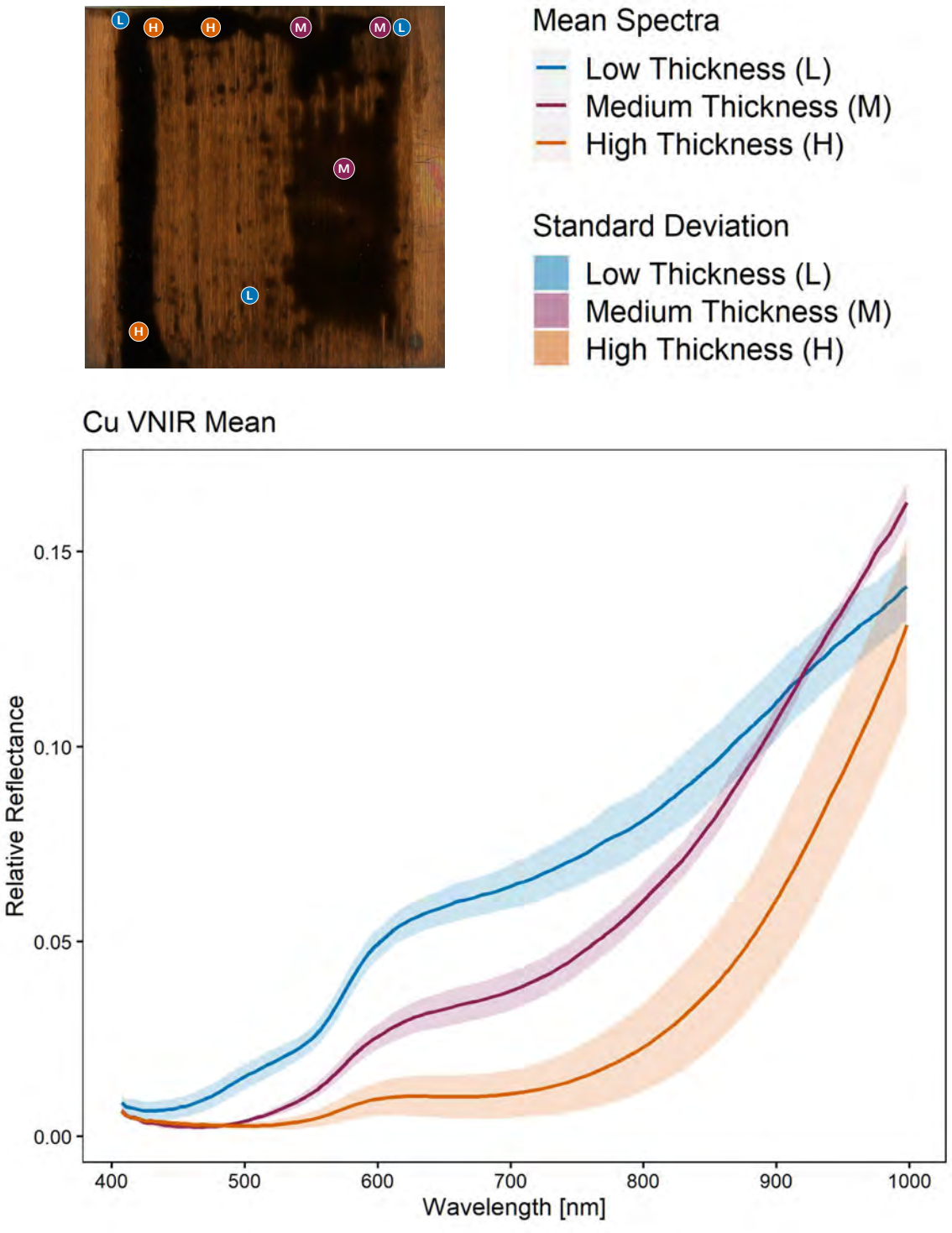

Figure 3.12: VNIR-HSI analysis of a copper sample (Cu09) coated with a non-homogeneous layer of linseed oil. Average relative reflectance spectra obtained from three 20×20 px^2 areas for low ($1 - 5$ µm), medium ($5 - 10$ µm) and high ($10 - 25$ µm) coating thickness, and respective standard deviations are shown.

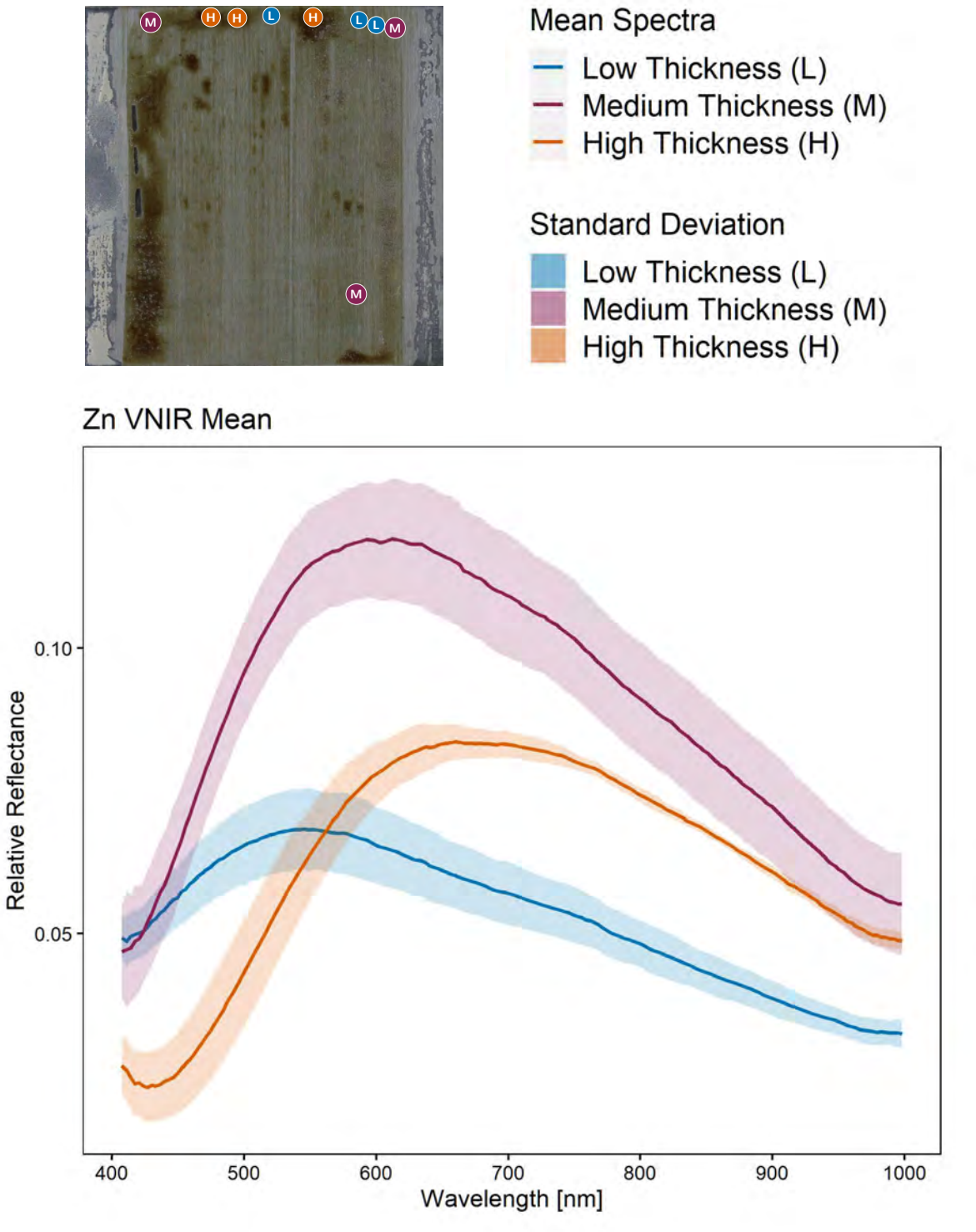

Figure 3.13: VNIR-HSI analysis of a zinc sample (Zn09) coated with a non-homogeneous layer of linseed oil. Average relative reflectance spectra obtained from three 20×20 px^2 areas for low ($1 - 5$ µm), medium ($5 - 10$ µm) and high ($10 - 25$ µm) coating thickness, and respective standard deviations are shown.

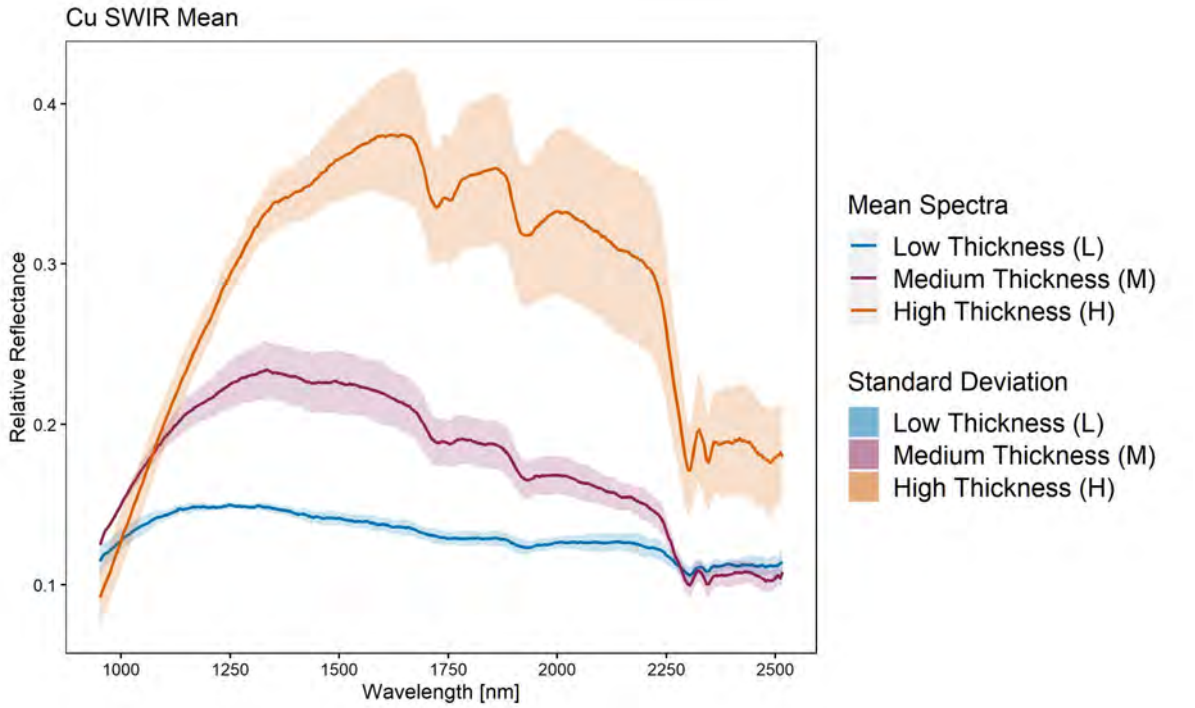

Figure 3.14: SWIR-HSI analysis of the copper sample (Cu09) coated with a non-homogeneous layer of linseed oil (as in Figure 3.12). Average relative reflectance spectra obtained from the three 20×20 px^2 areas for low ($1 - 5$ µm), medium ($5 - 10$ µm) and high ($10 - 25$ µm) coating thickness, and respective standard deviations are shown.

3.3.6 Colorimetry

Spectrocolorimetric data were collected in the range $400 - 700$ nm to complement the information given by the two hyperspectral cameras. By measuring two different copper and zinc brushed samples having inhomogeneous oil coating, similar trends could be observed for the thin ($1 - 5$ μm, blue), medium ($5 - 10$ μm, purple) and thick ($10 - 25$ μm, orange) coating areas. The reflectance spectra of the bare metals are provided for comparison (black) (Figure 3.15). The shape of the curves observed resembled the ones obtained by means of hyperspectral imaging analyses (Figure 3.12 and 3.13). Similarly to what was discussed in paragraph 3.3.5, for copper samples, the intensity of the reflectance signal of the metal decreased as the thickness of the coating increased. For the zinc coupons, this trend holds for the coated samples. However, the reflectance curve of the bare metal differs, possibly due to the lack of yellow-brown reflecting components in the original colour of the zinc substrate.

Bathochromic (red) effects were again visible, especially in the case of the zinc coupons (Figure 3.15b). The bare metal spectra are in fact characterised by a small band at lower wavelengths (~ 420 nm), only showing a slight decrease in intensity until 700 nm, i.e., the samples exhibit significant reflection at all wavelengths, resulting in a silver-grey appearance. Since the increasing thickness of the oil implies less transparent and darker red coatings, the band maxima experiencing bathochromic shifts is consistent behaviour. Copper reflectance spectra showed a small band maximum at about 500 nm, corresponding to a green component, and a significant increase in intensity for wavelengths equal to or greater than 550 nm (yellow, red, dark red, brown), resulting in a green-red-brownish colouration (Figure 3.15b). The appearance of the samples can be observed in Figure 3.12 and 3.13.

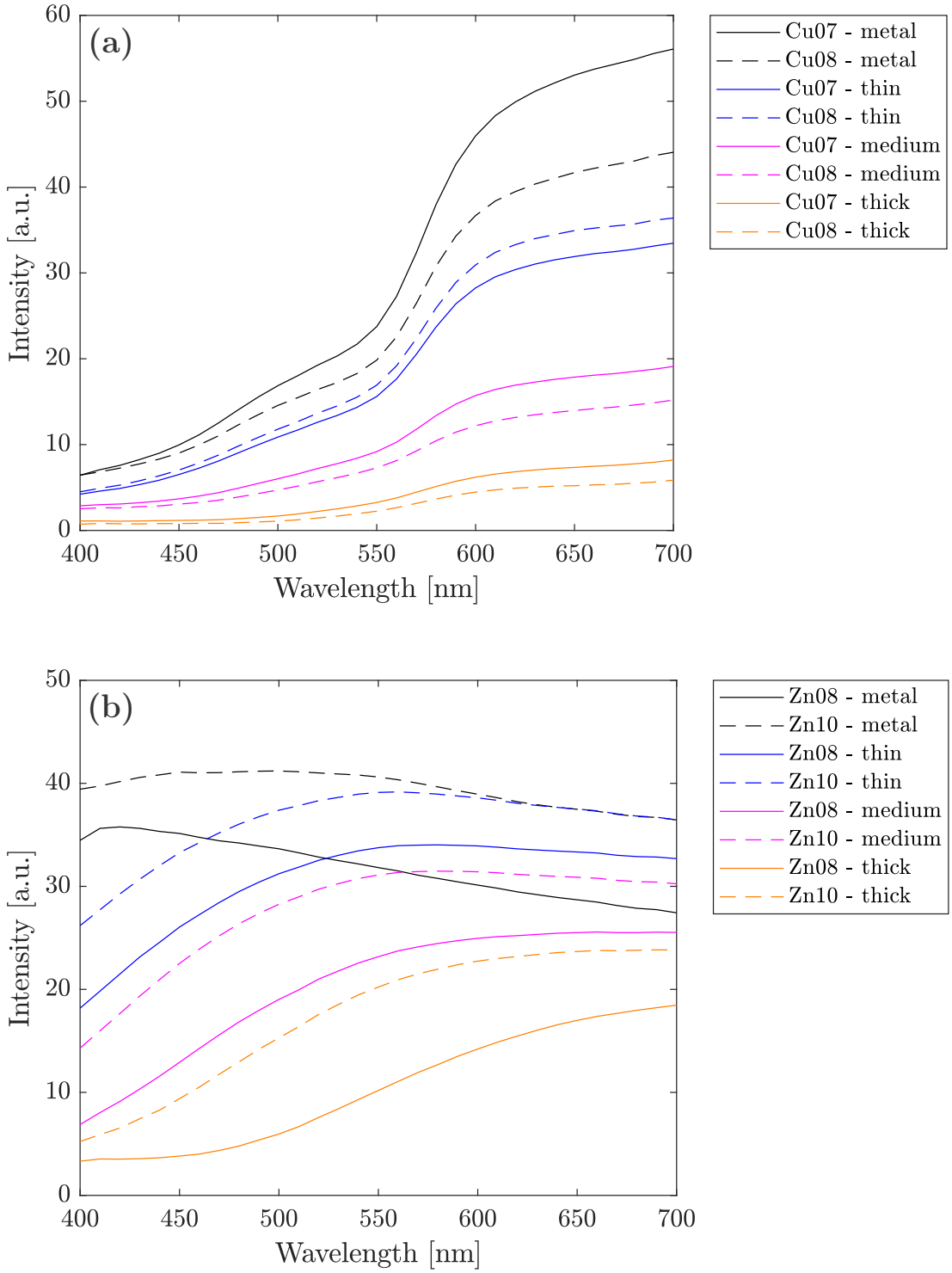

Figure 3.15: Reflectance spectra for copper (a; Cu07, Cu08) and zinc (b; Zn08, Zn10) oil-coated samples, showing decreasing signal for thicker coatings. In the case of zinc samples (b), a small bathochromic shift can be observed due to the prevalence of the oil colouration compared to the metal substrate.

3.3.7 Infrared thermography

A first proof of concept was provided by the analysis of the copper sample that had reacted with added palmitic acid to give the corresponding copper palmitate. As shown in Figure 3.16, both the heating and the cooling phases were characterised by the presence of vertical lines belonging to the brushed surface. However, within the circled area (Figure 3.16), where palmitic acid was deposited, no differences could be noticed compared to the rest of the sample that could hint toward the presence of metal soaps. These were expected to be seen as localised spots emitting heat differently than the metal and the oil bulk materials due to their thermochemical properties given by the ongoing formation and crystallisation process (Vázquez et al., 2015). Since metal soaps were previously identified in this area by FTIR spectroscopy, this behaviour could not be related to the absence of the targeted compounds.

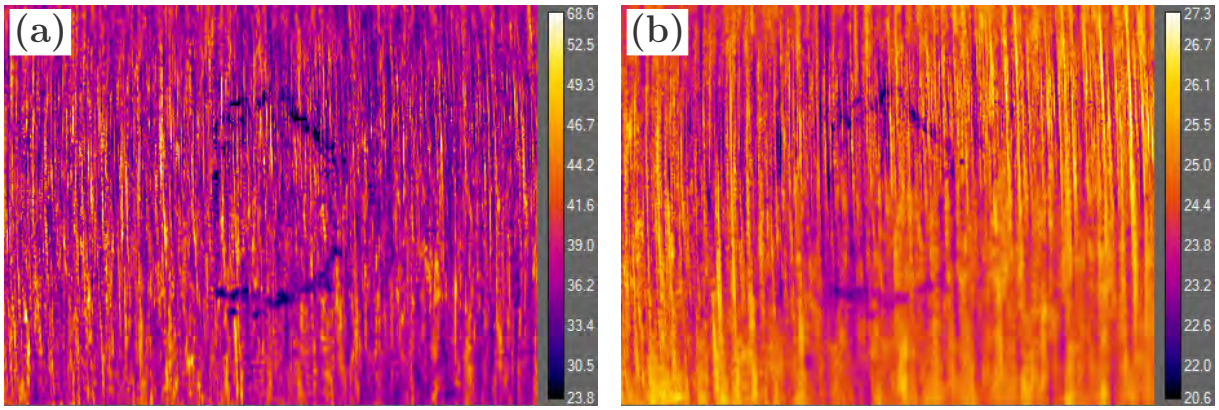

Figure 3.16: Uncoated brushed copper sample (Cu25), where a drop of palmitic acid (1 µL) was deposited to allow the formation of metal soaps (circled area). The thermograms indicate the maximum temperature reached during the heating (left) and the minimum temperature reached during the cooling (right) phases, respectively. Colour bars determine the range of temperatures from lowest (black) to highest (white). The measured area was 100×75 cm^2.

However, more analyses were performed on the copper and zinc samples that had undergone different ageing times (i.e., 5 and 21 months for copper (Figure 3.17), and 5 and 16 months for zinc samples) (Figure 3.18). Colder temperatures (purple-blue areas) corresponded to thicker layers of the oil coating, both during the heating and the cooling phases. This was probably due to the higher emissivity of the oil compared to the metal support (Table 3.2), i.e., poorer heat conductivity of the former (0.15 $\mathrm{W \cdot m^{-1} \cdot K^{-1}}$) compared to the metal (386 and 113 $\mathrm{W \cdot m^{-1} \cdot K^{-1}}$ for copper and zinc, respectively, at 20 °C and 1 bar (Carvill, 1993), in accordance with the exponential relationship described by Atallah, 1966.

In all cases, IR thermograms did not highlight relevant features for this study that might indicate the presence of metal soaps, despite the advanced specifications of the camera used (i.e., macro-lens with enhanced resolution).

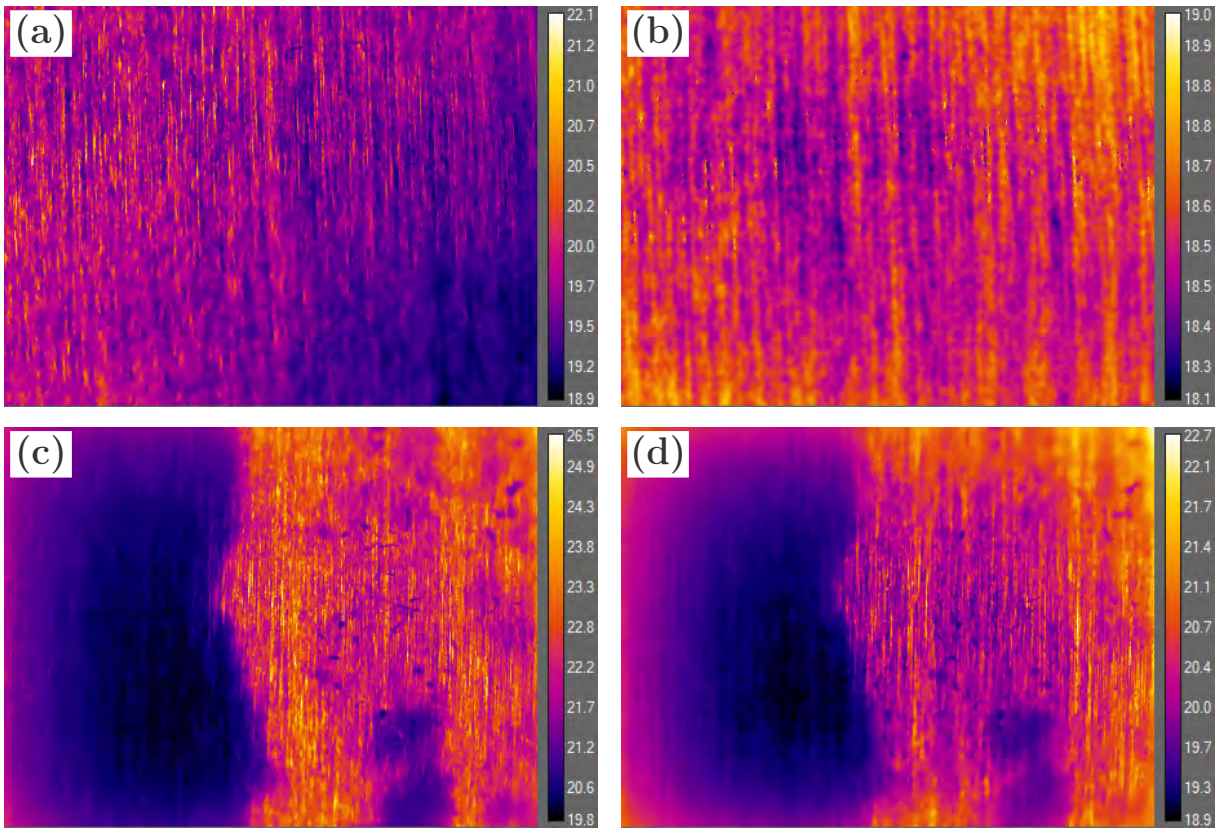

Figure 3.17: Brushed copper samples (a), (b) artificially aged for 30 days at 60 °C and 70 – 80% relative humidity, then naturally aged indoors for a total ageing time of 5 months (Cu35); (c), (d) artificially aged for 30 days at 80 °C and 70 – 80% relative humidity, then naturally aged indoors for a total ageing time of 21 months (Cu07). The thermograms indicate the maximum temperature reached during the heating (left) and minimum temperature reached during the cooling (right) phases, respectively. Colour bars determine the range of temperature from lowest (black) to highest (white). The measured area was 100×75 cm^2.

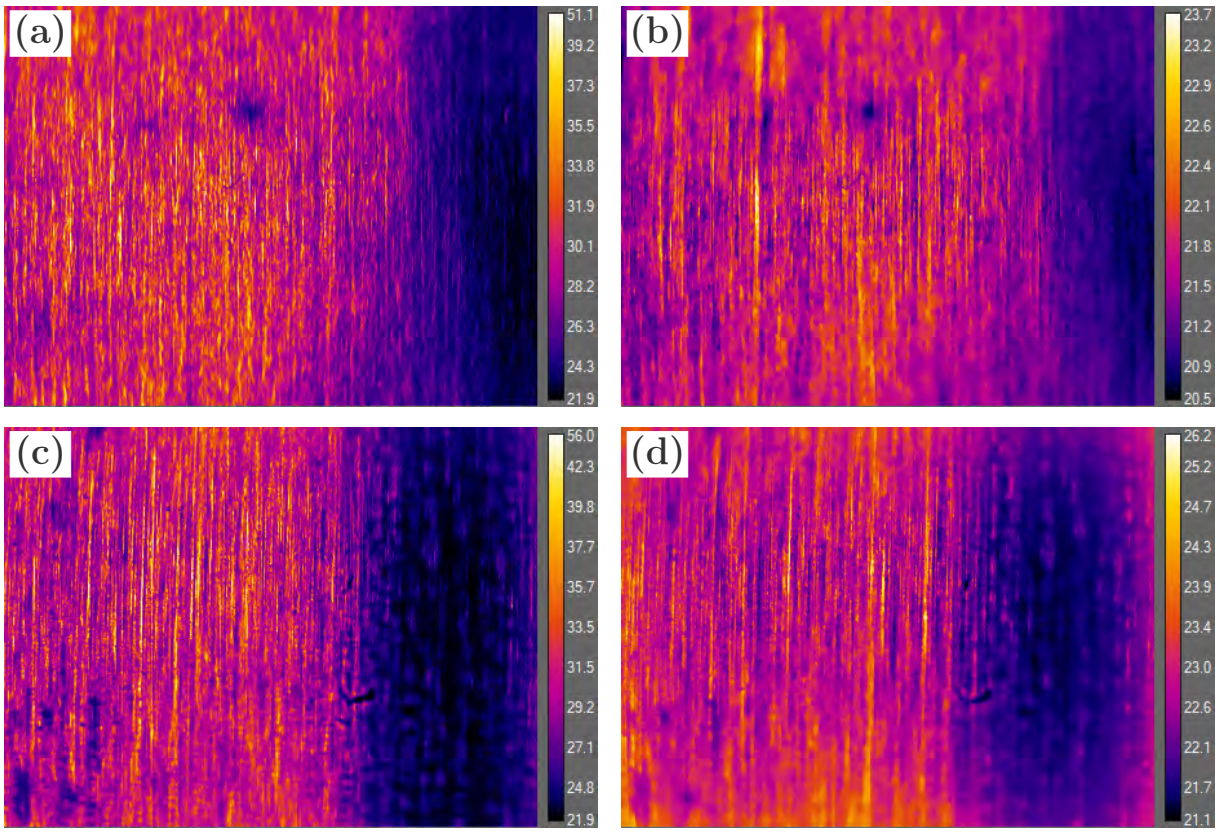

Figure 3.18: Brushed zinc samples coated with linseed oil (a), (b) artificially aged for 30 days at 60 °C and $70-80\%$ relative humidity, then naturally aged indoors for a total ageing time of 5 months (Zn31); (c), (d) artificially aged for 30 days at 80 °C and $70-80\%$ relative humidity, then naturally aged indoors for a total ageing time of 16 months (Zn08). The thermograms indicate the maximum temperature reached during the heating (left) and the minimum temperature reached during the cooling (right) phases, respectively. Colour bars determine the temperature range from lowest (black) to highest (white). The measured area was 100×75 cm^2.

3.4 Conclusions

In this chapter, the question of whether the selected non-destructive imaging and analytical techniques – namely μ-FTIR, μ-Raman, HSI, XRD and IR thermography – are suitable for the study of metal soaps on painted metal objects was addressed. In particular, the focus of the work concerned the ability of such analytical techniques to allow monitoring of the formation of metal soaps.

For the purpose of this research, it was fundamental to assess whether FTIR could be a suitable technique for detecting metal soaps in the presence of metal supports. In order to answer this question, the effects of the surface morphology and, therefore, on the FTIR reflected signal were investigated, showing how thickness, homogeneity and surface finishing are variables affecting the measurement and the detectability of the species of interest. μ-FTIR proved to be determinant in detecting metal soaps on the copper and zinc model samples. The characteristic vibrational bands (νCOO^-) in the range of wavenumbers around 1597 and 1540 cm^{-1} for copper and zinc, respectively and corresponding to the different crystalline and amorphous metal soaps forms were identified and discussed.

Similarly, μ-Raman spectroscopy single-point analyses proved to be appropriate for analysing metal soaps in the presence of a metal support. The identification of the chain length, hence the type of soap (e.g., oleate, stearate, palmitate) was made possible by different bands in the range $1000 - 1450$ cm^{-1}. The results obtained suggest that copper forms monounsaturated soaps (oleate, C18:1), whereas zinc forms soaps with fatty acids having saturated chains preferably (palmitate, C16:0 and stearate, C18:0). Depth profiling and SORS attempts, aiming at investigating the stratigraphic composition of the samples, allowed identification of a drying oil, but did not provide information on the presence or absence of metal soaps along the z-axis using the tested parameters. This result could be due to the physical characteristics of the samples (transparency of the fresh oil coating vs opacity of the aged one, also affected by differences in thickness) and the necessity to use consistent parameters throughout the experiment to allow comparison between different time-point analyses, which might not be appropriate as the chemico-physical characteristics of the samples change. Therefore, more analyses are required to understand the method's full potential. Additionally, the presence of the metal support also represent a challenge, requiring a systematic analysis of the signal and optimisation of the protocol to find the correct analytical parameters.

XRD and HSI also showed problems related to the presence of the metal support. In particular, XRD performed using the traditional setup suffered from the strong signal of the bulk substrate that may mask relevant diffraction patterns of crystalline metal soaps. However, few low-intensity features could be identified at compatible angles to those of metal soaps reported in the literature but differing from them in relative intensity values. The grazing angle method was used to investigate the system further and address the problem of bulk signal encountered. Nevertheless, no evident indications of metal soaps were found within the collected diffractograms. More experiments are needed to tune the parameters that might allow full characterisation of the metal soaps species at the metal-oil interface, as well as testing instruments having a different resolution (e.g., exploiting synchrotron radiation, see Chapter 5).

The detection of metal soaps using HSI cameras in the VNIR and SWIR spectral ranges was unsuccessful due to the absence of identifiable spectral features in these regions. This result could also be attributed to an insufficient resolution of the camera to detect these

few-micrometre-size compounds within a reflective matrix (i.e., the oil binder). However, this technique allowed to make considerations on the thickness of the oil coating according to the metal substrate and confirmed by colorimetric studies that could be extended to different applications in the field of cultural heritage, e.g., the study of unpigmented oil-coated technical objects. For the purpose of this work, the focus was on qualitative monitoring, but this could readily be extended to a full statistical analysis. In future research, the mid-wave infrared (MWIR) range can be explored for the hyperspectral imaging analysis of metal soaps, as MIR reflectance spectra are reported in the literature for these compounds (see Chapter 5).

Together with HSI, XRD and IR thermography were the most sensitive analytical techniques to highlight the differences in the thickness of the coating. For this reason, they could also be used as an indirect indication of the coating thickness by building a calibration curve that could allow comparing shape, intensity and position of the peaks – or bands – with the ones of reference samples.

Bibliography

Amato, S. R., Burnstock, A., and Michelin, A. (2020). A Preliminary Study on the Differentiation of Linseed and Poppy Oil Using Principal Component Analysis Methods Applied to Fiber Optics Reflectance Spectroscopy and Diffuse Reflectance Imaging Spectroscopy. *Sensors* **20**(24): 7125. DOI: 10.3390/s20247125.

Amigo, J. M. (2019). Hyperspectral and multispectral imaging: setting the scene. In: *Data Handling in Science and Technology*. Vol. 32. Elsevier: 3–16. DOI: 10.1016/B978-0-444-63977-6.00001-8.

Atallah, S. (1966). A relationship between emissivity and thermal conductivity of metals. *British Journal of Applied Physics* **17**(4): 573–574. DOI: 10.1088/0508-3443/17/4/120.

Babini, A., George, S., and Hardeberg, J. Y. (2021). Hyperspectral imaging workflow for the acquisition and analysis of stained-glass panels. In: *Proceedings Volume 11784, Optics for Arts, Architecture, and Archaeology VIII*. Online Only, 21-24 June 2021. Ed. by R. Groves and H. Liang: 51. DOI: 10.1117/12.2593735.

Babu, C. R. and Baldev, R. (2003). Study of engineering surfaces using laser-scattering techniques. *Sadhana* **28**(3): 739–761. DOI: 10.1007/BF02706457.

Balaras, C. and Argiriou, A. (2002). Infrared thermography for building diagnostics. *Energy and Buildings* **34**(2): 171–183. DOI: 10.1016/S0378-7788(01)00105-0.

Bersani, D., Conti, C., Matousek, P., Pozzi, F., and Vandenabeele, P. (2016). Methodological evolutions of Raman spectroscopy in art and archaeology. *Analytical Methods* **8**(48): 8395–8409. DOI: 10.1039/C6AY02327D.

Brereton, R. G. (2018). Principal Component Analysis and Unsupervised Pattern Recognition. In: *Chemometrics*. Chichester, UK: John Wiley & Sons Ltd: 163–214. DOI: 10.1002/9781118904695.ch4.

Capobianco, G., Bracciale, M. P., Sali, D., Sbardella, F., Belloni, P., Bonifazi, G., Serranti, S., et al. (2017). Chemometrics approach to FT-IR hyperspectral imaging analysis of degradation products in artwork cross-section. *Microchemical Journal* **132**: 69–76. DOI: 10.1016/j.microc.2017.01.007.

Carvalho, L. d. C. (2022). *Beyond Copper Soaps: Characterization of Copper Corrosion Containing Organics*. SpringerBriefs in Applied Sciences and Technology. Cham: Springer International Publishing. DOI: 10.1007/978-3-030-97892-1.

Carvill, J. (1993). Thermodynamics and heat transfer. In: *Mechanical Engineer's Data Handbook*. Elsevier: 102–145. DOI: 10.1016/B978-0-08-051135-1.50008-X.

Casadio, F., Daher, C., and Bellot-Gurlet, L. (2016). Raman Spectroscopy of cultural heritage Materials: Overview of Applications and New Frontiers in Instrumentation, Sampling Modalities, and Data Processing. *Topics in Current Chemistry* **374**(5): 62. DOI: 10.1007/s41061-016-0061-z.

Casadio, F., Keune, K., Noble, P., Van Loon, A., Hendriks, E., Centeno, S. A., and Osmond, G., eds. (2019). *Metal Soaps in Art: Conservation and Research*. Cultural Heritage Science. Cham: Springer International Publishing. ISBN: 978-3-319-90617-1.

Chebwogen, J., Munyati, O., Hatwaambo, S., Mwamburi, M., and Maghanga, C. (2020). Fabrication and Characterization of Cobalt Pigmented Anodized Zinc for Photocatalytic Application. *International Journal of Thin Films Science and Technology* **9**(2): 127–132. DOI: 10.18576/ijtfst/090206.

Coccato, A., Jehlicka, J., Moens, L., and Vandenabeele, P. (2015). Raman spectroscopy for the investigation of carbon-based black pigments: Investigation of carbon-based black pigments. *Journal of Raman Spectroscopy* **46**(10): 1003–1015. DOI: 10.1002/jrs.4715.

Corbeil, M.-C. and Robinet, L. (2002). X-ray powder diffraction data for selected metal soaps. *Powder Diffraction* **17**(1): 52–60. DOI: 10.1154/1.1431950.

Cucci, C., Webb, E. K., Casini, A., Ginanni, M., Prandi, E., Stefani, L., Vitorino, T., et al. (2019). Short-wave infrared reflectance hyperspectral imaging for painting investigations: A methodological study. *Journal of the American Institute for Conservation* **58**(1): 16–36. DOI: 10.1080/01971360.2018.1543102.

Cutajar, J. D., Babini, A., Deborah, H., Hardeberg, J. Y., Joseph, E., and Frøysaker, T. (2022). Hyperspectral Imaging Analyses of Cleaning Tests on Edvard Munch's Monumental Aula Paintings. *Studies in Conservation*: 1–10. DOI: 10.1080/00393630.2022.2054617.

Dieterle, F., Ross, A., Schlotterbeck, G., and Senn, H. (2006). Probabilistic Quotient Normalization as Robust Method to Account for Dilution of Complex Biological Mixtures. Application in ^{1} H NMR Metabonomics. *Analytical Chemistry* **78**(13): 4281–4290. DOI: 10.1021/ac051632c.

Dooley, K. A., Coddington, J., Krueger, J., Conover, D. M., Loew, M., and Delaney, J. K. (2017). Standoff chemical imaging finds evidence for Jackson Pollock's selective use of alkyd and oil binding media in a famous 'drip' painting. *Analytical Methods* **9**(1): 28–37. DOI: 10.1039/C6AY01795A.

Duchene, S., Detalle, V., Bruder, R., and Sirven, J. (2010). Chemometrics and Laser Induced Breakdown Spectroscopy (LIBS) Analyses for Identification of Wall Paintings Pigments. *Current Analytical Chemistry* **6**(1): 60–65. DOI: 10.2174/157341110790069600.

Filopoulou, A., Vlachou, S., and Boyatzis, S. C. (2021). Fatty Acids and Their Metal Salts: A Review of Their Infrared Spectra in Light of Their Presence in Cultural Heritage. *Molecules* **26**(19): 6005. DOI: 10.3390/molecules26196005.

Fischer, C. and Kakoulli, I. (2006). Multispectral and hyperspectral imaging technologies in conservation: current research and potential applications. *Studies in Conservation* **51** (sup1): 3–16. DOI: 10.1179/sic.2006.51.Supplement-1.3.

Forney, C. F. and Brandl, D. G. (1992). Control of Humidity in Small Controlled-environment Chambers using Glycerol-Water Solutions. *HortTechnology* **2**(1): 52–54. DOI: 10.21273/HORTTECH.2.1.52.

Foster, D. H. and Amano, K. (2019). Hyperspectral imaging in color vision research: tutorial. *Journal of the Optical Society of America A* **36**(4): 606. DOI: 10.1364/JOSAA.36.000606.

Garrappa, S., Kočí, E., Švarcová, S., Bezdička, P., and Hradil, D. (2020). Initial stages of metal soaps' formation in model paints: The role of humidity. *Microchemical Journal* **156**: 104842. DOI: 10.1016/j.microc.2020.104842.

Geladi, P., Swerts, J., and Lindgren, F. (1994). Multiwavelength microscopic image analysis of a piece of painted chinaware: Classification and regression. *Chemometrics and*

Intelligent Laboratory Systems **24**(2): 145–167. DOI: 10.1016/0169-7439(94)00035-2.

George, S., Hardeberg, J. Y., Linhares, J., MacDonald, L., Montagner, C., Nascimento, S., Picollo, M., et al. (2018). A Study Of Spectral Imaging Acquisition And Processing For Cultural Heritage. In: *Digital Techniques for Documenting and Preserving Cultural Heritage*. Ed. by A. Bentkowska-Kafel and L. MacDonald. Arc Humanities Press. DOI: 10.2307/j.ctt1xp3w16.15.

El-Gindy, A. and Hadad, G. M. (2012). Chemometrics in Pharmaceutical Analysis: An Introduction, Review, and Future Perspectives. *Journal of AOAC INTERNATIONAL* **95**(3): 609–623. DOI: 10.5740/jaoacint.SGE_El-Gindy.

Gonzalez, V., Loon, A. van, WT Price, S., Noble, P., and Keune, K. (2020). Synchrotron micro-XRD and micro-XRD-CT reveal newly formed lead–sulfur compounds in Old Master paintings. *Journal of Analytical Atomic Spectrometry* **35**(10): 2267–2273. DOI: 10.1039/D0JA00169D.

Grillini, F., Thomas, J.-B., and George, S. (2021). Comparison of Imaging Models for Spectral Unmixing in Oil Painting. *Sensors* **21**(7): 2471. DOI: 10.3390/s21072471.

Grinzato, E. (2012). IR Thermography Applied to the Cultural Heritage Conservation. In: *18th World Conference on Nondestructive Testing*. Durban, 16-20 April 2012.

Hanson, B. A. (2022). *ChemoSpec: Exploratory Chemometrics for Spectroscopy*. Version 6.1.3.

Héberger, K. (2008). Chemoinformatics—multivariate mathematical–statistical methods for data evaluation. In: *Medical Applications of Mass Spectrometry*. Elsevier: 141–169. ISBN: 978-0-444-51980-1.

Hermans, J. (2017). *Metal soaps in oil paint: structure, mechanisms and dynamics*. PhD thesis. Vianen ut: Proefschriftmaken.

Hermans, J., Zuidgeest, L., Iedema, P., Woutersen, S., and Keune, K. (2021). The kinetics of metal soap crystallization in oil polymers. *Physical Chemistry Chemical Physics* **23**(39): 22589–22600. DOI: 10.1039/D1CP03479K.

Izzo, F. C., Kratter, M., Nevin, A., and Zendri, E. (2021). A Critical Review on the Analysis of Metal Soaps in Oil Paintings. *ChemistryOpen* **10**(9): 904–921. DOI: 10.1002/open.202100166.

Jolliffe, I. T. and Cadima, J. (2016). Principal component analysis: a review and recent developments. *Philosophical Transactions of the Royal Society A: Mathematical, Physical and Engineering Sciences* **374**(2065): 20150202. DOI: 10.1098/rsta.2015.0202.

Kauffman, J. F., Tumuluri, V., Guo, C., Spencer, J. A., Doub, W. H., Nichols, G. A., Randle, S. R., et al. (2008). Near Infrared Spectroscopy of Magnesium Stearate Hydrates and Multivariate Calibration of Pseudopolymorph Composition. *Journal of Pharmaceutical Sciences* **97**(7): 2757–2767. DOI: 10.1002/jps.21006.

Khaksari, K., Nguyen, T., Hill, B. Y., Perrault, J., Gorti, V., Blick, E., Gonzalez Cano, T., et al. (2021). Review of the efficacy of infrared thermography for screening infectious diseases with applications to COVID-19. *Journal of Medical Imaging* **8** (S1). DOI: 10.1117/1.JMI.8.S1.010901.

Kleiman, L. (2003). Hyperspectral imaging: the colorimetric high ground. In: *Proceedings Volume 5008, Color Imaging VIII: Processing, Hardcopy, and Applications*. Santa Clara, 20-24 January 2003. Ed. by R. Eschbach and G. G. Marcu: 249. DOI: 10.1117/12.475439.

Korukçu, M. and Kilic, M. (2009). The usage of IR thermography for the temperature measurements inside an automobile cabin. *International Communications in Heat and Mass Transfer* **36**(8): 872–877. DOI: 10.1016/j.icheatmasstransfer.2009.04.010.

Li, Q., He, X., Wang, Y., Liu, H., Xu, D., and Guo, F. (2013). Review of spectral imaging technology in biomedical engineering: achievements and challenges. *Journal of Biomedical Optics* **18**(10): 100901. DOI: 10.1117/1.JBO.18.10.100901.

Lichtblau, D., Strlič, M., Trafela, T., Kolar, J., and Anders, M. (2008). Determination of mechanical properties of historical paper based on NIR spectroscopy and chemometrics – a new instrument. *Applied Physics A* **92**(1): 191–195. DOI: 10.1007/s00339-008-4479-1.

Lieber, C. A. and Mahadevan-Jansen, A. (2003). Automated Method for Subtraction of Fluorescence from Biological Raman Spectra. *Applied Spectroscopy* **57**(11): 1363–1367. DOI: 10.1366/000370203322554518.

Luna, A. S. and Gois, J. S. de (2018). Application of Chemometric Methods Coupled With Vibrational Spectroscopy for the Discrimination of Plant Cultivars and to Predict Physicochemical Properties Using R. In: *Comprehensive Analytical Chemistry*. Vol. 80. Elsevier: 165–194. DOI: 10.1016/bs.coac.2018.03.008.

Maeda, M. Y., Quintero, J. J. H., Izumi, M. T., Hupalo, M. F., and Cintho, O. M. (2017). Study of Cryogenic Rolling of FCC Metals with Different Stacking Fault Energies. *Materials Research* **20** (suppl 2): 716–721. DOI: 10.1590/1980-5373-mr-2017-0054.

Manfredi, M., Barberis, E., Aceto, M., and Marengo, E. (2017). Non-invasive characterization of colorants by portable diffuse reflectance infrared Fourier transform (DRIFT) spectroscopy and chemometrics. *Spectrochimica Acta Part A: Molecular and Biomolecular Spectroscopy* **181**: 171–179. DOI: 10.1016/j.saa.2017.03.039.

Marini, F., ed. (2013). *Chemometrics in food chemistry*. 1st ed. Data handling in science and technology volume 28. Amsterdam ; Boston: Elsevier. ISBN: 978-0-444-59528-7.

Ogino, K. and Saito, T. (1977). X-Ray Diffraction Studies of the Metal Soaps of Fatty Acids of Odd Carbon Numbers. *Bulletin of the Chemical Society of Japan* **50**(6): 1623–1624. DOI: 10.1246/bcsj.50.1623.

Otero, V., Sanches, D., Montagner, C., Vilarigues, M., Carlyle, L., Lopes, J. A., and Melo, M. J. (2014). Characterisation of metal carboxylates by Raman and infrared spectroscopy in works of art: Characterisation of metal carboxylates by Raman and infrared spectroscopy in works of art. *Journal of Raman Spectroscopy* **45**(11): 1197–1206. DOI: 10.1002/jrs.4520.

Peris-Díaz, M. D., Łydżba-Kopczyńska, B., and Sentandreu, E. (2018). Raman spectroscopy coupled to chemometrics to discriminate provenance and geological age of amber. *Journal of Raman Spectroscopy* **49**(5): 842–851. DOI: 10.1002/jrs.5357.

Perpetuini, D., Filippini, C., Cardone, D., and Merla, A. (2021). An Overview of Thermal Infrared Imaging-Based Screenings during Pandemic Emergencies. *International Journal of Environmental Research and Public Health* **18**(6): 3286. DOI: 10.3390/ijerph18063286.

Picollo, M., Cucci, C., Casini, A., and Stefani, L. (2020). Hyper-Spectral Imaging Technique in the Cultural Heritage Field: New Possible Scenarios. *Sensors* **20**(10): 2843. DOI: 10.3390/s20102843.

R Core Team (2022). *R: A Language and Environment for Statistical Computing*. Version 2022. Vienna, Austria.

Rao, C. R. (1964). The use and interpretation of principal component analysis in applied research. *Sankhyā: The Indian Journal of Statistics*. Series A: 329–358.

Raza, A., Dumortier, D., Jost-Boissard, S., Cauwerts, C., and Dubail, M. (2022). Accuracy of Hyperspectral Imaging Systems for Color and Lighting Research. *LEUKOS*: 1–19. DOI: 10.1080/15502724.2022.2067866.

Robinet, L. and Corbeil, M.-C. (2003). The Characterization of Metal Soaps. *Studies in Conservation* **48**(1): 23–40. DOI: 10.1179/sic.2003.48.1.23.

Rousaki, A., Vázquez, C., Aldazábal, V., Bellelli, C., Carballido Calatayud, M., Hajduk, A., Vargas, E., et al. (2017). The first use of portable Raman instrumentation for the *in situ* study of prehistoric rock paintings in Patagonian sites: First use of portable Raman spectroscopy in Patagonian sites. *Journal of Raman Spectroscopy* **48**(11): 1459–1467. DOI: 10.1002/jrs.5107.

Sakata, O. and Nakamura, M. (2013). Grazing Incidence X-Ray Diffraction. In: *Surface Science Techniques*. Ed. by G. Bracco and B. Holst. Vol. 51. Berlin, Heidelberg: Springer Berlin Heidelberg: 165–190. DOI: 10.1007/978-3-642-34243-1_6.

Salvadó, N., Butí, S., Pradell, T., Beltran, V., Cinque, G., and Juanhuix, J. (2019). Identification and Distribution of Metal Soaps and Oxalates in Oil and Tempera Paint Layers in Fifteenth-Century Altarpieces Using Synchrotron Radiation Techniques. In: *Metal Soaps in Art*. Ed. by F. Casadio, K. Keune, P. Noble, A. Van Loon, E. Hendriks, S. A. Centeno, and G. Osmond. Cham: Springer International Publishing: 195–210. DOI: 10.1007/978-3-319-90617-1_11.

Santos, H. T. L. dos, Oliveira, A. M. de, Melo, P. G. de, Freitas, W., and Freitas, A. P. R. de (2013). Chemometrics: Theory and Application. In: *Multivariate Analysis in Management, Engineering and the Sciences*. Ed. by L. Freitas. InTech. DOI: 10.5772/53866.

Schindelin, J., Arganda-Carreras, I., Frise, E., Kaynig, V., Longair, M., Pietzsch, T., Preibisch, S., et al. (2012). Fiji: an open-source platform for biological-image analysis. *Nature Methods* **9**(7): 676–682. DOI: 10.1038/nmeth.2019.

Schönemann, A. and Edwards, H. G. M. (2011). Raman and FTIR microspectroscopic study of the alteration of Chinese tung oil and related drying oils during ageing. *Analytical and Bioanalytical Chemistry* **400**(4): 1173–1180. DOI: 10.1007/s00216-011-4855-0.

Sciutto, G., Oliveri, P., Prati, S., Quaranta, M., Bersani, S., and Mazzeo, R. (2012). An advanced multivariate approach for processing X-ray fluorescence spectral and hyperspectral data from non-invasive in situ analyses on painted surfaces. *Analytica Chimica Acta* **752**: 30–38. DOI: 10.1016/j.aca.2012.09.035.

Shanks, K., Senthilarasu, S., and Mallick, T. K. (2016). Optics for concentrating photovoltaics: Trends, limits and opportunities for materials and design. *Renewable and Sustainable Energy Reviews* **60**: 394–407. DOI: 10.1016/j.rser.2016.01.089.

Silvennoinen, R., Peiponen, K.-E., and Muller, K. (2008). Light reflection from a rough surface. In: *Specular Gloss*. Elsevier: 53–77. DOI: 10.1016/B978-008045314-9.50007-4.

Tomita, K. and Chew, M. Y. L. (2022). A Review of Infrared Thermography for Delamination Detection on Infrastructures and Buildings. *Sensors* **22**(2): 423. DOI: 10.3390/s22020423.

Trafela, T., Strlič, M., Kolar, J., Lichtblau, D. A., Anders, M., Mencigar, D. P., and Pihlar, B. (2007). Nondestructive Analysis and Dating of Historical Paper Based on IR Spectroscopy and Chemometric Data Evaluation. *Analytical Chemistry* **79**(16): 6319–6323. DOI: 10.1021/ac070392t.

Vandenabeele, P. (2013). *Practical Raman spectroscopy: an introduction*. The Atrium, Southern Gate, Chichester, West Sussex, United Kingdom: Wiley. ISBN: 978-0-470-68319-4.

Vandenabeele, P., Conti, C., Rousaki, A., Moens, L., Realini, M., and Matousek, P. (2017). Development of a Fiber-Optics Microspatially Offset Raman Spectroscopy Sensor for Probing Layered Materials. *Analytical Chemistry* **89**(17): 9218–9223. DOI: 10.1021/acs.analchem.7b01978.

Vázquez, P., Thomachot-Schneider, C., Mouhoubi, K., Fronteau, G., Gommeaux, M., Benavente, D., Barbin, V., et al. (2015). Infrared thermography monitoring of the NaCl crystallisation process. *Infrared Physics & Technology* **71**: 198–207. DOI: 10.1016/j.infrared.2015.03.013.

Viguerie, L. de, Payard, P., Portero, E., Walter, P., and Cotte, M. (2016). The drying of linseed oil investigated by Fourier transform infrared spectroscopy: Historical recipes and influence of lead compounds. *Progress in Organic Coatings* **93**: 46–60. DOI: 10.1016/j.porgcoat.2015.12.010.

Visco, G., Plattner, S. H., Guida, G., Ridolfi, S., and Gigante, G. E. (2015). Rings or daggers, axes or fibulae have a different composition? A multivariate study on Central Italy bronzes from eneolithic to early iron age. *Chemistry Central Journal* **9**(1): 15. DOI: 10.1186/s13065-015-0090-7.

Vold, R. D. and Hattiangdi, G. S. (1949). Characterization of Heavy Metal Soaps by X-Ray Diffraction. *Industrial & Engineering Chemistry* **41**(10): 2311–2320. DOI: 10.1021/ie50478a056.

Vourlias, G. (2020). Application of X-rays Diffraction for Identifying Thin Oxide Surface Layers on Zinc Coatings. *Coatings* **10**(10): 1005. DOI: 10.3390/coatings10101005.

Wertz, J. H., McClelland, A. A., Mayer, D. D., and Knipe, P. (2022). Modeling Chemical Tests and Fiber Identification of Paper Materials Using Principal Component Analysis and Specular Reflection FTIR Data. *Heritage* **5**(3): 1960–1973. DOI: 10.3390/heritage5030102.

Wickham, H. (2016). *ggplot2: Elegant Graphics for Data Analysis*. 2nd ed. Use R! Cham: Springer International Publishing : Imprint: Springer. DOI: 10.1007/978-3-319-24277-4.

Zuena, M., Buemi, L. P., Stringari, L., Legnaioli, S., Lorenzetti, G., Palleschi, V., Nodari, L., et al. (2020). An integrated diagnostic approach to Max Ernst's painting materials in his Attirement of the Bride. *Journal of Cultural Heritage* **43**: 329–337. DOI: 10.1016/j.culher.2019.10.010.

CHAPTER 4

Understanding the formation of metal soaps

on oil-coated copper and zinc substrates

Adapted from Russo S., Brambilla L., Thomas J.B., and Joseph E. 2022. 2D Chemical Imaging for the Monitoring of the Formation of Metal Soaps on Oil-Painted Copper and Zinc Substrates. In: *Preventive Conservation, Predictive Analysis and Environmental Monitoring* E. Bosco, L. Fuster-Lopez, and A. Perles, eds. Springer [submitted].

Russo S., Brambilla L., Thomas J.B., and Joseph E. Understanding the formation of metal soaps on painted metal objects through the complementary use of μFTIR, OCT and LIBS analyses [in preparation].

Painted metal artworks are composite objects made of a metal support and a paint layer. As such, the approach to their conservation requires understanding the deterioration mechanisms of the different materials alone and in combination. In the case of oil-painted metal objects, corrosion of the metal support and hydrolysis of the oil film exerted by high or fluctuating relative humidity and temperature levels can be concerning for the preservation of the object as a whole. Furthermore, the metal ions and free fatty acids resulting from these degradation processes can form metal carboxylates and lead to loss of adhesion of the paint layer, delamination, and appearance of protrusions on the surface of the painting.

This chapter proposes the use of Fourier transform infrared micro-spectroscopy (μ-FTIR) for 2D chemical imaging of metal soaps formed on artificially aged oil-coated copper and zinc model samples. This study aims to understand the early stages of degradation of painted metals while identifying critical variables that may affect the reaction of formation of metal soaps, such as fatty acids concentration and ageing time. Moreover, in order to investigate the metal-oil interface non-invasively, spectral domain optical coherence tomography (SD-OCT) was employed to provide information on the location of metal soaps within the stratigraphy of the samples. This was a necessary step also in light of the results of prior attempts using a more traditional approach (i.e., cross sections, see Chapter 2, p. 49). The information provided by the SD-OCT

ivenstigation was complemented by Laser-induced breakdown spectroscopy (LIBS) analyses.

The FTIR semi-quantitative chemical maps showed that the metal soap formation could be traced by observing the modifications in shape and intensity of the bands in the $1650 - 1500$ cm^{-1} spectral range, corresponding to the asymmetric stretching vibration of the carboxylate group ($\nu_a COO^-$). These spectral features are affected by chemical and physical factors, such as the chemical structure of the metal complexes formed and the thickness of the paint layer. A derivative approach for processing the chemical maps to highlight the presence, evolution, and distribution of species of interest is discussed. SD-OCT allowed investigation of the interface between the metal support and the oil coating, suggesting that metal soaps form within the first paint layers (few microns), in close contact with the metal support. The migration of crystalline species to the surface of the coating was not observed within the experiment time.

The experimental setup proposed has proved effective for monitoring representative areas of model samples of reduced size (here, 6×6 cm^2). It could potentially be utilised to assess the conditions of small painted metal artefacts in museum collections. However, further experiments must be carried out to validate some of the hypotheses formulated, appraise the role of relative humidity on the degradation patterns, and provide a comprehensive explanation of the chemical reactions that bring to the early formation of metal soaps and subsequent degradation of the painted metal objects.

4.1 Introduction

Metals, particularly copper, lead, iron, and zinc, have historically been common supports for painted artworks due to their unique technical and aesthetic properties in comparison to canvas and wood (Pavlopoulou and Watkinson, 2006; Terenzi et al., 2006). Their use spread during the 16$^{\text{th}}$ century, with the establishment of the Mannerism tradition all around Europe, when the search for new aesthetical values and artistic virtuosity resulted in the use of thin laminated metal sheets as supports for oil paintings of different shapes and dimensions (Terenzi et al., 2006; Fuster-Lopéz, 2017). During this period, metal supports stimulated the artists' curiosity because they are durable and non-oil retentive. Copper was the first material utilised for artistic expression due to its ductility. It could be obtained as a smooth, red surface, having similar aesthetical characteristics to some preparatory layers of traditional paintings on canvas (Terenzi et al., 2006).

The practice of painting on metal did not extend after the latter half of the 17$^{\text{th}}$ century in Italy and the Netherlands, and the 18$^{\text{th}}$ century in Spain and France (Komanecky, 1999). Only during the 20$^{\text{th}}$ century did artists such as Frida Kahlo, David Smith, and John Chamberlain, amongst others, bring oil paint on metal support back into vogue in creating their masterpieces. These were 3D objects, usually consisting of an assembly of found metal offcuts, then painted with oil formulations, following the experimentation trends typical of some contemporary art movements of the 1960s – 1980s (Sasse, 2005). In contrast

with the 16th century artists' belief, from a conservation point of view, such artefacts are not immune to degradation and present several challenges and unique behaviours. In particular, the bendability of the support can induce mechanical stress on the paint layers. In addition, their composite nature can result in a chain of degradation reactions occurring independently at the metal surface, in the paint layer, and at the interface between the two systems. Of such degradation processes, this chapter focuses on the formation of metal soaps.

Metal soaps are a class of water-insoluble organic salts (carboxylates, R-COOM) that form ubiquitously on artworks whenever a reactive metal ion (M^{n+}) is in close contact with fatty acids (R-COOH), which typically come from an oil binder (Casadio et al., 2019). Many scientific studies have been conducted in the past couple of decades to investigate the technical aspects of the formation of such compounds (Rimer et al., 1999; Mecklenburg et al., 2013; Hermans et al., 2015; Hermans et al., 2016b; Gabrieli et al., 2017; Banti et al., 2018; Hermans et al., 2018; Baij et al., 2019; Osmond, 2019; Hermans et al., 2019; Garrappa et al., 2020; Hermans and Helwig, 2020). These spaced from the initial chemical reaction (Hermans et al., 2018; Baij et al., 2019; Casadio et al., 2019, p. 47; Garrappa et al., 2020), nucleation, aggregation, and migration mechanism of the crystalline species towards the surface of the painting (Hermans et al., 2015; Hermans et al., 2016b; Hermans et al., 2019; Hermans and Helwig, 2020), to the subsequent implications for the preservation of the objects (Rimer et al., 1999; Gabrieli et al., 2017; Banti et al., 2018). Some of these studies addressed aspects related to early-stage formation, where the nucleation and transport of zinc soaps and fatty acids were investigated within the polymerised oil matrix (Hermans et al., 2018); others dealt with metal soaps crystallisation and migration mechanism in selected artworks (Rimer et al., 1999) or in representative model samples (Mecklenburg et al., 2013), and their effects on the durability of oil paintings.

It was found that, for zinc-oxide-based oil formulations, zinc complexes form immediately when the pigment is mixed with the binder to create the paint (Izzo et al., 2021). Other studies focused on the pigment-binder interaction in the presence of different metal ions, showing how, for copper-rich pigments, the carboxylates could be mainly detected within azurite $Cu_3(CO_3)_2(OH)_2$ layers that had undergone humidity-driven conversion into malachite $CuCO_3 \cdot Cu(OH)_2$ (Mazzeo et al., 2008). In all cases, localisation of the metal soaps within the different layers was fundamental. Imaging techniques are particularly suitable for studying complex systems since they allow association between spatial information and chemical characteristics of the samples. They are usually non-destructive techniques (NDTs) that allow the elucidation of the degradation processes occurring on cultural heritage objects. A combination of well-chosen NDTs can also provide the in-depth information necessary to carry out conservation-restoration treatments (Ricca et al., 2021).

Most of the prior studies on metal soaps formation on painted artworks relied on using Fourier Transform Infrared micro-spectroscopy (μ-FTIR). 2D chemical imaging μ-FTIR is the most employed technique to study metal soaps in traditional paintings due to its versatility. It can be used both to characterise metal soaps and generate chemical maps to understand the relative distribution of the carboxylates (Gabrieli et al., 2017), allowing comparison between different regions of a sample and understanding of the degradation pathways as the reactions progress. Consequently, artworks can be sequentially monitored by obtaining spatially-resolved FTIR spectra of the same region of interest to generate a time series of chemical images.

From a scientific perspective, most approaches for studying paintings and painted metal objects demand collecting paint layer's samples and embedding them in a suitable resin to obtain cross-sections (Keune and Boon, 2007; Kaszowska et al., 2013; Hermans et al., 2018; Casadio et al., 2019, p. 195; Ortiz Miranda et al., 2020). In the case of painted metals, sampling the metal support together with the paint raises both technical and ethical concerns (see also Chapter 2, p. 65) because of the substantial risk of provoking irreversible damage; on the other hand, sampling the paint alone would not give exhaustive information to shed light on the system's complexity, because metal-oil interfacial information would be lost (Pavlopoulou and Watkinson, 2006; Gordon et al., 2019).

However, due to the peculiar optical features of metal soap structures, optical coherence tomography (OCT) is potentially suitable for their detection. Such a non-invasive, non-contact imaging technique has shown its ability to probe subtle changes in the optical properties of complex stratified materials (Vichi et al., 2019). OCT is an imaging technique based on the physical interference of light, which is used to calculate the length of the optical path in a sample. There exist two primary OCT techniques. The first one is *time-domain* OCT (TD-OCT), where the interference patterns are obtained by mechanically modifying the optical path — i.e., by translating the moving reference mirror — to match the one of the light travelling within the sample. The second one is the *frequency domain* OCT (FD-OCT), where the position of the reference mirror is fixed, allowing for ultra high-speed OCT imaging. FD-OCT can be further distinguished in *swept-source* OCT (SS-OCT) and *spectral-domain* OCT (SD-OCT). The latter method is the one utilised within this work. Here, all the reflections coming from the sample and created by irradiation with a broadband spectral source are measured simultaneously as a function of the depth (Koch Dandolo et al., 2019). The spectral bandwidth determines the axial resolution; the penetration depth depends on the characteristics of the sample. For this reason, recent studies highlighted how such instruments are more suitable for investigating transparent layers (e.g., varnishes and coatings) due to their lower scattering or absorption of near-infrared radiation compared to pigments (Koch Dandolo et al., 2022).

Laser-Induced Breakdown Spectroscopy (LIBS) is an atomic emission spectroscopy, which ability to perform both qualitative and quantitative analyses is one of the reasons why it has established itself in the ensemble of analytical techniques providing the elemental composition of a sample (Anglos, 2001). It is a micro-destructive technique where an intense nanosecond laser pulse is focused on the sample's surface, hence ablating it. As a result, a transient microplasma is produced, in which ion-emitted radiation is spectrally resolved. The characteristic peaks obtained from the ablated surface reflect the local composition of the sample. When the ablation crater size is known or can be measured, and a series of consecutive laser pulses can be focussed on the same area, each LIBS experiment can be spatially related to the depth-dependant characteristics of the sample. By doing so, the elemental composition of the sample's stratigraphy can be determined (Koch Dandolo et al., 2019). From this perspective, LIBS represents an alternative approach to depth profile analysis (Miziolek et al., 2006). Measurements in model samples and actual paintings, where typical thickness values for paint layers range from 5 μm to 50 μm, have shown that, on average, the ablation depth per pulse ranges from 0.5 μm to 2 μm (Miziolek et al., 2006). However, variations in the removal of material due to the laser pulse are also dependent on local imperfections within the paint layers (Miziolek et al., 2006). This makes it harder to predict the depth reached by each ablation for samples whose physical properties are not well known. Previous studies report craters

as deep as 10 μm due to this effect (Miziolek et al., 2006).

This work proposes a combination of μ-FTIR, SD-OCT, and LIBS to investigate the formation of metal soaps on oil-coated copper and zinc model samples. Such techniques were chosen for their ability to provide the molecular fingerprint of the species of interest and allow identification of specific crystalline and amorphous carboxylates (μ-FTIR), as well to allow investigation of the stratigraphy of the samples (therefore to access the metal-oil interface) through the generation of virtual cross-sections (SD-OCT), and to validate the hypotheses provided by the SD-OCT approach by means of micro-distructive elemental analyses (LIBS). Additionally, the differences in reactivity of the two substrates and the relationship between fatty acids concentration and metal soap formation in the presence of zinc or copper ions are further discussed.

4.2 Materials and methods

4.2.1 Samples preparation and artificial ageing

For the monitoring of the metal soaps evolution within oil-coated metal sheets, model samples were designed as the simplest system that would allow understanding of the formation of metal soaps in the systems considered. Triplicates of $60 \times 60 \times 1$ mm^3 hair-brushed copper and zinc samples (Tartaix, Paris) were chosen, and possible contaminants were removed with absolute ethanol (VWR Chemicals). Two series of samples were prepared, following the protocol described in Chapter 2, p. 50 (Figure 4.1):

a) One, where cold-pressed linseed oil ($\sim$ 80 μL, Kremer Pigmente) was applied as evenly as possible using a rectangular painter's spatula. All samples were cured overnight at 80 °C. Upon curing, due to the low wettability of the liquid-solid interface, the samples resulted in inhomogeneous coatings, with thicknesses ranging from 2 μm to 15 μm for the copper substrate and from 3 μm to 25 μm for the zinc samples. Thickness measurements were achieved using coating thickness gauge Surfix® by Phynix. The triplets were then placed into sealed boxes containing a glycerol-water solution (50% w/w) reaching $70 - 80\%$ relative humidity (RH) at 80 °C in a laboratory oven (Forney and Brandl, 1992). The samples were kept under these conditions for 30 days. After this period, the copper and zinc samples were removed from the oven and exposed to room conditions of temperature and RH up to 22 months and 17 months, respectively. During the entire period, the samples were monitored at spaced time intervals (i.e., 0, 10, 30 days, 9 months and up to 20 months) using μ-FTIR spectroscopy. The RH and temperature levels of the chamber were monitored in the gaseous phase surrounding the coupons using a PeakTech 5185 datalogger equipped with an immersion probe.

b) A second series of samples was also coated with cold-pressed linseed oil (Kremer Pigmente). In this case, however, the samples first underwent plasma treatment followed by spin-coating at 500 rpm. The samples were then cured overnight gradually between 20 °C and 80 °C, then aged in a laboratory oven for 30 days at 60 °C and $70 - 80\%$ RH in sealed boxes and in the presence of pre-conditioned silica gel beads. Pre-conditioned silica gel beads were obtained by positioning the silica gel in an inert tray that would ensure a large surface area and exposing it to the desired RH level in a climatic chamber at the desired temperature of utilisation. The samples were then removed from the oven and regularly monitored for 6 months.

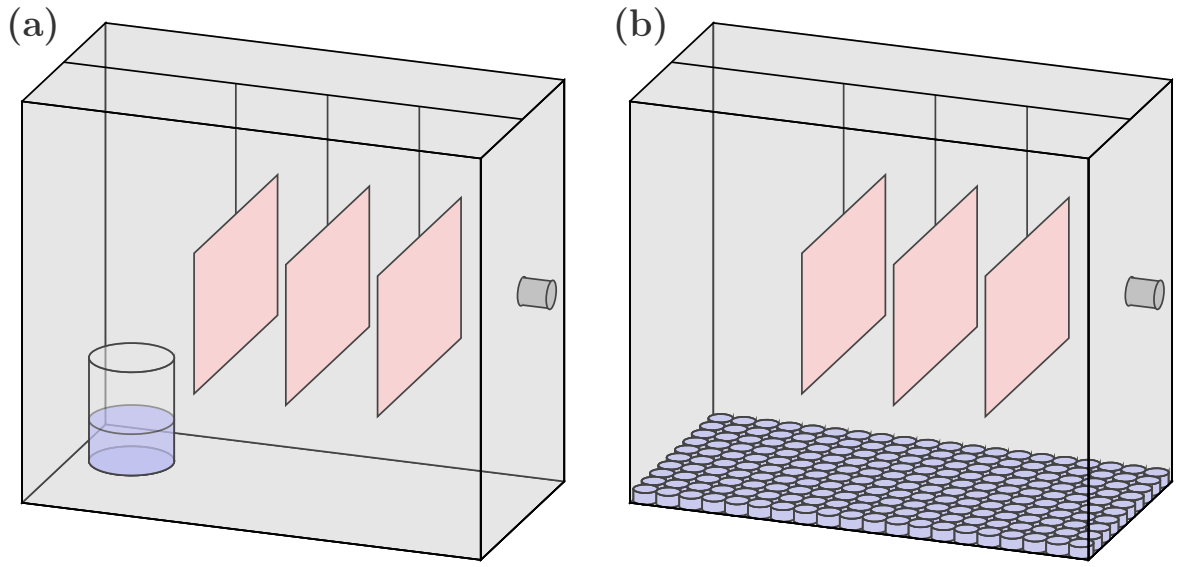

Figure 4.1: Schematic overview of the setup utilised to artificially age the copper and zinc samples of (a) series 'a' and (b) series 'b'. The immersion probe of the datalogger is shown schematically as the small grey cylinder on the side of the box.

For the investigation of the possible correlation between the concentration of fatty acids in the model samples and metal soap formation, different ethanol solutions having different concentrations of palmitic acid were prepared. Five different concentrations were chosen such that the lowest one would be a highly diluted solution (7.8×10^{-5} M); the others were obtained by incrementing up to three orders of magnitude (7.8×10^{-4} M, 7.8×10^{-3} M, 7.8×10^{-2} M) to reach a saturated solution (7.8×10^{-2} M). Concentration equal to 3.9×10^{-2} M was also tested as an additional point. Finally, 1 µL drop of the prepared solutions was deposited on the surface of uncoated hair-brushed copper and zinc samples. Metal soap formation was evaluated by monitoring the samples at spaced time intervals through single-point µ-FTIR measurements ($1 - 6$ hours and 13 months).

4.2.2 Fourier transform infrared micro-spectroscopy (µ-FTIR)

Fourier transform infrared 2D chemical maps were collected using a Thermo Scientific™ Nicolet™ iN10 MX infrared microscope, equipped with a motorised xyz-stage. At each time point considered, the coupons were placed manually on the stage using a combination of reference points drawn on the sample holder area and plastic masks for the area of analysis to guide their repositioning. Some discrepancies in the area analysed were observed, which will be addressed in the results section.

For the first series of samples (series 1), characterised by coating inhomogeneities, three regions of interest were chosen on each sample, such that they would be representative of the differences in the thickness of the coating. One of such regions of interest will be discussed in this chapter, being the one with the most considerable variability in measured thickness values to highlight its effect on the resulting data. For series 1, each region consisted of 600 single-scan spectra, collected in reflectance mode ($4000 - 650$ cm^{-1}) using

an aperture of 150×150 μm^2, step of 100 μm, and 4 cm^{-1} resolution over a total area of 1800×7500 μm^2, whereas for series 2 the accumulation was increased to four scans to improve signal/noise (S/N) ratio. Subtraction of residual signatures of atmospheric carbon dioxide (CO_2) and water (H_2O) in the spectra, baseline correction and normalisation, were the three pre-processing operations performed, in this sequence, using Omnic^{TM} 9.2.86 and Omnic^{TM} Atlus 9.2.91.

The corrected datasets were exported and further processed using Matlab R2021a®. A script was implemented for this purpose that allowed pre-visualisation of the data, selection of peaks and spectral region of interest, with automatic detection of the bands' minima, mathematical operations, and manipulation of the dataset considering peak shifts, alignment, and export of the results (Figure 4.2).

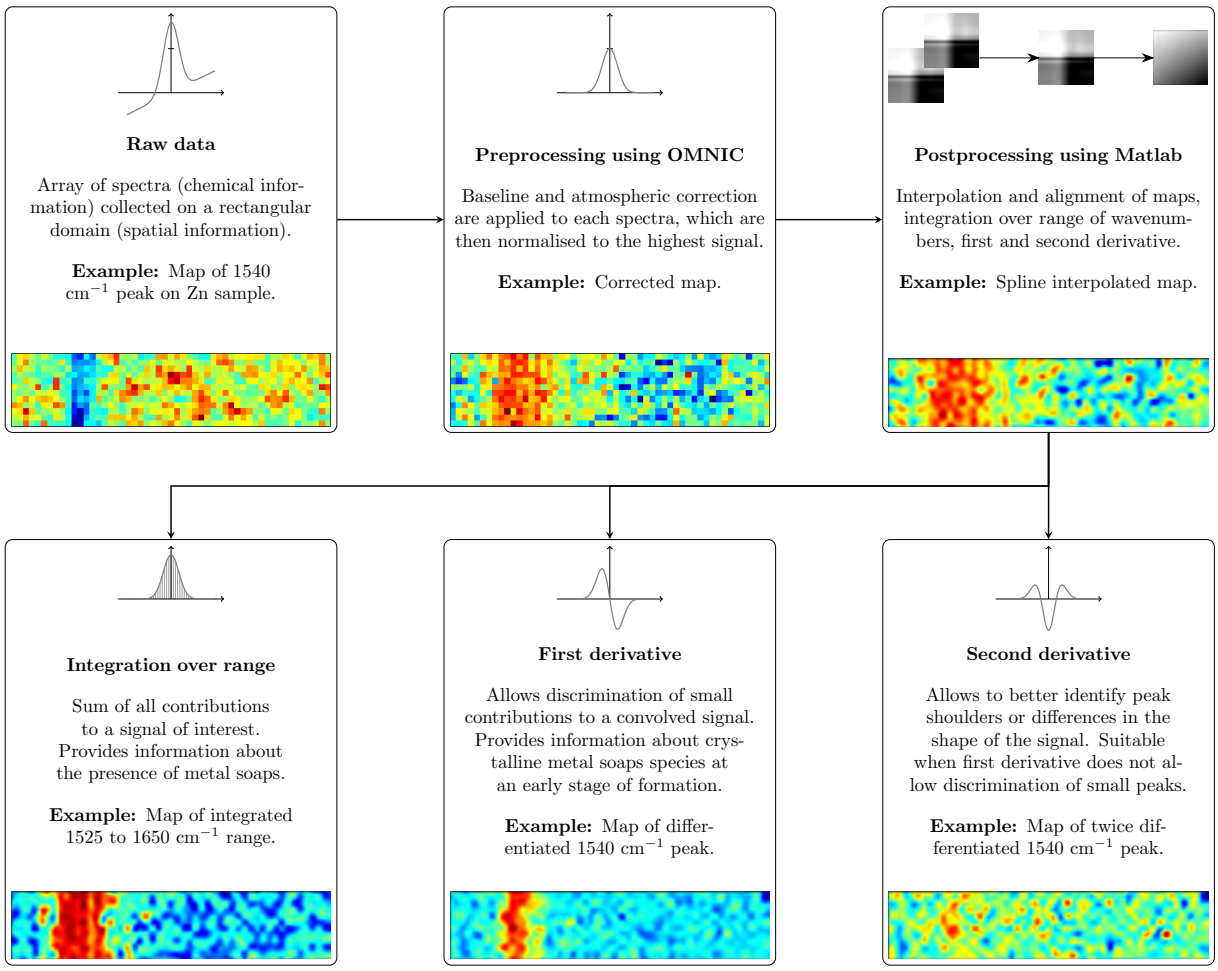

Figure 4.2: The post-processing workflow of the μ-FTIR data collected.

Heatmaps of the species of interest were generated using the red-to-blue scale convention, where red corresponds to maximum values in the dataset, and blue corresponds to minimum values. The heatmaps were then cropped for alignment. Due to the lack of distinct features on the coated surfaces, the reproducibility of the selected areas of analysis was not always achieved when monitoring over time. In particular, manually placing the samples on the stage was bound to introduce errors in consecutive analyses. For this reason, the script was tailored to allow additional alignment for better comparison. At its current stage of development, the process does not involve any registration algorithm, but it mainly relies

on counting the pixel difference between points in the area after having identified manually common reference points with the aid of microscopy images of the same region. Therefore, the images are shifted around those reference points and cropped to the common area to have a comparable sequence of chemical maps for interpretation and dissemination.

Band profiles in the range $1650 - 1500$ cm^{-1} for copper and $1650 - 1525$ cm^{-1} for zinc were generated to account for the diagnostic vibrational bands corresponding to metal soaps for the two metal cations ($\nu_a COO^-$). When needed to investigate different aspects of the metal soaps formation, first and second derivative chemical maps were computed at 1587 cm^{-1} and 1540 cm^{-1} peaks for copper and zinc, respectively. The first derivative is the slope of the tangent at a given point of a curve (Derrick et al., 1999). Assuming a perfectly flat baseline, the first derivative is zero unless a peak is present, in which case there will be an inversion of the slope that can be identified by its inflexion point. As such, the first derivative helps identify highly convolved peaks in a large band independently from the relative intensity of the neighbouring signals. It reflects the rate at which the intensity of the FTIR signal changes depending on the wavenumbers (Sadat and Joye, 2020). The second derivative represents the change in such rate, and it is commonly used in unveiling overlapping features and identifying changes in the peak shape, like the presence of a peak shoulder (Sadat and Joye, 2020). Finally, the band profile of the symmetric stretching of the carbonyl group in the linseed oil was also computed (νC=O, $1755 - 1740$ cm^{-1}).

4.2.3 Spectral domain-optical computed tomography (SD-OCT)

A Thorlabs GAN220-OCT^{TM} Base coupled with a Thorlabs OCTP900M Scanner was utilised. The system operates in the spectral range $804 - 1022$ nm (central wavelength 912 nm), which determines the axial resolution. The latter is also influenced by the refractive index. For an oil binder, where the refractive index assumes values in the range $1.47 - 1.49$, the resulting axial resolution is expected to be 3 µm/2 µm in air/oil. The lateral resolution of the system is limited by diffraction. Data recording was performed using a short focal length objective lens (field of view 6 mm, working distance 3.4 mm, imaging depth 1.9 mm/1.4 mm in air/water, lateral resolution 6.5 µm in y, 3.3 µm in x). The setup allowed the collection of 2D cross-sectional images and 3D volume datasets by scanning the sample using a xy-galvoscanner while the samples were kept stationary.

4.2.4 Laser-induced breakdown spectroscopy (LIBS)

The system is equipped with a Nd:YAG laser emitting radiation at a 266 nm wavelength capable of delivering 10.5 mJ. The laser's wavelength was chosen to allow the analysis of the elements of interest, particularly copper, zinc, and carbon-based compounds. The laser works at a frequency of 20 Hz, meaning it gives 20 pulses per second. The equipment was configured such that the gate opened 500 ns after the initial pulse and would collect the signal for 2000 ns, with a gain of 1500, to obtain a suitable signal for the analysis of the samples. The total range of wavelength covered was $281 - 427$ nm. 50 laser pulses were performed on the same spot, corresponding to 50 single in-depth LIBS analyses.

4.3 Results and discussion

4.3.1 Fourier transform infrared micro-spectroscopy (μ-FTIR)

To estimate the relationship between the formation of metal soaps on painted metals and the duration of exposure to harsh conditions of relative humidity and temperature (80 °C and 70 – 80% RH), selected areas of the copper and zinc model samples were first monitored using μ-FTIR over a period of 30 days. The formation of metal soaps at an early stage was investigated by observing the spectral region between 1650 cm^{-1} and 1500 cm^{-1} where copper soaps can be detected by FTIR spectroscopy (Table 4.1), as well as several coordination geometries of the most common zinc carboxylates (Hermans et al., 2019; Hermans and Helwig, 2020).

Table 4.1: Major asymmetric stretching vibrational bands for the different zinc and copper carboxylates and coordination geometries in the range 1650 – 1500 cm^{-1}.

			Zinc	Copper	References
Crystalline	*Palmitate*		1539 – 1536 s	1586 – 1583 s	Izzo et al., 2021 Hermans et al., 2019 Hermans et al., 2021 Carvalho, 2022
	Stearate		1540 – 1539 s	1586 – 1585 s	
	Oleate		1547 vs, 1527 vs	1588 – 1583 vs	
	Azelate		1556 – 1535 vs	1588 vs	
	2D coordination polymer	Type A	1524 s, 1545 s, 1590 w		
		Type B	1536 s		
Amorphous	*Oxo*		1590 s		Hermans et al., 2021
	Chain		1544 s, 1565 w, 1630 s		

vs = very strong; s = strong; w = weak signal.
all values refer to vibrational mode $\nu_a COO^-$.

[1] According to J. Hermans' definition, two geometry types for zinc soaps can be identified, differing in the forces governing the arrangement of the atoms in the molecule. Type A geometry optimises the coordination around zinc ions, whereas type B crystalline structures maximise Van Der Waals interactions of the alkyl chains (Hermans and Helwig, 2020).

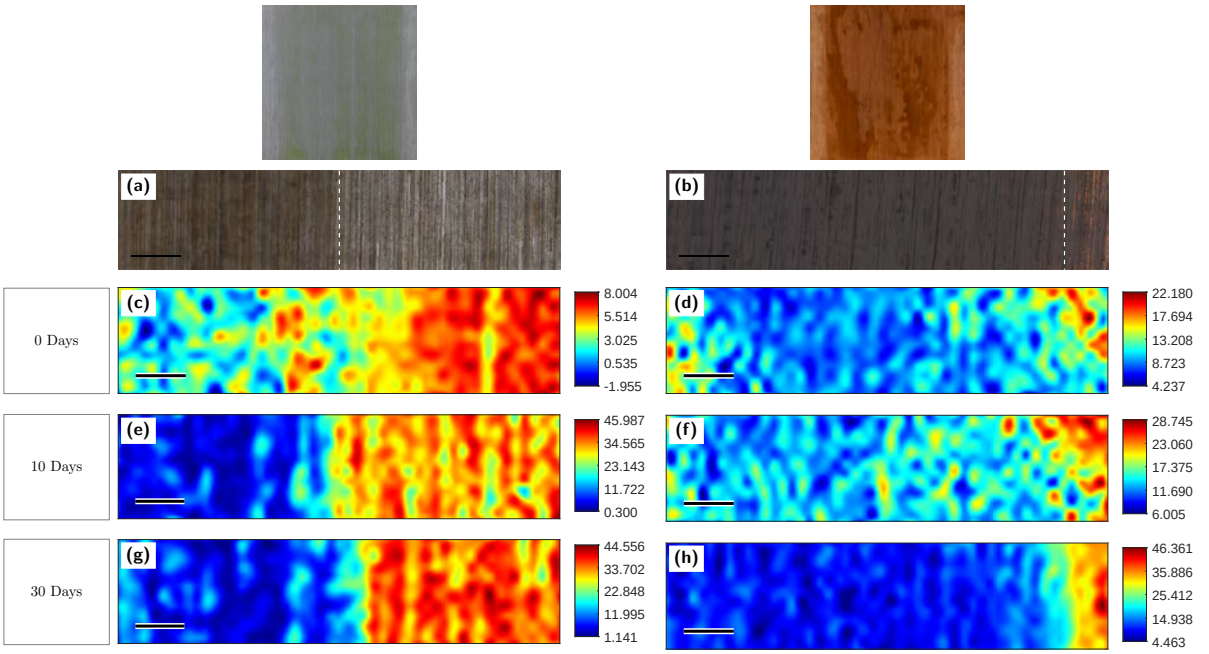

Figure 4.3: Zinc (Zn08; left) and copper (Cu07; right) coupons coated with linseed oil and respective analysed regions of interest (a, b). The dashed line separates areas showing higher (darker, > 10 μm) and lower (lighter, < 10 μm) coating thickness. The time series of μ-FTIR chemical images are obtained in the range $1650 - 1525$ cm^{-1} and $1650 - 1500$ cm^{-1} for zinc and copper respectively, after curing overnight at 80 °C (c, d), and after ageing for 10 days (e, f) and 30 days (g, h) at 80 °C and $70 - 80\%$ RH. The intensity ranges from red (maximum) to blue (minimum). The scale bar indicates 1000 μm.

The qualitative monitoring using heatmaps highlighted some differences in the rate of reaction (Figure 4.3). In particular, the integration over a range of wavenumbers ($1650 - 1525$ cm^{-1} for zinc and $1650 - 1500$ cm^{-1} for copper) showed that zinc soaps formed immediately after the oil coating is applied on the surface of the metal (Figure 4.3c). Their formation increased rapidly in the first 10 days (Figure 4.3e), remaining almost consistent until 30 days (Figure 4.3g). This was shown by an initial increase in red pixels in the rendered heatmap, which value is indicated by the colour bar and corresponds to the intensity of the signal of the characteristic $\nu_a COO^-$ vibrational bands for the zinc and copper carboxylates. The reaction proceeded at a slower pace for copper substrates, where, even though it was still possible to detect metal soaps already after the initial curing of the oil coating (Figure 4.3d), copper soaps formation increased significantly only between 10 days and 30 days (Figure 4.3f, h). This difference in the reaction rate of the two substrates was consistent with what was reported by previous studies on the reactivity of the two ions (Greenwood and Earnshaw, 1997), and of that of zinc pigments in oil paintings (Eumelen et al., 2019; Hermans et al., 2019; Hermans et al., 2021). The metal soap formation trends with time were confirmed for more extended periods of time considered (Figure 4.4), and in the analysis of the homogeneously coated samples from the second protocol (Figure 4.5). In Figure 4.5, it is possible to observe an increase in copper soaps during the time considered, followed by stabilisation after 27 days of monitoring.

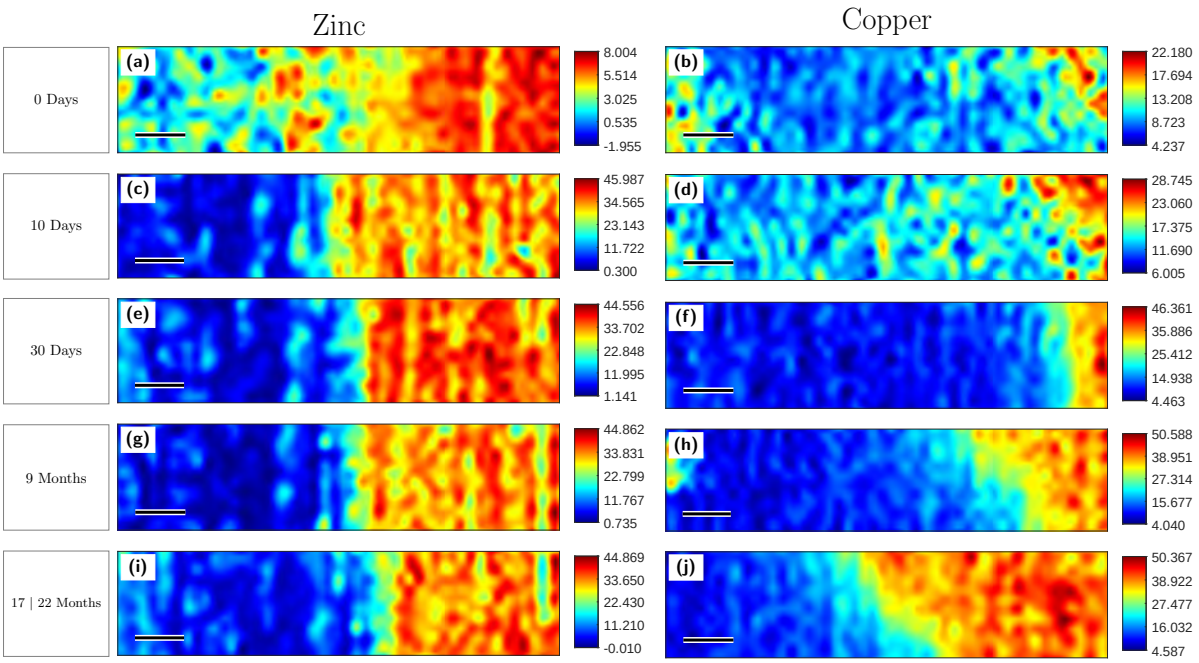

Figure 4.4: Time series of μ-FTIR chemical images obtained in the range of 1650 – 1525 cm^{-1} and 1650 – 1500 cm^{-1} for zinc (Zn08; left) and copper (Cu07; right), respectively, after curing overnight at 80 °C (a, b), and after ageing for 10 days (c, d) and 30 days (e, f) at 80 °C and 70 – 80% RH, followed by additional natural indoors ageing until 9 months (g, h) and 17/22 months (i, j) at room conditions. Intensity range goes from red (maximum) to blue (minimum). The scale bar indicates 1000 μm.

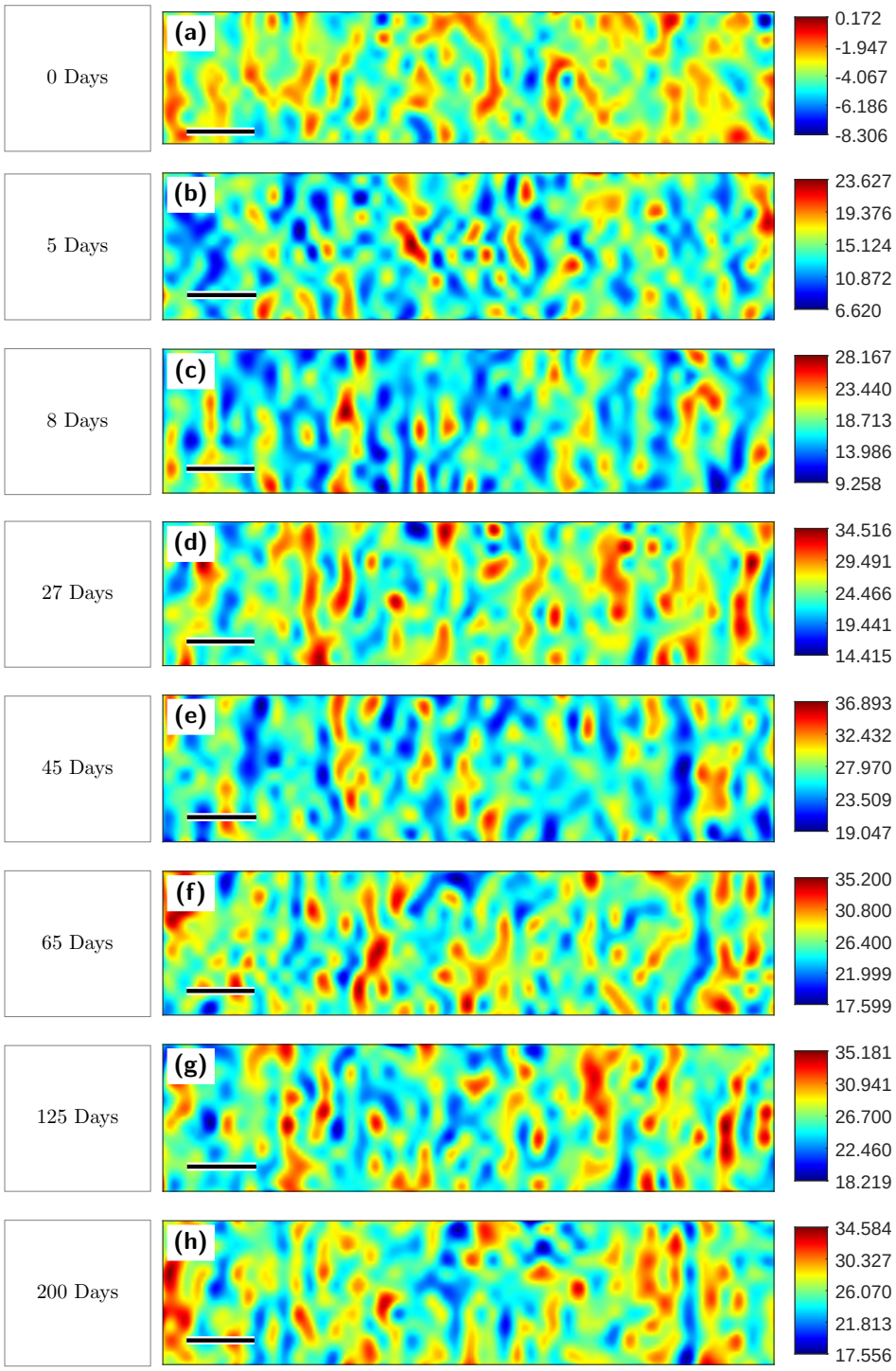

Figure 4.5: Plasma treated spin-coated copper sample (Cu35) monitored over time at (a) after curing overnight gradually from 20 °C to 80 °C, (b) 5, (c) 8, (d) 27 days ageing at 60 °C and 70 – 80% RH, and, after (e) 45, (f) 65, (g) 125, (h) 200 days from curing at room conditions.

A customised Matlab script for data post-processing The approach discussed thus far relied on the detection and monitoring of metal soaps through the computation of band profiles that correspond to the sum of all contributions from different aggregation geometries (Hermans et al., 2019; Hermans et al., 2021). As such, this approach does not allow us to understand if crystalline forms are present and how they are spatially distributed. From a conservation perspective, such chemical species are of interest since they can aggregate, migrate, and form protrusions that are harmful to the mechanical strength of the paint layer (Hermans et al., 2019).

The question of whether specific geometries and crystalline forms are present was addressed through the use of a customised post-processing approach to describe the system deeply (Figure 4.2). This consisted of a series of steps, including baseline-adapted integration over a range of interest (i.e., $1755-1740$ cm^{-1} for the νC=O of linseed oil, $1650-1525$ cm^{-1} and $1650-1500$ cm^{-1} for zinc and copper soaps, respectively), alignment of areas monitored at different times, and computation of first and second derivatives to map the presence of crystalline forms. This tailored approach allowed for greater control over the process, which in turn granted a more reliable interpretation of the results. Due to the peculiar nature of the material under study, the different refractive indices of the components forming the composite object (i.e., the metal support and the oil coating), the thickness of the coating, the morphology of the substrate, and the incoming formation of degradation products, there was much variability in the shape of the curve. This was reflected in both the position of the maxima and the minima and the width of the band (Figure 4.6).

To address this problem, the customised script was designed to perform adaptive integration, where the nearest minima to the given extrema of the interval were automatically determined, and the integral was performed taking into consideration the characteristics of the single spectra pixel by pixel. By using the proposed solution, the integrated peaks presented had a reduced risk of being underestimated. Following the procedure described in Figure 4.2, the chemical maps discussed hereafter were also aligned for better comparison.

First and second derivatives were calculated on the zinc and copper chemical images (Figure 4.7 and 4.8) to identify single species of interest. In Figure 4.7, which refers to the processing of the zinc chemical maps, the first derivative was performed on the diagnostic peak at 1540 cm^{-1} (ν_aCOO$^-$) to visualise the distribution of crystalline species in the area analysed (Figure 4.7 c′-f′). The formation of crystalline species on zinc samples occurred at a very early stage, in parallel with what was observed for the overall zinc soap contribution. It can be noticed that, after 10 days, crystalline species were already detected, and they made up the majority, although not the totality, of the species present. This is shown by the density and position of red pixels in prime and non-prime-letter maps in Figure 4.7. The remaining contribution could then be generally attributed to different geometries and amorphous forms, according to previous studies (Hermans et al., 2019; Hermans et al., 2021). The detailed positions of the single peaks maxima are highlighted in Table 4.1.

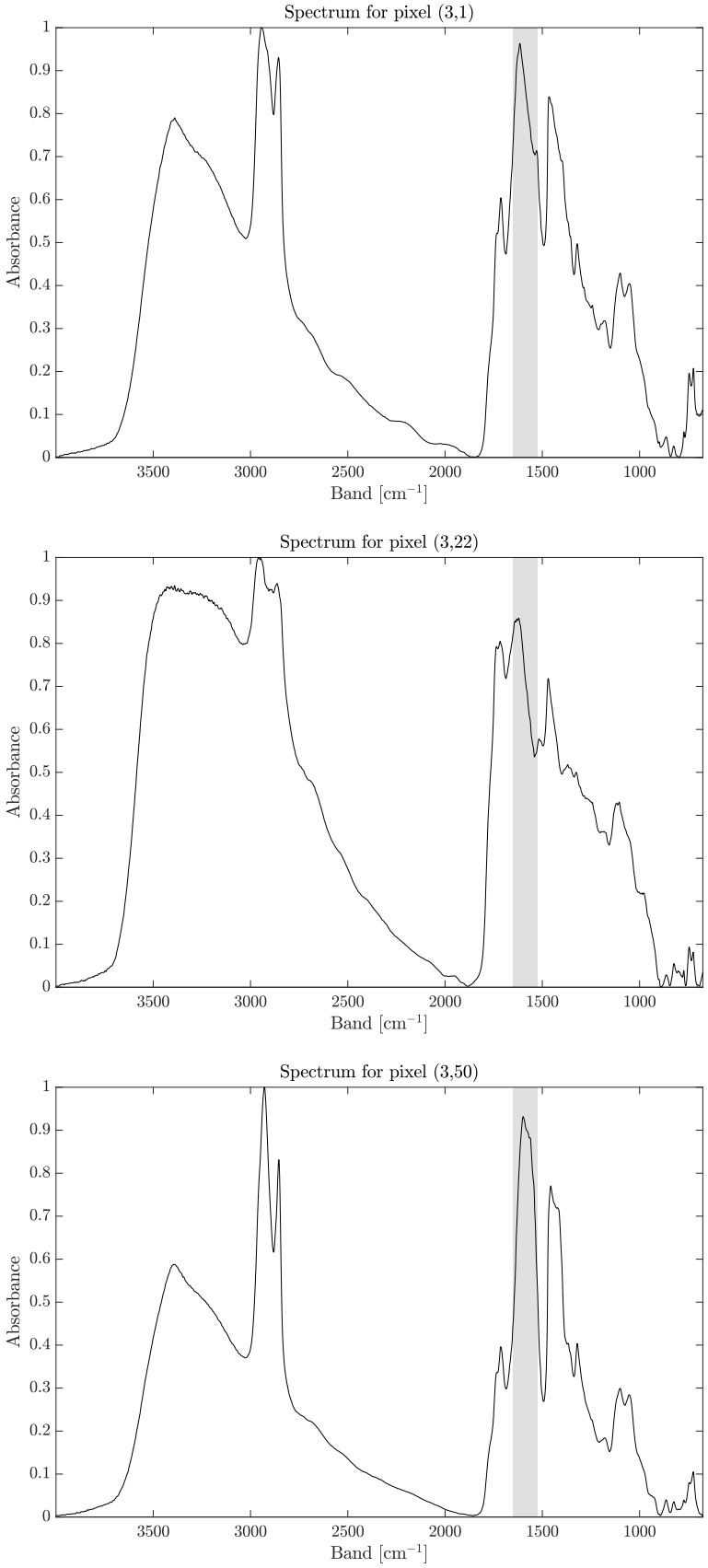

Figure 4.6: Examples of different FTIR spectra measured on a zinc sample (Zn08). Note especially the difference in shape, position of the maxima and width of the peak(s) between $1650 - 1525$ cm^{-1} (region marked in grey).

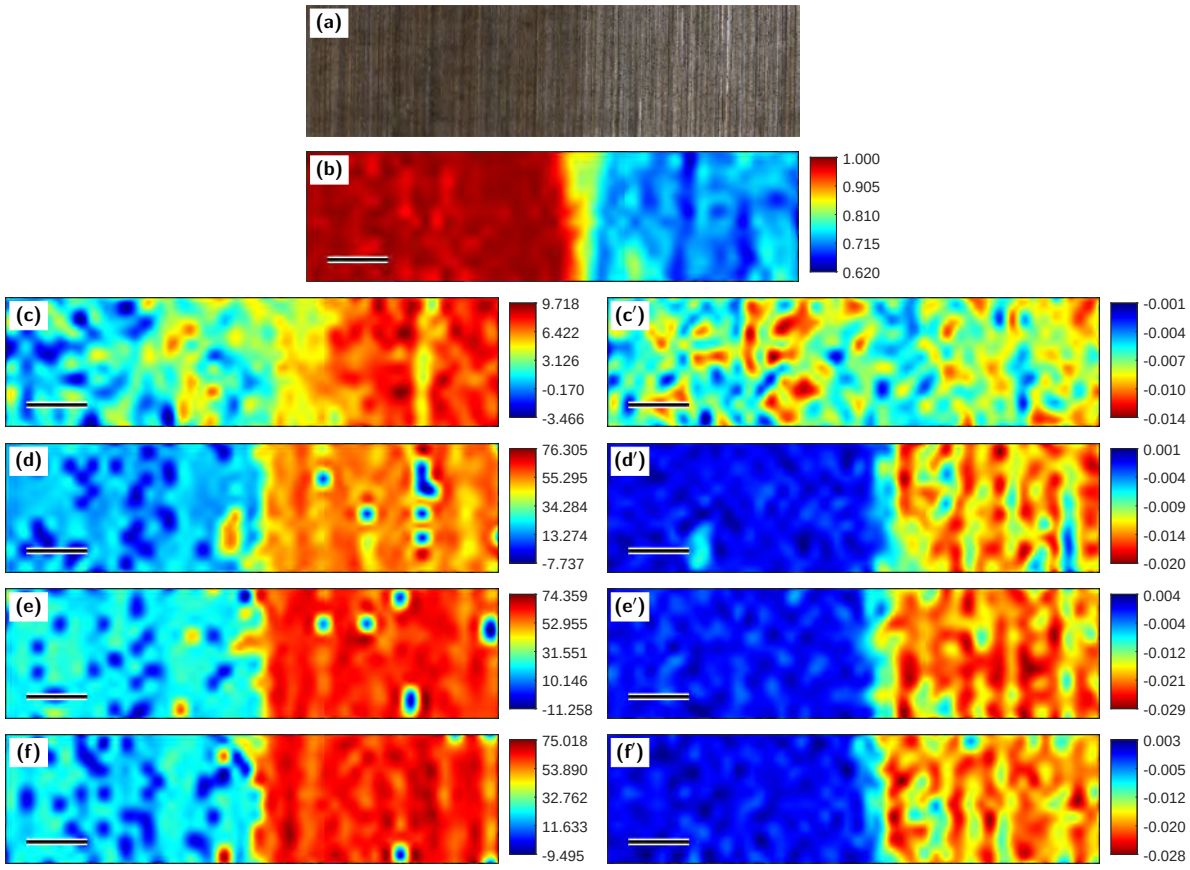

Figure 4.7: Chemical maps of a zinc coupon (Zn08) coated with cold-pressed linseed oil. (a) Optical image of the area of analysis selected; (b) band profile for the carbonyl symmetric stretching of the esters in the linseed oil (νC=O, $1755 - 1740$ cm^{-1}), showing differences in the coating thickness on the sample, where red pixels indicate thicker coatings; (c – f) band profiles of all contributions of metal soaps in the range $1650 - 1525$ cm^{-1} after (c) curing overnight at 80 °C, (d) 10 days artificial ageing at 80 °C/$70 - 80$% RH, (e) 30 days artificial ageing at 80 °C/$70 - 80$% RH and (f) after additional 8 months of exposure to uncontrolled indoor conditions. Prime letters indicate the first derivative chemical images of the peak of crystalline zinc carboxylate (1540 cm^{-1}) in the same area of analysis (red pixels indicate more crystalline forms present). The scale bar indicates 1000 μm.

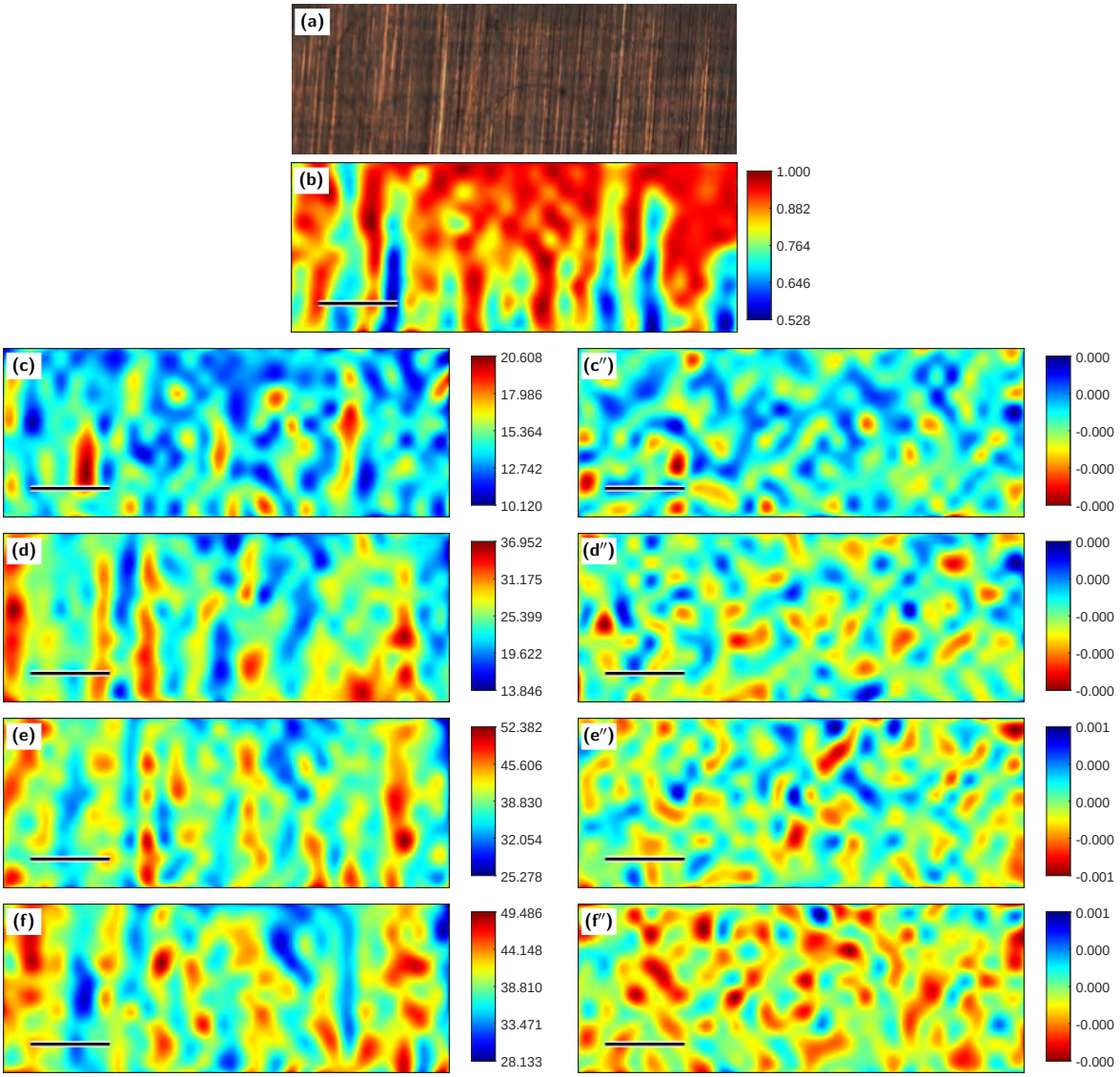

Figure 4.8: Chemical maps of a copper coupon (Cu07) coated with cold-pressed linseed oil. (a) Optical image of the area of analysis selected; (b) band profile for the symmetric stretching of the carbonyl group in the linseed oil (νC=O, $1755 - 1740$ cm^{-1}), showing differences in the coating thickness on the sample, where red pixels indicate thicker coatings; (c – f) band profiles of all contributions of metal soaps in the range $1650 - 1500$ cm^{-1} after (c) curing overnight at 80 °C, (d) 10 days artificial ageing at 80 °C/70 – 80% RH, (e) 30 days artificial ageing at 80 °C/70 – 80% RH and (f) after additional 8 months of exposure to uncontrolled indoor conditions. Double prime letters indicate second derivative chemical images of the peak of crystalline copper carboxylate (1587 cm^{-1}) in the same area of analysis (red pixels indicate more crystalline forms present). The scale bar indicates 1000 µm.

It is essential to bear in mind that such a derivative approach is only suitable when the S/N ratio is high since derivatives are increasingly sensitive to the presence of noise in the original signal as their order increases (O'Haver and Begley, 1981). In the case of the copper sample (Figure 4.8c″–f″), where the peak of crystalline forms of metal soaps ($1588 - 1583$ cm^{-1}) were not well-defined, second derivative analysis was chosen. Here, a slight increase of metal soaps over nine months could be observed, indicated by a higher density of red pixels in the second derivative maps (Figure 4.8f″). However, the spatial distribution of such species did not overlap with the one of the overall contributions of metal soaps in the range $1650 - 1500$ cm^{-1}, as opposed to what was observed for the zinc soaps when the first derivative analysis was performed. A hypothesis could be to attribute this effect to the presence of noise of comparable magnitude to the peak of interest. This aspect confirms the need to consider the influence of the S/N ratio on the spatial distribution of the chemical species of interest when their contribution is small. In accordance with this hypothesis, this effect was not observed in the case of the zinc coupons since a more defined peak was present that could be identified. More targeted experiments are needed to elucidate this aspect, where the crystallisation of the metal soap species could be induced by increasing temperature values locally (Hermans et al., 2019), and the effect on the FTIR-derived signal evaluated.

Together with the question of whether it would be possible to distinguish between different amorphous and crystalline forms of copper and zinc metal soaps within the signal of the general ionomer structure (Hermans et al., 2016a), the observation and analysis of the heatmaps raised additional research questions:

a) Whether the thickness of the oil coating could affect the formation or the detection of the metal soaps. This question was raised from the consideration that metal soaps were observed and mapped only for thinner layers of the oil coating.
b) Whether we could further investigate the differences between the reactivity of the two substrates and the correlation between metal soaps formation and the concentration of fatty acids present. An experiment was designed for this purpose that will be discussed in the last section of this chapter, Section 4.3.4.

In Figures 4.3, 4.4, 4.7 and 4.8 it can be noted that the detection of metal soaps is also a function of the thickness of the oil, which could impede their detection when values are higher. This can be observed in the resulting heatmaps, where the metal soaps have a higher signal in thinner layers of the coating (Figure 4.3, 4.4, 4.7, 4.8) for both substrates. An example of this can be found by comparing the left and right parts of panel (b) and (c) in Figure 4.7, corresponding to the distribution of the oil coating (band profile in the range $1755 - 1740$ cm^{-1}) and of zinc soaps (band profile in the range $1600 - 1525$ cm^{-1}), respectively. Metal soaps were apparently more present in correspondence with thinner layers of oil coating (< 25 μm, right side of the area analysed). On the copper coupons (Figure 4.8), the wettability of the surface allowed for a higher affinity to linseed oil, resulting in overall thinner coatings (< 15 μm) and localised areas of homogeneity (Figure 4.8a, b). This permitted to record the formation of metal soaps more efficiently within the whole region of interest (Figure 4.8c – f). Considering also the penetration depth of the infrared beam in the oil sample, which, at a given wavelength, depends on the refractive index of the material analysed (e.g., fresh or cured oil coating, oil paint layers) (Derrick et al., 1999), a correspondence between the detectability/presence of metal carboxylates and the thickness of the coating could be observed.

To validate the observed relationship between the presence of metal soaps and the thickness of the coating, Figure 4.9 shows a comparison between different areas of the samples that present a range of thicknesses of the oil coating and their respective chemical images integrated for the relevant bands related to the presence of metal carboxylates ($1650 - 1500$ cm^{-1} for copper and $1650 - 1525$ cm^{-1} for zinc). The distribution of red pixels, corresponding to thicker coatings in (a_1), (b_1), (c_1), and (d_1), and to higher metal soaps signal in (a_2), (b_2), (c_2), and (d_2), highlights the same relation: metal soaps are only detectable for thinner coatings (< 25 µm). This information is essential if one considers approaching the non-invasive study of genuine artefacts, where the coating might be originally composed of several overlapping layers or be the result of subsequent interventions on the object, and where the overall thickness of the sample would realistically be unknown.

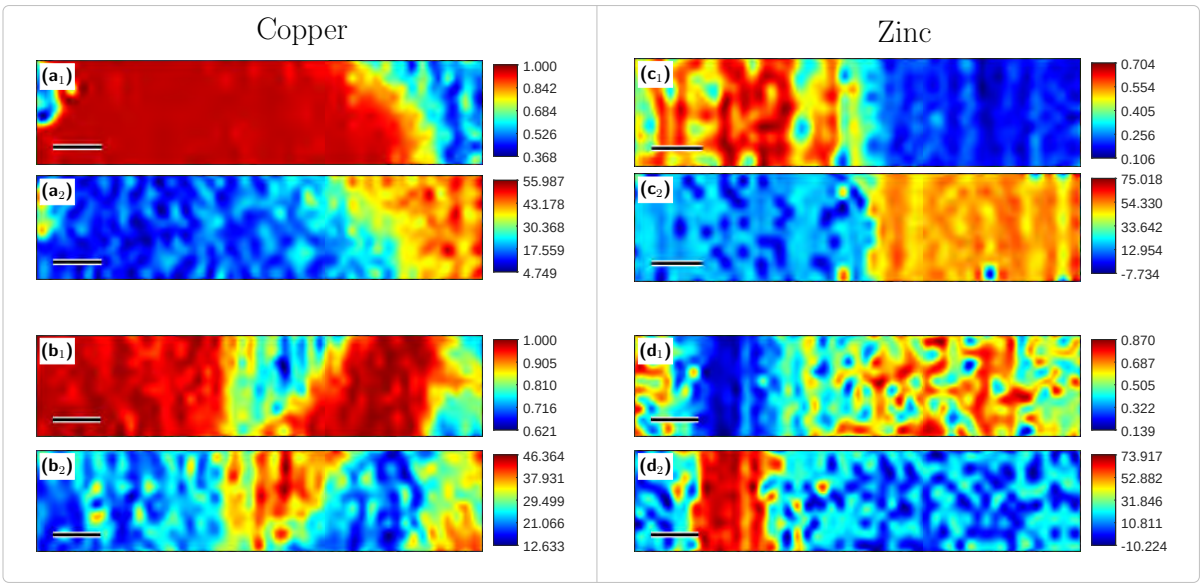

Figure 4.9: Chemical images of copper (Cu07) and zinc (Zn08) coupons in different areas of coating inhomogeneity. (a_1), (b_1), (c_1), (d_1) Band profile for the symmetric stretching of the carbonyl group in linseed oil (νC=O, $1755 - 1740$ cm^{-1}); (a_2), (b_2) band profiles of all contributions of copper carboxylates in the range $1650 - 1500$ cm^{-1}; (c_2), (d_2) band profiles of all contributions of zinc carboxylates in the range $1650 - 1525$ cm^{-1}. The scale bar indicates 1000 µm.

4.3.2 Spectral domain-optical computed tomography (SD-OCT)

The dependency of the detectability of metal soaps from the thickness of the oil coating observed through μ-FTIR analyses suggested that the reaction of formation of metal soaps could occur and be limited to the metal-oil interface, where the products could be found in contact with the metal rather than in the upper oil layers. Due to the difficulties in sampling and embedding metal samples together with their coating (Chapter 2, p. 65), SD-OCT was proposed as a non-invasive tool to obtain a virtual slice of the sample and access the metal-oil interface.

SD-OCT was used to scan representative areas of 4 months and 20 months artificially aged copper samples to identify the presence of metal soaps at different stages of formation. The OCT tomograms illustrate the separation of materials having different refractive indices at their contact points. The stratigraphy suggested by the OCT analysis on 6-month-aged copper samples is schematically shown in Figure 4.10 for a clearer interpretation, and it is based on the acquisitions performed on artificially aged copper samples presenting different oil-coating thicknesses (Figure 4.11).

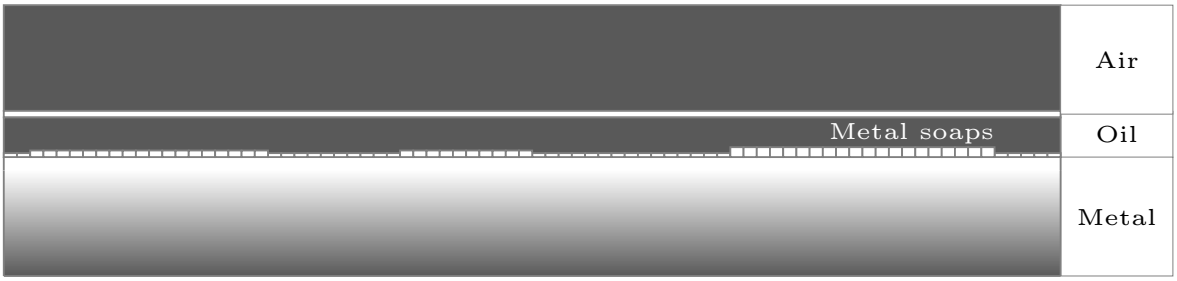

Figure 4.10: Schematic stratigraphy suggested by the OCT analysis.

By analysing the tomograms from top to bottom,

- a first white line at the top could be identified, corresponding to the air-oil interface, at which the back-reflection is maximal due to the significant difference in refractive indices of the two media ($n = 0.64$ for copper and $1.47 - 1.49$ for linseed oil, Polyanskiy, 2022).
- An underlying dark area representing the oil layer in its entire depth was observed, its thickness varying from a few microns to several microns (Figure 4.11A and 4.11B).
- A second thicker white line was then encountered in correspondence with the metal substrate (oil-metal interface), followed by a blurred area or "ghost radiation" due to the multiple scattering of photons (Koch Dandolo et al., 2022).

A zoom into the 2D cross-sectional slide is provided for more details (Figure 4.11b). The observation of the inset suggested that two separate signals formed the white line representing the interface oil/metal, one more continuous and another less homogeneously distributed, and even showing little agglomerates. It is hypothesised that this feature represented an indicator of the presence of metal soaps in deeper oil layers, i.e., in the proximity of the metal support. The possibility of distinguishing between oil, metal soaps, and bulk metal is due to the ability of OCT systems to discriminate between different

materials in close contact having different refractive indices. Thicker coatings allowed us to better highlight the interfacial layer of additional material, possibly attributed to metal soaps formed in contact with the metal support (Figure 4.11A).

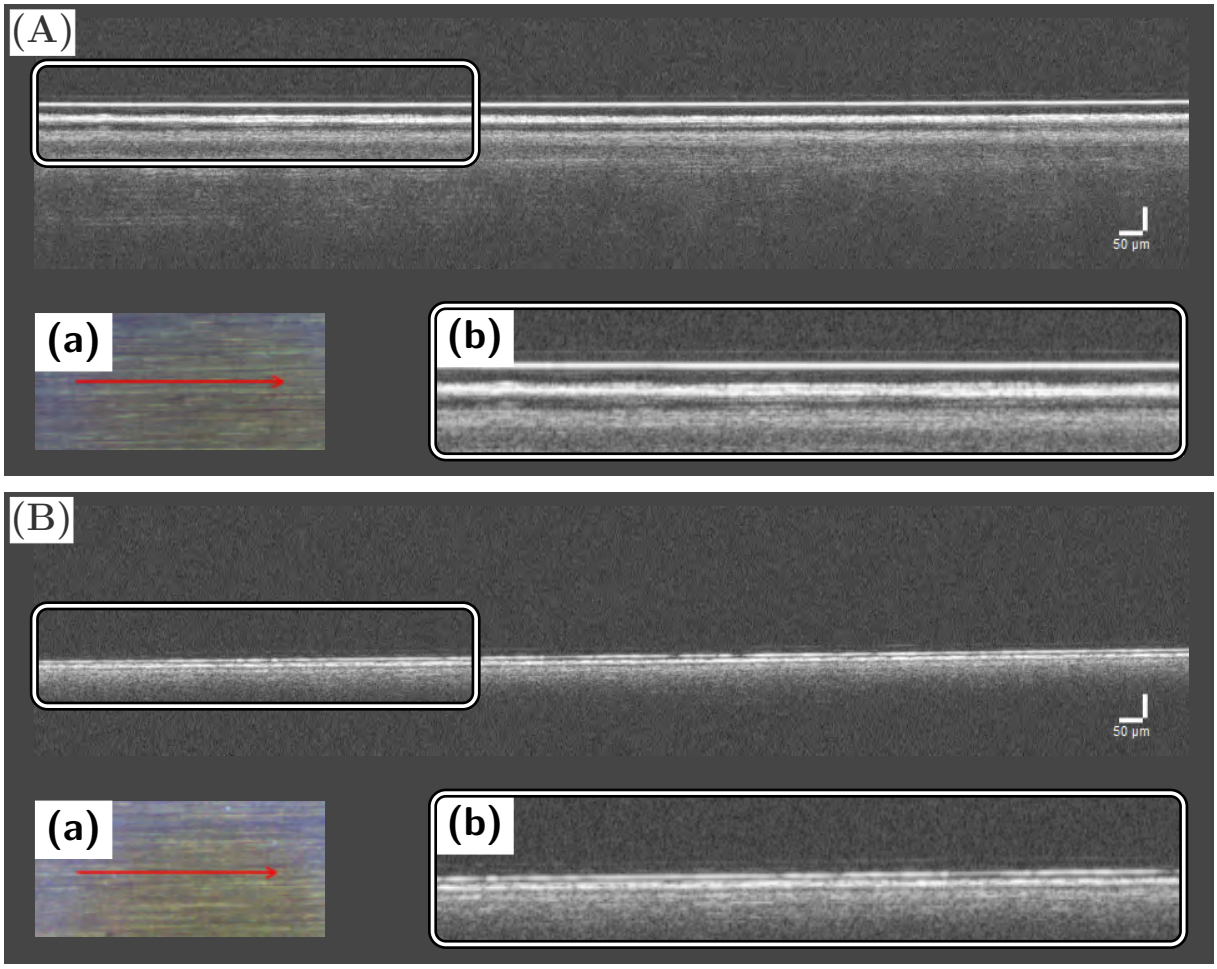

Figure 4.11: Tomogram of 4-month artificially aged copper samples (A, Cu38 (control); B, Cu35) coated with linseed oil. (a) Full tomogram showing the virtual section of the sample; (b) inset showing the presence of an interfacial compound, possibly metal soaps. (A) and (B) aim to show the in-depth differences between thick and thin coatings with regard to the formation of metal soaps.

For older samples (20 months), the two white lines appeared fused into a thicker one, indicating that a more compact layer of the interface material (metal soaps) was present in contact with the metal support (Figure 4.12).

In the case of zinc supports, taking into consideration the effect that coating thickness has on the visual separation of the different layers, similar features could be observed. Differently from copper samples, however, interfacial compounds were more heavily formed already after 4 months compared to copper substrates (Figure 4.13). After 15 months, a thick layer of such compounds could be observed (Figure 4.14).

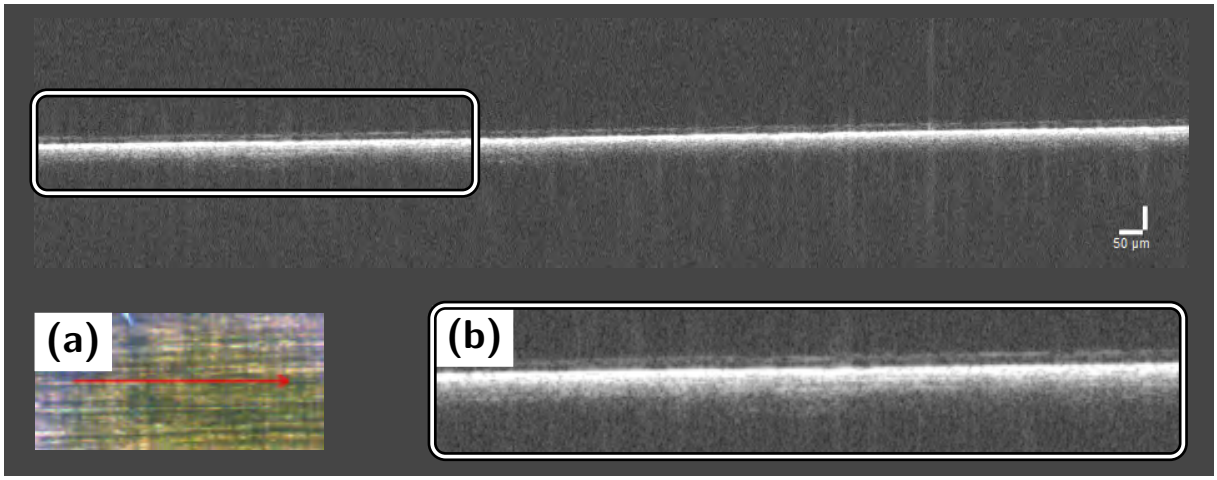

Figure 4.12: Tomogram of a 20-month artificially aged copper sample (Cu07) coated with linseed oil. (a) Full tomogram showing the virtual section of the sample; (b) inset showing the presence of an interfacial compound, possibly metal soaps.

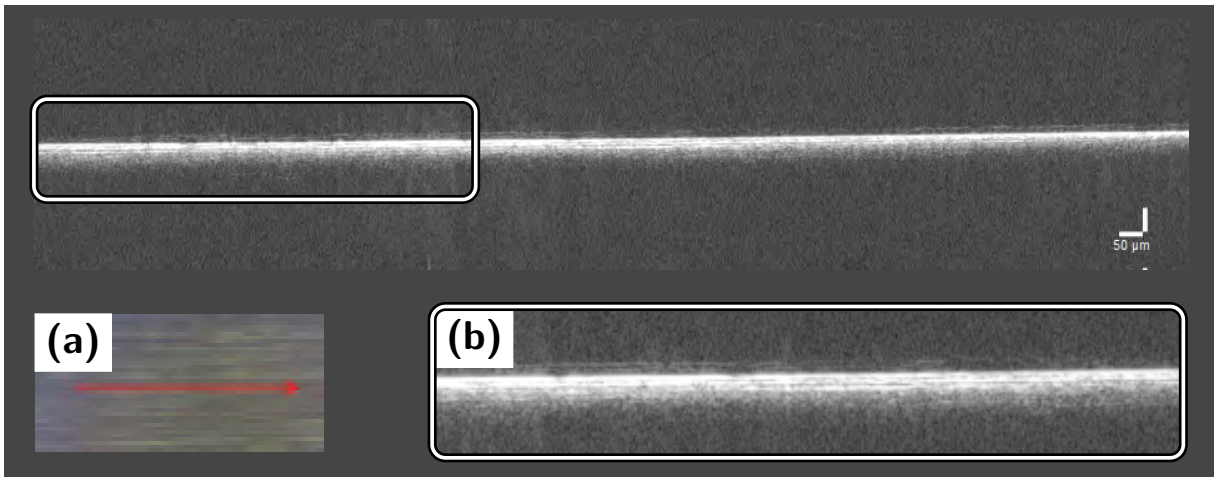

Figure 4.13: Tomogram of a 4-month artificially aged zinc sample (Zn31) coated with linseed oil. (a) Full tomogram showing the virtual section of the sample; (b) inset showing the presence of an interfacial compound, possibly metal soaps.

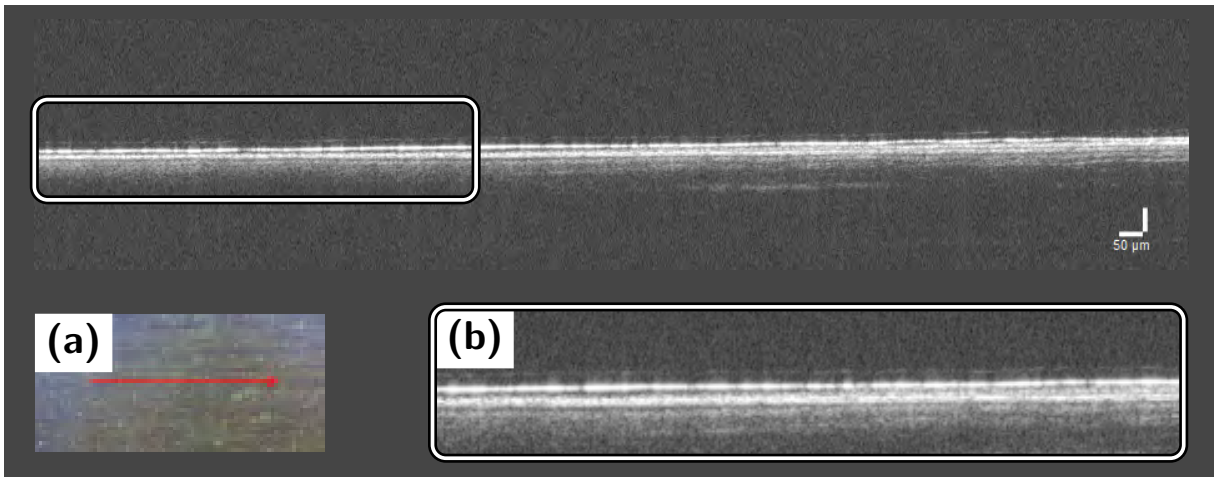

Figure 4.14: Tomogram of a 15-month artificially aged zinc sample (Zn08) coated with linseed oil. (a) Full tomogram showing the virtual section of the sample; (b) inset showing the presence of an interfacial compound, possibly metal soaps.

4.3.3 Laser-induced breakdown spectroscopy (LIBS)

A validation of the hypothesis for which metal soaps are visible at the interface between the metal surface and the oil coating was provided by LIBS analysis. The copper and zinc samples previously analysed with μ-FTIR and SD-OCT were investigated using such analytical technique. First considerations came from simply observing the differences between the first (outer layers) and the last (inner layers) measurements (Figure 4.15). A significant increase in the intensity of the peaks at 324 nm and 327 nm corresponding to Cu(I) could be noticed as the ablation progressed toward the surface of the metal at the expense of the carbon-rich component (organic, C_2; $385 - 388$ nm). The series of peaks at 385, 386, 387, and 388 nm has been previously mentioned in some studies on olive oil and palmitic acid (Gyftokostas et al., 2021; Mousavi et al., 2016; Stefas et al., 2021). The authors attributed the signals to C-N emission from the recombination of atomic carbon or C_2 molecules in the sample plasma with the atmospheric nitrogen through the following reactions (Mousavi et al., 2016):

$$C + N + M \longrightarrow CN + M \quad \textbf{(1)}$$

$$C + N_2 \longrightarrow CN + N \quad \textbf{(2)}$$

$$C_2 + N \longrightarrow CN + C \quad \textbf{(3)}$$

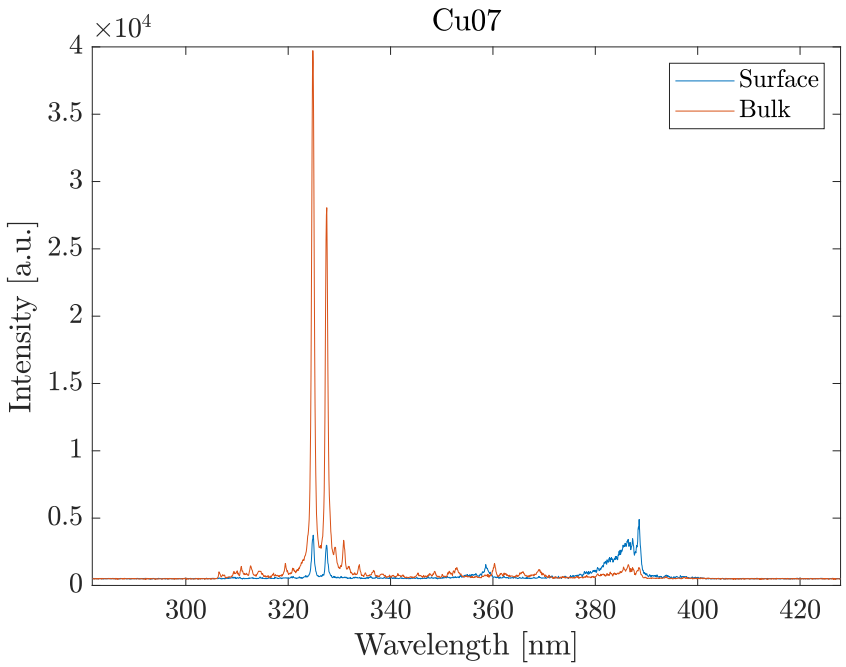

Figure 4.15: Comparison between first (pulse 1, in blue) and last (pulse 50, in orange) layer analysed using LIBS.

The complete temporal evolution of LIBS spectra for the linseed oil-coated copper samples is shown in Figure 4.16a and 4.16b for 5- and 21-month aged samples, respectively. This shows a progressive increase in the Cu(I) signal, with a decrease of the samples' organic component starting after the fifth laser ablation iteration.

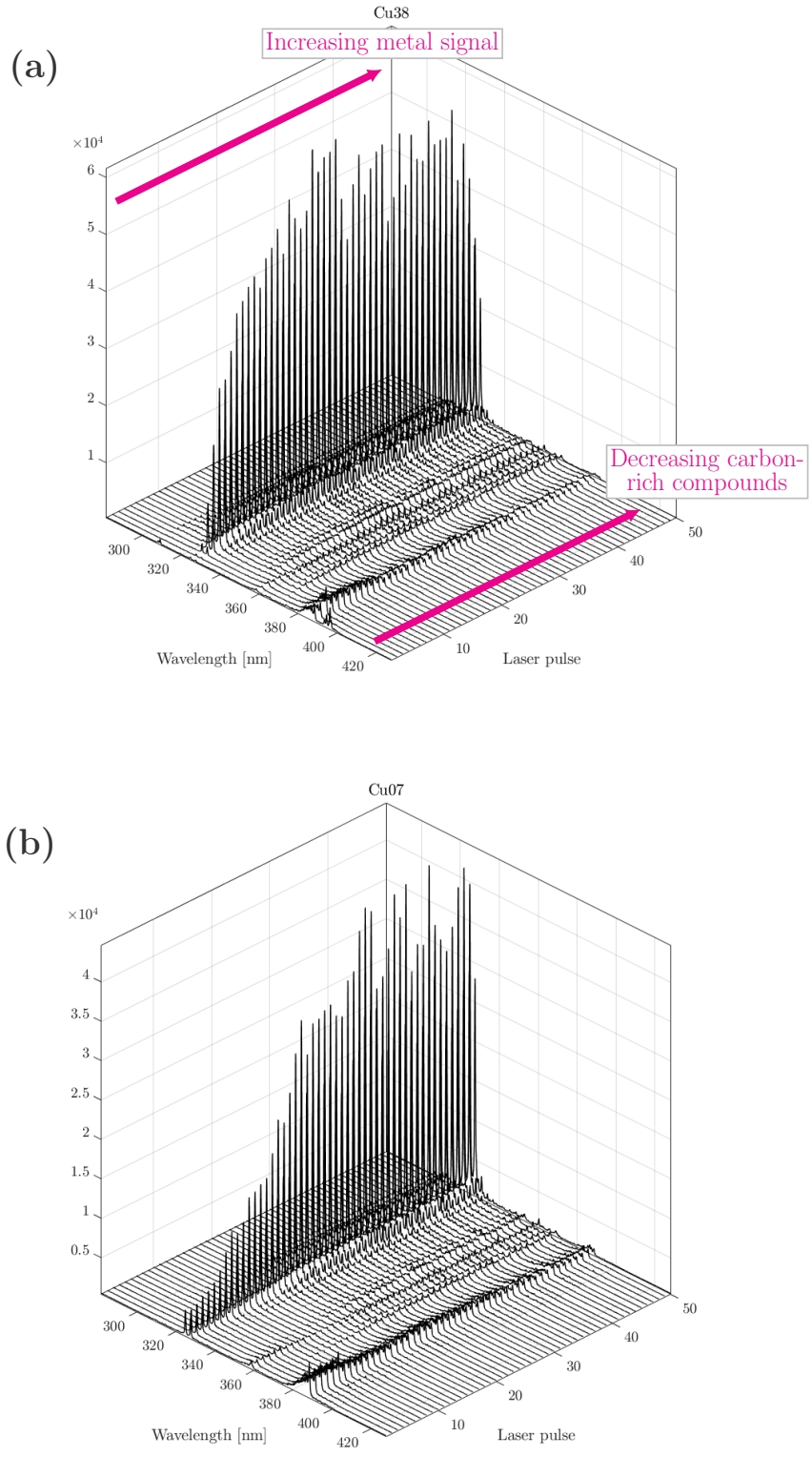

Figure 4.16: Sequence of LIBS spectra for (a) 5-month (Cu38) and (b) 21-month (Cu07) aged copper samples coated with linseed oil, showing increasing metal substrate (324 nm and 327 nm) and decreasing organic component (385 – 388 nm) signals as the ablation reaches inner layers.

A more visually impactful representation of the data is provided in Figure 4.17, where the in-depth evolution is represented on the abscissa (as the number of laser pulses), the wavelength on the ordinate axis, and the intensity is given by a colour-coded density map.

The 2D chemical image for 5-month-aged copper samples showed a strong signal at 324 nm and 327 nm corresponding to the emission of Cu(I) ions from the temporary plasma generated by the interaction of the sample with the laser (Figure 4.17a). This signal became more prominent with subsequent analyses (increasing number of laser pulses) on the same spot, indicating that the metal ions were more present in the bulk of the sample than at more superficial layers. On the contrary, the signals characteristic of C and O interactions were stronger at the sample's surface. The depth at which the metal support started appearing is both a function of the thickness of the coating as well as of the presence of metal-organic compounds (soaps). Metal ion signals appeared in co-presence with the carbon-rich component emissions for intermediate layers.

Schematically, whereas at the sample surface, all the elements composing the oil binder were present, as the analysis reached inner layers, the presence of compounds containing simultaneously metal ions and organic components was determined. Finally, only metal ions could be detected in the last layers.

Copper samples that underwent longer ageing time followed a similar trend, the difference being in the layers where C, O and Cu signals coexist ($10 - 30$ laser pulses, Figure 4.17b). For these samples, such overlap concerned a larger number of layers in the sample.

However, this degradation phenomenon was not only a function of the ageing time and thickness of the oil but also of the reactivity of the metal support. Figure 4.18 suggests that, for zinc samples, the observed behaviour was accentuated, with metal-organic species being more present in both 5 months and 16 months aged samples than for the copper-based system (Figures 4.18a and 4.18b, respectively). Co-existence of C_2 ($385 - 388$ nm), Zn (202, 206 nm Zn(I) and 213, 329, 334 nm Zn(II)) signals was more pronounced than the respective copper samples and ubiquitous for older samples. This feature confirmed the increased reactivity of zinc supports towards free fatty acids already highlighted by μ-FTIR and SD-OCT measurements.

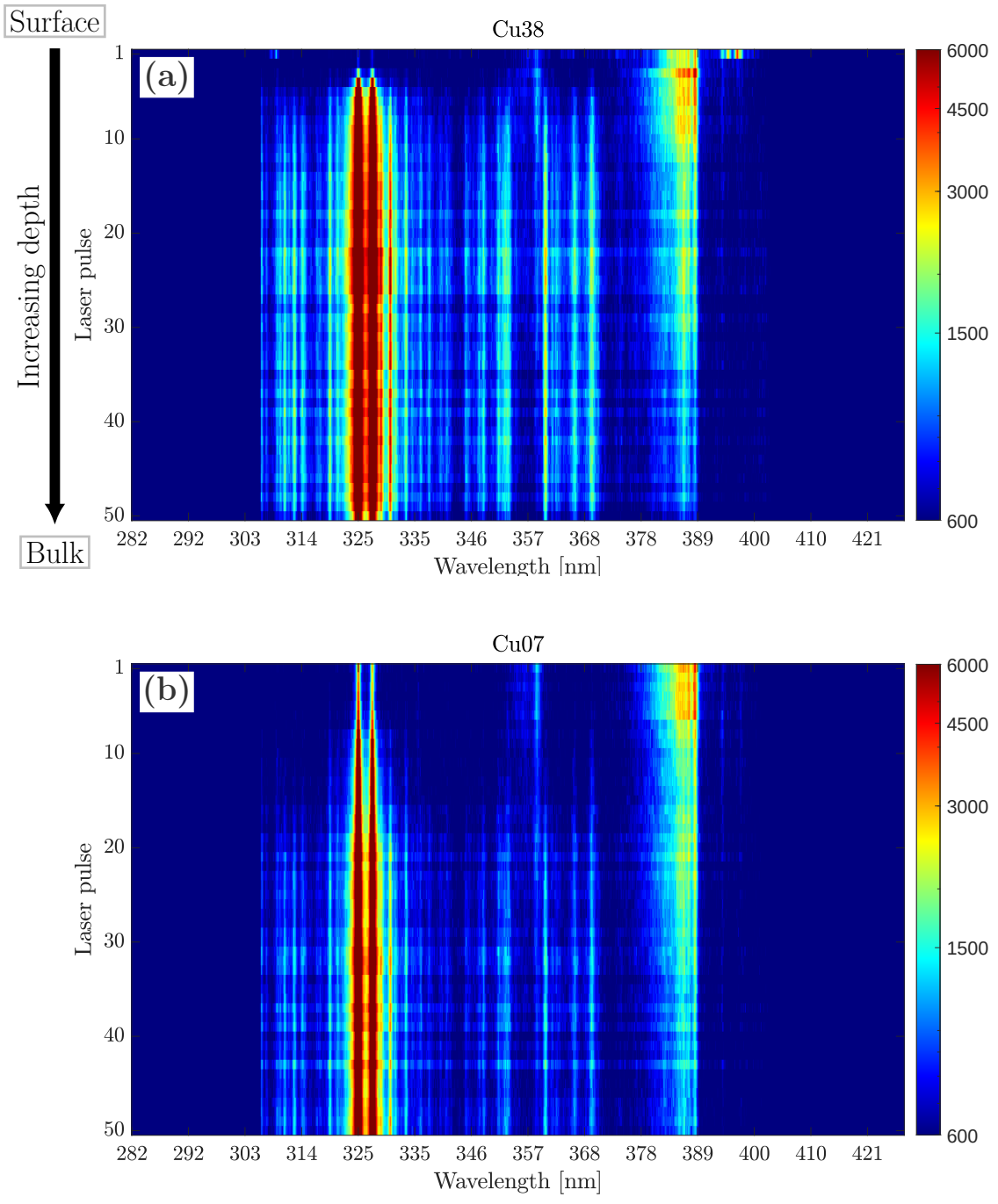

Figure 4.17: 2D chemical image of (a) 5-month (Cu38) and (b) 21-month (Cu07) aged copper samples coated with linseed oil. The copper substrate emits at 324 nm and 327 nm and the carbon-rich component has characteristic signals in the range $385 - 388$ nm. Intensity range varies from red (maximum) to blue (minimum).

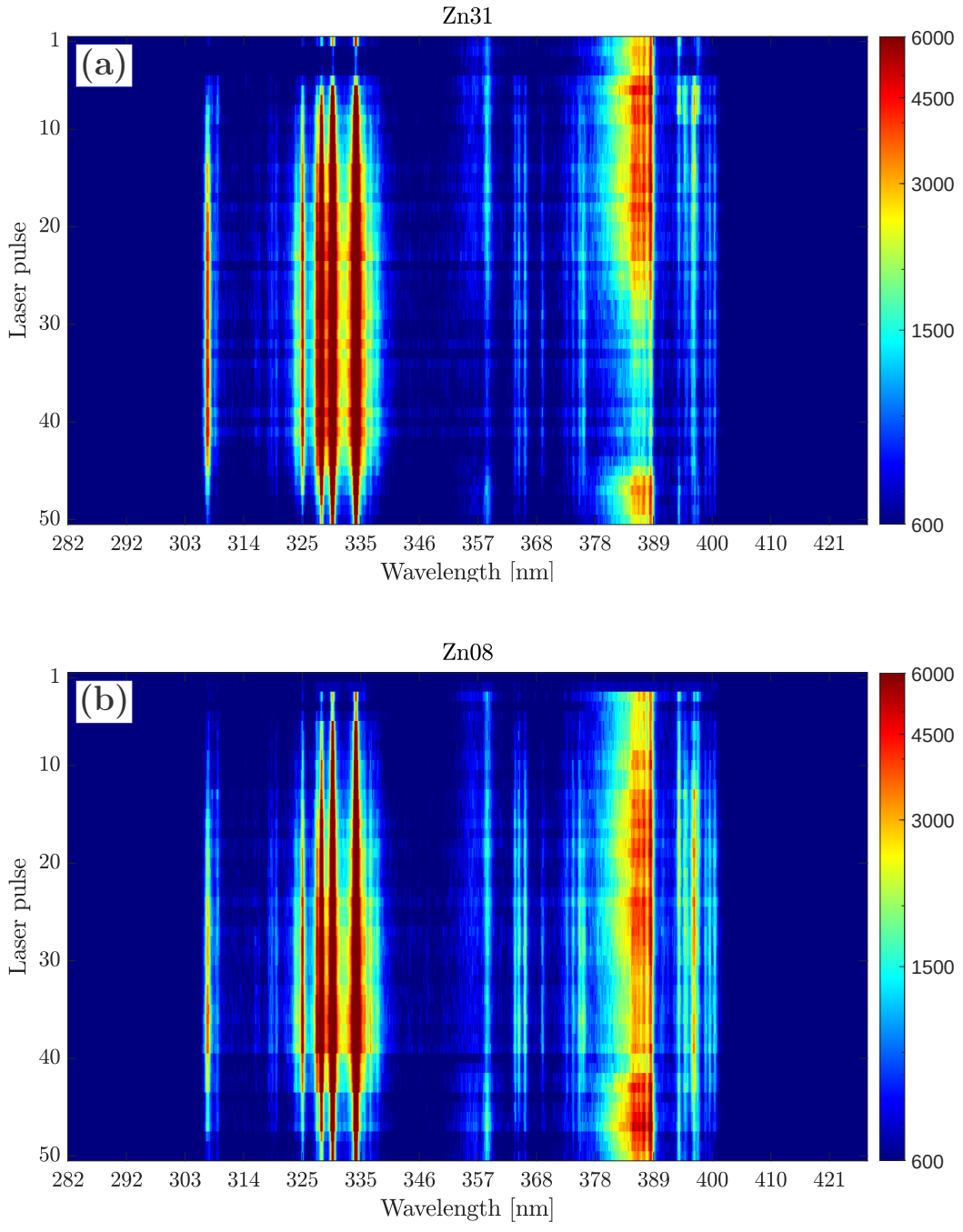

Figure 4.18: 2D chemical image of (a) 5-month (Zn31) and (b) 16-month (Zn08) aged zinc sample coated with linseed oil. The zinc substrate emits at 329 nm and 334 nm, and the carbon-rich component has characteristic signals in the range 385 – 388 nm. The intensity ranges from red (maximum) to blue (minimum).

4.3.4 Investigating the correlation between fatty acids concentration and metal soaps formation

The following experiment was designed to investigate the behaviour of different metal supports when exposed to various concentrations of palmitic acid solutions. It was based on the use of μ-FTIR single-point analysis to monitor copper and zinc substrates when 1 μL of different solutions of palmitic acid in ethanol were deposited on the surface. The approach consisted of collecting subsequent spectra and computing the area under the curve delimited by the range of wavenumbers corresponding to crystalline metal soaps of the two metals considered ($1595 - 1581$ cm^{-1} for copper and $1555 - 1528$ cm^{-1} for zinc).

Figure 4.19 shows the reactivity of copper and zinc substrates towards various concentrations of palmitic acid (7.8×10^{-5} M, 7.8×10^{-3} M, 7.8×10^{-2} M). It highlights the trends at different monitoring times, where both substrates behave similarly for all time points. In particular, there is a clear linear correlation between the concentration of the solution deposited on the surface of the metal and the area of the vibrational band corresponding to the formed metal soaps ($1595 - 1581$ cm^{-1} and $1555 - 1528$ cm^{-1} for copper and zinc, respectively). The plots show that the formation of metal soaps was moderate at lower concentrations, and it increased drastically for higher concentrations. We could therefore identify a limit concentration (7.8×10^{-3} M) at which metal soaps started being highly detectable. When looking at the two substrates in comparison, it was evident that, as previously noticed, the zinc substrate reacted more strongly to free fatty acids than the copper one. This was suggested by higher values on the ordinate for the zinc samples, about three orders of magnitude higher, and it could be an indication that the two substrates differ in the kinetic of the reaction. In particular, zinc appears to be kinetically favoured.

To verify the linear trend, additional concentration points were investigated for copper samples (Figure 4.20). Five different concentrations were utilised in this case including the ones previously considered (i.e., 7.8×10^{-5} M, 7.8×10^{-4} M, 7.8×10^{-3} M, 3.9×10^{-2} M, and 7.8×10^{-2} M). The trend was confirmed, where a linear correlation was observed (here expressed as an exponential behaviour on a logarithmic scale). Negative values are due to the spectra baseline. Depending on the quality of the baseline, in the absence of a peak in the selected range, the integral computation might return negative values. Additionally, some variability is present due to the repositioning of the samples for monitoring. This is enhanced by the increased number of points considered.

It can be seen that the same limit concentration (7.8×10^{-3} M) was observed at which the formation of copper soaps increased drastically. At lower concentrations, corresponding to an extremely diluted solution of palmitic acid in ethanol (7.8×10^{-5} M), copper soaps were not easily detected; at saturated concentrations (7.8×10^{-2} M), the formation of metal soaps is evident already after one hour and a half from the solution deposition.

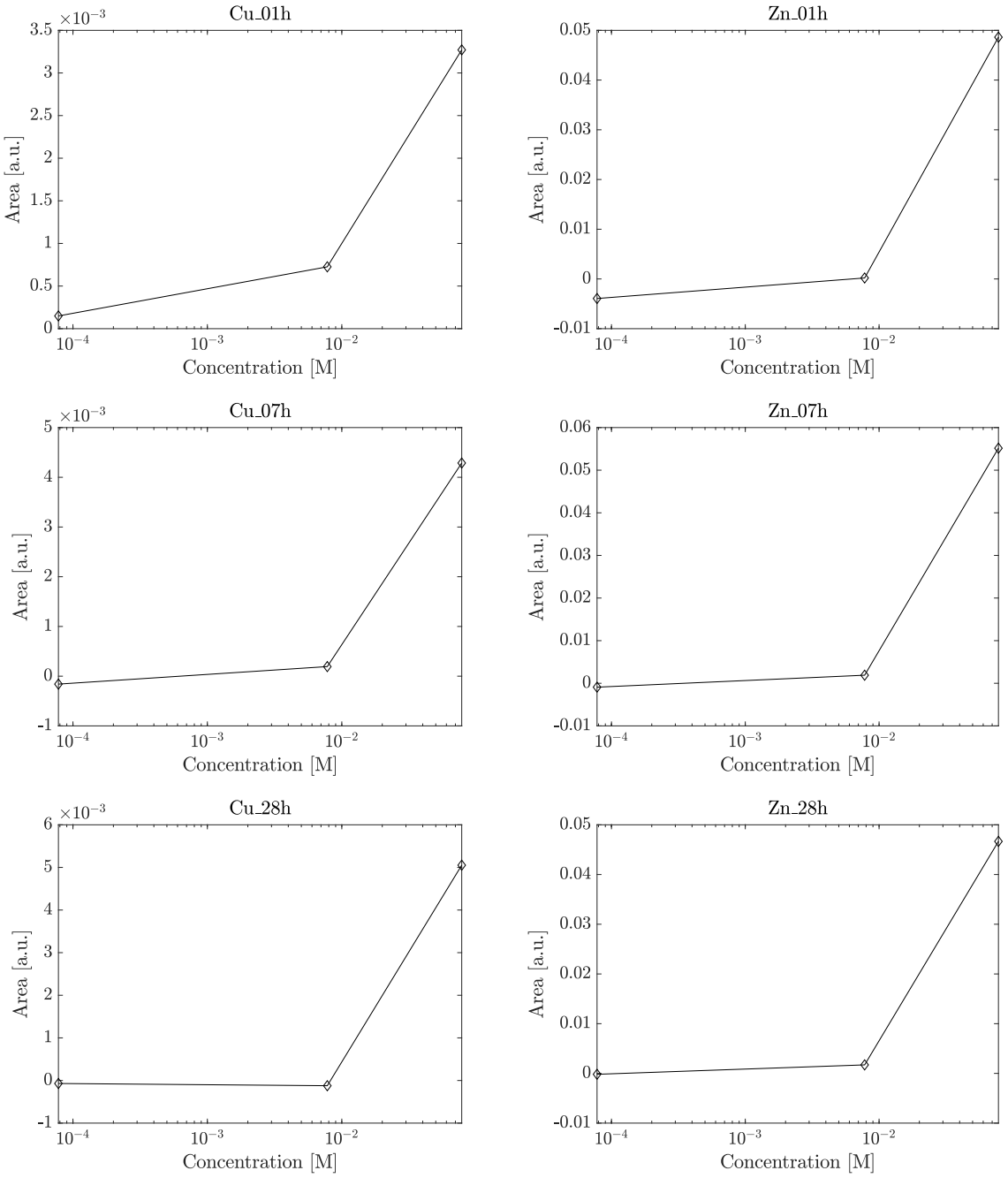

Figure 4.19: Reactivity trends of copper (Cu_DoE_drop1) and zinc (Zn_DoE_drop2) substrates towards various concentrations of palmitic acid solutions over time. The points on the x axis represent the different concentrations of palmitic acid solutions (7.8×10^{-5} M, 7.8×10^{-3} M, and 7.8×10^{-2} M). These are plotted against the area under the metal carboxylates curve, i.e., in the spectral range $1595 - 1581$ cm^{-1} and $1555 - 1528$ cm^{-1} for copper and zinc, respectively. The linear relation is shown as an exponential trend because the data is plotted against a logarithmic scale on the abscissa for easier visualisation so as to have equally spaced data points.

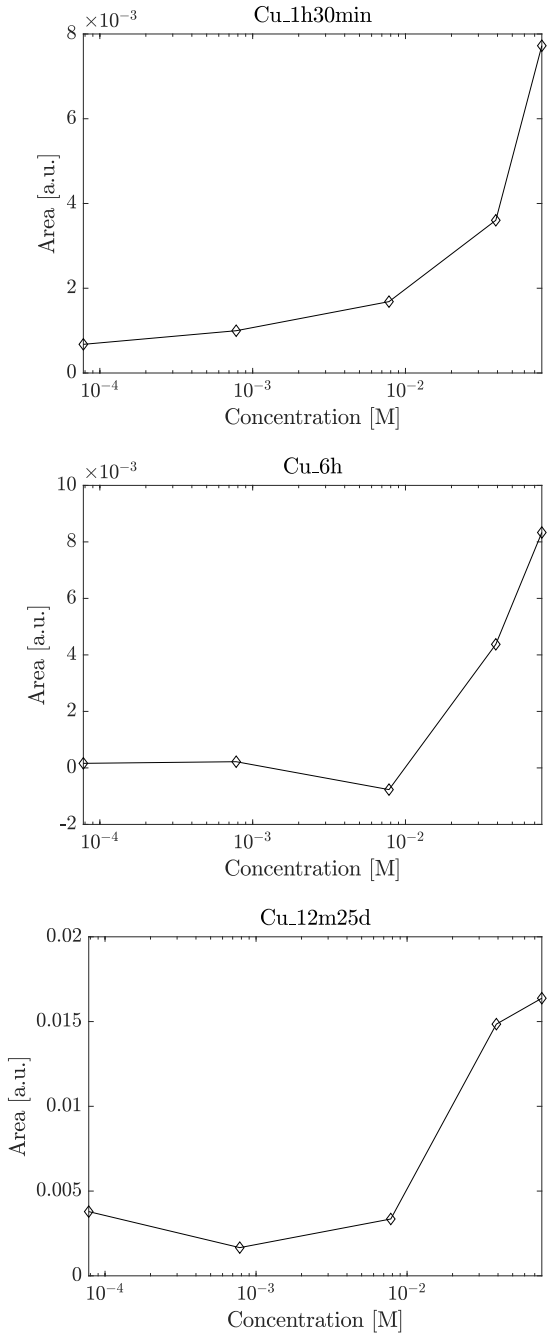

Figure 4.20: Reactivity trends of a copper sample (Cu25) toward various concentrations of palmitic acid solutions (7.8×10^{-5} M, 7.8×10^{-4} M, 7.8×10^{-3} M, 3.9×10^{-2} M, and 7.8×10^{-2} M).

4.4 Conclusions

A non-invasive multi-analytical protocol to understand the mechanism of formation of metal soaps on painted metal substrates was evaluated. μ-FTIR was used to monitor the evolution of the reaction over time. Zinc samples proved to be more reactive towards fatty acids, forming metal soaps already after the coating was applied and cured. Copper soaps, on the contrary, were more challenging to detect in the first 10 days of monitoring. Their formation was detected especially between 10 and 30 days and regularly increased over the first nine months monitoring period; it then stabilised for the remaining ageing time up to 22 months.

First and second derivatives were computed to highlight the presence of specific crystalline species within the matrix. A tailored script was written for this purpose that allowed bulk analysis of the μ-FTIR data and increased control of the band integration process. The derivative approach was more beneficial for zinc samples, where the signal was strong enough for the peak to be effectively detected in the first derivative.

Having noticed during μ-FTIR analyses that the thickness of the oil coating influenced the detectability of the species of interest, and as an alternative method to the preparation of cross-sections, SD-OCT was employed to investigate the metal-oil interface. Here, features that could be attributed to the presence of compounds having different refractive indices than the one of the oil and the metal were found, suggesting the presence of metal soaps in contact with the metal surface. In accordance with this hypothesis, these features were more prominent for increasingly aged samples (up to 17 and 22 months for zinc and copper samples, respectively) and more evident for zinc than for copper substrates. These results aligned with the observations made during the μ-FTIR monitoring.

LIBS provided an in-depth elemental analysis of the samples. The spectra showed characteristic signals of the two metal substrates and of carbon-rich chemical structures. The former signals were more present in the inner layers of the samples, whereas the latter were more prominent in the outer layers. An area of overlap between the two signals could be identified, indicating the simultaneous presence of metal ions and carbon-rich species. This overlap was more evident for the more reactive zinc substrates and for heavily aged samples. The results suggested the existence of an interfacial area where metal soaps could be present.

The relationship between the fatty acids concentration and the reactivity of the metal substrates was also investigated. FTIR spectra were collected over time on copper and zinc substrates put in contact with palmitic acid solutions having different concentrations. Linear trends between the concentration of the solutions and the area of the metal soaps FTIR bands could be observed in all cases. A concentration limit was identified (7.8×10^{-3} M), above which the metal soaps could be easily detected.

In conclusion, this multi-analytical approach indicated that metal soaps were produced on both zinc and copper substrates. The data presented supported the hypothesis that their formation occurs at the metal-oil interface and is a function of time and of the initial concentration of free fatty acids present in the binder.

Bibliography

Anglos, D. (2001). Laser-Induced Breakdown Spectroscopy in Art and Archaeology. *Applied Spectroscopy* **55**(6): 186A–205A. DOI: 10.1366/0003702011952398.

Baij, L., Chassouant, L., Hermans, J. J., Keune, K., and Iedema, P. D. (2019). The concentration and origins of carboxylic acid groups in oil paint. *RSC Advances* **9**(61): 35559–35564. DOI: 10.1039/C9RA06776K.

Banti, D., La Nasa, J., Tenorio, A. L., Modugno, F., Jan van den Berg, K., Lee, J., Ormsby, B., et al. (2018). A molecular study of modern oil paintings: investigating the role of dicarboxylic acids in the water sensitivity of modern oil paints. *RSC Advances* **8**(11): 6001–6012. DOI: 10.1039/C7RA13364B.

Carvalho, L. d. C. (2022). *Beyond Copper Soaps: Characterization of Copper Corrosion Containing Organics*. SpringerBriefs in Applied Sciences and Technology. Cham: Springer International Publishing. DOI: 10.1007/978-3-030-97892-1.

Casadio, F., Keune, K., Noble, P., Van Loon, A., Hendriks, E., Centeno, S. A., and Osmond, G., eds. (2019). *Metal Soaps in Art: Conservation and Research*. Cultural Heritage Science. Cham: Springer International Publishing. ISBN: 978-3-319-90617-1.

Derrick, M. R., Stulik, D., and Landry, J. M. (1999). *Infrared spectroscopy in conservation science*. Scientific tools for conservation. Los Angeles: Getty Conservation Institute. ISBN: 978-0-89236-469-5.

Eumelen, G., Bosco, E., Suiker, A., Loon, A. van, and Iedema, P. (2019). A computational model for chemo-mechanical degradation of historical oil paintings due to metal soap formation. *Journal of the Mechanics and Physics of Solids* **132**: 103683. DOI: 10.1016/j.jmps.2019.103683.

Forney, C. F. and Brandl, D. G. (1992). Control of Humidity in Small Controlled-environment Chambers using Glycerol-Water Solutions. *HortTechnology* **2**(1): 52–54. DOI: 10.21273/HORTTECH.2.1.52.

Fuster-Lopéz, L., ed. (2017). *Paintings on copper and other metal plates: production, degradation and conservation issues = La pintura sobre cobre y otras planchas metálicas: producción, degradación y conservación*. València: Universitat Politècnica. ISBN: 978-84-16846-96-2.

Gabrieli, F., Rosi, F., Vichi, A., Cartechini, L., Pensabene Buemi, L., Kazarian, S. G., and Miliani, C. (2017). Revealing the Nature and Distribution of Metal Carboxylates in Jackson Pollock's *Alchemy* (1947) by Micro-Attenuated Total Reflection FT-IR Spectroscopic Imaging. *Analytical Chemistry* **89**(2): 1283–1289. DOI: 10.1021/acs.analchem.6b04065.

Garrappa, S., Kočí, E., Švarcová, S., Bezdička, P., and Hradil, D. (2020). Initial stages of metal soaps‘ formation in model paints: The role of humidity. *Microchemical Journal* **156**: 104842. DOI: 10.1016/j.microc.2020.104842.

Gordon, J., Normand, L., Genachte-Le Bail, A., Mirabaud, S., Loeper-Attia, M.-A., Catillon, R., Carré, A.-L., et al. (2019). New strategies for the conservation of paintings on metal. In: *Metal 2019 proceedings of the Interim Meeting of the ICOM-CC Metals Working Group, September 2-6, 2019, Neuchâtel, Switzerland*. Ed. by C. Chemello, L. Brambilla, and E. Joseph. Neuchatel: International Council of Museums - Committee for Conservation (ICOM-CC). ISBN: 978-92-9012-458-0.

Greenwood, N. N. and Earnshaw, A. (1997). *Chemistry of the elements*. 2nd ed. Oxford ; Boston: Butterworth-Heinemann. ISBN: 978-0-7506-3365-9.

Gyftokostas, N., Stefas, D., Kokkinos, V., Bouras, C., and Couris, S. (2021). Laser-induced breakdown spectroscopy coupled with machine learning as a tool for olive oil authenticity and geographic discrimination. *Scientific Reports* **11**(1): 5360. DOI: 10.1038/s41598-021-84941-z.

Hermans, J. and Helwig, K. (2020). The Identification of Multiple Crystalline Zinc Soap Structures Using Infrared Spectroscopy. *Applied Spectroscopy* **74**(12): 1505–1514. DOI: 10.1177/0003702820935183.

Hermans, J., Osmond, G., Loon, A. van, Iedema, P., Chapman, R., Drennan, J., Jack, K., et al. (2018). Electron Microscopy Imaging of Zinc Soaps Nucleation in Oil Paint. *Microscopy and Microanalysis* **24**(3): 318–322. DOI: 10.1017/S1431927618000387.

Hermans, J., Zuidgeest, L., Iedema, P., Woutersen, S., and Keune, K. (2021). The kinetics of metal soap crystallization in oil polymers. *Physical Chemistry Chemical Physics* **23**(39): 22589–22600. DOI: 10.1039/D1CP03479K.

Hermans, J. J., Keune, K., Loon, A. van, Corkery, R. W., and Iedema, P. D. (2016a). Ionomer-like structure in mature oil paint binding media. *RSC Advances* **6**(96): 93363–93369. DOI: 10.1039/C6RA18267D.

Hermans, J. J., Keune, K., Loon, A. van, and Iedema, P. D. (2015). An infrared spectroscopic study of the nature of zinc carboxylates in oil paintings. *Journal of Analytical Atomic Spectrometry* **30**(7): 1600–1608. DOI: 10.1039/C5JA00120J.

Hermans, J. J., Keune, K., Loon, A. v., and Iedema, P. D. (2016b). The crystallization of metal soaps and fatty acids in oil paint model systems. *Physical Chemistry Chemical Physics* **18**(16): 10896–10905. DOI: 10.1039/C6CP00487C.

Hermans, J. J., Baij, L., Koenis, M., Keune, K., Iedema, P. D., and Woutersen, S. (2019). 2D-IR spectroscopy for oil paint conservation: Elucidating the water-sensitive structure of zinc carboxylate clusters in ionomers. *Science Advances* **5**(6): DOI: 10.1126/sciadv.aaw3592.

Izzo, F. C., Kratter, M., Nevin, A., and Zendri, E. (2021). A Critical Review on the Analysis of Metal Soaps in Oil Paintings. *ChemistryOpen* **10**(9): 904–921. DOI: 10.1002/open.202100166.

Kaszowska, Z., Malek, K., Pańczyk, M., and Mikołajska, A. (2013). A joint application of ATR-FTIR and SEM imaging with high spatial resolution: Identification and distribution of painting materials and their degradation products in paint cross sections. *Vibrational Spectroscopy* **65**: 1–11. DOI: 10.1016/j.vibspec.2012.11.018.

Keune, K. and Boon, J. J. (2007). Analytical Imaging Studies of Cross-Sections of Paintings Affected by Lead Soap Aggregate Formation. *Studies in Conservation* **52**(3): 161–176. DOI: 10.1179/sic.2007.52.3.161.

Koch Dandolo, C. L., Detalle, V., Bodiguel, J.-B., Lopez, M., Bai, X., Martos-Levif, D., Genty-Vincent, A., et al. (2022). Insights into the Blanching of Water-Damaged Varnish by Means of Spectral-Domain Optical Coherence Tomography. *Studies in Conservation* **67**(3): 151–160. DOI: 10.1080/00393630.2020.1825901.

Koch Dandolo, C. L., Lopez, M., Bai, X., and Detalle, V. (2019). La tomographie en cohérence optique pour examiner les objets du patrimoine. *Photoniques* 95): 24–28. DOI: 10.1051/photon/20199524.

Komanecky, M. (1999). Copper as canvas: two centuries of masterpiece paintings on copper, 1575-1775. In: *Copper as canvas: two centuries of masterpiece paintings on copper, 1575-1775*. Ed. by Phoenix Art Museum, Nelson-Atkins Museum of Art, and Mauritshuis (Hague, Netherlands). New York: Oxford University Press. ISBN: 0-19-512397-2.

Mazzeo, R., Prati, S., Quaranta, M., Joseph, E., Kendix, E., and Galeotti, M. (2008). Attenuated total reflection micro FTIR characterisation of pigment–binder interaction in reconstructed paint films. *Analytical and Bioanalytical Chemistry* **392**(1): 65–76. DOI: 10.1007/s00216-008-2126-5.

Mecklenburg, M. F., Tumosa, C. S., and Vicenzi, E. P. (2013). The Influence of Pigments and Ion Migration on the Durability of Drying Oil and Alkyd Paints. In: *New Insights into the Cleaning of Paintings: Proceedings from the Cleaning 2010 International Conference, Universidad Politecnica de Valencia and Museum Conservation Institute*. Ed. by M. F. Mecklenburg, A. E. Charola, and R. J. Koestler. Washington, DC: Smithsonian Institution: Smithsonian Contributions to Museum Conservation: 59–67.

Miziolek, A. W., Palleschi, V., and Schechter, I. (2006). *Laser-induced breakdown spectroscopy (LIBS): fundamentals and applications*. ISBN: 978-0-511-54126-1.

Mousavi, S. J., Hemati Farsani, M., Darbani, S. M. R., Mousaviazar, A., Soltanolkotabi, M., and Eslami Majd, A. (2016). CN and C2 vibrational spectra analysis in molecular LIBS of organic materials. *Applied Physics B* **122**(5): 106. DOI: 10.1007/s00340-016-6371-6.

O'Haver, T. C. and Begley, T. (1981). Signal-to-noise ratio in higher order derivative spectrometry. *Analytical Chemistry* **53**(12): 1876–1878. DOI: 10.1021/ac00235a036.

Ortiz Miranda, A. S., Kronkright, D., and Walton, M. (2020). The influence of commercial primed canvases in the manifestation of metal soaps protrusions in Georgia O'Keeffe's oil paintings. *Heritage Science* **8**(1): 107. DOI: 10.1186/s40494-020-00451-7.

Osmond, G. (2019). Zinc Soaps: An Overview of Zinc Oxide Reactivity and Consequences of Soap Formation in Oil-Based Paintings. In: *Metal Soaps in Art*. Ed. by F. Casadio, K. Keune, P. Noble, A. Van Loon, E. Hendriks, S. A. Centeno, and G. Osmond. Cham: Springer International Publishing: 25–46. DOI: 10.1007/978-3-319-90617-1_2.

Pavlopoulou, L.-C. and Watkinson, D. (2006). The degradation of oil painted copper surfaces. *Studies in Conservation* **51** (sup1): 55–65. DOI: 10.1179/sic.2006.51.Supplement-1.55.

Ricca, M., Alberghina, M. F., Randazzo, L., Schiavone, S., Donato, A., Albanese, M. P., and La Russa, M. F. (2021). A Combined Non-Destructive and Micro-Destructive Approach to Solving the Forensic Problems in the Field of Cultural Heritage: Two Case Studies. *Applied Sciences* **11**(15): 6951. DOI: 10.3390/app11156951.

Rimer, B. W., Fiedler, I., Miller, M., Cunningham, M., and Jorrit D. J., v. d. B. (1999). Investigation of fatty acid migration in alizarin crimson oil paint in two works by Frank Stella. In: *Postprints (American Institute for Conservation of Historic and Artistic Works. Paintings Specialty Group)*.

Sadat, A. and Joye, I. J. (2020). Peak Fitting Applied to Fourier Transform Infrared and Raman Spectroscopic Analysis of Proteins. *Applied Sciences* **10**(17): 5918. DOI: 10.3390/app10175918.

Sasse, J. (2005). *Paint on metal: modern and contemporary explorations and discoveries, January 29 - May 1, 2005*. Arizona: Tucson Museum of Art. ISBN: 978-0-911611-30-4.

Stefas, D., Gyftokostas, N., Nanou, E., Kourelias, P., and Couris, S. (2021). Laser-Induced Breakdown Spectroscopy: An Efficient Tool for Food Science and Technology (from the Analysis of Martian Rocks to the Analysis of Olive Oil, Honey, Milk, and Other Natural Earth Products). *Molecules* **26**(16): 4981. DOI: 10.3390/molecules26164981.

Terenzi, M. G., Ferrucci, F., and Amadori, M. L. (2006). *Dipinti su rame: storia, tecnica, fenomeni di degrado, diagnostica, indicazioni per la conservazione e il restauro*. I talenti 19. Padova: Il prato. ISBN: 978-88-89566-36-7.

Vichi, A., Artesani, A., Cheung, C. S., Piccirillo, A., Comelli, D., Valentini, G., Poli, T., et al. (2019). An exploratory study for the noninvasive detection of metal soaps in paintings through optical coherence tomography. In: *Proceedings Volume 11058, Optics for Arts, Architecture, and Archaeology VII*. Münich 24-27 June 2019. Ed. by P. Targowski, R. Groves, and H. Liang: 4. DOI: 10.1117/12.2527569.

Sitography

Polyanskiy, M. (2022). *Optical constants of Ag (Silver)*. URL: https://refractiveindex.info/?shelf=main&book=Ag&page=Johnson (visited on 09/02/2022).

This page was intentionally left blank.

Chapter 5

General conclusions and future perspectives

General conclusions The work presented aimed to set the basis for developing a methodology for detecting and studying metal soaps on painted metal artefacts.

In particular, several non-invasive and micro-invasive analytical techniques (i.e., μ-FTIR, μ-Raman, XRD, HSI, IR thermography, OCT, LIBS) were tested on oil-coated copper and zinc model samples to evaluate their capability to detect metal soaps. The first step towards developing the protocol consisted of designing model samples with suitable physical characteristics (i.e., surface roughness, wettability) and chemical properties (i.e., metal ion's affinity to fatty acids). After a literature review, which included treaties from the 1700s describing good practices for painting on metals, the physical and chemical characteristics of the samples were examined qualitatively and quantitatively using a range of tools and techniques such as thickness measurement and laser scanning microscopy, which provided an estimation of the metal surface roughness before and after coating. It was established that brushed surfaces would favour the homogeneity of the linseed oil coating, confirming the indications provided by historical sources. Multivariate methods for data exploration and pattern recognition (PCA) were utilised to investigate the impact of the surface finishing on the FTIR signal, revealing that brushed samples would allow for better reproducibility of the measure compared to mirror-polished ones.

An ageing protocol was put in place to exert the reaction of the formation of metal soaps on coated samples. The ageing process was monitored using the selected analytical techniques, which consistently revealed differences in the reactivity of the two substrates. In detail, copper samples were found to produce crystalline metal soap phases at a later stage, when at all present.

2D FTIR chemical images showed an increasing trend of formation of metal soaps that would form immediately after the deposition of the coating. For zinc samples, the growth would happen mainly during the first days and then stay almost constant, whereas, for copper samples, the most significant production could be seen between 10 and 30 days of ageing at 80 °C and 80% RH values.

μ-Raman spectroscopy allowed to characterise metal soap types for both substrates, showing a prevalence of unsaturated soaps formed on the copper samples (oleate) compared to the zinc ones, where soaps from fatty acids having saturated chains were more common

(stearate and palmitate).

Finding a non-invasive approach for the study of the metal-oil interface was a fundamental step of this research, especially in light of the difficulties encountered in preparing cross-sections of the coated metals (see Chapter 2). Spectral domain-optical computed tomography (OCT) provided an opportunity to examine the interface between the metal and the oil non-invasively and to locate the presence of compounds in contact with the metal. The hypothesis that the layer of compounds observed could be related to the presence of metal soaps was corroborated by laser-induced breakdown spectroscopy (LIBS) analyses. Although the results ontained will need to be further investigated, the use of analytical techniques that enable the examination of the metal-oil interface revealed to be a key-point in the investigation of the degradation of painted metal surfaces.

Alternative approaches for detecting and monitoring metal soap formation were considered and tested. In particular, grazing angle X-ray diffraction (XRD) showed high potential in studying the crystalline phases forming in the samples. However, from the preliminary tests, it was noticed that the analytical parameters should be accurately chosen to lower the diffraction patterns' intensity of the bulk metal and enhance possible signals due to metal soaps formation. An IR thermal camera and hyperspectral imaging cameras operating in the visible-near infrared and short-wave infrared ranges were employed to search for possible indicators of the presence of metal soaps within the thermograms and the reflectance spectra. From a first analysis of the results, it would appear that these two methods mostly provided information related to the thickness of the coating rather than the presence of absence of the searched compounds, and would require more testing and investigation.

Future perspectives This study paved the way to understanding the degradation mechanism due to metal soap formation on coated metals. Future efforts should be devoted to complement the results obtained and optimise the preliminary analytical protocol. In particular, it would be important to explore different resolutions and setups to obtain a standardised protocol starting from the preliminary results presented within this work, taking into consideration the singularities of the different case studies.

For what concerns the sample preparation for stratigraphy studies, that would permit direct investigation of the different layers, i.e., metal, interface, oil, using a range of analytical imaging techniques (e.g., SEM, μ-FTIR, μ-Raman), a method using a microtome is envisioned to create cross-sections and thin-sections of the model samples and enable direct analysis and monitoring of the interface. The preparation of thin sections suitable for a multitude of applications using microtomes is a common practice in many laboratories, including synchrotron facilities.

Synchrotron radiation applications could also be explored since this source presents several advantages; being highly collimated, it provides increased resolution in measurement due to its spatial precision. In particular, synchrotron radiation X-ray diffraction mapping (2D-SR-XRD) would be of interest for the characterisation and monitoring of the different phases and geometries of the formed soaps (Gonzalez et al., 2020; Janssens and Cotte, 2020). A pilot study has been initiated at the recently developed alternative access modality to the European Synchrotron Radiation Facility (ESRF) beamtime, i.e., the *Block Allocation Group (BAG)* mode, particularly the newly implemented "historical materials BAG" facilities (Cotte et al., 2022).

Given the results of the FTIR spectroscopy, VNIR, and SWIR hyperspectral imaging (HSI), Mid-wave infrared hyperspectral imaging (MWIR-HSI) could be promising for the study of painted metals since it would conjugate the potentialities of the hyperspectral cameras (e.g., simultaneous spatial and spectral information and versatility) with the ones given by analysis in the mid-infrared spectral range. Over the past ten years, MWIR-HSI acquisitions and the related post-processing of hypercubes have been explored more in-depth in the conservation discipline. Nevertheless, there still remains a paucity of information in the literature, especially regarding descriptions of systems and setups, and standards for acquiring and interpreting data. To date, the pioneering works of (Rosi et al., 2013a; Rosi et al., 2013b) and the review by (Catelli et al., 2019) remain two of the most holistic approaches. The latest study (Sandak et al., 2021) demonstrates the promising use of VNIR, SWIR and MWIR-HSI when used synergically. All the works on MWIR-HSI found in the literature focus on the identification and mapping of pigments and binders on varnished oil paintings or manuscripts (Catelli et al., 2019). In contrast, there has not hitherto been any work focusing on the study of the degradation products on painted metal artworks using MWIR-HSI, and especially not on unvarnished oil paintings on different kinds of supports[1].

The analytical approach discussed in this doctoral thesis relied on the use of model samples for the identification of metal soaps and the understanding of their formation. An evolution of this methodology would entail the validation of the results on case studies from museum or private collections. For this purpose, a collaboration has been established with the Musée du Louvre (France) concerning the investigation of selected original and imitation paintings on metal by Flemish artist J. Brueghel the Elder (1568 – 1625).

Further experiments would encompass the in-depth investigation of possible competition between metal substrates and mineral pigments in providing metal ions for the reaction with fatty acids that results in metal soap formation. To do so, an approach could consist in preparing dedicated model samples by painting copper and zinc substrates with zinc and copper–based oil formulations with their combinations and permutations, as shown in Figure 5.1[2]. Additionally, computational approaches to the study of the reaction could allow for the development of mathematical models for predictive analysis that could describe the expected outcomes in terms of the formation of the species and consequent degradation when the variable *time* is considered in the model. Some work in this direction was performed recently, which concerned the prediction of the chemo-mechanical degradation of oil paintings on canvas (Eumelen et al., 2019), and that could represent the basis to develop similar studies specific to painted metals.

Similarly, the formation of other heavy metal soaps (e.g., iron soaps) should be further investigated by designing experiments in which significant variables, such as the initial

[1] In November 2021, an application titled *MOCKED-UP: Mapping of Organic Compounds as Key Elements of Degradation in Unvarnished Paintings* was submitted to the Hyperion HS consortium, that is awaiting review at the current date and would grant access to the MWIR-HSI facilities at the IPANEMA fixlab in France. This application was co-authored with ITN-CHANGE fellow Jan Cutajar (ESR10) and was designed to investigate degradation products resulting from metal soap formation and soiling on unvarnished paintings on canvas and metal through MWIR-HSI.

[2] A pilot study is ongoing in collaboration with the Soleil French national Synchrotron facilities (AILES beamline. The project was written in collaboration with Nicoletta Palladino (C2RMF/IPANEMA/ Université Paris-Saclay), and under the supervision of Dr. Brubach Jean-blaise), and aimed to investigate the interaction pigment-binder of zinc white paints on different supports (i.e., canvas and metal) upon natural and accelerated ageing in the far- and mid-infrared spectral ranges (FIR/MIR).

metal salts, pH, temperature and relative humidity values, are varied.

Another development of this project could concern the extraction of information from the data acquired using data fusion algorithms. This approach would allow the unification of data from different modalities and resolutions. Due to the heterogeneity of the data collected, data mining approaches should also be explored through the establishment of collaborations involving diverse expertise that could help entangle this challenging aspect common to most multi-modal methodologies to cultural heritage queries.

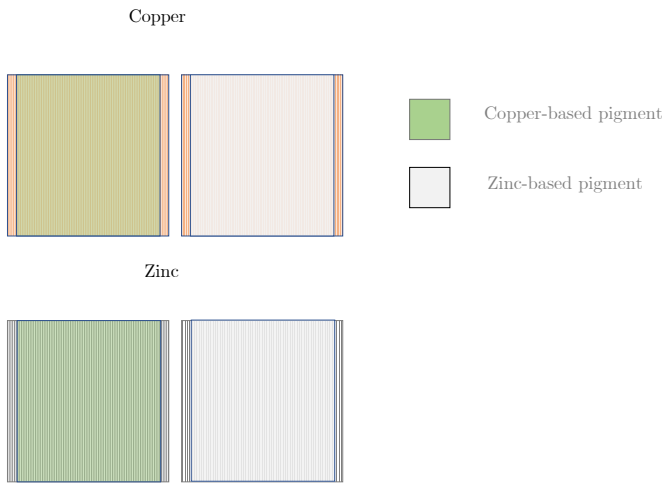

Figure 5.1: Future experiments aimed to investigate the competition between pigments and metal substrates in the formation of metal soaps.

Bibliography

Catelli, E., Sciutto, G., Prati, S., and Mazzeo, R. (2019). MID-FTIR macro mapping and clustering-based automatic brushing: an advanced diagnostic tool for in situ investigations of artworks. In: *Proceedings Volume 11058, Optics for Arts, Architecture, and Archaeology VII*. Münich, 24-27 June 2019. Ed. by P. Targowski, R. Groves, and H. Liang: 26. DOI: 10.1117/12.2526117.

Cotte, M., Gonzalez, V., Vanmeert, F., Monico, L., Dejoie, C., Burghammer, M., Huder, L., et al. (2022). The "Historical Materials BAG": A New Facilitated Access to Synchrotron X-ray Diffraction Analyses for Cultural Heritage Materials at the European Synchrotron Radiation Facility. *Molecules* **27**(6): 1997. DOI: 10.3390/molecules27061997.

Eumelen, G., Bosco, E., Suiker, A., Loon, A. van, and Iedema, P. (2019). A computational model for chemo-mechanical degradation of historical oil paintings due to metal soap formation. *Journal of the Mechanics and Physics of Solids* **132**: 103683. DOI: 10.1016/j.jmps.2019.103683.

Gonzalez, V., Cotte, M., Vanmeert, F., Nolf, W., and Janssens, K. (2020). X-ray Diffraction Mapping for Cultural Heritage Science: a Review of Experimental Configurations and Applications. *Chemistry – A European Journal* **26**(8): 1703–1719. DOI: 10.1002/chem.201903284.

Janssens, K. and Cotte, M. (2020). Using Synchrotron Radiation for Characterization of Cultural Heritage Materials. In: *Synchrotron Light Sources and Free-Electron Lasers*. Ed. by E. J. Jaeschke, S. Khan, J. R. Schneider, and J. B. Hastings. Cham: Springer International Publishing: 2457–2483. DOI: 10.1007/978-3-030-23201-6_78.

Rosi, F., Harig, R., Miliani, C., Braun, R., Sali, D., Daveri, A., Brunetti, B. G., et al. (2013a). Mid-infrared hyperspectral imaging of painting materials. In: *Proceedings Volume 8790, Optics for Arts, Architecture, and Archaeology IV*. Münich, 13-16 May 2013. Ed. by L. Pezzati and P. Targowski: 87900Q. DOI: 10.1117/12.2020477.

Rosi, F., Miliani, C., Braun, R., Harig, R., Sali, D., Brunetti, B. G., and Sgamellotti, A. (2013b). Noninvasive Analysis of Paintings by Mid-infrared Hyperspectral Imaging. *Angewandte Chemie International Edition* **52**(20): 5258–5261. DOI: 10.1002/anie.201209929.

Sandak, J., Sandak, A., Legan, L., Retko, K., Kavčič, M., Kosel, J., Poohphajai, F., et al. (2021). Nondestructive Evaluation of Heritage Object Coatings with Four Hyperspectral Imaging Systems. *Coatings* **11**(2): 244. DOI: 10.3390/coatings11020244.

This page was intentionally left blank.

S

Supplementary materials

This page was intentionally left blank.

Table S - 1: Summary of all samples prepared and commented throughout the manuscript. The colour coding indicates the chapter(s) and sections concerned.

● Chapter 2 - Model samples ● Chapter 3 - Detection ● Chapter 4 - Understanding formation

Sample	Coating method	Accelerated ageing (1 month)		3D laser scanning microscopy	FTIR	Raman	OCT	LIBS	XRD	IR Thermography	SEM	HSI	Colorimetry
Fe01	N/A	1uL PA - 7.8x10-2	(choice of substrate)		(choice of substrate)								
Fe02	N/A	1uL PA - 7.8x10-2	(choice of substrate)		(choice of substrate)								
Al01	N/A	1uL PA - 7.8x10-2	(choice of substrate)		(choice of substrate)								
Al02	N/A	1uL PA - 7.8x10-2	(choice of substrate)		(choice of substrate)								
Cu01	N/A	1uL PA - 7.8x10-2	(choice of substrate)		(choice of substrate)								
Cu02	N/A	1uL PA - 7.8x10-2	(choice of substrate)		(choice of substrate)								
Cu03	Spatula	20-30°C / 70-80% (NaCl, aq)	(ageing protocol)		(ageing protocol)								
Cu04	Spatula	20-30°C / 70-80% (NaCl, aq)	(ageing protocol)		(ageing protocol)								
					(ageing protocol)								
					up to 22m (detection)								
Cu07	Spatula	80°C / 70-80% (glycerol-water solution)	(ageing protocol)		up to 22m (understanding)	26m (detection)	20m (understanding)	21m (understanding)		21m (detection)		14m (detection)	14m (detection)
					(ageing protocol)								
					up to 22m (detection)								
Cu08	Spatula	80°C / 70-80% (glycerol-water solution)	(ageing protocol)		up to 22m (understanding)		20m (understanding)	21m (understanding)			12m (SEM)	14m (detection)	14m (detection)
					(ageing protocol)								
					up to 22m (detection)								
Cu09	Spatula	80°C / 70-80% (glycerol-water solution)	(ageing protocol)		up to 22m (understanding)		20m (understanding)	21m (understanding)				14m (detection)	14m (detection)
					up to 48 hours (signal evaluation)								
Cu25	Spatula	5x1uL PA - 7.8x(10-5, 10-4, 10-3, 10-2), 3.9x10-2	(signal evaluation)		up to 13m (correlation FA-MS)					21m (detection)		14m (detection)	14m (detection)
Cu28	Spatula	5x1uL PA - 7.8x(10-5, 10-4, 10-3, 10-2), 3.9x10-2	(signal evaluation)										
Cu31	N/A								(detection)				
					up to 6m (detection)								
Cu35	Spin-coating	60°C / 70-80% (silica beads)	(ageing protocol)	(surface finishing)	(understanding)	up to 10m (detection)	4m (understanding)	5m (understanding)		5m (detection)			
					up to 6m (detection)								
Cu36	Spin-coating	60°C / 70-80% (silica beads)	(ageing protocol)	(surface finishing)	(understanding)		4m (understanding)	5m (understanding)					
					up to 6m (detection)								
Cu37	Spin-coating	60°C / 70-80% (silica beads)	(ageing protocol)	(surface finishing)	(understanding)		4m (understanding)	5m (understanding)					
					up to 6m (detection)								
Cu38	Spin-coating	uncontrolled indoors conditions	(ageing protocol)	(surface finishing)	(understanding)		4m (understanding)	5m (understanding)		5m (detection)			
					up to 6m (detection)								
Cu39	Spin-coating	uncontrolled indoors conditions	(ageing protocol)	(surface finishing)	(understanding)		4m (understanding)	5m (understanding)					
Cu40	Spin-coating												
Cu41	Spin-coating												
Cu43	Spin-coating												
Cu44	Spin-coating												
Cu45	Dip-coating								9m (detection)				
Cu46	Dip-coating												
					up to 6m (detection)								
Cu47	Spin-coating	uncontrolled indoors conditions	(ageing protocol)	(surface finishing)	(understanding)		4m (understanding)	5m (understanding)					
Zn01	N/A	1uL PA - 7.8x10-2	(choice of substrate)		(choice of substrate)								
Zn02	N/A	1uL PA - 7.8x10-2	(choice of substrate)		(choice of substrate)								
Zn03	Spatula	20-30°C / 70-80% (NaCl, aq)	(ageing protocol)		(ageing protocol)								
Zn04	Spatula	20-30°C / 70-80% (NaCl, aq)	(ageing protocol)		(ageing protocol)								
					(ageing protocol)								
					up to 17m (detection)								
Zn08	Spatula	80°C / 70-80% (glycerol-water solution)	(ageing protocol)		up to 17m (understanding)	21m (detection)	15m (understanding)	16m (understanding)		16m (detection)		9m (detection)	9m (detection)
					(ageing protocol)								
					up to 17m (detection)								
Zn09	Spatula	80°C / 70-80% (glycerol-water solution)	(ageing protocol)		up to 17m (understanding)		15m (understanding)	16m (understanding)				9m (detection)	9m (detection)
					(ageing protocol)								
					up to 17m (detection)								
Zn10	Spatula	80°C / 70-80% (glycerol-water solution)	(ageing protocol)		up to 17m (understanding)		15m (understanding)	16m (understanding)			7m (SEM)	9m (detection)	9m (detection)
Zn26	N/A								(detection)				
Zn27	Spatula	5x1uL PA - 7.8x(10-5, 10-4, 10-3, 10-2), 3.9x10-2	(signal evaluation)										
					up to 6m (detection)								
Zn31	Spin-coating	60°C / 70-80% (silica beads)	(ageing protocol)	(surface finishing)	(understanding)	up to 10m (detection)	4m (understanding)	5m (understanding)		5m (detection)			
					up to 6m (detection)								
Zn32	Spin-coating	60°C / 70-80% (silica beads)	(ageing protocol)	(surface finishing)	(understanding)	up to10m (detection)	4m (understanding)	5m (understanding)					
					up to 6m (detection)								
Zn33	Spin-coating	60°C / 70-80% (silica beads)	(ageing protocol)	(surface finishing)	(understanding)		4m (understanding)	5m (understanding)					
					up to 6m (detection)								
Zn34	Spin-coating	60°C / 70-80% (silica beads)	(ageing protocol)	(surface finishing)	(understanding)		4m (understanding)	5m (understanding)		5m (detection)			
					up to 6m (detection)								
Zn35	Spin-coating	60°C / 70-80% (silica beads)	(ageing protocol)	(surface finishing)	(understanding)		4m (understanding)	5m (understanding)					
Zn36	Spin-coating												
Zn37	Spin-coating												
					up to 6m (detection)								
Zn38	Spin-coating	60°C / 70-80% (silica beads)	(ageing protocol)	(surface finishing)	(understanding)		4m (understanding)	5m (understanding)					
Zn45	Spin-coating												
Zn46	Spin-coating								9m (detection)				
Zn48	Dip-coating												
Zn49	Dip-coating												
Cu00_polished	Spatula			(surface finishing)									
Cu01_polished	Spin-coating												
Cu02_polished	Spin-coating												
Cu03_polished	Dip-coating												
Cu04_polished	Dip-coating												
Zn01_polished	Spin-coating												
Zn02_polished	Spin-coating												
Zn03_polished	Dip-coating												
Zn04_polished	Dip-coating												
Cu01_polished_drop	Spatula	5x1uL PA - 7.8x(10-5, 10-4, 10-3, 10-2), 3.9x10-2	(signal evaluation)		up to 48 hours (signal evaluation)								
Cu02_polished_drop	Spatula	5x1uL PA - 7.8x(10-5, 10-4, 10-3, 10-2), 3.9x10-2	(signal evaluation)										
Zn01_polished_drop	Spatula	5x1uL PA - 7.8x(10-5, 10-4, 10-3, 10-2), 3.9x10-2	(signal evaluation)										
Zn02_polished_drop	Spatula	5x1uL PA - 7.8x(10-5, 10-4, 10-3, 10-2), 3.9x10-2	(signal evaluation)										
DoE_1	Spatula	uncontrolled indoors conditions	(DoE)		(DoE)								
DoE_2	Spatula	uncontrolled indoors conditions	(DoE)		(DoE)								
DoE_3	Spatula	uncontrolled indoors conditions	(DoE)		(DoE)								
DoE_4	Spatula	uncontrolled indoors conditions	(DoE)		(DoE)								
DoE_5.1	Spatula	uncontrolled indoors conditions	(DoE)		(DoE)								
DoE_6	Spatula	uncontrolled indoors conditions	(DoE)		(DoE)								
DoE_7	Spatula	uncontrolled indoors conditions	(DoE)		(DoE)								
DoE_8	Spatula	uncontrolled indoors conditions	(DoE)		(DoE)								
DoE_9	Spatula	80°C / 80% RH	(DoE)		(DoE)								
DoE_10	Spatula	80°C / 80% RH	(DoE)		(DoE)								
DoE_11.1	Spatula	80°C / 80% RH	(DoE)		(DoE)								
DoE_12	Spatula	80°C / 80% RH	(DoE)		(DoE)								
DoE_13	Spatula	80°C / 80% RH	(DoE)		(DoE)								
DoE_14	Spatula	80°C / 80% RH	(DoE)		(DoE)								
DoE_15	Spatula	80°C / 80% RH	(DoE)		(DoE)								
DoE_16	Spatula	80°C / 80% RH	(DoE)		(DoE)								
DoE_17	Spatula	room temperature / 80% RH	(DoE)		(DoE)								
DoE_18	Spatula	room temperature / 80% RH	(DoE)		(DoE)								
DoE_19	Spatula	room temperature / 80% RH	(DoE)		(DoE)								
DoE_20	Spatula	room temperature / 80% RH	(DoE)		(DoE)								
DoE_21	Spatula	room temperature / 80% RH	(DoE)		(DoE)								
DoE_22	Spatula	room temperature / 80% RH	(DoE)		(DoE)								
DoE_23	Spatula	room temperature / 80% RH	(DoE)		(DoE)								
DoE_24.1	Spatula	room temperature / 80% RH	(DoE)		(DoE)								
DoE_5.2	Spatula	uncontrolled indoors conditions	(DoE)		(DoE)								
DoE_11.2	Spatula	80°C / 80% RH	(DoE)		(DoE)								
DoE_24.2	Spatula	room temperature / 80% RH	(DoE)		(DoE)								
Cu_XRD_01	N/A	10x3.9x10-2 (5 days)							up to 72h (detection)				
Zn_XRD_01	N/A	10x3.9x10-2 (5 days)							up to 72h (detection)				
Cu_DoE_drop_1	Spatula	5x1uL PA - 7.8x(10-5, 10-4, 10-3, 10-2)			up to 28h (correlation FA-MS)								
Zn_DoE_drop_2	Spatula	5x1uL PA - 7.8x(10-5, 10-4, 10-3, 10-2)			up to 28h (correlation FA-MS)								
DoE_drop_5 (Cu)	Spatula	3.9x10-2							7m (detection)				
DoE_drop_6 (Zn)	Spatula	3.9x10-2							7m (detection)				

This page was intentionally left blank.

S.1 Chapter 1

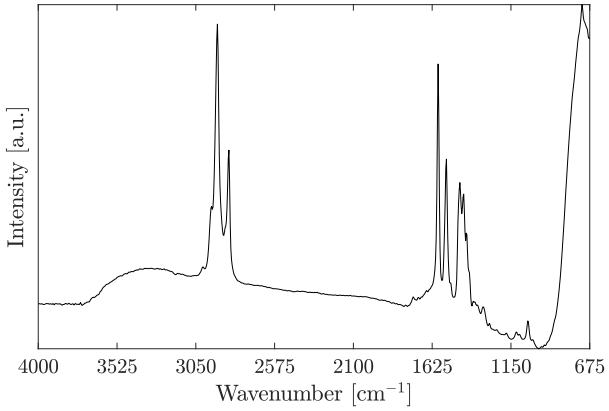

Figure S - 1: FTIR spectrum of object number 11127b.

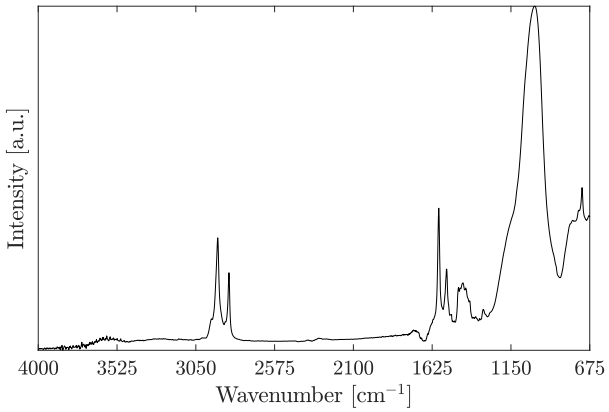

Figure S - 2: FTIR spectrum of object number 11127c.

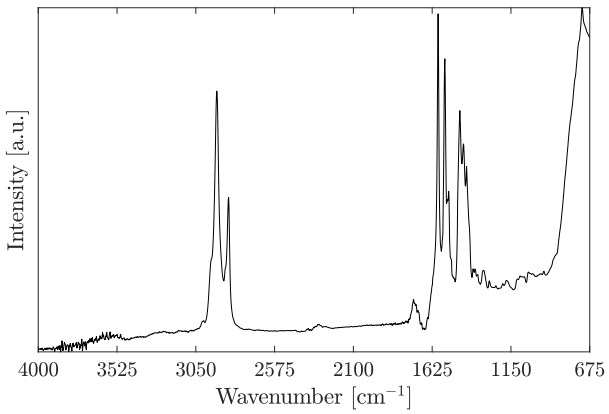

Figure S - 3: FTIR spectrum of object number 11127d.

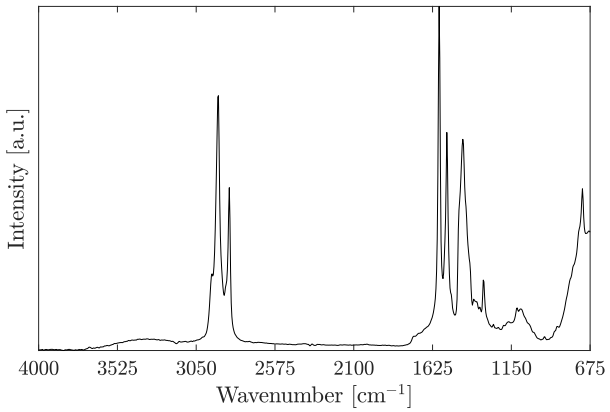

Figure S - 4: FTIR spectrum of object number 09733b.

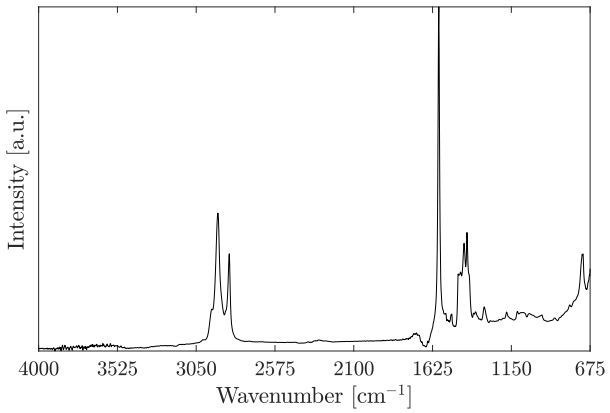

Figure S - 5: FTIR spectrum of object number 12137c.

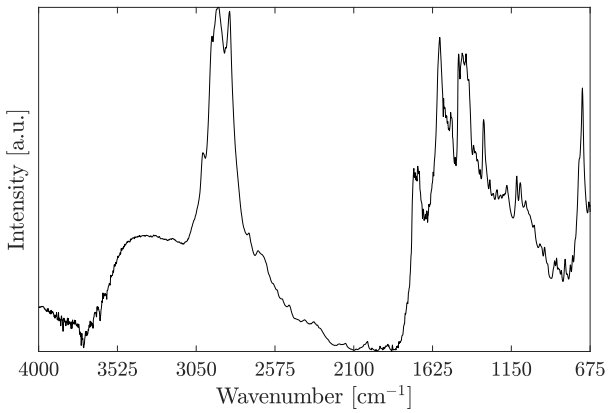

Figure S - 6: FTIR spectrum of object number 11228b.

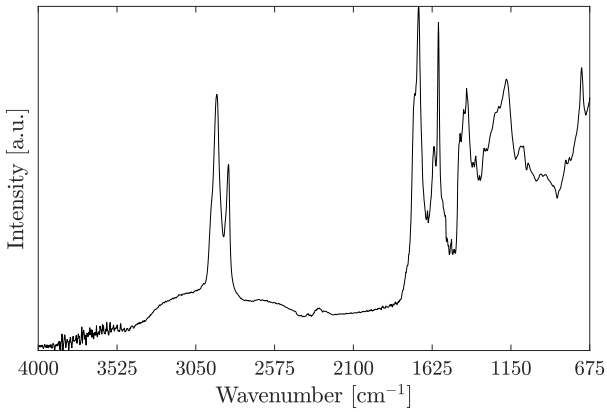

Figure S - 7: FTIR spectrum of object number 10315.

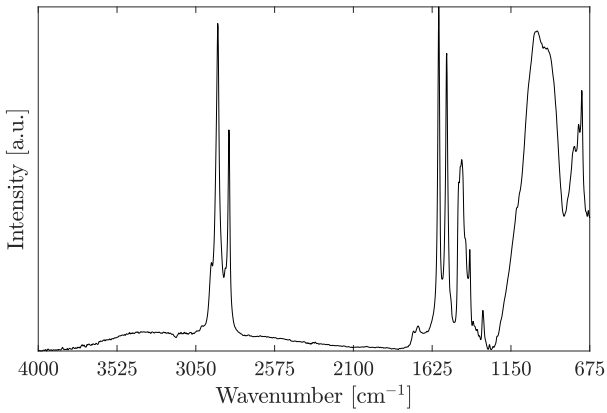

Figure S - 8: FTIR spectrum of object number oNr. 0563.

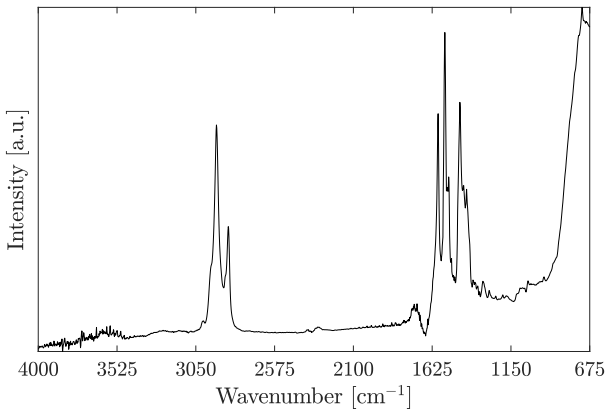

Figure S - 9: FTIR spectrum of object number oNr. 0564.

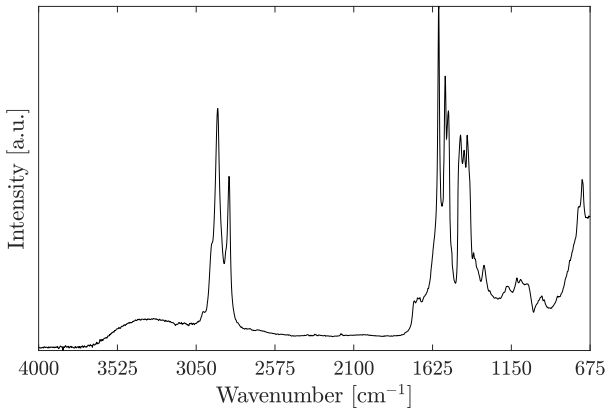

Figure S - 10: FTIR spectrum of object number oNr. 4096.

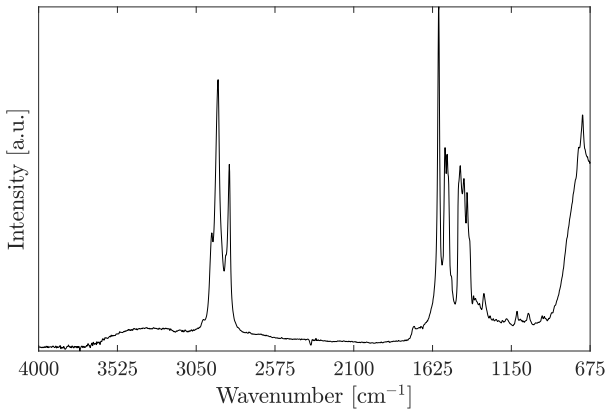

Figure S - 11: FTIR spectrum of object number 12205e.

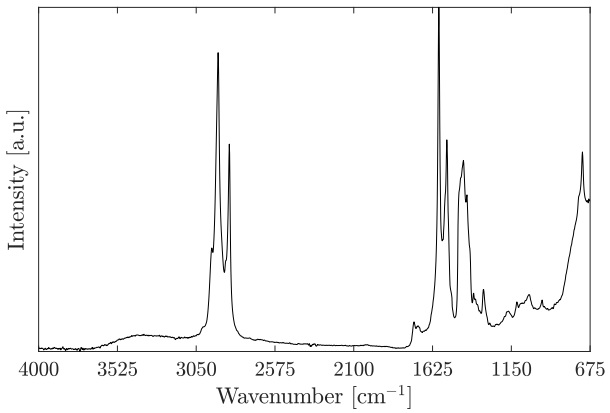

Figure S - 12: FTIR spectrum of object number 17982.

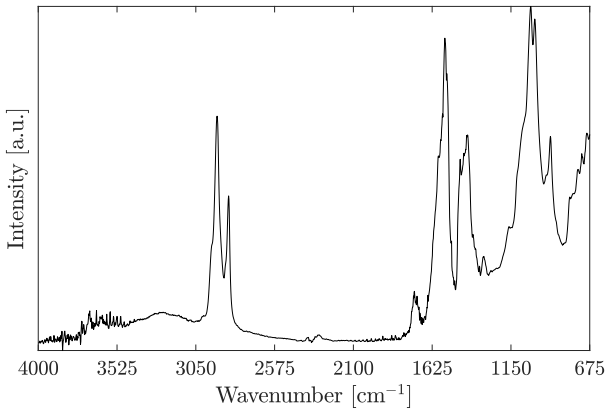

Figure S - 13: FTIR spectrum of object number 12687.

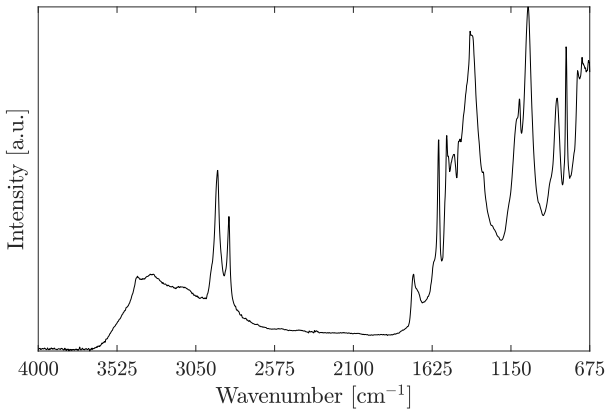

Figure S - 14: FTIR spectrum of object number MJ.1989.61.

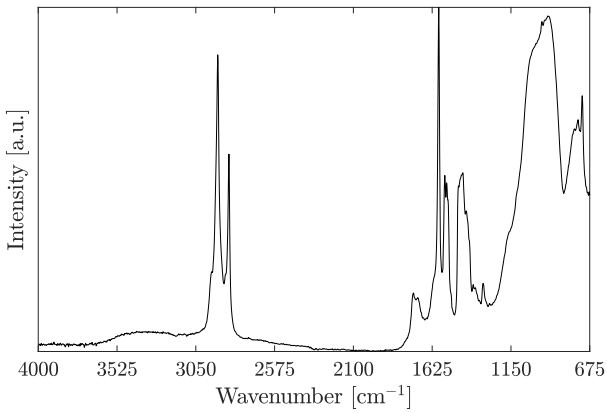

Figure S - 15: FTIR spectrum of 'pochette'.

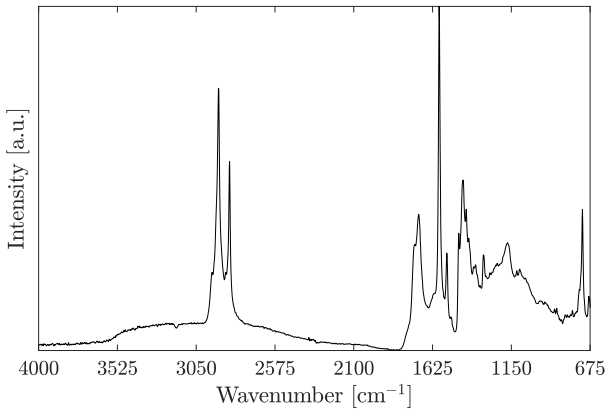

Figure S - 16: FTIR spectrum of 'cartonnier'.

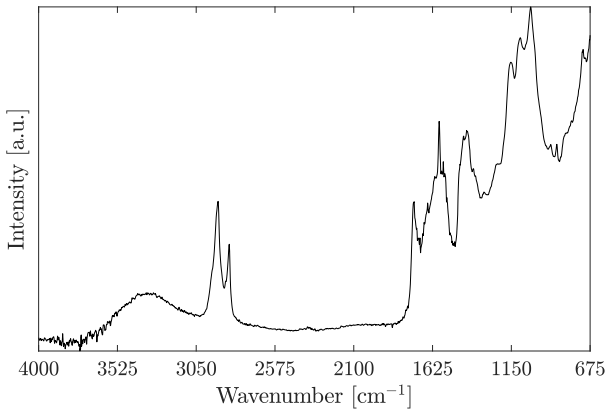

Figure S - 17: FTIR spectrum of object number D.131.

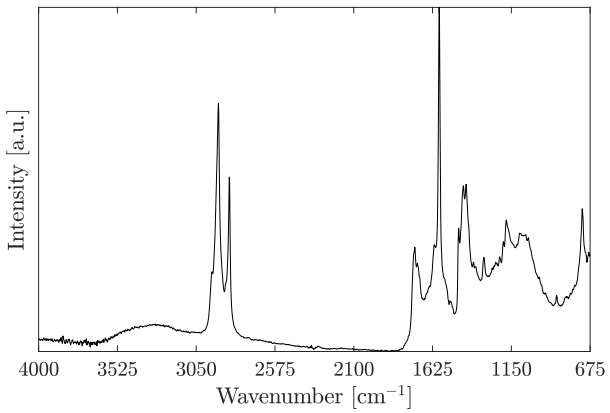

Figure S - 18: FTIR spectrum of object number D.130.

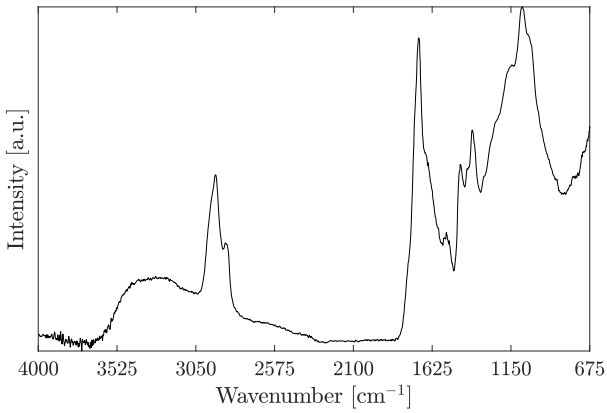

Figure S - 19: FTIR spectrum of 'St. Therese of Avila'.

S.2 Chapter 2

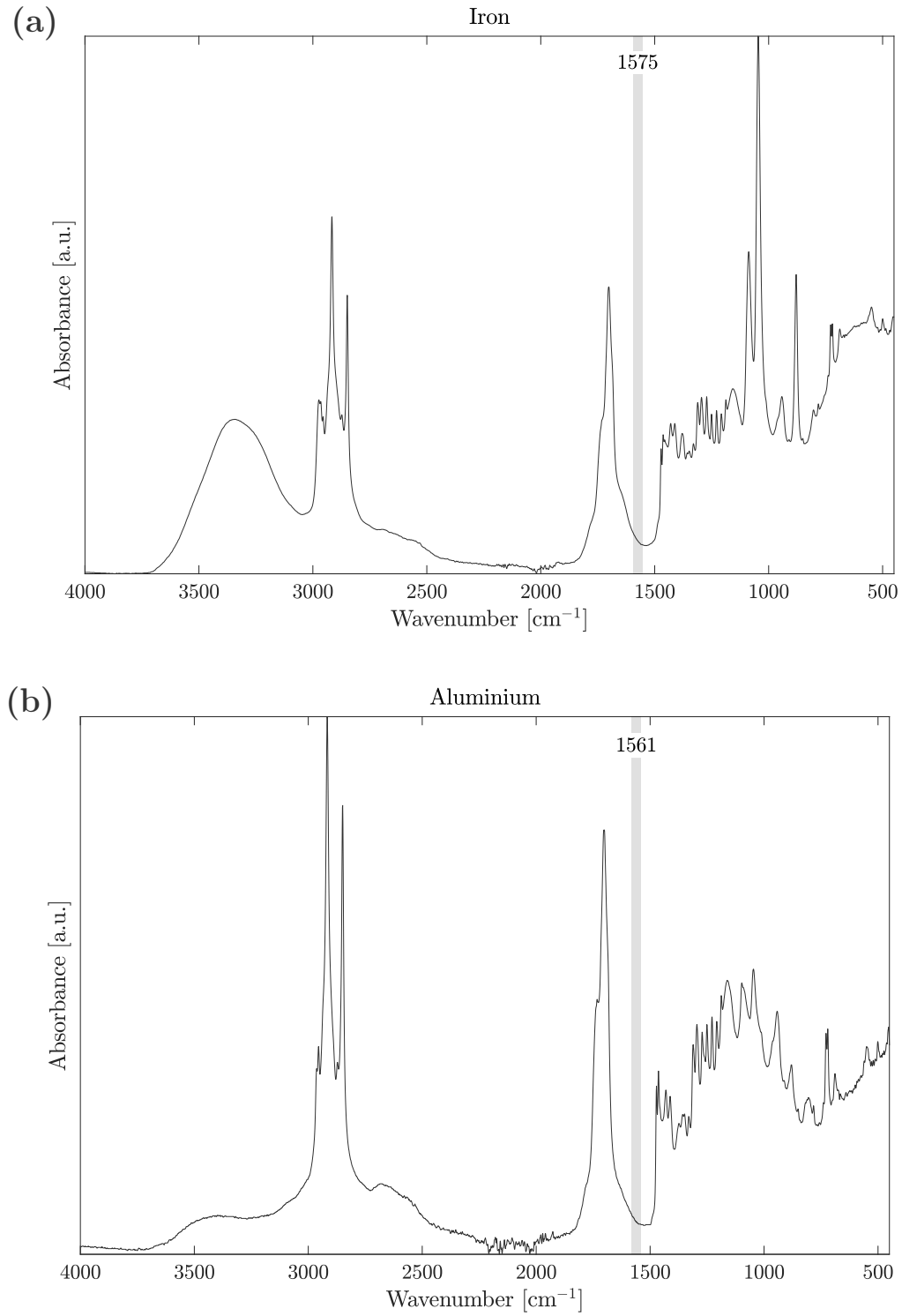

Figure S - 20: FTIR spectra of (a) iron (Fe01) (b) aluminium (Al01) coupons after reaction overnight with palmitic acid. The characteristic peak for the carboxylate group vibrational mode $\nu_a COO^-$ is highlighted by the shaded area.

S.3 Chapter 3

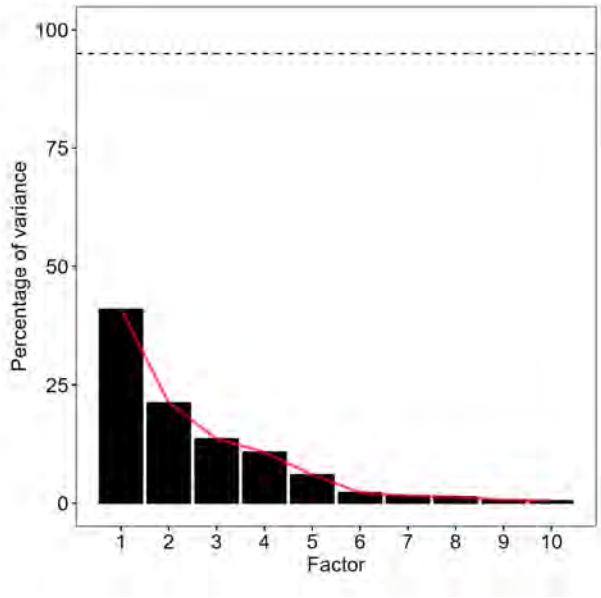

Figure S - 21: Scree plot of the hair-brushed copper sample (Cu25).

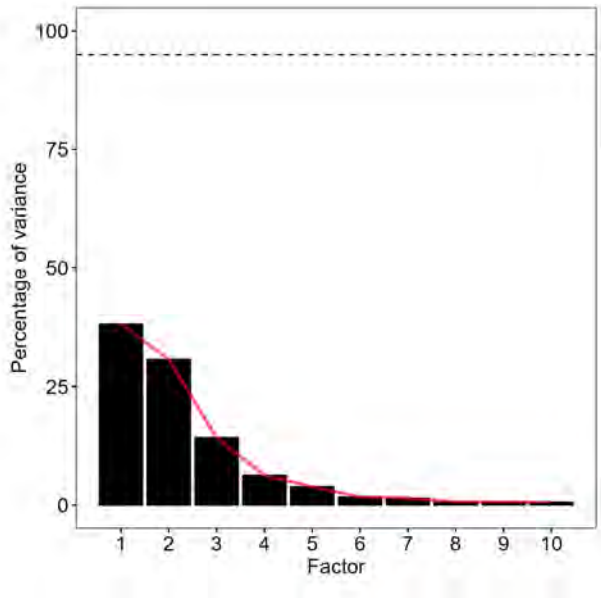

Figure S - 22: Scree plot of the polished copper sample (Cu01_polished_drop).

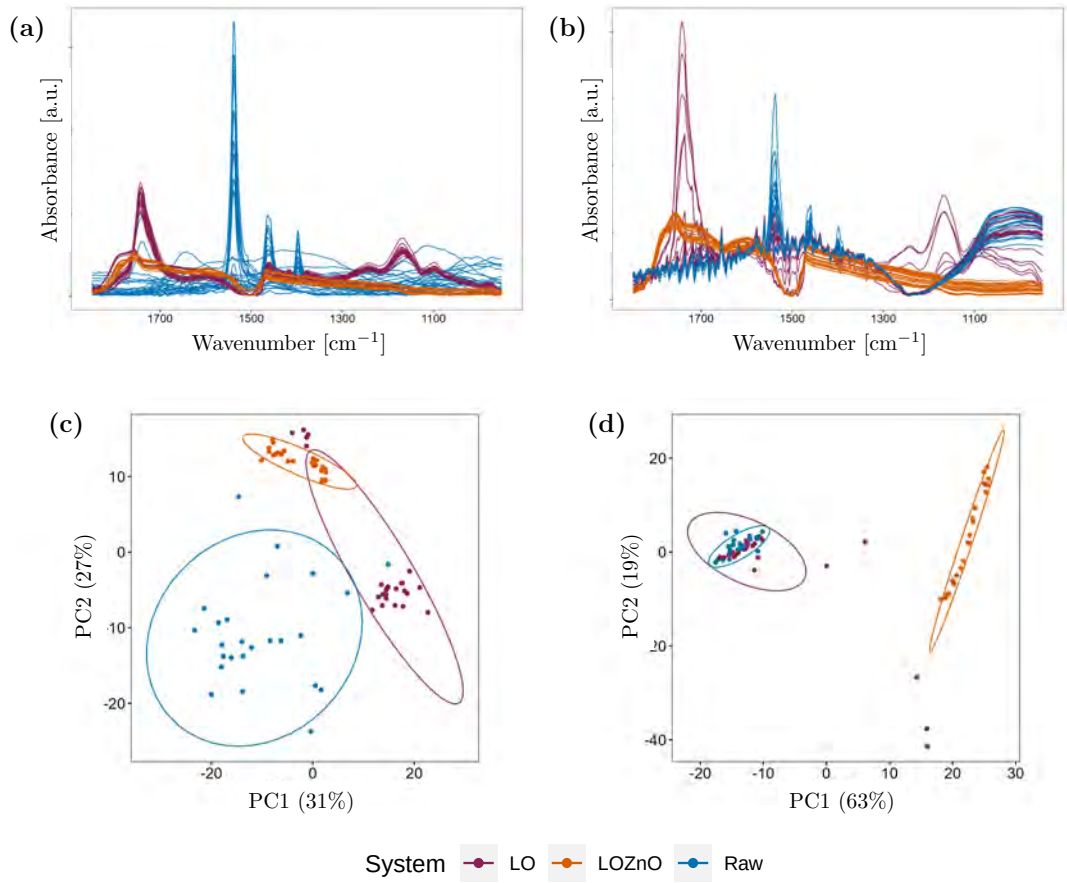

Figure S - 23: Results of the PCA analysis on the zinc hair-brushed (Zn27, left) and mirror-polished (Zn01_polished_drop, right) samples. (a) and (b) show the FTIR spectra acquired and cropped to highlight the region of interest ($1850 - 950$ cm^{-1}); (c) and (d) show the score plots for hair-brushed and mirror-polished samples, respectively.

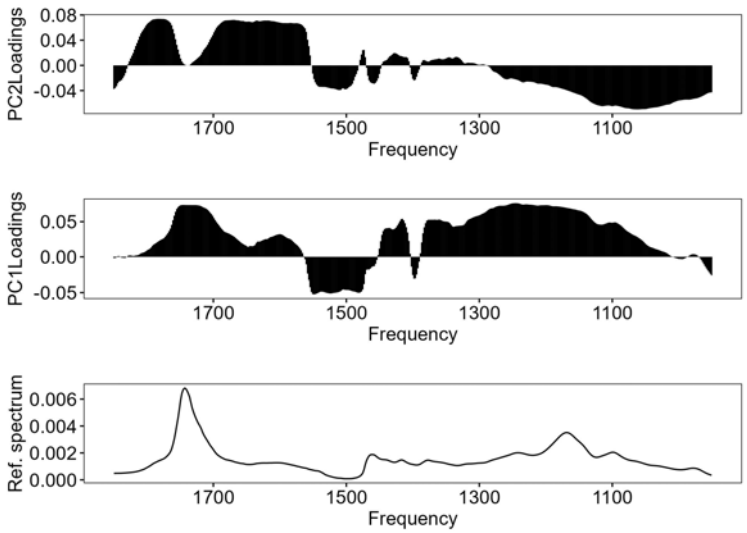

Figure S - 24: PCA loadings associated with the hair-brushed zinc sample (Zn27).

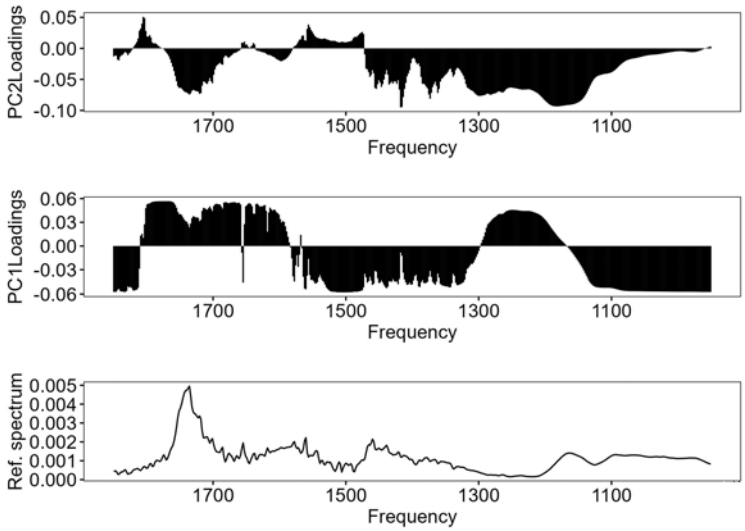

Figure S - 25: PCA loadings associated with the polished zinc sample (Zn01_polished_drop).

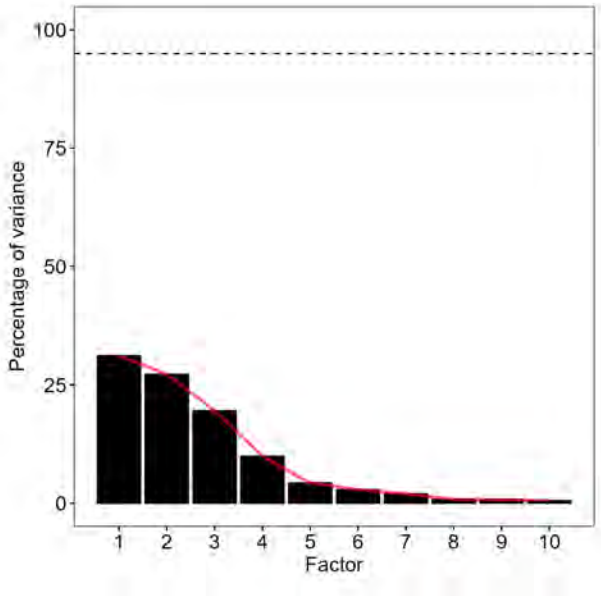

Figure S - 26: Scree plot of the hair-brushed zinc sample (Zn27).

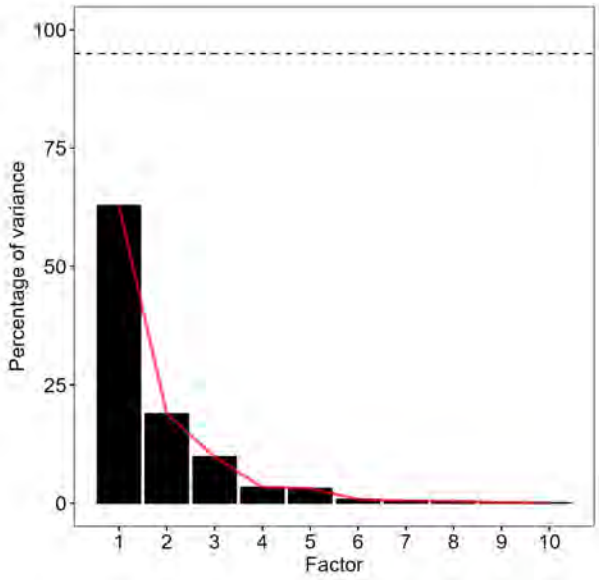

Figure S - 27: Scree plot of the polished zinc sample (Zn01_polished_drop).

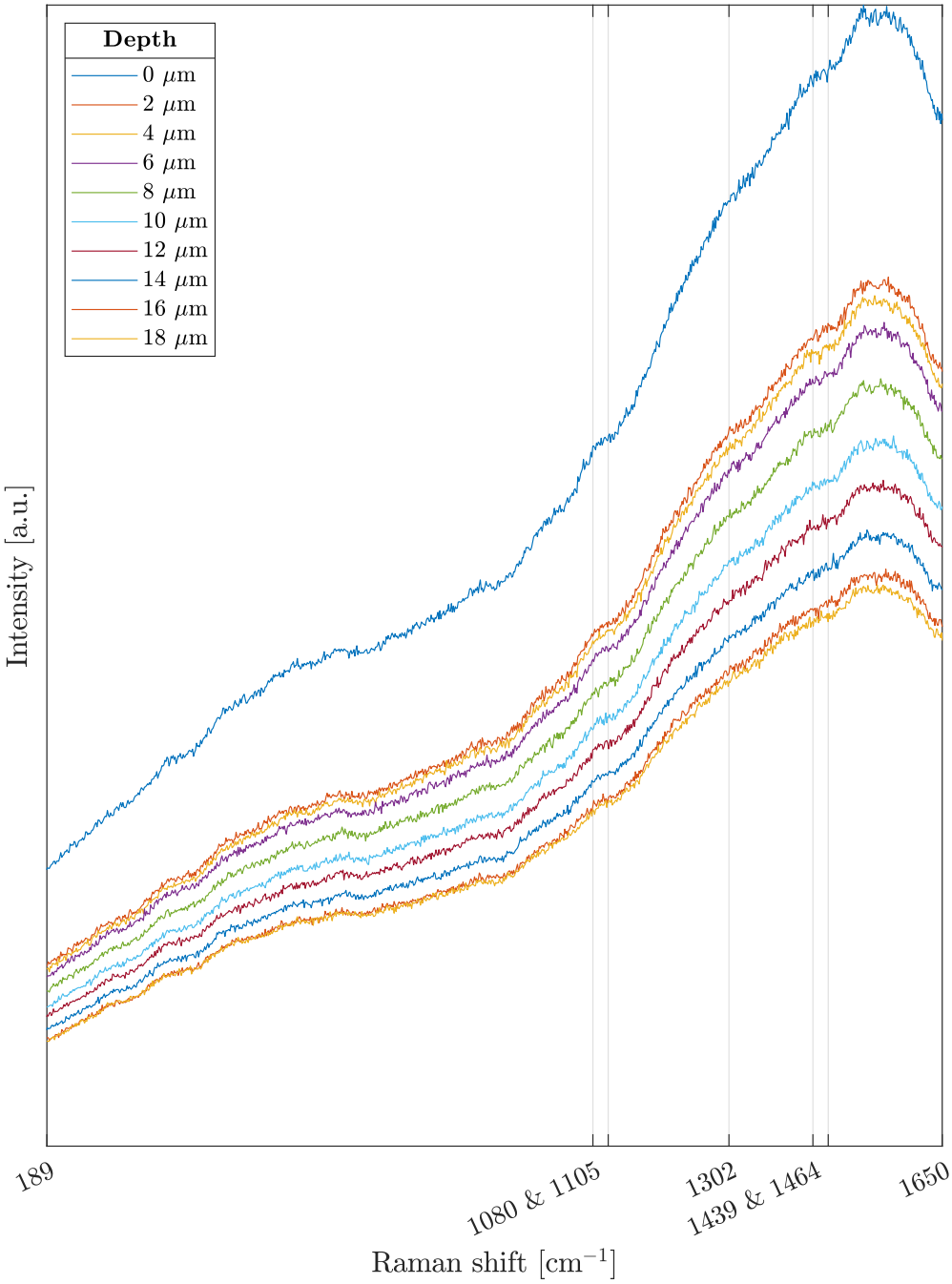

Figure S - 28: Raman depth profile for Cu35 (70 days ageing).

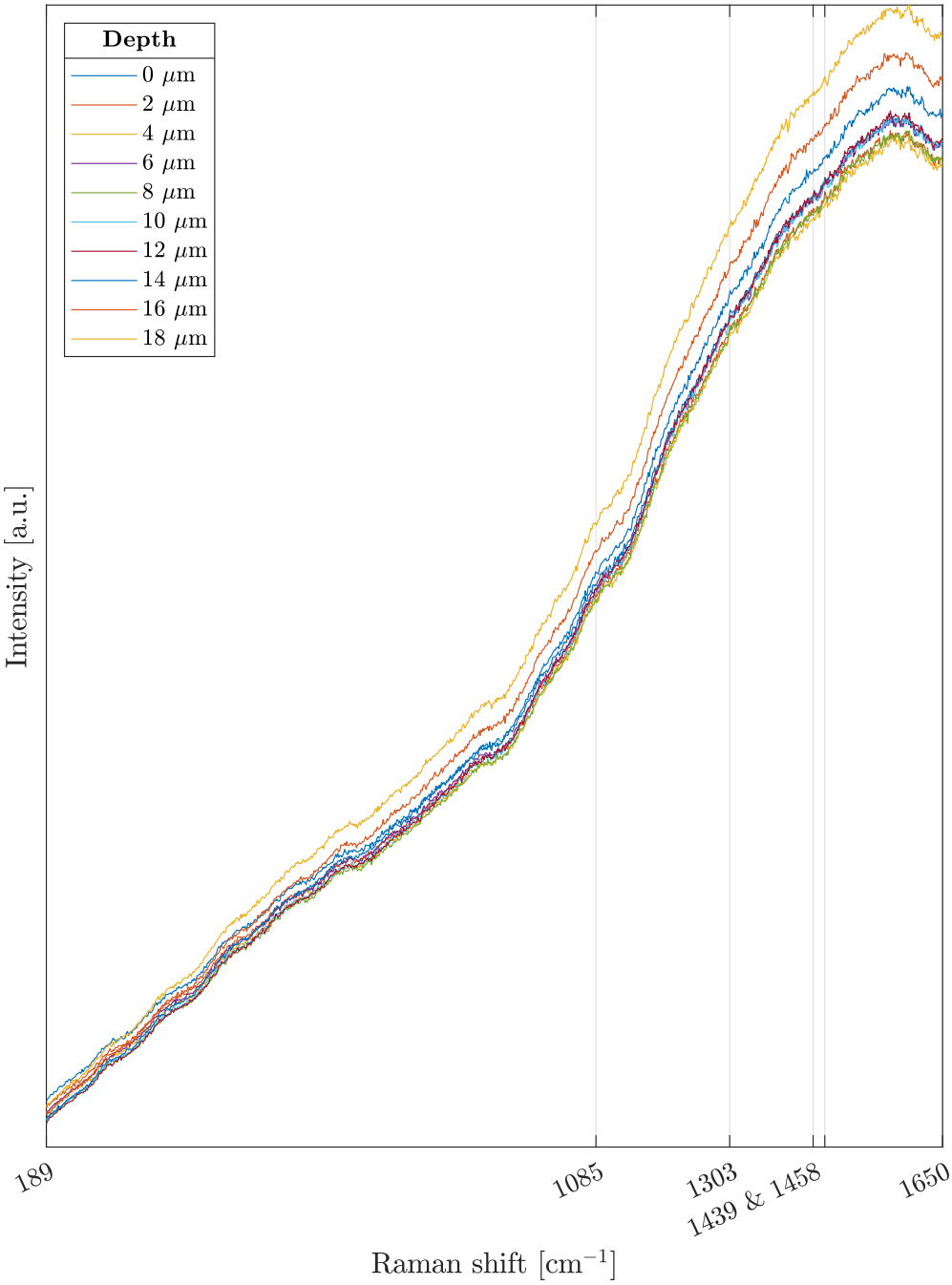

Figure S - 29: Raman depth profile for Zn32 (70 days ageing).

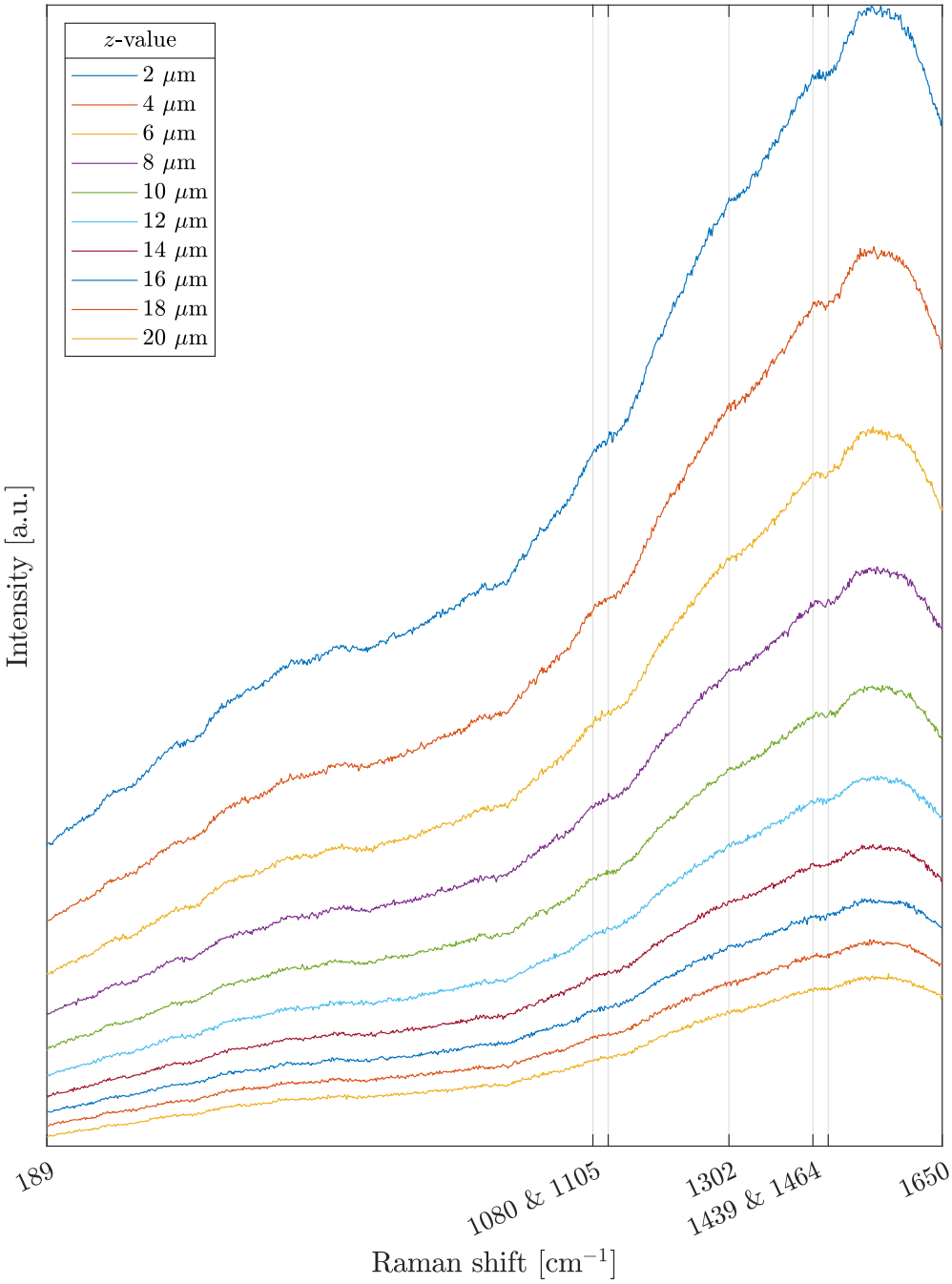

Figure S - 30: SORS spectra for Cu35 (120 days ageing).

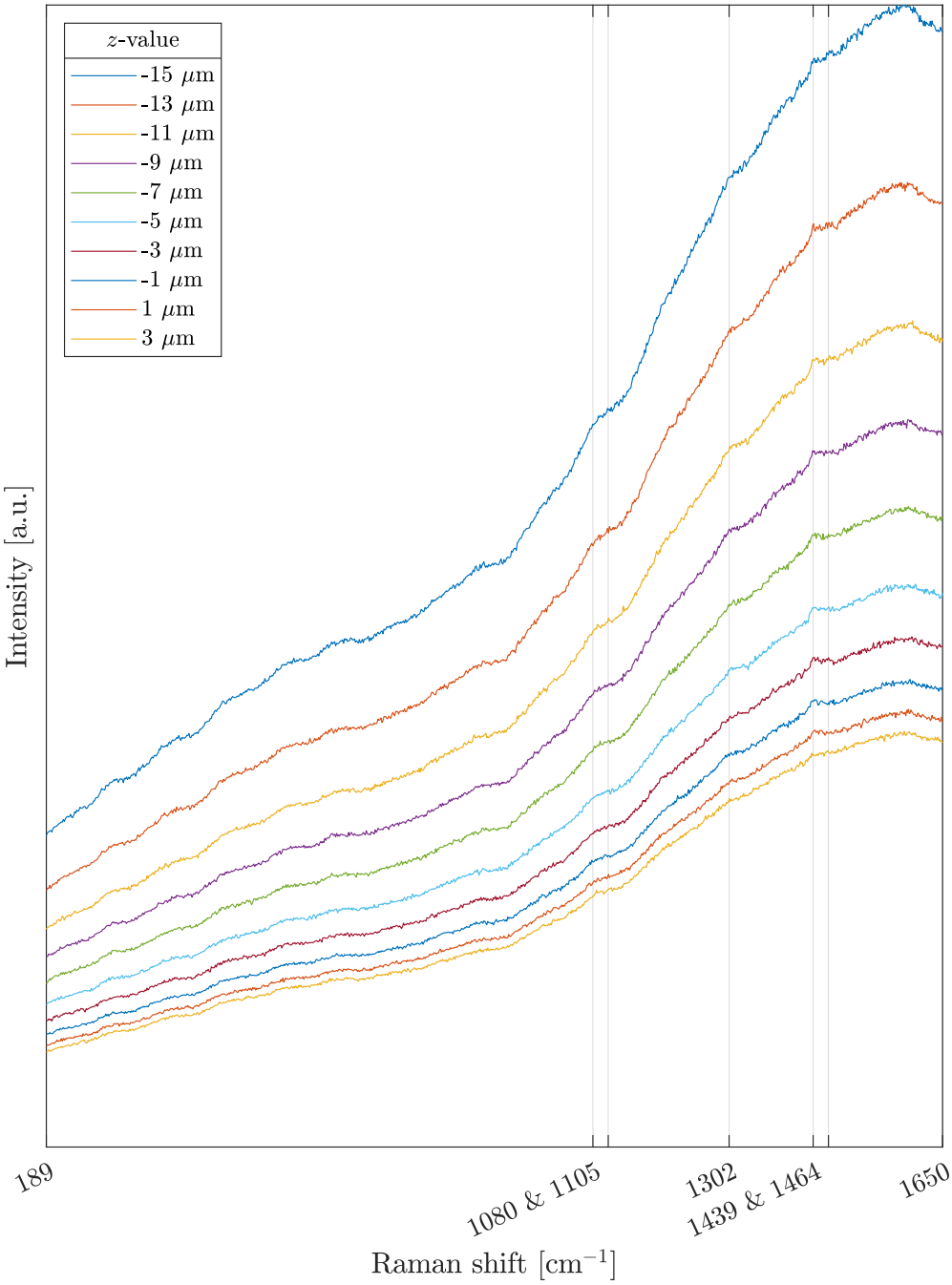

Figure S - 31: SORS spectra for Cu38 (120 days ageing).

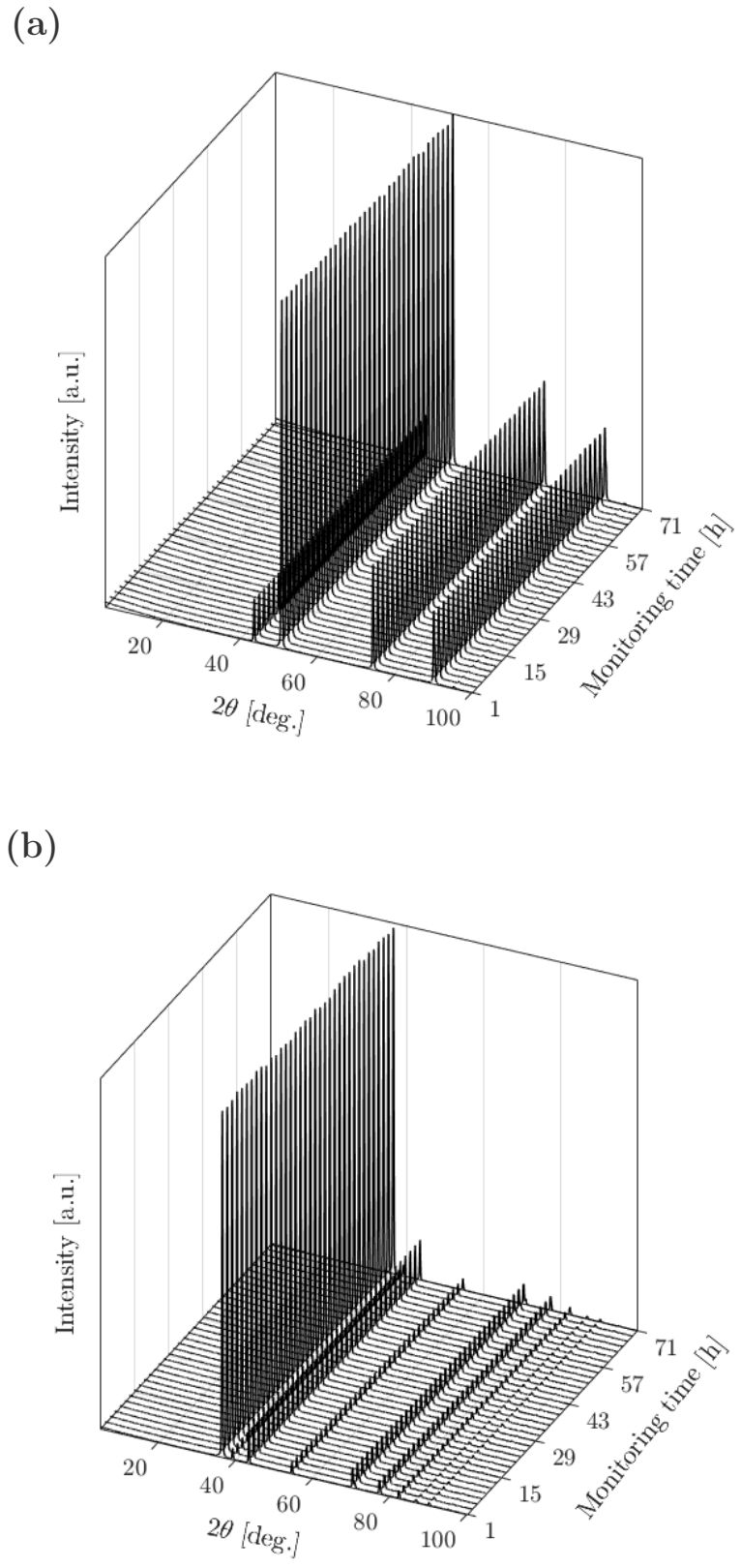

Figure S - 32: X-ray diffractograms for copper (a; Cu_XRD_01) and zinc (c; Zn_XRD_01) samples, after deposition of 1 μL-drop of a solution of palmitic acid in ethanol and monitoring for 72 hours.

This page was intentionally left blank.

A

Acknowledgments

> ...Let me start at the beginning, one picture at a time. But first let me pack my bag. I have a flight leaving soon.
>
> Mia Kankimäki. The women I think about at night. 2021

Dutiful and heartfelt thanks to:

Overall help with the writing of the manuscript Vì Cecilia Erik Kronberg (LaTeX assistance) and Roshan Paladugu, Arianna Passaretti and Amalia Siatou, Laura Brambilla and Edith Joseph.

Technical help in coding and production of figures and plots Vì Cecilia Erik Kronberg (Matlab) and Roshan Paladugu (R).

Discussion on potential applications of mathematical modelling approaches for simulated data Emanuela Bosco, Thomas Mayerhoefer, Vì Cecilia Erik Kronberg.

Providing samples, objects and insights from a conservation perspective Léa Girardin, Elodie Granget, Naïma Gutknecht, Alessandra Lefebvre, Florentine Le Vaillant, Markus Küffner, Jacek Martusewicz, Julie Schröeter, Jan Cutajar, Amalia Siatou.

Help with sample preparation and data acquisition Laure Jeandupeaux (plasma treatment, dip and spin coating), Calixe Heidi Marie-Claude Bénier (laser scanning microscopy), Arianna Passaretti (Raman spectroscopy), Agnese Babini, Jan Cutajar and Federico Grillini (hyperspectral imaging), Saba Zabihzadeh (XRD), David Giovannacci (IR Thermography), Xueshi Bai (OCT and LIBS) and Sarah Richiero (LIBS), Nicoletta Palladino and Brubach Jean-Blaise (SR-FTIR), and Ida Fzalic (SR-XRD).

Hosting institutions and scientific support Clotilde Boust, Katrien Keune, Stefano Mischler, Marine Cotte, Mitra Almasian.

Supervising experience Léa Girardin and Ingrid González Díaz

General support and discussion Osvaldo Russo, Mariateresa Ottavio and Valentina Russo, Caterina Acampora and Matilde D'Accardi, Roshan Paladugu, Vì Ceclia Erik Kronberg, Naïma Gutknecht, Amalia Siatou, Arianna Passaretti, Jan Cutajar, Agnese Babini, Miriam Truffa Giachet, Elodie Granget, Andrea Ramirez Calderon, the ITN-CHANGE team and fellows, the LATHEMA group and the HE-Arc team, Nicoletta Palladino, Yuri Lopez De Meneses, Andrea Giustini, Arianna Sinibaldi and Natalia Macro, Noëlle Lynn Wenger, Katrien Keune, Nicoletta Palladino, Fabio Talarico, Eleonora Balliana, Edith Joseph, Laura Brambilla, Jean Baptiste Thomas, all of the above and many more.

B

Short biography

Silvia received a BSc Degree in Chemistry at Sapienza University of Rome (Italy) in 2015, with a thesis on the characterization of yellow acrylic formulations in collaboration with the Superior Institute for the Conservation and the Restoration (ISCR, Rome, Italy). In 2018, she obtained a MSc Degree in Science and Technologies for the Conservation and the Restoration of Cultural Heritage as part of the European Master Programme in Archaeological Material Science. She concluded her Master with a study on the characterization and conservation of Roman iron nails hosted at Cà Foscari University of Venice (Italy), using analytical and digital techniques. During her studies, she trained privately as a conservator-restorer of paintings, archaeological and cellulosic materials. In 2019, she worked on the development of nanoscaled treatments for the conservation and the restoration of metal and stone objects at University of L'Aquila (Italy). From 2019 to 2022 she joined the the Haute Ecole Arc Conservation Restoration research team in Neuchatel (Switzerland), where she worked on the study of the degradation of painted metal objects as a doctoral candidate (University of Neuchatel) within the MSCA ITN-CHANGE Programme. Passionate about contemporary art, informatics, corrosion and conservation science, she has been trained in chemometrics (Radboud University, The Netherlands, 2018; University of Genova, Italy, 2020-2021) and imaging techniques for Cultural Heritage (IPERION CH Training Camp, Comacchio, Italy, 2018, ITN-CHANGE Training Schools, 2019-2022) and developed skills in the study of metal objects and their degradation processes at the Soprintendenza Archeologia, Belle Arti e Paesaggio delle Marche (Italy, 2016), Soprintendenza Capitolina at Palazzo Braschi (Roma, Italy, 2016) and at The British Museum (UK, 2017). Since 2020, she is Wiki editor of the infrared radiation imaging page promoted by the American Institute of Conservation (AIC) Imaging Working Group.

Contributions

Conference presentations

- 5 SEP 2022 – 9 SEP 2022: "Revealing the Degradation Patterns: Imaging Techniques for the Study of the Formation of Metal Soaps on Painted Metal Objects". *Metal2022 interim meeting of the ICOM-CC Metal Working Group*, https://metal2022.org/
- 9 JUL 2022 – 15 JUL 2022: "Analysis and assessment of degradation of polychrome metal artefacts". *Gordon Research Conference (GRC) and Gordon Research Seminar (GRS) Scientific Methods in Cultural Heritage Research*, https://www.grc.org/scientific-methods-in-cultural-heritage-research-conference/2022/
- 20 MAY 2022: "Analysis and assessment of degradation of polychrome metal artefacts". *Journée Doctorale HES-SO*, https://www.hes-so.ch/recherche-innovation/formation-doctorale-et-releve/journee-doctorale
- 27 APR - 29 APR 2022: "Monitoring metal soaps formation on painted metals: challenges in processing reflectance FTIR time-series chemical images in absence of sharp features". *Computational approaches for technical imaging in cultural heritage (7th IP4AI meeting)*, https://art-ict.github.io/artict/Conference.html
- 1 DEC 2021 – 3 DEC 2021: "2D chemical imaging for the monitoring of the formation of metal soaps on oil-painted copper and zinc substrate". *CollectionCare: new challenges in preventive conservation, predictive analysis and environmental monitoring*, https://www.collectioncare.eu/conference/
- 18 JAN 2021 – 19 JAN 2021: "La dégradation des métaux peints : échantillons-modèles pour l'étude de la formation de savons métalliques". *Journée ICOM Métal France - Métal: support de décor ou élément du décor. Approches et Traitements pour leur Conservation*, https://www.loire-atlantique.fr/44/culture-et-patrimoine/journee-icommetal-france/c_1358342
- 2 SEP 2019 – 6 SEP 2019: "CHANGE: Cultural Heritage Analysis for New GEnerations". *Metal2019 interim meeting of the ICOM-CC Metal Working Group*, https://metal2019.org/

Publications

- Russo S., Brambilla L., Thomas J.B., and Joseph E. 2022. Revealing degradation patterns: imaging techniques for the study of metal soap formation on painted metal objects. In: *Proceedings of the interim meeting of the ICOM-CC Metal Working Group*, Helsinki 5 – 9 September 2022.
- Russo S., Brambilla L., Thomas J.B., and Joseph E. 2022. 2D Chemical Imaging for the Monitoring of the Formation of Metal Soaps on Oil-Painted Copper and Zinc Substrates. In: *Preventive Conservation, Predictive Analysis and Environmental Monitoring* E. Bosco, L. Fuster-Lopez, and A. Perles, eds. Springer [submitted].

Collaborative articles

Joseph E., Albelda-Berenguer M., Cornet E., Cuvillier, L., James S., Mathys L., Monachon M., Passaretti A. and Russo S. (2020). Innovative approaches towards a green and sustainable metal conservation. *Chimia* **74**(611). DOI: 10.2533/chimia.2020.611.